Magnetic and photoluminescent properties of rare-earth complexes of pyrazole-substituted 1,10-phenanthroline

Zur Erlangung des akademischen Grades eines

DOKTORS DER NATURWISSENSCHAFTEN

(Dr. rer. nat.)

von der KIT-Fakultät für Chemie und Biowissenschaften

des Karlsruher Instituts für Technologie (KIT)

genehmigte

DISSERTATION

von

M. Sc., Sören Schlittenhardt

1. Referent: Prof. Dr. Mario Ruben
2. Referentin: Prof. Dr. Annie K. Powell

Tag der mündlichen Prüfung: 12.12.2023

Eidesstattliche Erklärung

Eidesstattliche Versicherung gemäß§13 Absatz 2 Ziffer 3 der Promotionsordnung des Karlsruher Instituts für Technologie für die KIT-Fakultät für Chemie und Biowissenschaften:

1. Bei der eingereichten Dissertation zu dem Thema “Magnetic and photoluminescent properties of rare-earth complexes of pyrazole-substituted 1,10-phenanthroline” handelt es sich um meine eigenständig erbrachte Leistung..
2. Ich habe nur die angegebenen Quellen und Hilfsmittel benutzt und mich keiner unzulässigen Hilfe Dritter bedient. Insbesondere habe ich wörtlich oder sinngemäß aus anderen Werken übernommene Inhalte als solche kenntlich gemacht.
3. Die Arbeit oder Teile davon habe ich bislang nicht an einer Hochschule des In- oder Auslands als Bestandteil einer Prüfungs- oder Qualifikationsleistung vorgelegt.
4. Die Richtigkeit der vorstehenden Erklärung bestätige ich.
5. Die Bedeutung der eidesstattlichen Versicherung und die strafrechtlichen Folgen einer unrichtigen oder unvollständigen eidesstattlichen Versicherung sind mir bekannt.

Ich versichere an Eides statt, dass ich nach bestem Wissen die reine Wahrheit erklärt und nichts verschwiegen habe.

....	....
Ort und Datum	Unterschrift

Acknowledgements

First of all, I want to thank my supervisor Prof. Mario Ruben for giving me the opportunity to do my PhD in his group and his continuous supervision of my project. A huge thank you to Dr. Senthil Kuppusamy who has been vital for establishing the topic of this thesis and who has been very supportive throughout, especially concerning the optical measurements and their interpretation. A big thank you to Prof. David Hunger and his students, Evgenij Vasilenko, Vishnu Unni and Jannis Hessenauer who performed the SHB studies presented. As a major part of this thesis is based on results obtained from X-ray diffraction measurements, I want to thank Dr. Olaf Fuhr and Prof. Dieter Fenske for their helpful comments on XRD measurements and refinement. A very very special thank you, therefore, also to Dr. Andreas Eichhöfer, who sadly passed away unexpectedly not even two months prior to submission of this thesis. Andreas was always extremely helpful and welcoming, whenever I had trouble with the diffractometer or any other instrument one could think of. Scientifically, I also want to thank Dr. Eufemio Moreno-Pineda, who left our group at the very beginning of my PhD. Nevertheless, he was the one building my foundation, especially in the fields of molecular magnetism and X-ray crystallography. Other than that, he was also still always willing to help, even though living on the other side of the globe. Of course a big thank you to the whole Karlsruhe Ruben group and the Mayor group between 2019 and 2023, for always being welcoming and helpful.

And last but not least, thank you to all my friends and family inside and outside of the work group for keeping me sane throughout the duration of the PhD and being the best people I know.

Abstract

Trivalent lanthanide ions have shown fascinating physical properties that are a consequence of their unique electronic configuration. They have been studied both magnetically and optically, revealing remarkable behaviour. In magnetism, they have been employed for a long time in the fabrication of high coercivity permanent magnets, while their optical features led to the fabrication of LEDs among others. Most famously, the europium-based marking of the euro bank notes. While many of those applications of lanthanide ions have used the ions in inorganic host materials, molecular Ln(III) complexes have attracted a lot of attention in recent time. As both the magnetic and optical properties are dependent on the environment of the ion, molecular materials allow control over the observed properties of a given compound, by adjusting the coordination chemically. Shifting to molecular materials has led to the discovery of single-molecule magnet behaviour in a complex of a single Ln(III) ion, while earlier reports were based on multinuclear transition metal compounds. In photoluminescence spectroscopy, the emission of Ln(III) ions can be achieved by sensitization of so-called antenna ligands, drastically increasing the otherwise low efficiency of Ln(III)-based emission. Molecular Ln(III) systems have been proposed to function as qubits for quantum information processing schemes, which is one of the most ambitious goals of modern research. Both the magnetic and the optical properties give access to establishing quantum superposition, which is the foundation of any quantum algorithm. In fact, the first experiments of quantum algorithms using molecular Ln(III) compounds have already been successfully carried out.

In this thesis, a well established antenna ligand 1,10-phenanthroline (phen) has been substituted with pyrazole and dimethyl-pyrazole moieties to obtain a ligand suited for the complexation of trivalent lanthanide ions. The ligands were employed to obtain complexes of the whole lanthanide series, which are fully characterized. Magnetic and optical measurements were performed to understand the relationship between the molecular structure and the observed physical properties. Highly specialized optical measurements were carried out in order to draw a comparison to other Ln(III)-based complexes in the literature. The observation of narrow optical linewidths which correspond to long coherence lifetimes associated with the $^5D_0 \rightarrow ^7F_0$ transition of Eu(III) could indicate that the obtained Eu(III) complexes can be pursued to realize molecule-based quantum information processing architectures.

Zusammenfassung

Aufgrund ihrer besonderen Elektronenkonfiguration, zeigen dreiwertige Ionen der Lanthanide faszinierende physikalische Eigenschaften. Sowohl im Hinblick auf ihre magnetischen, als auch auf ihre optischen Eigenschaften wurde bemerkenswerte Forschungsergebnisse erzielt. Die Herstellung der stärksten kommerziell erhältlichen Dauermagnete basiert auf Lanthanidionen, und deren optischen Eigenschaften werden bei der Herstellung von LEDs ausgenutzt. Die bekannteste optische Anwendung von Lanthanidionen, ist wohl die Fluoreszenzmarkiering der Euro-Banknoten auf Europiumbasis. In jüngerer Vergangenheit haben molekulare Lanthanidkomplexe zusätzliches Interesse geweckt. Da sowohl die magnetischen, wie auch die optischen Eigenschaften auf der chemischen Umgebung des Ions basieren, erlauben molekulare Verbindungen die chemische Funktionalisierung entsprechend der gewünschten physikalischen Eigenschaften. Die intensive Forschung an Komplexen der Lanthanide hat zur Entdeckung von Einzelmolekülmagneten auf Basis eines einzigen Metallions geführt. Frühere Einzelmolekülmagnete basierten auf multinuklearen Übergangsmetallkomplexen. Durch die Benutzung sogenannter Antennenliganden konnte die Emission von Ln(III)-Ionen verstärkt werden, die ohne die Sensibilisierung durch die Liganden sehr ineffizient verläuft. Des Weiteren, werden Ln(III)-basierte Moleküle als Qubits für Quanten-Informationsverarbeitung diskutiert, was eines der aktivsten Felder der modernen Wissenschaft markiert. Der quantenphysikalische Effekt der Superposition, der die Grundlage für alle Quantenalgorithmen ist, kann sowohl durch die magnetischen wie auch die optischen Eigenschaften erreicht werden. Es konnten bereits erfolgreiche Experimente durchgeführt, bei denen Lanthanidkomplexe als Basis für Quantenalgorithmen verwendet wurden.

Diese Arbeit behandelt die Modifikation eines bekannten Antennenliganden 1,10-Phenanthrolin durch Substitution mit Pyrazol- und Dimethylpyrazol-Gruppen. Die synthetisierten Liganden wurden für die Komplexierung der gesamten Reihe der Lanthanidionen verwendet und die resultierenden Komplexverbindungen wurden vollständig charakterisiert. Um den Einfluss der molekularen Struktur auf die physikalischen Eigenschaften zu verstehen, wurden magnetische SQUID- und optische Photolumineszenz-Messungen durchgeführt. Außerdem wurden spezialisierte optische Messungen durchgeführt, um die Eigenschaften im Hinblick auf quantentechnologische Anwendung zu überprüfen und in Relation zu bereits bekannten Komplexen zu setzen. Das Auftreten von schmalen optischen Linienbreiten in dem $^5D_0 \rightarrow {}^7F_0$ Übergang von Eu(III)-basierten Komplexen bedeutet ein lange Kohärenzzeit und deutet darauf hin, dass Quanten-Informationsverarbeitung auf molekularer Ebene möglich ist.

Contents

List of Figures

List of Tables

Abbreviations used

AC	Alternating current
AI	Artificial intelligence
CASSCF	Complete active space self consistent field
CC	Coupled cluster
CI	Configuration interaction
CN	Coordination number
Cp	Cyclopentadienyl
CShM	Continuous shape measure
DC	Direct current
EPR	Electron paramagnetic resonance
HF	Hartree Fock
IR	Infrared
ISC	Inter system crossing
KD	Kramer's doublet
LED	Light emitting diode
Ln	Lanthanide
NMR	Nuclear magnetic resonance
NV	Nitrogen vacancy
Pc	Phthalocyanine
phen	1,10-phenanthroline
PL	Photoluminescence
PXRD	Powder X-ray diffraction
QIP	Quantum information processing
QTM	Quantum tunnelling of magnetization
RASSCF	Restricted active space self consistent field
REE	Rare earth element
REI	Rare earth ion
SHB	Spectral hole burning
SMM	Single molecule magnet
SOC	Spin orbit coupling
SQUID	Superconducting quantum interference device
TA-QTM	Thermally assisted quantum tunnelling of magnetization
UV	Ultraviolet
XRD	X-ray diffraction
ZFS	Zero field splitting

1 Motivation

On November 30th 2022, OpenAI released the first online demo version of ChatGPT, a chatbot that allows users to interact with artificial intelligence (AI). Within less than a week, ChatGPT had reached over one million users and 100 million active monthly users after approximately two months, making it the fastest growing application in history.[1,2] The success of ChatGPT is undoubtedly linked to its versatility, as a user can obtain everything from answers to specific questions over program code to creative outputs like newly generated poems. Simultaneously, machine learning algorithms are rising in popularity to evaluate trends in large data sets, for example in pharmaceutics, or in advancing image recognition software.[3] Obviously, such applications require immense amounts of computational power, only accessible through modern day supercomputers. The miniaturization of basic physical components has already led to an unthinkable increase in data storage density and computational efficiency throughout the last decades, as transistors can be built at a nanometer scale, fitting 100 million transistors in a square millimeter of an integrated circuit.[4] However, the minimal size of classical transistors is limited, as the processes of extremely small units and particles are following quantum mechanics. Therefore, in order to achieve further improvements a different approach has to be undertaken, which is computation on a quantum level. The concept of quantum computation has already been established in the early 1980's by Paul Benioff,[5] Yuri Manin[6] and Richard Feynman,[7] and the first quantum algorithms were published soon after in 1985 by David Deutsch and Richard Jozsa,[8,9] while there was no technological platform available to perform quantum information processing (QIP). The most widely known quantum algorithms are Peter Shor's algorithm for prime factorization of large integers[10,11] and Lov Grover's search algorithm in an unsorted data base,[12] published in 1994 and 1997, respectively. Both algorithms demonstrate a speedup compared to classical algorithms (exponential speedup for Shor's and quadratic speedup for Grover's algorithm) while tackling common problems of computer science, as for example the prime factorization is the basis of cryptography. Researchers believe that the first beneficiaries of applicable quantum computers will be quantum chemical calculations, while for example quantum machine learning is a more long-term application. Nevertheless, there have already been reports of simulations where a quantum based model using 60 parameters would achieve similar results to a classical neural network working with 59000 parameters, while also demanding less training iterations.[3] In order to manufacture a working quantum computer, quantum bits (Qubits) which are the quantum analogue of classical bits are needed. There have been several different proposals and approaches to the construction of qubits, that will be discussed in more detail in section 2.5. The currently largest quantum computer is “IBM’s” Osprey with 433 individual qubits,[13] already significantly larger than “Google’s” 2019 processor Sycamore that had 53 qubits.[14] Both Osprey and Sycamore are based on super-conducting transmon qubits.[15] Another approach for the construction of qubits are molecular systems, which offer a variety of benefits. Complex molecules of lanthanide ions are promising candidates due to their physical properties.[16,17] Both their optical[18] and magnetic properties[19] can be exploited to create two-level systems that can function as qubits. Depending on the employed lanthanide ion, multi-state systems can be established, that function as so-called qu*d*its, allowing even higher computational complexity.[20,21] In fact Lov Grover’s algorithm has been demonstrated on a single lanthanide-based molecule.[22,23] One great advantage of molecular compounds is their monodispersity which is a consequence of chemical synthesis opposed to fabrication by various technological procedures. Every molecule of a given compound is an exact copy of its neighbours, allowing scalable fabrication of quantum processors. Besides, by means of chemical synthesis the properties of a molecule can be fine-tuned to the requirements that are given by the QIP setup. Despite the possibilities to act as qubits, lanthanide systems have been employed as molecular spin valves[24,25] and transistors[26] as well as in non-quantum technologies like the fabrication of LEDs[27] or strong permanent magnets[28,29] and photovoltaic cells,[30] among others.

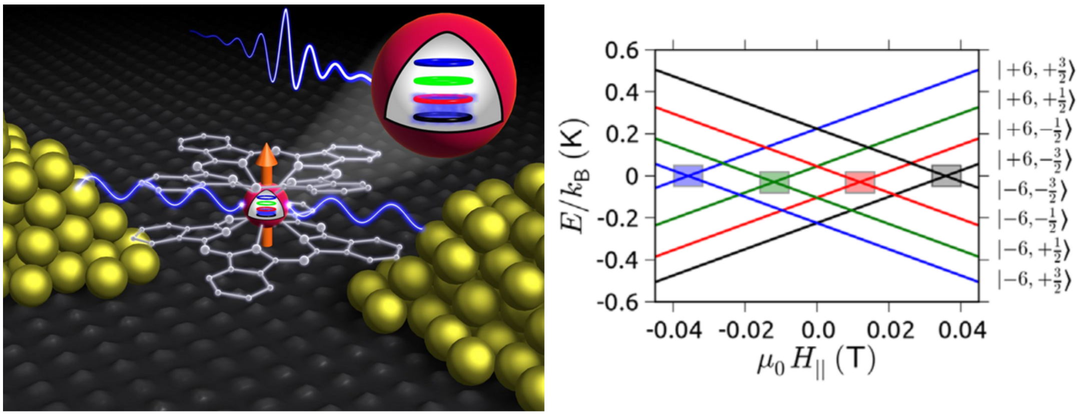

Figure 1.1: A single molecule is being employed as a qudit to perform a quantum algorithm.[22,31]

In this thesis a series of rare-earth coordination compounds has been synthesized and chemically characterized. Studies of their magnetic and optical properties are aimed to provide a contribution to the understanding of the interplay between the chemical structure and the observed physical properties. Specifically the europium and ytterbium complexes have been tested by means of spectral hole burning techniques (see section 2.3) in order to evaluate on the possibility of optical qubit fabrication.

2 Introduction

The following chapter is designed to both provide a brief historical background to the important topics within this thesis as well as to paint a picture of recent advances in the fields. Also measuring techniques and fundamentals will be discussed, which are the foundation to proper understanding of the results presented in the later chapters of this thesis.

2.1 Lanthanides and Rare Earth Elements

The lanthanides or the lanthanide series refers to the 15 elements from La (Z = 57) to Lu (Z = 71) in the periodic table. When referring to them in a general sense the symbol Ln is commonly used to replace the atomic symbol of the element in question.

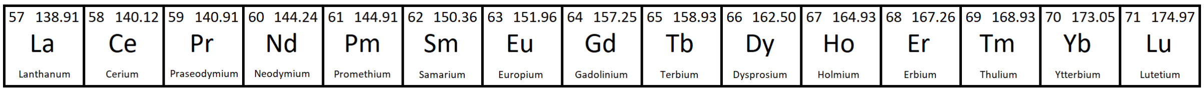

57 138.91	58 140.12	59 140.91	60 144.24	61 144.91	62 150.36	63 151.96	64 157.25	65 158.93	66 162.50	67 164.93	68 167.26	69 168.93	70 173.05	71 174.97
La	Ce	Pr	Nd	Pm	Sm	Eu	Gd	Tb	Dy	Ho	Er	Tm	Yb	Lu
Lanthanum	Cerium	Praseodymium	Neodymium	Promethium	Samarium	Europium	Gadolinium	Terbium	Dysprosium	Holmium	Erbium	Thulium	Ytterbium	Lutetium

Figure 2.1: Elements of the Lanthanide series.

They were first discovered in the late 18th century in minerals found in Ytterby (Sweden), however, it took researchers until the early 20th century to separate all the elements. Because large deposits of Ln-containing minerals are very uncommon throughout the earth's crust, scientists coined the term rare earth elements (REEs). However, the REEs are including the elements scandium (Z = 21) and yttrium (Z = 39) in addition to the lanthanides, because both Sc and Y are often found in minerals alongside lanthanides due to their chemical resemblance, *vide infra*. It should be mentioned that the term rare earth element can be misleading as the REEs are much more abundant than the term suggests. The most abundant REEs are cerium, neodymium and lanthanum which each are approximately as abundant on earth as copper. Figure 2.2 shows the abundancies of the elements up to Pb within the earth's crust. Importantly promethium (Z = 61) is, alongside technetium (Z = 43), one of only two elements of the periodic table below Z = 83 without any stable isotope. Out of the 16 stable REEs thulium is the rarest, followed by lutetium.

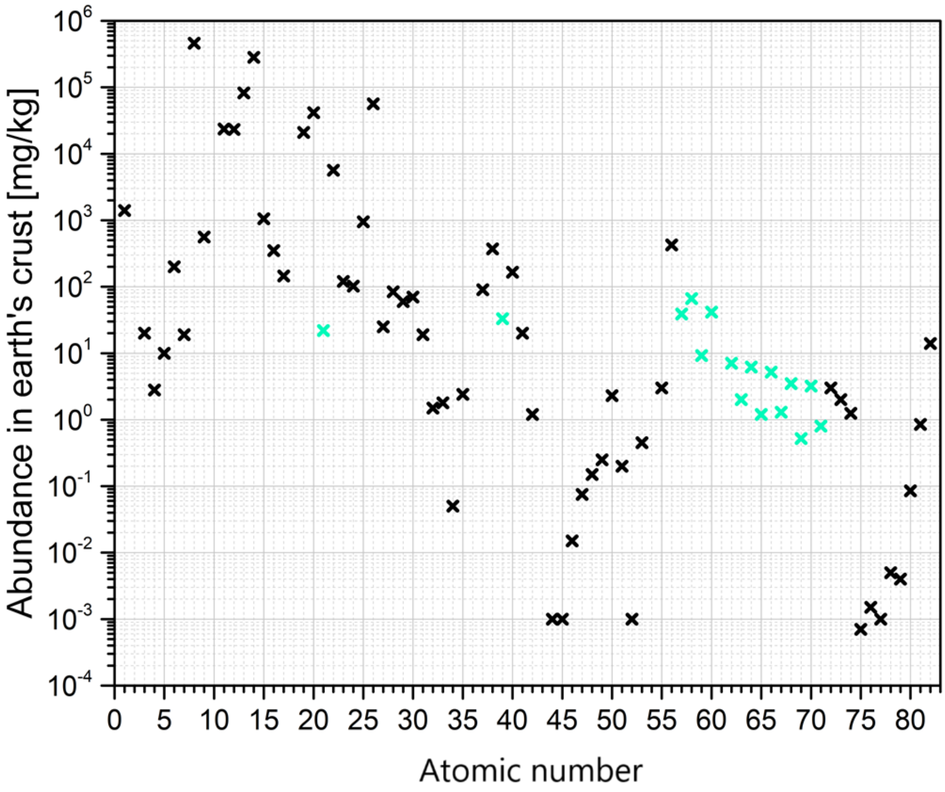

Figure 2.2: Natural abundance of elements in the earth's crust. The REEs are highlighted in cyan, the noble gasses, Tc and Pm were left out on purpose. The values are taken from the Handbook of Physics and Chemistry.[32]

The general electronic configuration of a lanthanide atom is $[\mathrm{Xe}]6s^2 4f^{n+1}$, with n = 0 for Lanthanum (exceptions are Ce, Gd and Lu, where the electron configurations takes the form $[\mathrm{Xe}]6s^2 5p^1 4f^n$). Therefore, stable trivalent cations are observed for all the elements within the lanthanide series, showing an electron configuration of $[\mathrm{Xe}]4f^n$. This is comparable to the behaviour of 3d transition metals, which commonly appear as divalent ions due to their general electron configuration of $[\mathrm{Ar}]4s^2 3d^n$. However, transition metals also show a wide variety of accessible oxidation states besides +II, while lanthanides generally don't show oxidation states other than +III. This is a consequence of the different properties of the 3d and 4f shells. In Ln's the 4f orbitals are in closer proximity to the atomic nucleus than the fully occupied 5s and 5p orbitals, which are providing efficient shielding of the 4f electrons against the chemical environment. Such shielding is not available to the d-orbitals of transition metals which, therefore, show more diverse redox chemistry. Due to the general rule of empty, half-filled and fully filled shells being more stable than partially filled shells, scandium and yttrium exclusively form trivalent ions. It is due to this property, that they show chemical resemblance to lanthanides and are, therefore, included to the group of rare earth elements. Oxidation states other than

+III are observed in some lanthanides, where removal or addition of an electron causes an empty, half-filled or fully filled shell, e.g. Ce(IV) or Eu(II). It should be mentioned that nowadays researchers have reported a variety of uncommon oxidation states achievable for lanthanide ion under very specific conditions, but these are generally extremely sensitive and only stable under strictly inert conditions. The aforementioned proximity of the 4f orbitals towards the nucleus causes several interesting effects which are in turn majorly responsible for the physical and chemical properties of lanthanides. Spin orbit coupling (SOC) is a general phenomenon observed in open shell systems with $L > 0$ (where L is the orbital angular momentum quantum number). In heavy atoms, the electrons which are close to the nucleus show an increased mass due to relativistic effects based on their high velocities. In closed shell systems, this does not affect SOC (because $L = 0$), however, in lanthanides relativistic effects are not negligible and, as the 4f shell is only partially occupied, cause very strong SOC. As a reference figure 2.3 shows a schematic energy diagram of a lanthanide ion emphasizing the different contributions. In Ln's the SOC is playing a major role, stronger than the effect of the ligand field exerted by the chemical environment. In comparison, for transition metals SOC is typically only viewed as a perturbation much weaker than the splitting caused by the ligand field.

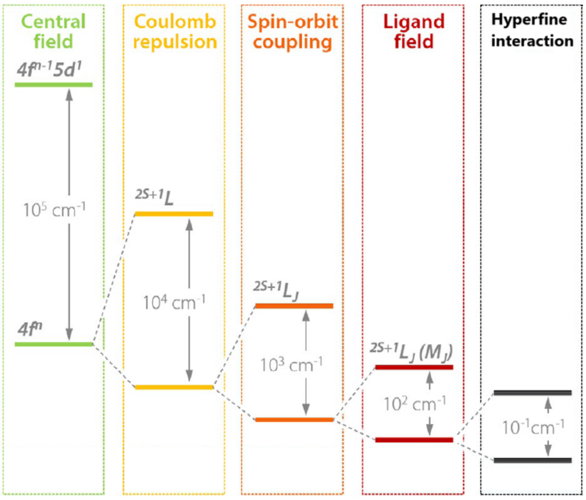

Figure 2.3: Generalized energy diagram of a Ln(III) ion based on different effects.[33]

Instead of describing a system using the two quantum numbers S, the electronic spin, and L, the orbital angular momentum, a third, combined quantum number becomes relevant, termed the total orbital momentum J. The coupling of S and L to J is referred to as Russel-Saunders coupling. J takes all values from $|L - S|$ to $L + S$ in integer steps. For less than half-filled shells (Ce - Eu) the ground state is characterized with $|J = L - S|$, while $J = L + S$ is the ground state in systems with a more than half-filled shell (Tb - Yb). For La, Gd and Lu $L = 0$ and therefore, $J = S$. The spin-orbit coupled state of a lanthanide ion is typically given by its so-called term symbol, which represents all three quantum numbers in the form: ${}^{2S+1}L_J$, where S and J are given as number values and L is represented with S, P, D, F, G, H, I for $L = 0, 1, 2, 3, 4, 5, 6$, respectively. Let's take the ground state of Eu(III) as an example: There are six unpaired electrons in the 4f shell, giving $L = 3+2+1+0-1-2 = 3$ and $S = 6 \cdot \frac{1}{2} = 3$. As the shell is less than half-filled we get $J = L - S = 0$, therefore, the term symbol is: ${}^7F_0$. The term symbols and quantum numbers are the foundation to understanding the physics of lanthanide ions.

A second effect that is a consequence of the nature of the 4f electrons is referred to as lanthanide contraction. Due to the diffuse nature of the 4f orbitals the nuclear charge is only weakly shielded and the outer lying 6s and 5p shells are more strongly attracted, causing an unusual high decrease of the ionic radii among the Ln's. Table 2.1 lists the ionic radii of all Ln(III) ions.

Table 2.1: Ionic radii of Ln(III)-ions. Values are taken from the Handbook of Physics and Chemistry for CN = 6.[32]

Element	Number of 4f electrons	Ionic radius [pm]
La	0	104.5
Ce	1	101.0
Pr	2	99.7
Nd	3	98.3
Pm	4	97.0
Sm	5	95.8
Eu	6	94.7
Gd	7	93.8
Tb	8	92.3
Dy	9	91.2
Ho	10	90.1
Er	11	89.0
Tm	12	88.0
Yb	13	86.8
Lu	14	86.1

The ionic radii of Ho(III) (90.1 pm) and Er(III) (89.0 pm) are very close to the ionic radius Y(III) at 90.0 pm, as a consequence of the lanthanide contraction, even though yttrium is much lighter of an atom. The similar radii of the trivalent ion explains the chemical resemblance mentioned above. Chemically Ln's tend to form exclusively non-covalent bonds, which is again based on the shielded nature of the 4f electrons. Therefore, Lanthanides are generally found as inorganic salts or as coordination complexes. The lanthanide contraction results in all Ln(III) ions being considerably hard ions, therefore, making hard donor ligands like O-donors preferable. In transition metals the symmetry of the coordination sphere in a complex is strongly influenced by the electronic configuration, as the ligand field strongly influences the energy of the system at hand. As an example, it is known that Ni(II) shows a preference to forming square planar complexes,[34] stabilizing the $3d^8$ configuration, while $3d^6$ in Fe(II) benefits from octahedral coordination.[35] In Ln's however, the ligand field doesn't have a strong enough effect to influence the resulting symmetry, rather Ln(III) ions try to fill as much of the coordination sphere as sterically possible. This leads to high coordination numbers in lanthanide complexes and symmetries that are mainly defined by the ligand's structure and the ionic radius of the central ion.[36,37] Low coordination numbers are only accessible through very bulky ligands, which are sterically demanding and prevent other ligands from entering the coordination sphere. Without the steric hindrance very often solvent molecules will coordinate to the Ln, filling the coordination sphere. The lowest coordination number observed for lanthanides is three, which can be for example achieved using the bulky bis-(trimethylsilyl)amide ligand.[38–40]

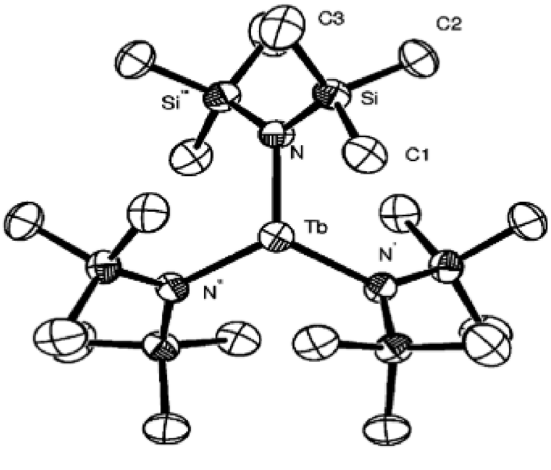

Figure 2.4: Molecular structure of the three-coordinate $[Tb(N(SiMe_3)_2)_3]$.[39]

Four- and five-coordinate complexes are accessible with the same ligand in the forms of for example $[La(N(SiMe_3)_2)_3(Ph_3PO)]$ and $[Y(N(SiMe_3)_2)_3(CyNC)_2]$ (Cy = cyclohexyl).[38] Six is a rather commonly observed coordination number, as it appears for example in the anhydrous chlorides. However, lanthanide halide salts are generally hygroscopic adopting hexa-, hepta- and octahydrated stoichiometries under air. In aqueous solution the observed $[Ln(H_2O)_n]^{3+}$ ions are found with $n = 9$ for the early lanthanides La - Sm and $n = 8$ for Dy - Lu, due to their smaller radius. The metals Eu, Gd and Tb show a mixture of eight- and nine-coordinate species.[38] These coordination numbers are the preferred for the ions and can be obtained by many combinations of ligands. Significantly higher coordination numbers are only observed for organometallic sandwich-type systems with aromatic π-bonded ligands. The highest coordination number reported for trivalent Ln's this way is 17 in sandwich complexes with one cyclooctatetraenyl- (COT^{2-}) and one cyclononatetraenyl-ligand (CNT^{-}),[41] shown in figure 2.5 (left).

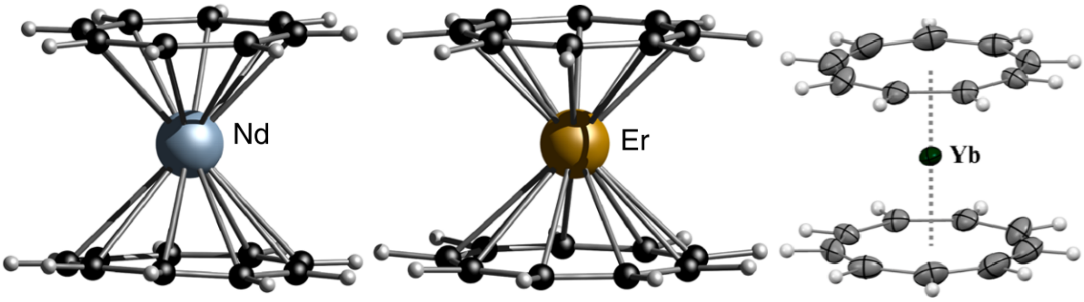

Figure 2.5: Molecular structure of the 17-coordinate $[(\eta^9\text{-}C_9H_9)Ln(\eta^8\text{-}C_8H_8)]$ complexes[41] (left) and the 18-coordinate $[Ln(\eta^9\text{-}C_9H_9)_2]$ complex[42] (right).

It is noteworthy, that comparable 18 coordinate structures have been reported for divalent lanthanide ions with two CNT^{-} ligands[42] (figure 2.5, right).

As the coordination environment around REI's is so diverse, the nuclearity of complexes can be easily increased through the usage of bridging ligands. Having multiple lanthanide ions in close proximity can lead to fascinating molecular structures as well as interesting properties. However, the effect of Ln$\cdots$Ln interactions can be both beneficial and disruptive to the physical properties of the molecule *vide infra*. Monometallic complexes can be achieved employing simple terminating ligands like halides, β-diketonates among others. Combinations of such ligands with tailor-made bridging ligands allows molecular engineered multinuclear complexes.

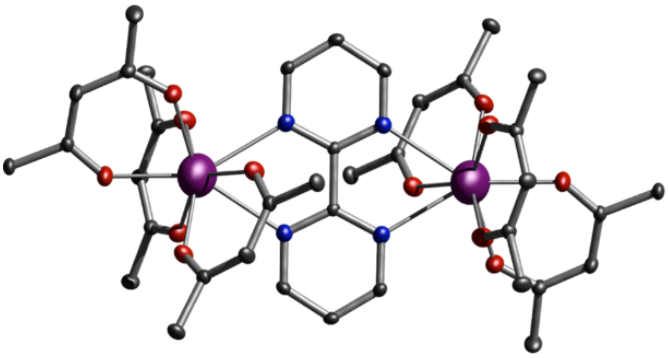

Figure 2.6: Molecular structure of the dimeric $[Dy(thmd)_3]_2bpm$ complex.[43] Where thmd = 2,2,6,6-tetramethyl-3,5-haptanedionate and bpm = 2,2'-bipyrimidine.

The dimeric complex shown in figure 2.6. is constructed by choosing the 2,2'-bipyrimidine ligand as a discrete bridging unit to link two Ln(III) ions, while the β-diketonate-type ligands terminate the ligand sphere and prevent complexes of higher nuclearity.[43] Many ligands can act both as terminating and bridging ligands, in which case a prediction of the molecular structure of a complex is near impossible. Figure 2.7. shows the structure of a nonanuclear complex, where the nine Ln's adopt a sandglass-like architecture.[44]

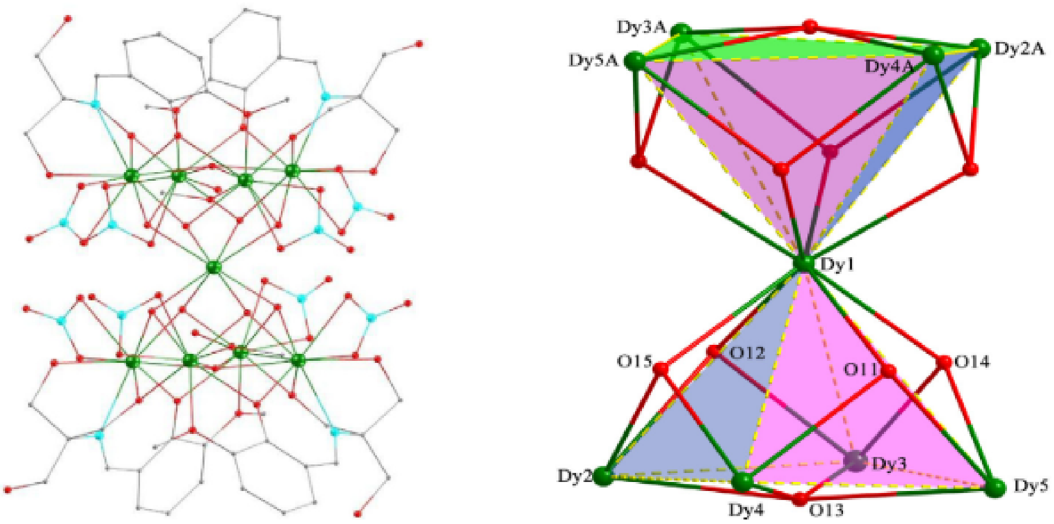

Figure 2.7: Molecular structure of $[Ln_9L_4(OH)_{10}(NO_3)_8(CH_3OH)_2(H_2O)_2]$, where L = 2-(((2-hydroxy-3-methoxyphenyl)methylene)amino)-2-(hydroxymethyl)-1,3-propanediol.[44]

This nonanuclear sandglass has been reported for several different combinations of ligands. Research on lanthanide coordination has produced compounds with many different nuclearities, from mono-, di-, tri- and tetranuclear complexes up to cluster compounds with more than 50 Ln ions in a single molecule.[45–47]

The variety that is chemically available for lanthanide coordination compounds, already makes them a field worth to be studied. However, it is this aspect in combination with their intrinsic physical properties that make lanthanides one of the most important topics in modern research. Their magnetic and luminescent properties, *vide infra*, are technologically relevant and their chemical tunability allows to find molecules with the required qualities.

2.2 Molecular Magnetism

Molecular Magnetism refers to the observation of classical magnetic phenomena on a molecular level. As the compounds under investigation are quantum objects, also non-classical phenomena, e.g. quantum tunnelling of the magnetization (QTM), *vide infra*, are observed. Any closed shell atom, ion or molecule is considered diamagnetic, meaning it does not show any magnetic moment and under the application of an external magnetic field the induced field is opposite of the applied field. In open-shell systems however, the electronic spin of the unpaired electrons yields an observable magnetic moment. Materials with a non-zero magnetic moment are called paramagnetic and their magnetic moments align in an external magnetic field. Irrespective of the system, most electrons will be paired, meaning there are always diamagnetic contributions to the observed magnetic behaviour. However, paramagnetic effects are about three orders of magnitude stronger than diamagnetic effects, allowing the observation of paramagnetism, even in systems with only a single unpaired electron. The magnetic moment of a given system is characterized by:

$$\mu = g_s\sqrt{S(S+1)}\,\mu_B \tag{2.1}$$

μ : Magnetic moment
g_s : Landé factor
S : Spin quantum number
μ_B : Bohr magneton

In systems without considerable orbital contribution $S = \Sigma\, s$, where $s = \frac{1}{2}$ is the spin of a single electron.

The magnetic susceptibility is a very important measure when describing magnetic materials. Upon application of an external field, the magnetic response of a sample can be recorded, with the volume magnetic susceptibility describing the ratio:

$$\chi_V = \frac{M_V}{H} \tag{2.2}$$

χ_V : Volume magnetic susceptibility
M_V : Volume magnetization
H : External magnetic field

$$\chi_V \cdot V = \chi_{mol} \cdot \frac{m}{M} \tag{2.3}$$

V : Volume
χ_{mol} : Molar magnetic susceptibility

m : Mass of the sample
M : Molar mass of the sample

In most cases, especially when dealing with molecular magnetism, the molar magnetic susceptibility is derived from the volumetric susceptibility, as given in equation 2.3. Measurements of the susceptibility are performed at small applied fields, as the definition is only then valid. At higher fields, the magnetization can reach saturation, when all magnetic moments in the sample are aligned. The magnetization and with that the magnetic susceptibility are temperature dependent measures. At high temperatures, the thermal movement of the particles counteracts the alignment within any external field, resulting in M being inversely proportional to T. Therefore, the temperature product with the molar magnetic susceptibility is an even more convenient measure when analysing magnetic materials, as it is (following these assumptions), temperature independent. The Curie law describes the value of the temperature product of the susceptibility based on the magnetic moment of the sample:

$$\chi_{mol} \cdot T = \frac{N_A \cdot g_s^2 \cdot \mu_B^2}{3 \cdot k_B} \cdot S(S+1) \tag{2.4}$$

N_A : Avogadro's constant
k_B : Boltzmann's constant

As discussed previously in section 2.1, S is not a good quantum number in case of lanthanide ions or any other system with strong spin orbit interactions. Instead Curie law can be expressed as a function of the total angular momentum J:

$$\chi_{mol} \cdot T = \frac{N_A \cdot g_J^2 \cdot \mu_B^2}{3 \cdot k_B} \cdot J(J+1) \tag{2.5}$$

$$g_J = \frac{3J(J+1) + S(S+1) - L(L+1)}{2J(J+1)} \tag{2.6}$$

N_A : Orbital angular momentum quantum number
k_B : Total orbital momentum quantum number

Using equation 2.5 it is easy to derive the expected $\chi_{mol}T$ values for any given lanthanide, as shown in table 2.5:

Table 2.2: Magnetic properties of Ln(III) ions.[48]

Element	g_J	$\chi_{mol}T$ [cm^3 K mol^{-1}]
La	-	0.00
Ce	6/7	0.80
Pr	4/5	1.60
Nd	8/11	1.64
Pm	3/5	0.90
Sm	2/7	0.09
Eu	5	0.00
Gd	2	7.88
Tb	3/2	11.82
Dy	4/3	14.17
Ho	5/4	14.07
Er	6/5	11.48
Tm	7/6	7.15
Yb	8/7	2.57
Lu	-	0.00

As expected La(III) and Lu(III) are diamagnetic ions, as they are closed-shell systems. Following the table, also Eu(III) is expected to be diamagnetic, despite being open-shell. This is due to the spin-orbit coupled ground state showing $J = 0$, *vide supra*. However, in case of Eu(III) (and Sm(II)), the energy gap towards the first excited state with $J = 1$ is small enough, so that weakly paramagnetic behaviour is observed for Eu(III) at room temperature. The $\chi_{mol}T$ values observed at room temperature are typically around 1.5 cm^3 K mol^{-1}. Following the assumption given, a plot of $\chi_{mol}T$ vs. T, should give a temperature-independent, therefore horizontal, line. In practice however, this is usually only observed at high temperatures. Upon cooling down molecular materials, depopulation of the Stark sublevels causes a decrease of the magnetic susceptibility and a deviation from Curie's law. The Stark splitting of the magnetic ground state is an effect of the ligand field onto the central magnetic ion. Another influence on the T-dependent behaviour are magnetic interactions. If two (or more) magnetic moments are placed in close enough proximity to each other, they will feel the field created by the neighbouring moment. Magnetic interactions can both be through-space interactions, so-called dipolar interactions, as well as ligand-promoted exchange interactions. Generally exchange interactions are stronger, however they depend on the given structure of a complex molecule. The energy resulting from magnetic interactions can be expressed as a Hamiltonian, in the simplest case between two magnetic centers:

$$\hat{H} = -2J(\hat{S_1} \cdot \hat{S_2}) \tag{2.7}$$

$\hat{H}$: Hamiltonian
J : Interaction constant
$\hat{S}_i$: Spin of the magnetic center i

The factor of -2 is arbitrary and differs between different references, therefore, the Hamiltonian employed by the authors must always be checked when comparing coupling values.[49,50] When discussing interactions in this thesis, the convention given in equation 2.7 is applied. The dipolar interaction between two magnetic moments can be calculated using:

$$J_{1,2}^{dip} = \frac{\mu_B^2}{R^3}\left[\mathbf{g_1} \cdot \mathbf{g_2} - 3\frac{(\mathbf{g_1} \cdot \mathbf{R})(\mathbf{R} \cdot \mathbf{g_2})}{|R|^2}\right] \tag{2.8}$$

$\mathbf{R}$: Vector connecting 1 and 2
$\mathbf{g_i}$: G-tensor for 1 and 2

The strength of the dipolar interaction is inversely proportional to the distance between the magnetic centers cubed, meaning it decreases quickly with growing distances. Typically distances above 10 Å are too big and dipolar interactions become negligible.[51] Importantly, magnetic interactions can occur both intra- and intermolecularly. As the intramolecular distances between two magnetic ions are generally smaller than intermolecular distances, intramolecular interactions are considerably stronger. The sign of the coupling constant J can take positive and negative values. In the $-2J$-formalism, a positive sign represents ferromagnetic coupling, where the two magnetic moments align with each other, while a negative sign represents an antiferromagnetic interaction, where the moments align antiparallel to one another. Similar to the magnetic alignment induced by an external field, alignment via magnetic interactions is counteracted by the thermal movement of the particles. Magnetic interactions in molecular systems are typically of the order of 10^{-2} to 10^{0} cm^{1} and are, therefore, only observable at low temperatures. Figure 2.8 shows a schematic representation of $\chi_{mol}T$ vs. T, in an idealized system with different J-couplings.

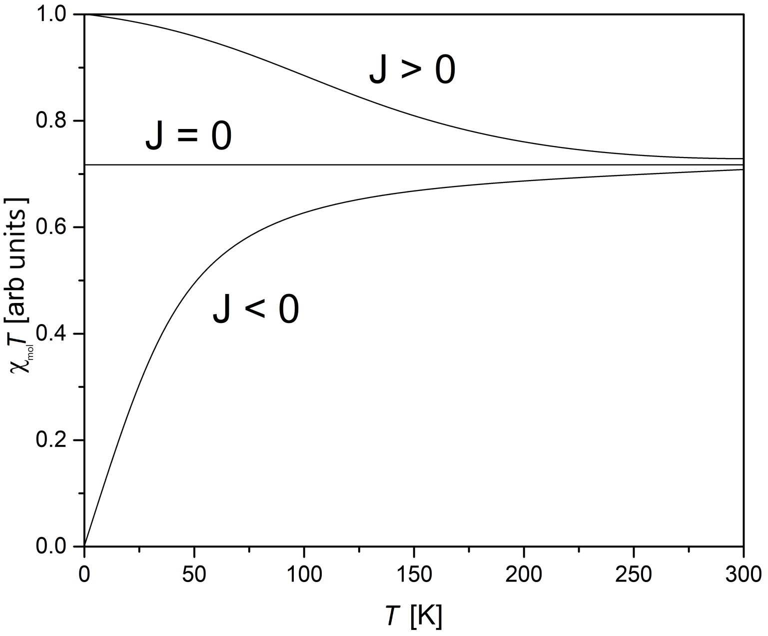

Figure 2.8: Schematic plot of the temperature product of the molar magnetic susceptibility with and without the influence of (anti-)ferromagnetic interactions.

In order to experimentally derive the J parameters, a fit of the $\chi_{mol}T$ vs. T data can be performed. As mentioned above, the depopulation of the Stark levels in molecular materials causes a similar decrease to antiferromagnetic interactions, making it hard to differentiate between those two effects solely based on the visual appearance of the T-dependent behaviour without any mathematical analysis. The behaviour discussed in this chapter so far describes only the interaction with a non-changing DC magnetic field and holds up for any paramagnetic system.

In molecular magnetism however, the behaviour of a molecule in an alternating magnetic field (AC) is of much more value. Similar to the DC magnetic susceptibility discussed prior, an AC susceptibility can be determined as a function of the frequency at which the magnetic field is oscillating. The AC susceptibility has both a real and an imaginary part which can be determined individually and are given by the generalized Debye model:

$$\chi'(\omega) = \chi_S + \frac{(\chi_T - \chi_S)[1 + (\omega\tau)^{1-\alpha} sin(\pi\alpha/2)]}{1 + 2(\omega\tau)^{1-\alpha} sin(\pi\alpha/2) + (\omega\tau)^{2-2\alpha}} \tag{2.9}$$

$$\chi''(\omega) = \frac{(\chi_T - \chi_S)(\omega\tau)^{1-\alpha} cos(\pi\alpha/2)}{1 + 2(\omega\tau)^{1-\alpha} sin(\pi\alpha/2) + (\omega\tau)^{2-2\alpha}} \tag{2.10}$$

χ' : Real or in-phase component of the AC susceptibility
χ'' : Imaginary or out-of-phase component of the AC susceptibility
ω : Radial frequency of the oscillating field
χ_S : Adiabatic susceptibility
χ_T : Isothermal susceptibility
τ : Relaxation time
α : Dispersion parameter

The real or in-phase component χ' describes the response of a magnetic system as it changes with the alternating field, while the imaginary or out-of-phase component χ'' is measured with a phase shift of $\frac{\pi}{2}$, it can be considered as the first derivative of the real component. In an idealized paramagnetic system, the magnetic moments of the sample can follow the applied field, therefore, no out-of-phase signal can be recorded. However, if there is an energy barrier that has to be overcome in order for the magnetic moment to switch, a frequency-dependent maximum is observed in the out-of-phase component. Figure 2.9 shows an idealized behaviour of the AC susceptibility's components.

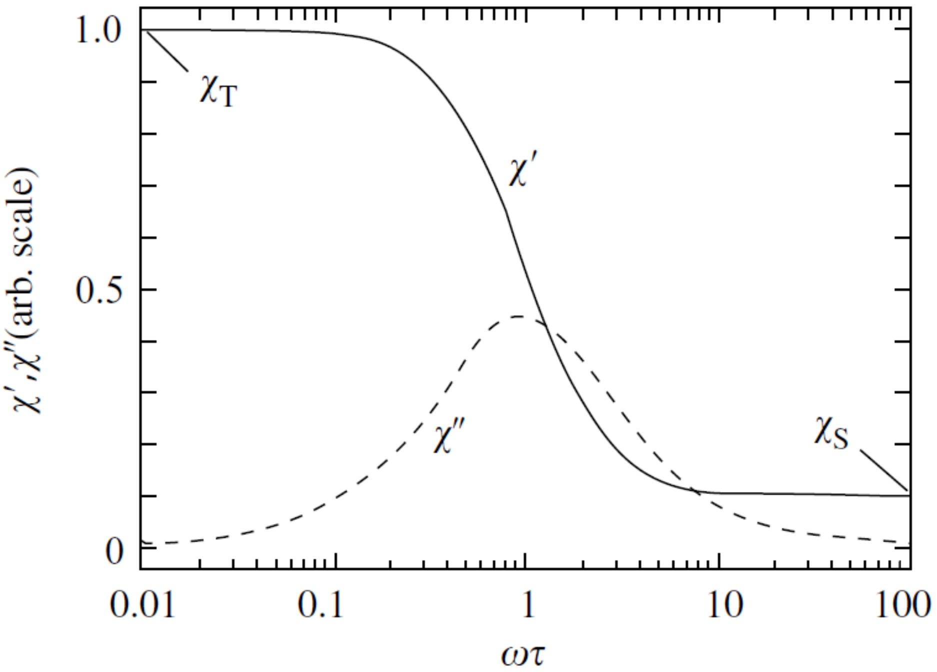

Figure 2.9: Frequency-dependency of the in- and out-of-phase component of the AC susceptibility.[49]

At low enough frequencies the magnetic moments have enough time to align with the applied field at all times, resulting in a compound specific value for the in-phase component called the isothermal susceptibility $\chi'(\omega \to 0) = \chi_T$ and no out-of-phase signal $\chi''(\omega \to 0) = 0$. At the high frequency limit, the magnetic moments of the sample have not enough time to exchange energy with their environment, meaning they are fully unable to follow the oscillating field. In this case, the observed in-phase component is equal to the adiabatic susceptibility $\chi'(\omega \to \infty) = \chi_S$ and the out-of-phase component becomes again zero, as it averages over time $\chi''(\omega \to \infty) = 0$. The actual dynamics of a sample can be observed in the intermediate regime. With increasing frequency the in-phase component drops with a simultaneous increase of the out-of-phase component. The latter reaches its maximum when $\omega\tau = 1$, where τ is the system-specific relaxation time. The shape of the curves is strongly influenced by the dispersion parameter α in equations 2.9 and 2.10, which describes a distribution of relaxation times and can take values between 0 and 1. If $\alpha = 0$, the relaxation dynamics are described by a single process with a distinct relaxation time, giving a narrow curve of $\chi''(\omega)$. Higher values of α describe relaxation via a distribution of processes and relaxation times, giving rise to a more flat profile of $\chi''(\omega)$. A convenient way of visualization of the dispersion is the so-called Argand or Cole-Cole plot, which gives χ'' as a function of χ'. If $\alpha = 0$, the shape of the Argand curve will be a perfect semi-circle, which flattens out with an increase of α, as shown in figure 2.10.

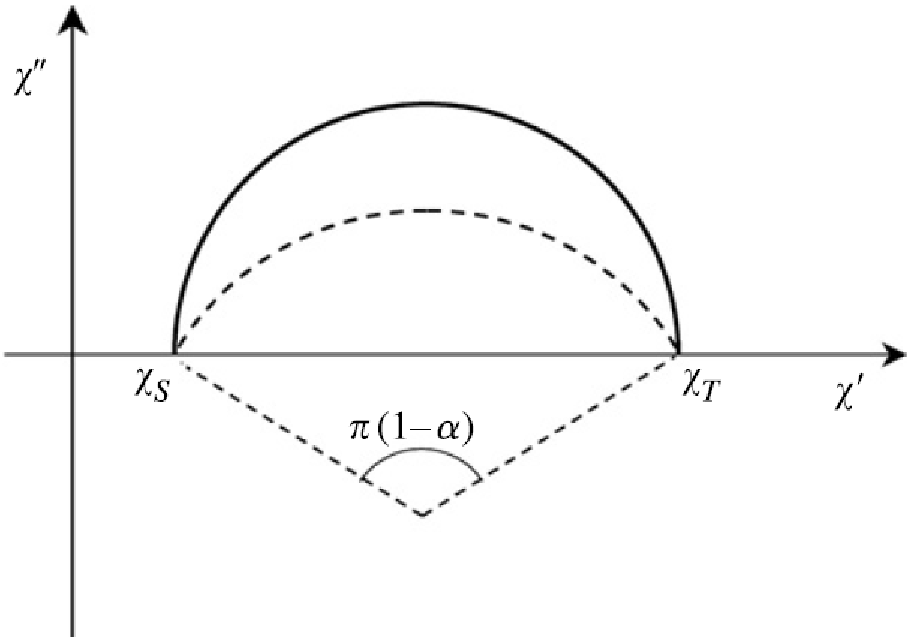

Figure 2.10: Schematic Argand or Cole-Cole plot.[49]

As the relaxation described is related to an energy barrier, it is T-dependent. An increase in temperature causes a decrease in relaxation times, therefore, faster relaxation. This is observed as a frequency shift of the maximum in $\chi''(\omega)$ towards higher frequencies, as $\omega\tau = 1$ has to be satisfied. In order to fully characterize the relaxation dynamics, frequency-dependent χ' and χ'' curves are measured at varying temperatures. The processes involved in magnetic relaxation show different T-dependencies, therefore, analysis of the τ vs. T data, gives a proper insight into the relaxation dynamics. The first and most straight forward mechanism to magnetic relaxation is the so-called Orbach process. Orbach relaxation describes the relaxation over the energy barrier, which results in Arrhenius type behaviour known from classical chemical kinetics with an exponential T-dependency. Due to that, Orbach relaxation becomes the dominant process at high temperatures, where k_BT becomes big enough to bridge the energy barrier U_{eff}. In the quantum regime, however, relaxation can also occur below the energy barrier. One process of under-barrier relaxation is quantum tunnelling of the magnetization (QTM), where the orientation of the magnetic axis flips spontaneously. In strongly anisotropic systems the efficiency of QTM is low, while transverse components of the g-tensor benefit QTM. The process is T-independent and with that most relevant at low temperatures. As there is no energy exchange with the environment involved in QTM, it can only occur in systems where the two magnetic states of opposite orientation are energetically degenerate. Application of an external DC field can lift the degeneracy and with that suppress QTM. Generally QTM describes the tunnelling within a degenerate ground state. Tunnelling in an excited state can also occur, which is referred to as thermally assisted QTM (TA-QTM). If the tunnelling is very efficient between the two opposing states of an excited doublet, the process is kinetically identical to an over-the-barrier Orbach process, where the energy barrier is the energy gap between the ground and the excited state. Such efficient TA-QTM is a very common behaviour in lanthanide based systems with low symmetry, but usually it is then still referred to as Orbach relaxation. In the intermediate T-regime between dominant QTM and Orbach relaxation, usually Raman processes are the most effective means of magnetic relaxation. Raman relaxation is caused by the interaction of the molecular magnet with the phonon bath of the lattice via inelastic scattering and proceeds through virtual energy levels. The most common treatment is a phenomenological term with T^n dependency, where n is determined by fits of τ vs. T data. As this treatment doesn't have a directly relatable physical meaning also other mathematical treatments have been proposed more recently, e.g. also using an exponential term. The power law is still the most commonly used. For Ln's it is theoretically expected to obtain $n = 9$, however, lower values are commonly observed. The final mechanism is characterized by absorption or emission of a phonon equal to the energy gap between the two states. Such relaxation is called direct relaxation and is proportional to T. Direct processes become more important under the application of external DC fields. Figure 2.11 is a visual representation of the different mechanisms involved in magnetic relaxation.

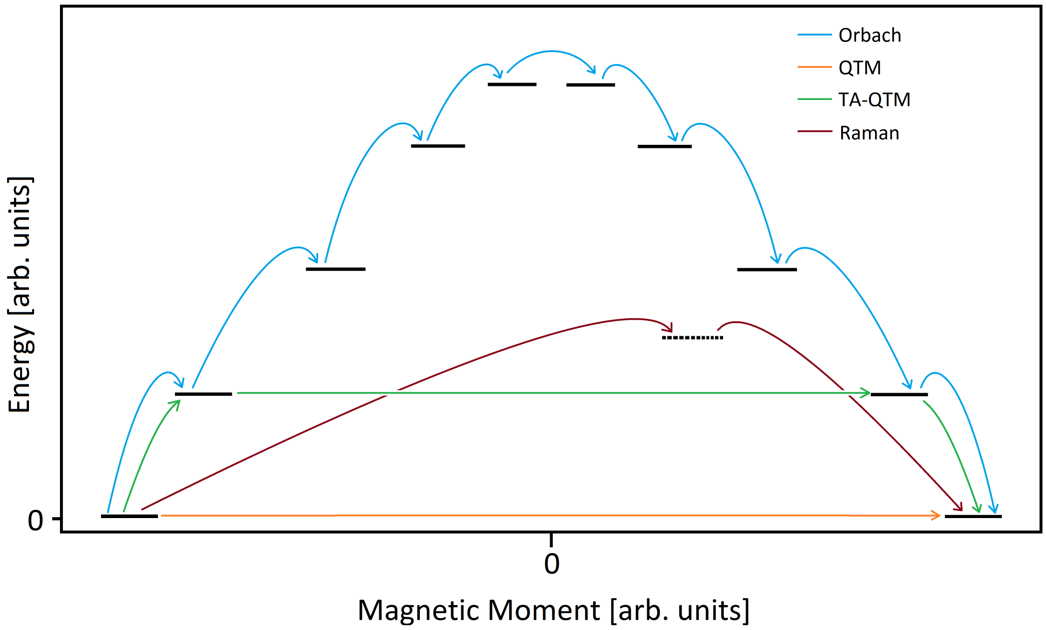

Figure 2.11: Energy diagram with different mechanisms of magnetic relaxation

Quantitative analysis is achieved by performing a fit $\tau(T)$ using equation 2.11. The fits are commonly shown in graphs of $ln(\tau)$ vs. $1/T$, as the exponential Orbach relaxation gives a straight line, with the slope representing the energy barrier.

$$\tau^{-1} = \tau_0^{-1} exp\left(-\frac{U_{eff}}{k_B T}\right) + CT^n + AT + \tau_{QTM}^{-1} \tag{2.11}$$

τ : Experimentally determined relaxation time
τ_0 : Orbach relaxation time
U_{eff} : Effective energy barrier
C, n : Raman parameters
A : Direct relaxation parameter
τ_{QTM} : QTM relaxation time

If a molecular system exhibits slow relaxation as described here, it is referred to as a single molecule magnet (SMM). The necessary energy barrier for magnetic reversal is a consequence of magnetic anisotropy. A magnetically isotropic system will behave as a paramagnet, but not as an SMM. If the temperature is low with respect to the energy barrier and other relaxation processes are inefficient within the timescale of a measurement, hysteresis can be observed in SMMs. Hysteresis refers to the behaviour of a system, showing remanent magnetisation at zero applied field after being subjected to an external field before. In order to fully remove the magnetization of a sample showing remanence, a magnetic field in opposite direction has to be applied. The strength of the negative field is the so-called coercivity. Upon increasing temperature, the remanence and coercivity decrease, causing the hysteresis loops to close. The highest temperature at which open hysteresis is observed is usually referred to as the blocking temperature T_B, marking an important quality measure of SMMs. However, a more quantitative definition of T_B is given as the derived temperature where $\tau = 100s$. If blocking temperatures are given within this thesis, this definition will be applied.

The first molecule in which slow magnetic relaxation was observed, was a Mn_{12}-acetate cluster reported in 1993 by Sessoli *et al.*[52,53] In the molecule eight of the Mn ions are Mn^{3+} with $S = 2$ arranged as a ring and ferromagnetically coupled to give $S = 16$. The other four ions are Mn^{4+} with $S = 3/2$ also ferromagnetically coupled to give $S = 6$. The Mn_4 substructure is placed in the middle of the Mn_8-ring and antiferromagnetic coupling between the two subunits yields the molecules total spin ground state $S = 10$.

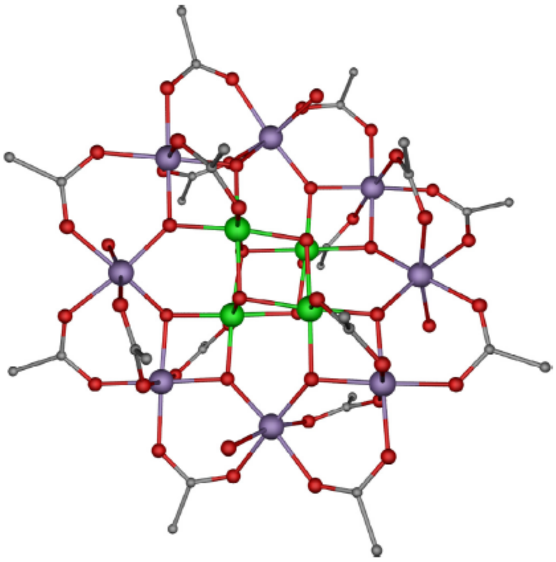

Figure 2.12: Molecular structure of Sessoli's Mn_{12} cluster. Mn(IV) represented in green, Mn(III) in purple.[54]

Without the effect of zero field splitting (ZFS), the $S = 10$ ground state would be 21-fold degenerate taking all integer steps between $m_S = -10$ to $m_S = 10$. As the name suggests, ZFS lifts the degeneracy of the m_S-manifold causing an energy barrier to spin relaxation. The effective energy barrier U_{eff} that was found for Mn_{12} was 61 K. After ten years, where all reports of new SMMs were similarly based on 3d transition metal clusters, Ishikawa *et al.* reported the first lanthanide-based SMMs in 2003.[55] The molecules in question were anionic Ln-phthalocyanine sandwich complexes as shown in figure 2.13.

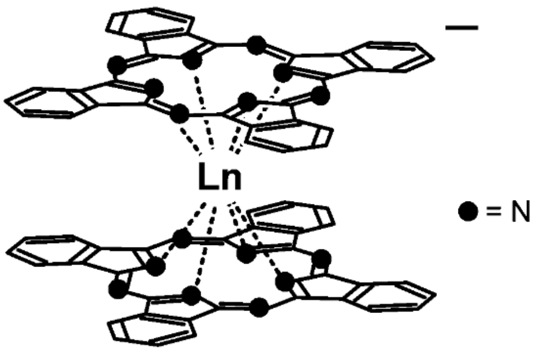

Figure 2.13: Molecular structure of the anionic $\mathrm{LnPc_2}$ sandwich complex.[55]

The reported U_{eff} values for the Dy and the Tb analogues were 28 and 230 $\mathrm{cm^{-1}}$, respectively. At the time, the latter was significantly higher than the energy barrier for most reported transition metal SMMs, starting a new approach of implementing lanthanide ions in molecular magnetism. Rinehart and Long published a paper in 2011, introducing a qualitative explanation of the magnetic behaviour of the different Ln(III) ions in coordination complexes.[56] Figure 2.14 shows the calculated shapes of the 4f electron shells for the Ln(III) series. La, Lu and Eu are left out due to $J = 0$. Gadolinium shows a spherical, isotropic distribution as $L = 0$. In all other cases, the shapes are either referred to as prolate (elongated along the z-axis) or oblate (elongated within the x-y-plane).

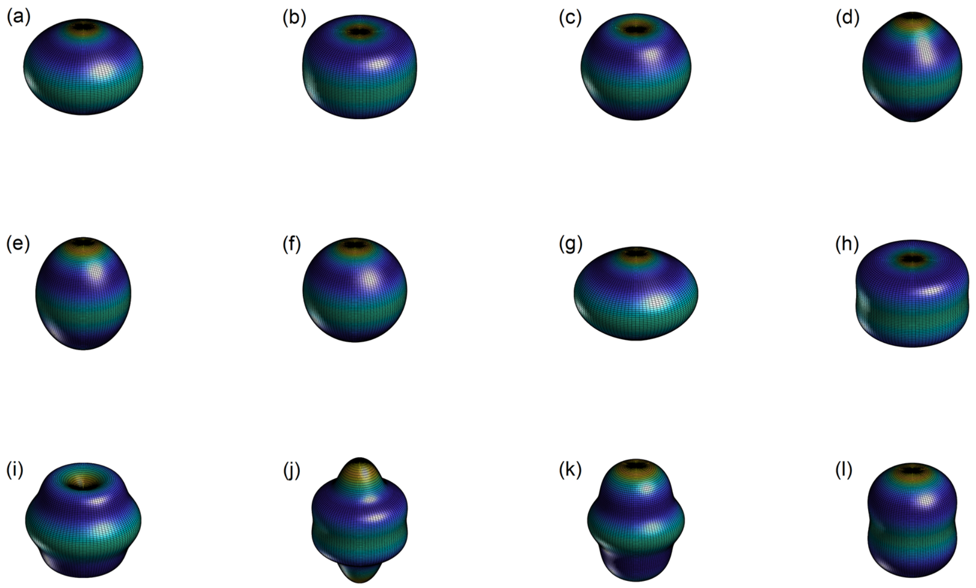

Figure 2.14: 4f electron density distribution of Ln(III)-ions. (a): Ce, (b): Pr, (c): Nd, (d): Pm, (e): Sm, (f): Gd, (g): Tb, (h): Dy, (i): Ho, (j): Er, (k): Tm, (l): Yb.

In order to stabilize the anisotropic ground states and with that generate a energy barrier to magnetic relaxation, oblate ions (like e.g. Dy(III)) prefer an axial ligand field, where strong donor ligands are located on the z-axis. Prolate ions (such as e.g. Er(III)), on the other hand, benefit off of an equatorial ligand field with weak donors along the z-axis and stronger donors in the x-y-plane. Employing this knowledge researchers have created tailor-made ligand systems in order to reach higher and higher blocking temperatures and energy barriers. The high spin ground state of Dy(III) ($J = 15/2$) in combination with its strong anisotropic character make dysprosium the most successful lanthanide employed for record-holding SMMs. Strong axial ligand fields can be exerted by cyclopentadienyl-type (Cp) ligands, leading to a whole family of SMMs with high energy barrier. Two Cp based Dy complexes that broke the record for the effective energy barrier in 2017 and 2018 are shown in figure 2.15.[57,58]

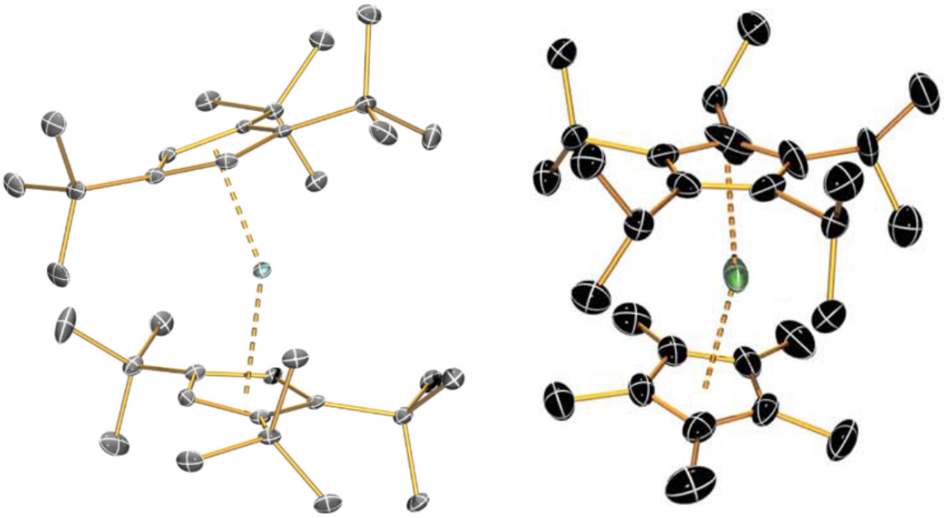

Figure 2.15: Molecular structure of two cyclopentadienyl-based Dy(III) SMMs. Left: $[\mathrm{DyCp}_2^{ttt}]^-$; Right: $[\mathrm{DyCp}^{iPr_5}Cp^{Me_5}]^-$.[57,58]

Both complexes are monovalent anions, stabilized by a bulky $[\mathrm{B(C_6F_5]}^+$ cation. The sterically demanding substituents on the Cp ligand allow for Cp-Dy-Cp angles, that are close to 180°, causing a strong axial LF, which resulted in U_{eff} values of 1223 cm^{-1} and 1541 cm^{-1}, respectively. The blocking temperatures were 60 and 80 K, respectively, making $[\mathrm{DyCp}_2^{iPr5}]^-$ the first reported SMM showing hysteresis above the temperature of liquid nitrogen. In both compounds the high symmetry causes low probability for TA-QTM and ground state QTM, which means the relaxation follows a more traditional Orbach route via higher excited states. The current record-holding SMM was reported in 2022 by Gould *et al* and similarly uses the Cp^{iPr5} ligand, however, being a Dy(III) dimer bridged by a I_3^{4-} triangle.[59]

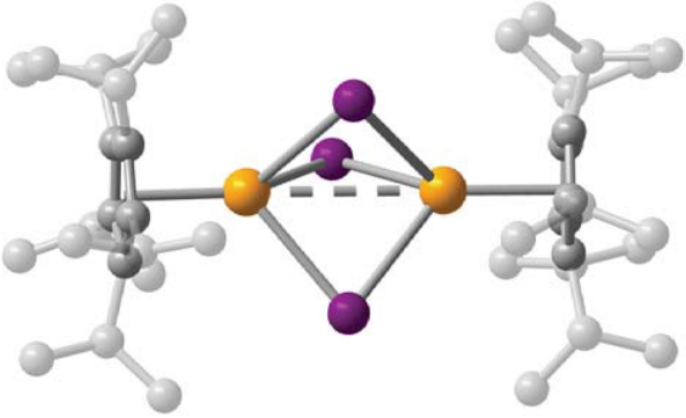

Figure 2.16: Molecular structure of $[\mathrm{Dy_2I_3Cp_2^{\mathit{iPr5}}}]$.[59]

The Dy-Dy distance observed in $[\mathrm{Dy_2I_3Cp_2^{\mathit{iPr5}}}]$ is 3.713 Å, which is suggesting metal-metal bonding. With this, strong exchange interactions are observed, collinear to the direction of magnetic anisotropy, resulting in suppression of Raman and QTM processes, ultimately giving the highest energy barrier of 1631 $\mathrm{cm^{-1}}$ observed to this day.

The bistable nature of the magnetic ground state in SMMs has made them interesting candidates for several different technological applications. For example the different states can be used to encode information, therefore, allowing the construction of high density data storage devices. In these, however, the relaxation mechanisms offer a way of data loss, which remains a big challenge in realizing such devices. However, the finding of Guo *et al.* with the first SMM showing hysteresis above liquid nitrogen temperature was a milestone towards real world application. Another possible way of exploiting the interesting quantum behaviour of SMMs is in employing them as quantum bits (Qubits) for quantum information processing schemes. In this application, the relaxation mechanisms are not necessarily problematic, as long as the relaxation times are long in respect to the duration of the carried out algorithms. A more detailed overview will be given in section 2.5.

2.3 Photoluminescence

Luminescence describes the process of a material emitting light. The general process by which luminescence is observed, is an excitation of a given system into one of its excited states, followed by relaxation to the ground state. The energy difference between the excited and the ground state is released in form of a photon upon relaxation. The excitation can be a consequence of different external stimuli, like irradiation with electrons,[60,61] application of strong electric fields[62] or irradiation with light. The latter case is referred to as photoluminescence (PL). The basic principles of PL can be visualized in the so-called Jablonski diagram.

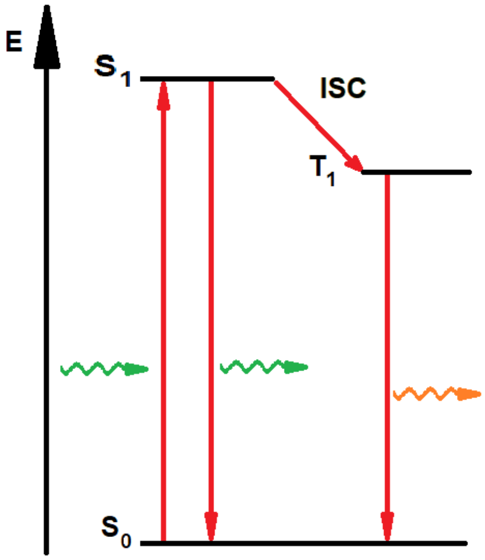

Figure 2.17: Prototypical Jablonski diagram showing photoluminescent transitions.

The first process shown in figure 2.17, is an excitation from the singlet ground state S_0 to the excited singlet state S_1, mediated by the absorption of a photon. In spectroscopy, the transition between two states is given using an arrow to represent the direction of the transition, while the state with higher energy is always given on the left, therefore, the aforementioned excitation process can be written as $S_1 \leftarrow S_0$. When the system relaxes from S_1 back into the ground state ($S_1 \rightarrow S_0$), a photon with similar energy to the absorbed photon is reemitted; such luminescence is termed fluorescence. The second process shown in figure 2.17 is referred to a phosphorescence. After the initial excitation, the system undergoes a transition from the excited singlet state (S_1) into a lower lying triplet state (T_1) called inter system crossing (ISC). As the energy gap between S_0 and T_1 is smaller than the one between S_0 and S_1, upon relaxation the emitted photon has less energy. This loss of energy is termed a redshift or bathochromic shift, as a lower energy of a photon in the visible region is linked to a colour shift towards red. In most scenarios, a redshift is also observed for fluorescent pathways, as the $S_1 \leftarrow S_0$ excitation is often times linked to an excitation of vibrational modes of the S_1 state. Relaxation within the vibrational levels typically occurs in a non-radiative process, exchanging energy with the environment. The timescale of luminescence phenomena can be described with a single exponential decay:

$$I(t) = I(0) \cdot exp\left(\frac{-t}{T_{1,opt}}\right) \tag{2.12}$$

$I(t)$: Measured intensity at time t
$I(0)$: Measured intensity at time $t = 0$
$T_{1,opt}$: Optical lifetime of the excited state

The relaxation described in equation 2.12, is an overlap of radiative and non-radiative decay, with the ratio between these being strongly influenced by the chemical environment of an emitting particle. The optical lifetimes in phosphorescence is significantly longer than the lifetimes observed for fluorescence, as the $T_1 \rightarrow S_0$ relaxation is linked to a spin-flip. As discussed in section 2.1, trivalent lanthanide ions show well defined energy levels, that are near independent of their environment. As a result Ln(III) ions show fingerprint emission, specific to the individual ion. The energy differences observed cover the visual (approx. 400 nm to 800 nm) and near IR region (approx. 800 nm to 2000 nm) of the electromagnetic spectrum. However, excitation of Ln(III) ions is problematic, as the transitions are 4f-4f-transitions. According to Laporte's rule, electronic transitions which conserve the parity of the state are forbidden. The parity is given as g (gerade) for s and d orbitals and u (ungerade) for p and f orbitals. In this sense, no transitions should be observable in lanthanide ions, because the transitions are u → u transitions. However, Laporte's rule only strictly applies to atoms and centrosymmetric molecules and PL can be observed in lanthanides, where a low symmetry environment causes mixing of the wavefunction with orbitals of other parity. Nevertheless, the probability for the 4f-4f excitation remains low, leading to a small photon absorption cross-section. In order to populate the excited states, strong lasers can be used, where the highly intense irradiation is sufficient, applicable in for example Ln(III) ions in inorganic host materials. Another method of circumventing the low absorption cross-section is sensitized photoluminescence. Here molecular coordination compounds of Ln(III) ions are employed where an organic ligand can efficiently absorb photons to reach an excited state and later transfer the energy to the central ion. The absorption of photonic energy by an organic ligand and the transfer to the metal ion is called antenna effect. Figure 2.18 is a schematic representation of the antenna effect.

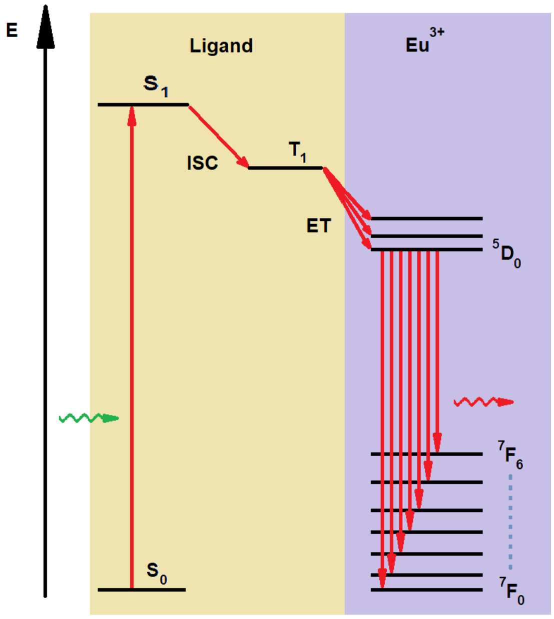

Figure 2.18: Schematic representation of the antenna effect of a Eu(III) complex, leading to Eu(III)-based sensitized f-f emission.

Upon irradiation of the antenna ligand, the aforementioned $S_1 \leftarrow S_0$ transition is induced, followed by ISC to T_1. The energy transfer (ET) to the excited state of the lanthanide ion ($^5D_0$ of Eu^{3+} in figure 2.18) occurs from T_1, if the energy difference is sufficiently small. Luminescence of the ligand can still be observed in Ln coordination compounds, however, the intensity is typically very low compared to the Ln transitions. Generally the observed emission is linked to the relaxation from the lowest state of the excited manifold. In the given example of Eu(III) the observed transitions are $^5D_0 \rightarrow {}^7F_J$, where $J = 0, 1, 2, 3, 4, 5, 6$. Emission bands from higher states like $^5D_1$, are termed hot bands and can be observed at sufficiently high temperatures. Recording PL spectra at low T suppresses these hot bands, while also increasing the PL efficiency by lowering the non-radiative decay through interactions with vibronic modes. Especially C-H, N-H and O-H oscillators in close proximity of an Ln(III) ion can offer non-radiative relaxation channels, leading to a quenching of the luminescence. Therefore, ligands that do not have any such oscillators are beneficial for the PL properties of molecular Ln compounds. Figure 2.19 shows a variety of known antenna ligands. Typical organic ligands functioning as antennas are often based on aromatic or conjugated systems, which show efficient absorption. The measured extinction coefficients are 10^2 to 10^3 times higher than those of lanthanide ions.[33] Their excitation frequencies are typically in the UV region. As mentioned, the ligand-based luminescence can still be observed in Ln coordination compounds, although often covered by the transitions of the lanthanide.

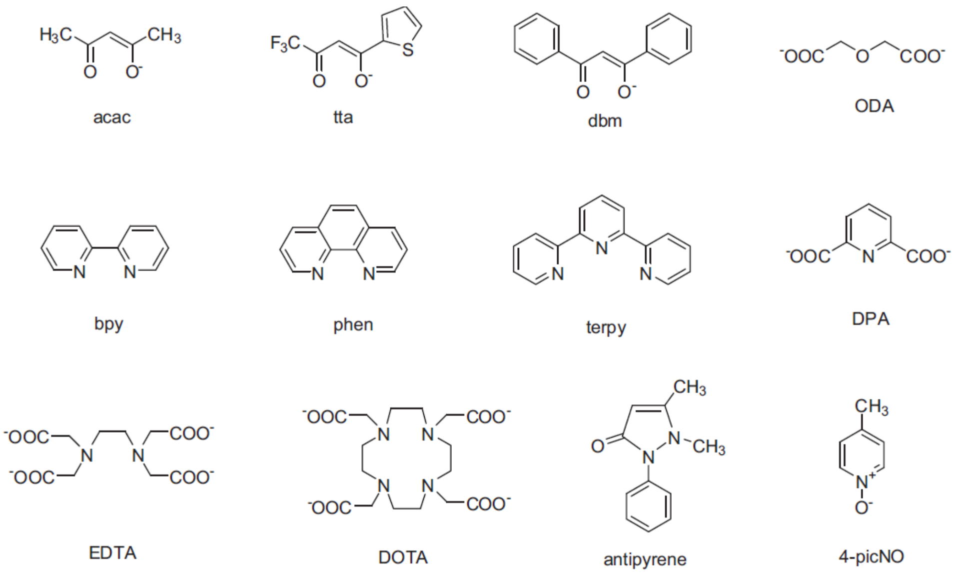

Figure 2.19: Some known antenna ligands for sensitized PL.[63]

However, the coordination of the ligand towards a central ion, significantly alters the ligand's structure and with that its luminescent properties. The influence on the ligands property is called heavy atom effect.[64] A good probe to observe the ligand's luminescence properties in coordination are Gd(III)-based compounds. Gd^{3+} shows a much larger energy separation towards the first excited state than other Ln^{3+} ions, which results in the ion's excited state being higher in energy than the excited state of the ligand. A simplified representation of this is given in figure 2.20. With that, PL data of Gd(III) compounds allow the measurement of the triplet state's energy.

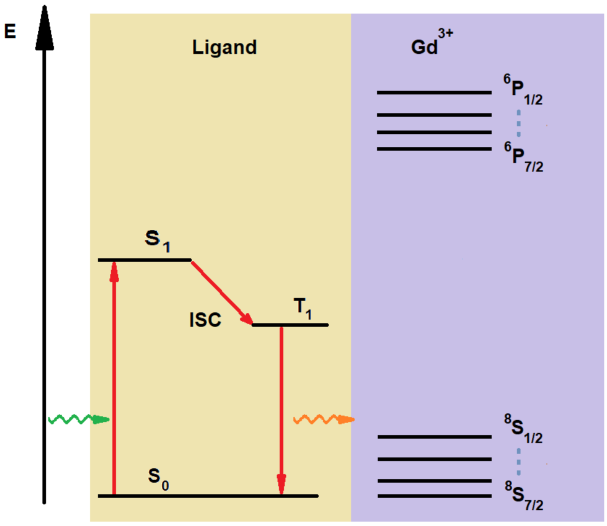

Figure 2.20: Schematic ligand luminescence with the heavy atom effect in Gd(III) complex.

Excitation and emission spectra are the two most commonly reported PL spectra. In an emission spectrum the sample is irradiated with a constant source of light at a given excitation wavelength (λ_{ex}), while the detector is sweeping over the wavelength window of interest. Due to the redshift induced by the nature of the process the minimum detected wavelength of the emission is always bigger than λ_{ex}. Due to multi photon absorption, peaks will be observed in emission spectra when $\lambda = n\lambda_{ex}$, however, the use of properly chosen filters removes those peaks. Excitation spectra are recorded by keeping the detector at a single wavelength, at which strong emission is observed, and scanning the excitation wavelength. In order to obtain meaningful PL spectra, typically an emission spectrum is recorded first using an arbitrary excitation wavelength within the estimated region of the ligand's absorption. Afterwards an excitation spectrum can be recorded setting the detector to the wavelength where a maximum emission was observed. By going back an forth between measuring emission and excitation spectra, the optimal parameters can be obtained.

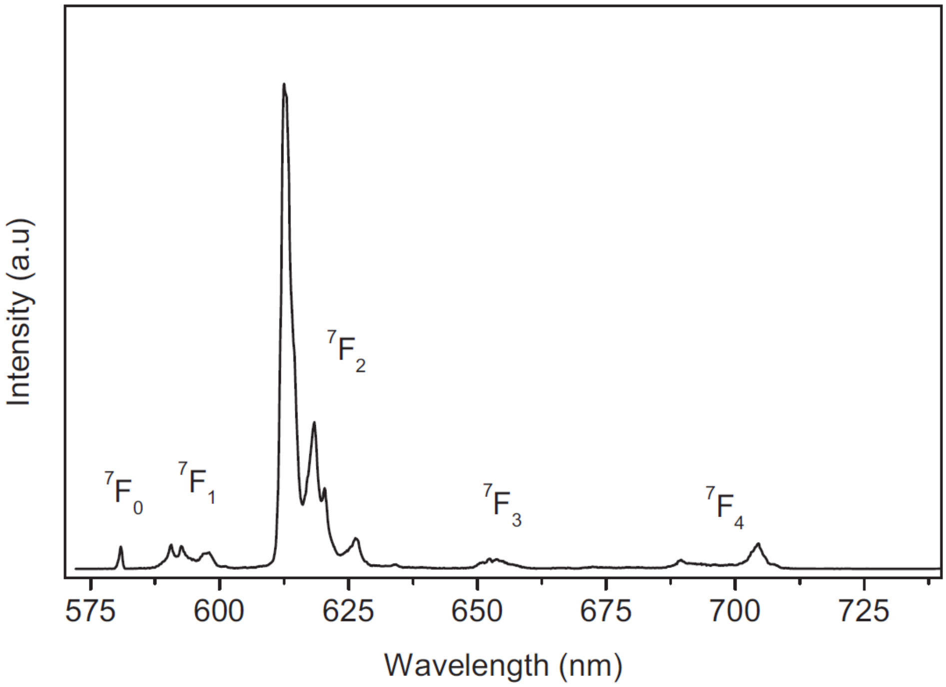

Figure 2.21: Emission spectrum of [Eu(tta)$_3$(phen)] at 77 K, $\lambda_{ex} = 396$ nm.[63]

Figure 2.21 shows an example of an emission spectrum recorded for a luminescent Eu(III)-complex. The individual $^5D_0 \rightarrow {}^7F_J$ transitions described earlier can be seen up to $J = 4$. As the wavelength is directly linked to the energy, the order in which the transitions are observed in the spectrum matches the energy levels of the system. The intensities of the individual transitions differ due to the selection rules and the different characters of the transitions. Most transitions in lanthanides are induced electric dipole transitions, some are magnetic dipole transitions. In case of Eu(III), ${}^5D_0 \rightarrow {}^7F_1$ is a magnetic dipole transition, while all other are induced elctric dipole transitions. The selection rule for induced electric dipole transitions is $\Delta J = 2, 4, 6$ if $J = 0$ and $\Delta J \leq 6$ otherwise. For magnetic dipole transitions $\Delta J = 0, \pm 1$, but $0 \rightarrow 0$ is forbidden. For Eu(III), this results in the transitions ${}^5D_0 \rightarrow {}^7F_1$, ${}^5D_0 \rightarrow {}^7F_2$ and ${}^5D_0 \rightarrow {}^7F_4$ to generally be of higher intensity. In the example at hand, ${}^5D_0 \rightarrow {}^7F_0$ and ${}^5D_0 \rightarrow {}^7F_3$ are observed with low intensities, due to the low symmetry, *vide supra*. The ${}^5D_0 \rightarrow {}^7F_5$ and ${}^5D_0 \rightarrow {}^7F_6$ transitions are not observed in figure 2.21, as their energies lie outside of the measured wavelength window. As discussed in section 2.1, the ligand field effect removed the degeneracy of the m_J states of lanthanide ions. If the resolution of the spectrometer is sufficient in relation to the energy splitting, individual peaks can be observed for each m_J level. In figure 2.21, this is observed for the ${}^5D_0 \rightarrow {}^7F_1$ and ${}^5D_0 \rightarrow {}^7F_2$ transition. ${}^5D_0 \rightarrow {}^7F_1$ is composed of three individual lines corresponding to the $\mathrm{m}_J = 0, \pm 1$ levels, with $\mathrm{m}_J = \pm 1$ being lower in energy, whereas, ${}^5D_0 \rightarrow {}^7F_2$ reveals four distinct transitions. As the splitting should yield five states $\mathrm{m}_J = 0, \pm 1, \pm 2$, the resolution is not high enough to differentiate between two of the states. In cases of high symmetry, the splitting might not be complete and less lines are observed. For example the ${}^5D_0 \rightarrow {}^7F_1$ transition of Eu(III) will only split into three distinct lines in symmetries lower than D_{2h}. However, in molecular compounds the symmetries around the central ion are typically low, so that complete splitting is observed. Beside the information that can be gained from the position of the transition lines, the shape of the measured peaks contains more relevant information. In a first approximation, measuring the luminescence of perfectly identical molecules would yield a narrow transition line, with the linewidth defined by the optical lifetime of the excited state $T_{1,opt}$, defined earlier. In reality this so-called homogeneous linewidth is directly linked to the optical coherence lifetime $T_{2,opt}$, which takes into account dephasing mechanisms. Such dephasing mechanisms include for example interactions with the lattice's phonon bath or magnetic dipolar interactions between neighbouring REI's. The excited state lifetime is, however, defining the lower limit of the homogeneous linewidth and with that the upper limit of the coherence lifetime.

$$\Gamma_h = \frac{1}{\pi \cdot T_{2,opt}} = \frac{1}{2\pi \cdot T_{1,opt}} + \frac{1}{2\pi \cdot T_{2,d}} \tag{2.13}$$

Γ_h : Homogeneous linewidth
$T_{2,opt}$: Optical coherence lifetime
$T_{1,opt}$: Optical lifetime of the excited state
$T_{2,d}$: Decoherence

The recorded transition peaks in a spectrum are further broadened, as the observed molecules are not identical. This broadening is called inhomogeneous broadening and it is caused by multiple reasons, like defects in molecular crystals that lead to minimal changes in the molecular geometries and the effect of different nuclear spin states of the lanthanide ion. The inhomogeneously broadened line can be understood as an overlap of many homogeneously broadened lines (Figure 2.22 left). The homogeneous linewidth can be measured directly by photon echo experiments or indirectly via spectral hole burning (SHB). In spectral hole burning a short laser pulse is applied to the sample, which will excite all molecules for which the photon energy matches the transition energy between the state. If this burning pulse is long with respect to $T_{1,opt}$, this causes a depopulation of the ground state of one group of molecules of the measured ensemble. Scanning over the full width of the inhomogeneous peak immediately after, results in a signal which shows a spectral hole exactly at the position at which the burning pulse was applied. The width of the hole is simply double the homogeneous linewidth:

$$\Gamma_h = \frac{\Gamma_{hole}}{2} \tag{2.14}$$

Γ_{hole} : Width of the spectral hole

As one ground state is depopulated by the burning pulse, this can result in another state being significantly overpopulated, leading to a so-called antihole that can also be observed while scanning. A schematic representation of the SHB process is given in figure 2.22 (right).

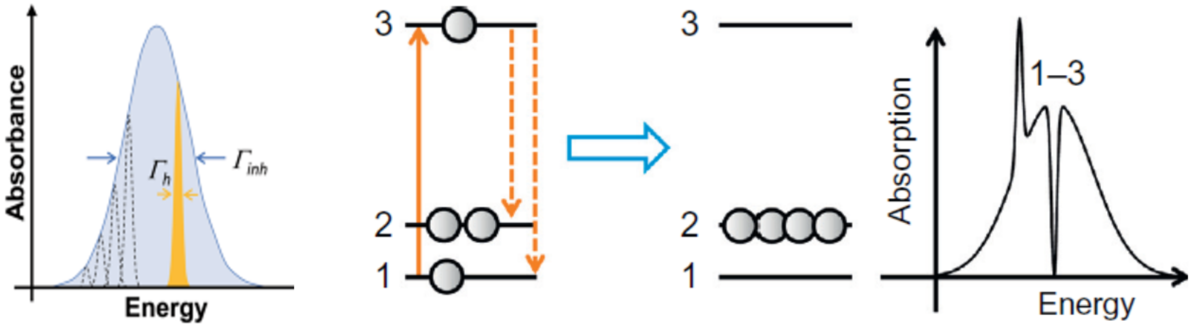

Figure 2.22: Inhomogeneous linebroadening (left) and spectral hole burning scheme (right).[65]

As mentioned, the depopulated state is a nuclear spin state of the Ln(III) ion. The lifetime of the spectral hole is dependent on the nuclear spin lifetime $T_{1,spin}$. Time-dependent measurements of the spectral hole depth, therefore, offer a way of obtaining the nuclear spin lifetime in luminescent lanthanide complexes. As discussed, the inhomogeneously broadened lines are a consequence of overlapping homogeneous lines originating from molecules in different crystallographic environments. Very narrow homogeneous linewidths, therefore, offer the possibility of addressing only a few molecules, or even a single molecule, within a molecular crystal by carefully choosing the excitation energy.

The luminescence properties of lanthanides have been known for a long time and have been extensively studied in solution[66,67] or doped into crystalline materials[68,69] as well as in a multitude of different host materials like zeolites[70,71] or metal-organic frameworks.[72] Cerium doped yttrium aluminium garnet (YAG:Ce) and europium-doped yttrium oxide (YOX:Eu) are among the most relevant technologically used luminescent Ln materials.[73–75] Due to the intrinsic narrow optical transitions, their tuneability and the quantum nature of the optical transitions, luminescent lanthanide compounds have been proposed to function as optical Qubits more recently, *vide infra*. Most studies have been carried out on Eu(III)-based compounds, as they are known to show longer $T_{1,opt}$ than other Ln's while also emitting in the visible region.[65,76] Nevertheless, other lanthanide ions have been proposed to have beneficial characteristics, like Er(III) and Yb(III), where the near IR emission matches the wavelength window in which telecommunication optical fibres experience the lowest loss.[77–79]

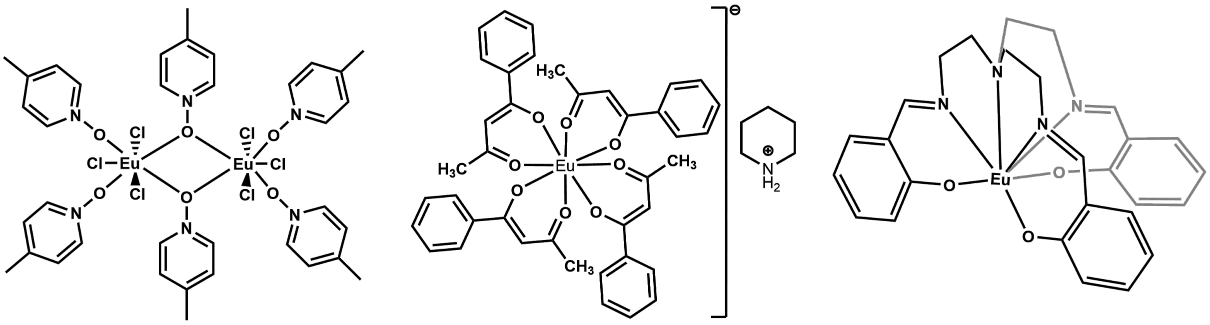

Figure 2.23: Molecular structures of [Eu_2(4-picNO)$_6$$Cl_6$], [Eu(BA)$_4$](pip) and [Eu(trensal)].[80]

In a recent article the linewidth and optical lifetimes of three luminescent Eu(III) complexes have been compared.[80] The complexes in question are shown in figure 2.23. The dinuclear complex [Eu_2(4-picNO)$_6$$Cl_6$] showed the longest $T_{1,opt}$ of 880 μs at 20 K among those three, which is attributed to the absence of any C-H vibrations in close proximity to the Eu(III) ion, compared to the remaining two complexes. The observed $T_{1,opt}$'s were 540 μs at 1.4 K and 354 μs at 2.3 K for the anionic complex [Eu(BA)$_4$]$^-$ and the neutral [Eu(trensal)], respectively. The lower $T_{1,opt}$ of [Eu(trensal)] can be explained by its $^5D_0 \rightarrow {}^7F_0$ oscillator strength. The coordination symmetry around the Eu(III) ion is lower in [Eu(trensal)] compared to the other reported complexes, which facilitated J-mixing of the ground state's wavefunction. With that, the $^5D_0 \rightarrow {}^7F_0$ transition gains intensity, but also $T_{1,opt}$ is lowered. This is an important behaviour in the design of luminescent coordination compounds, where a low symmetry is required in order to observe certain transitions but a higher symmetry could lead to longer $T_{1,opt}$'s. As discussed before, $T_{1,opt}$ creates the upper limit of $T_{2,opt}$. Interestingly, comparison of the three complexes revealed that [Eu$_2$(4-picNO)$_6$Cl$_6$], which shows the longest $T_{1,opt}$, to have the shortest $T_{2,opt}$ of 14.5 *ns*. The observed value of $T_{2,opt}$ of 370 ns at 4 K for [Eu(BA)$_4$]$^-$ is about three times higher than for [Eu(trensal)] with 114 ns at 4.2 K, matching the trend seen for $T_{1,opt}$. All mentioned $T_{2,opt}$ here, are values obtained from SHB experiments. The low $T_{2,opt}$ value of [Eu$_2$(4-picNO)$_6$Cl$_6$] is a consequence of Eu$\cdots$Eu interactions within the dimeric complex, which are not a factor in the mononuclear complexes [Eu(BA)$_4$]$^-$ and [Eu(trensal)]. The study of these three complexes gives a good foundation to understand trends for $T_{1,opt}$ and $T_{2,opt}$ values of luminescent lanthanide-based complexes. However, more data on different molecules will be helpful for proper understanding.

Besides obvious applicability of luminescent REI complexes in technological fields such as LED fabrication or luminescence marking techniques, they have been proposed as optically addressable Qubits. As the ground and excited states create a superpositioned state on the timescale of $T_{2,opt}$, molecules can be used as light-matter interfaces for QIP schemes, see section 2.5.

2.4 Ab initio CASSCF calculations

Computational quantum chemistry is nowadays an extremely important scientific field, which allows the prediction as well as the validation of experimental data. The term *ab initio* marks that only a set of atomic coordinates is given as a basis of the calculation, opposed to empiric or semi-empiric methods, in which experimental parameters are included. The foundational equation is the well-established time-independent Schrödinger equation.

$$\hat{H}\Psi = E\Psi \tag{2.15}$$

$\hat{H}$: Hamilton operator of the total energy
Ψ : Wavefunction
E : Eigenvalue of the energy

Generally, the Hamiltonian is the sum of kinetic energy of all the electrons and nuclei in a given system as well as the potential energy between all those particles. In computational chemistry, however, the energy of the nuclei is neglected and the problem is treated as electrons moving inside a static potential of the nuclei, which is justified by the lower mass and with that higher velocities of the electrons. This approach is called Born-Oppenheimer approximation and leads to a purely electronic problem. None the less, solving the Schrödinger equation remains difficult and is analytically only possible for systems with a single electron. In order to approximate the total energy of the wavefunction, trial wavefunctions are constructed with variable parameters which are optimised iteratively to find the best solution. For this approach it can be shown that the energy of the trial wavefunction is always higher (or in best case equal) to the exact solution, therefore the set of variational parameters that obtains the minimal energy is best. The trial wavefunction is represented by the molecular orbitals as a linear combination of atomic orbitals, which are known from solving the Schrödinger equation for a hydrogen atom.

$$\phi_i = \sum_{a}^{N_{basis}} c_{ai}\chi_a \tag{2.16}$$

ϕ_i : Molecular orbital i
N_{basis} : Amount of basis functions
c_{ai} : Linear coefficient
χ_a : Atomic orbital

The size and composition of the basis set can be freely chosen. The minimal size describes all atomic orbitals, that are necessary to place all electrons, for example a single s-orbital for a hydrogen atom, however, in order to give a proper description of polarization effects and chemical bonding, usually more than the minimal basis set is given, also including more complex orbitals (e.g. p-orbitals in the case of hydrogen). The trial wavefunction is constructed as a slater-determinant in order to suffice the requirement of antisymmetry and normalized by the number of electrons.

$$\Phi_{SD} = \frac{1}{\sqrt{N!}} \begin{vmatrix} \phi_1(1) & \phi_2(1) \cdots & \phi_N(1) \\ \phi_1(2) & \phi_2(2) \cdots & \phi_N(2) \\ \vdots & \vdots \quad \ddots & \vdots \\ \phi_1(N) & \phi_2(N) \cdots & \phi_N(N) \end{vmatrix} \tag{2.17}$$

Φ_{SD} : Slater determinant type wavefunction
N : Number of electrons
$\phi_i(j)$: Molecular orbital i, occupied by electron j

Optimising a slater-determinant wavefunction as given here, and solving the Schrödinger equation is referred to as the so-called Hartree-Fock (HF) method. The electronic energies that are obtained via this approach are reasonably close to reality, as the HF method accounts to about 99% of the total energy. However, the determination of molecular properties through solving the electronic wavefunction is extremely dependent on the most precise solution possible. The error of the HF approach are the electron-electron interactions, which are averaged by the construction of the wavefunction. A full description of the electron-electron interactions requires a multi-configurational approach in which all possible electronic configurations are included in the trial wavefunction.

$$\Psi = a_0 \Phi_{HF} + \sum_i a_i \Phi_i \tag{2.18}$$

Φ_{HF} : Hartree-Fock wavefunction
a_i : Linear coefficient
Φ_i : Excited Slater determinant

Such a treatment is referred to as configuration interaction (CI), but in systems with more than just a few electrons a full CI calculation becomes computationally impossible, due to the immense amount of possible excitations. Computationally feasible post Hartree-Fock methods include coupled cluster (CC) and complete active space self-consistent field (CASSCF) methods. In coupled cluster theory excited states are mathematically created employing excitation operators, which can be chosen to act as single, double, triple, etc. excitation. Usually excitations higher than quadruple are not calculated, as the increase in accuracy does not hold up with the computational effort. In the CASSCF approach a set of orbitals is chosen as the active space and all possible excitations within that space are taken into account. A subset of the space can be reduced to allow only single or double excitations, which is referred to as restricted active space. The creation of possible excitations for CASSCF and RASSCF methods are visualized in figure 2.24.

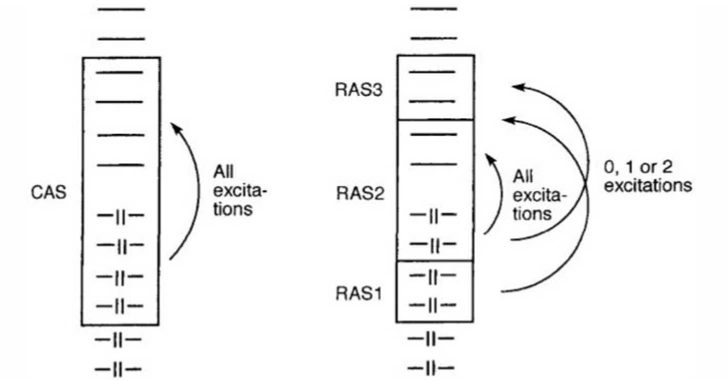

Figure 2.24: Schematic excitations in a CASSCF and RASSCF approach.[81]

The approach that CASSCF takes works particularly well for systems in which electrons are found in a subset of degenerate orbitals, like it is the case of d-block transition metals and f-block elements like the lanthanides. In lanthanides the active space is intuitively chosen as the seven 4f orbitals, while the amount of active electrons is given by the element to be calculated. Due to this, the usage of CASSCF methods for the calculation of molecular Ln systems has become a standard procedure in modern research. The parameters that can be generally obtained from CASSCF calculations for all lanthanides independent of the molecular symmetry are the crystal field parameters, as they are a representation of the electronic structure of the molecule.

$$\hat{H}_{CF} = \sum_{k=2,4,6} \sum_{q=-k}^{k} B_k^q \, \hat{O}_k^q \tag{2.19}$$

$\hat{H}_{CF}$: Crystal field Hamiltonian
B_k^q : Crystal field parameter
$\hat{O}_k^q$: Steven's operator

The crystal field Hamiltonian for the description of lanthanide systems is represented by a set of 27 parameters. Employing the Hamiltonian yields the energies of the spin-orbit coupled states as well as the m$_J$ composition of each individual state. Ions with half-integer spin (ions with an uneven amount of unpaired electrons) are referred to as

Kramer's ions. The Kramer's theorem gives, that such a system will always possess doubly degenerate states due to time-reversal symmetry of the wavefunction. For lanthanides this yields a degeneracy of the ±m_J states for Ce, Nd, Sm, Dy, Er and Yb, which is extremely beneficial for slow magnetic relaxation, *vide supra.* In the non-Kramer's ions Pr, Pm, Tb, Ho and Tm, degeneracy is only observed for high symmetry coordination environments.[82] If degeneracy is given, the doublet states can be treated as systems with effective spin one half giving effective g-tensors that can be derived by CASSCF calculations, that allow for an immediate evaluation of the anisotropy.

$$S_{eff} \cdot g_{eff} = J \cdot g_J \tag{2.20}$$

S_{eff} : Effective spin
g_{eff} : Effective g-tensor

In the approach of an effective spin formalism, the effective g-tensor is obtained from equation 2.20. The anisotropy of the g-tensor is given by the relation of the diagonal elements g_{xx}, g_{yy} and g_{zz}. A perfectly isotropic system would yield $\mathrm{g}_{xx} = \mathrm{g}_{yy} = \mathrm{g}_{zz}$, while an idealized anisotropic system gives $\mathrm{g}_{xx} = \mathrm{g}_{yy} = 0$, $\mathrm{g}_{zz} = \mathrm{g}_{eff}$. The direction of the anisotropy axis in respect to the molecular structure is also obtained, which is especially relevant in multinuclear systems.

The accessibility to obtaining a good understanding of the properties of lanthanide based compounds solely based on calculations, without the need of difficult SQUID magnetometry and photoluminescence spectroscopy, is a strong argument to the success of CASSCF methods. In the optimal case, both experimental and *ab initio* results are available side by side, as the additional information gained from calculations can validate experimental results as well as provide a proper understanding of the foundational processes. It is, however, important to acknowledge the limitations of CASSCF calculations. As mentioned, the CASSCF approach is very well suited for lanthanides, as the active space resembles the degenerate 4f space. None the less, the description is still not complete and the results have to be viewed accordingly. Methods like CASPT2 (NEVPT2), yield further improvements on the accuracy of the calculation, but are also more computationally demanding. All *ab initio* results presented later in this thesis are following the described CASSCF approach. The second important limitation is that the computational effort becomes increasingly high very quickly and calculations of multinuclear complexes are not possible. In order to obtain good approximations, the calculations are performed on parts of the molecules containing only a single Ln ion, or all Ln's but the ion in question are replaced by inactive species, like Y(III). Employing the CF parameters for each individual ion allows simulations of interactions between neighbouring lanthanides.

2.5 Quantum information processing (QIP)

Classical computation describes the manipulation of data which is encrypted as zeros and ones in the form of bits. In a classical bit a zero is represented with a state of low electric potential, and a one is a state of high electric potential. In order to enter the realm of quantum information processing (QIP), the classical bits are replaced with qubits. Different platforms that can function as qubits are presented later in this chapter. The first requirement of a qubit is that it has two (or more) accessible states, that can be labelled with $|0\rangle$ and $|1\rangle$. Other than in classical bits, the wavefunction describing the qubit can also be a superposition of the basic states, represented as a linear combination.

$$|\psi\rangle = \alpha\,|0\rangle + \beta\,|1\rangle \tag{2.21}$$

$|\psi\rangle$: Qubit state
α, β : Linear coefficients
$|0\rangle\,, |1\rangle$: Basic states

The basic states of a qubit are orthogonal to each other spanning the so-called Hilbert space that acts as the computational space. A visual representation is the Bloch sphere, where $|1\rangle$ and $|0\rangle$ are the vectors pointing to the south and north pole of the sphere, respectively. The superpositioned state $|\psi\rangle$ is represented as any vector pointing onto the surface of the sphere.

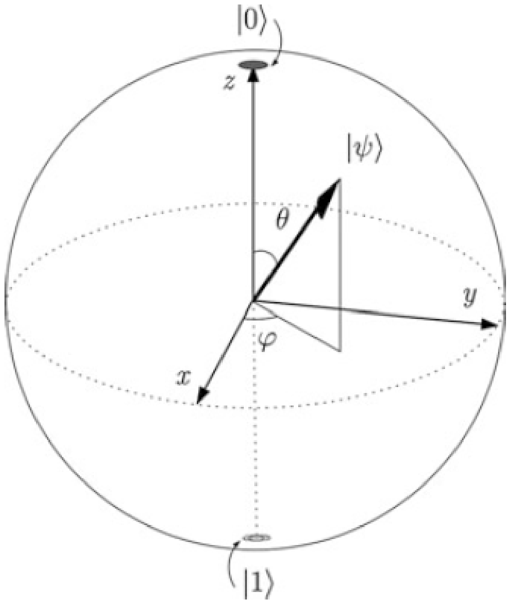

Figure 2.25: Bloch sphere representing the state of a qubit.[4]

According to the rules of quantum mechanics a measurement of the qubit's state causes a collapse of the superposition into either one of the basic states and the probability for each outcome is given by $|\alpha|^2$ and $|\beta|^2$. The normalization criteria gives:

$$|\alpha|^2 + |\beta|^2 = 1 \tag{2.22}$$

The equations presented, are describing only a single qubit system. In case of an array of n qubits or if so-called qudits are employed, which are quantum bits with a number of accessible states $d > 2$, the superpositioned state would be given by:

$$|\psi\rangle = \sum_{i=0}^{d^n-1} \alpha_i |i\rangle \tag{2.23}$$

With the normalization:

$$\sum_{i=0}^{d^n-1} |\alpha_i|^2 = 1 \tag{2.24}$$

A unitary transformation describes an operation on the wavefunction, which does not obtain a result of the qubits' state, therefore, preserving the superposition. A quantum algorithm is constructed off an initialization, where the superposition is created, a series of unitary operations that drive the superposition onto the wanted result and a measuring step, where the final state of the system is measured. Using Grover's algorithm as an example for a simple quantum algorithm, all qubits are initialized in their respective state $|0\rangle$. Then a so-called Hadamard gate is applied which creates the state of superposition. The unitary Grover operator $\hat{G}$ causes a rotation of the superpositioned state $|\psi\rangle$ towards the searched state.

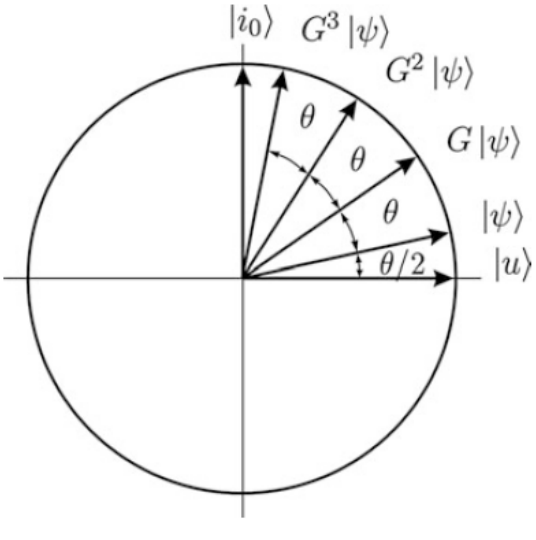

Figure 2.26: Visual representation of Grover's algorithm.[4]

In a general formulation the searched state $|i_0\rangle$ and the superposition of all other states $|u\rangle$ can be used as base vectors of the problem. The states are then given as:

$$|u\rangle = \sum_{i=0, i \neq i_0}^{N} |i\rangle \tag{2.25}$$

and

$$|\psi\rangle = \sqrt{1 - \frac{1}{N}}\,|u\rangle + \frac{1}{\sqrt{N}}\,|i_0\rangle \tag{2.26}$$

Each Grover operator consists of a quantum oracle applied first, which inverts the amplitude of the searched state. The second step is an inversion about the mean. The resulting state $\hat{G}\,|\psi\rangle$ is rotated by an angle θ towards $|i_0\rangle$, where:

$$\theta = 2\, arccos \sqrt{1 - \frac{1}{N}} \tag{2.27}$$

It can be shown that the amount that $\hat{G}$ needs to be applied in order to find the desired state with a probability p is proportional to $\sqrt{N}$, which is a significant improvement to classical search algorithms. The probability p shows an anomaly at $n = 3$, where the chance of finding the searched state is 94.5%, however, for higher values of n the probability approaches 1, as shown in figure 2.27.

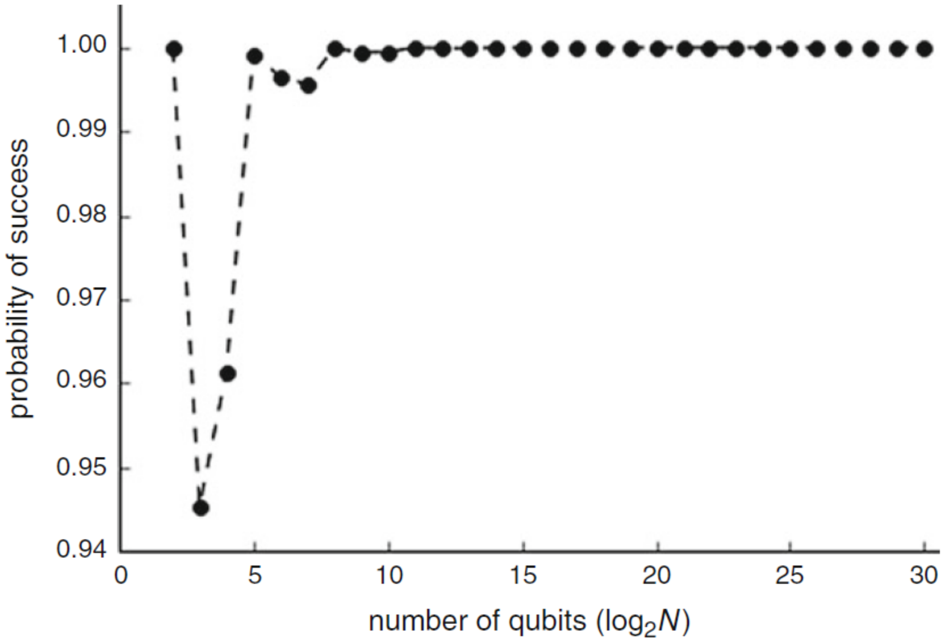

Figure 2.27: Probability of finding the searched state after $\sqrt{N}$ applications of the Grover operator.[4]

The foundation of applicable QIP schemes are realizable implementations of qubits. Over the past years, there have been several different approaches to the construction of qubits, some of which have already been tested successfully. The most important features that a system must display, are the availability of at least two states, that can be addressed, manipulated and read out by the application of electrical or magnetic fields or photons. Secondly, the coherence times of the superpositioned state must be long in respect to the duration of the quantum processing scheme. The first implementation of Shor's quantum algorithm was carried out on the Zeeman states of an iron complex of (2,3-^{13}C)hexafluorobutadiene using nuclear magnetic resonance (NMR) techniques.[11] However, NMR techniques are considered impractical in terms of scalability. Another possibility are nitrogen vacancy (NV) centers in diamonds, where two carbon atoms are missing in the diamond lattice, one of them being replaced by a nitrogen atom.[83,84] The generated vacancy is a paramagnetic center that can be addressed both using electron paramagnetic resonance (EPR) as well as by optical means. A schematic NV center is depicted in figure 2.28 (left). The most successfully implemented approach for qubit fabrication are superconducting transmon qubits. The largest quantum computers that are available today are arrays of transmon qubits (433 in case of "IBM's" Osprey,[13] see section 1). Transmon qubits are created by the introduction of a Josephson-junction into a superconducting curcuit.[15,85] Figure 2.28 (right) shows a schematic Josephson circuit, that acts as a transmon qubit.

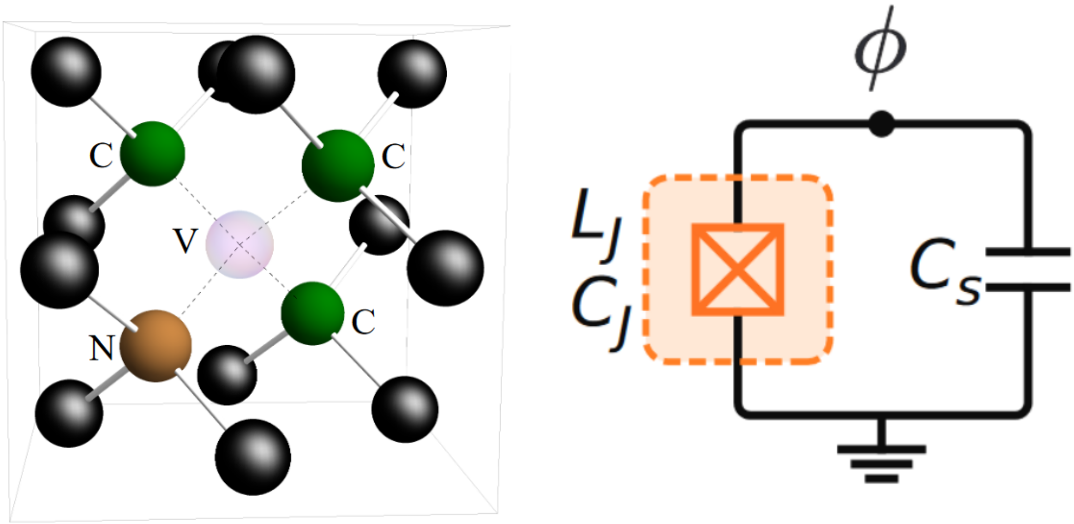

Figure 2.28: Left: Nitrogen-vacancy center in diamond.[84] Right: Schematic Josephson circuit.[85]

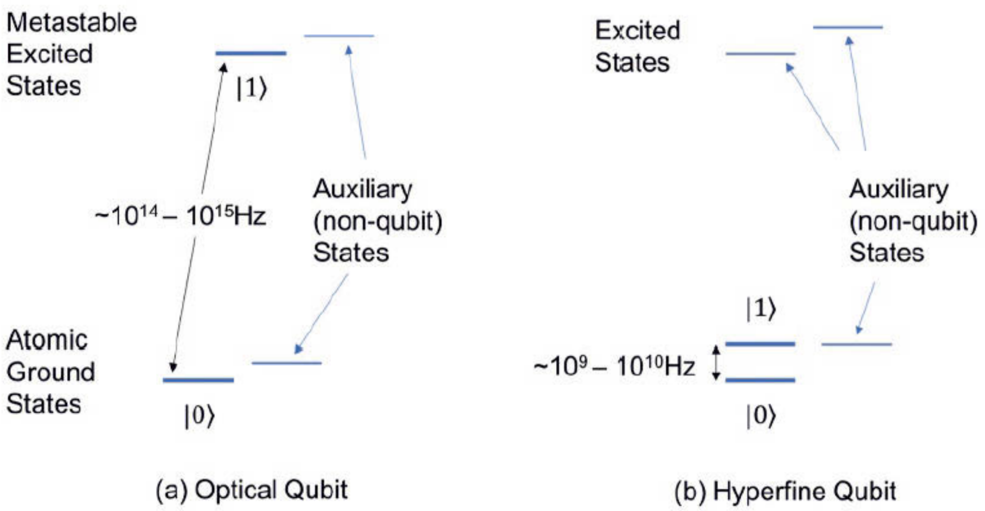

Figure 2.29: Representation of an optical (a) and hyperfine (b) qubit in a trapped ion.[86]

Using strong lasers to ionize atoms under vacuum, those ions can be trapped in an electrical field.[87] The properties of such trapped, so-called Rydberg ions are linked to the trapped element and the oxidation state of the ion. A qubit in a trapped ion can be encoded in the optical transitions (optical qubit) or in the nuclear spin states (hyperfine qubit), visualized in figure 2.29.

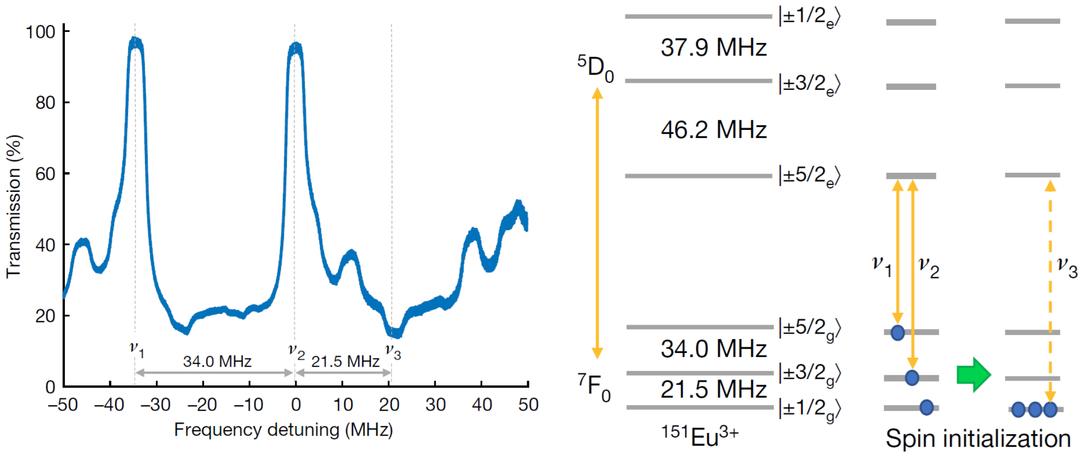

Figure 2.30: Addressing specific nuclear states by adjusting the excitation frequency.[76]

Similarly, optical and hyperfine qubits can be realized using molecular systems. Lanthanide-based systems can show photoluminescent properties, as discussed in section 2.3 with intrinsically narrow transitions and long lifetimes.[76,80] The optical transitions can also be used as a coupling mechanism in order to address the hyperfine levels and with that construct hyperfine qubits on the basis of photoluminescent Ln complexes. For the implementation of QIP schemes in optical molecules, narrow linewidths are a prerequisite as they allow to specifically address molecules within the ensemble. Additionally, considering hyperfine qubits, the individual hyperfine levels can be addressed by choosing specific excitation wavelengths, as their energies are not equally spaced (figure 2.30).

As hyperfine coupling describes the interaction between the nuclear and the electronic spin, the nuclear spin array can also be indirectly accessed through magnetic techniques on Ln-based SMMs. In 2017 Grover's algorithm was performed on a magnetic hyperfine qudit realized as a $TbPc_2$ SMM.[22,23] The small magnetic field that is exerted by the nuclear spin can be understood as a perturbation on the SMM properties observed in a bulk sample. The nuclear spin of Tb is $I = 3/2$, giving four different orientations on the quantization axis $m_I = \pm 1/2, \pm 3/2$. The Zeeman diagram for this case is shown in figure 2.31.

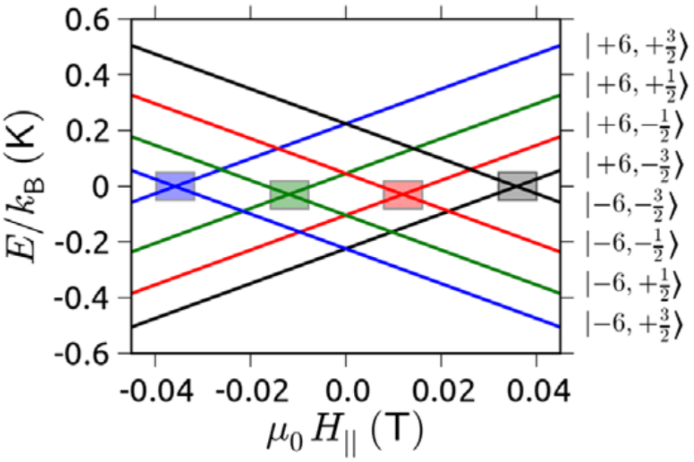

Figure 2.31: Zeeman diagram for $TbPc_2$ with the splitting induced by the nuclear spin states.[31]

As a consequence of the nuclear spin states, the magnetic field at which QTM is observed is shifted, therefore, a magnetic field sweep offers a way of probing the nuclear spin state of the molecule. The necessary Hadamard and Grover manipulations, *vide supra*, were carried out by applying microwave frequency pulses matching the transition energies between the m_I states.

The realization of qubits (or hyperfine qudits) on the basis of molecular lanthanide compounds is the motivation of this thesis. The presented magnetic and photoluminescent properties of the complexes have been tested in order to gain a better understanding and investigate the feasibility of QIP based on molecular compounds.

3 Structural characterization

3.1 The ligand system

In order to study the photoluminescence properties of lanthanide ions in molecular complexes, the employed ligands must be photoactive molecules, that function as an antenna to absorb the photon energy and transfer it to the central metal ion (see section 2.3.). A prerequisite for this mechanism is that the energy difference towards the ligands excited state has to be greater than the energy gap of the lanthanide. The electronic excitation of organic aromatic systems usually occurs in the near UV region of the electromagnetic spectrum, which matches nicely with the desired property, as Ln emission occurs within the visible and near IR region. 1,10-phenanthroline (phen) is a well studied bidentate neutral organic ligand that acts as an antenna causing sensitized luminescence of Ln(III) ions. The steric demand of phen is relatively low, so that a multitude of co-ligands usually fill up the coordination sphere of the metal ion. The results presented in this chapter are based on a phen-ligand substituted with two pyrazole units in the 2 and 9 positions ($\mathbf{L}_H$, Figure 3.1, left). The additional pyrazole units give two extra nitrogen donors, resulting in a tetradentate ligand with increased sterical demand. The multidentate nature of the ligand results in an increased stability of formed complexes due to entropic effects. This ligand has been reported by Li *et al.* who had employed it in an octacoordinated Fe(II) complex.[88] As discussed in section 2.3, C-H, N-H and O-H oscillators in close proximity to a lanthanide ion have strong influences on its PL properties. In order to study the influence of such vibrators, a second version of this ligand was designed, where the two pyrazole subunits have been additionally substituted with methyl-groups in the 3 and 5 positions ($\mathbf{L}_{Me}$, Figure 3.1, right).

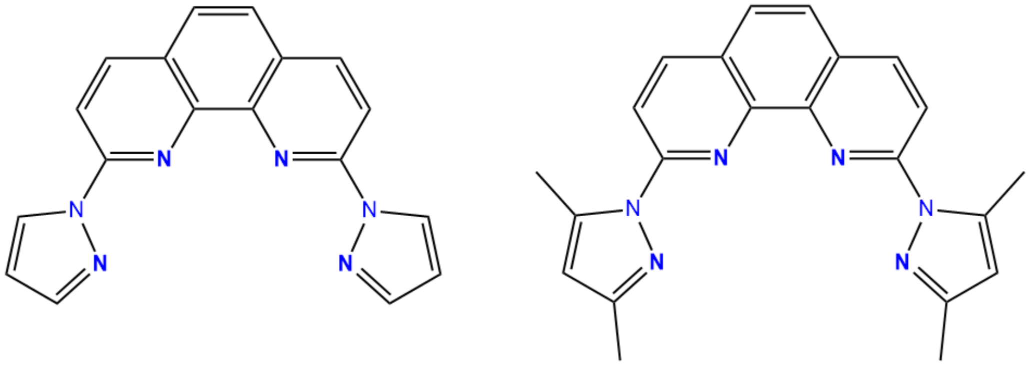

Figure 3.1: Molecular structures of $\mathbf{L}_H$ and $\mathbf{L}_{Me}$. The nitrogen donor atoms are highlighted using bold font.

Successful synthesis of the ligands was achieved by condensation of 2,9-dichloro-1,10-phenanthroline with 1H-pyrazole (**L**$_H$) and 3,5-dimethyl-1H-pyrazole (**L**$_{Me}$), using potassium carbonate as a base (figure 3.2, see section 7). The reaction takes place following a nucleophilic aromatic substitution (S$_N$Ar) mechanism, loosing two equivalents of HCl.

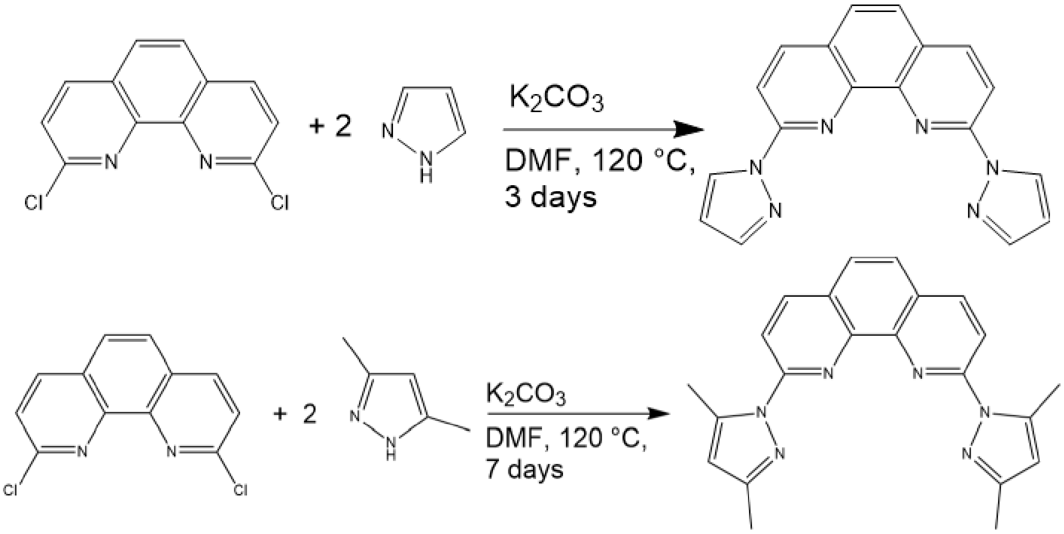

Figure 3.2: Synthetic scheme for **L**$_H$ and **L**$_{Me}$.

The UV-vis absorption spectrum (Figure 3.3, left) for **L**$_H$ and **L**$_{Me}$ confirms the expected bands in the UV region. For both ligands two absorption bands are observed, the first at 272 nm for **L**$_H$ and 271 nm for **L**$_{Me}$ and the second at 313 nm for both **L**$_H$ and **L**$_{Me}$.

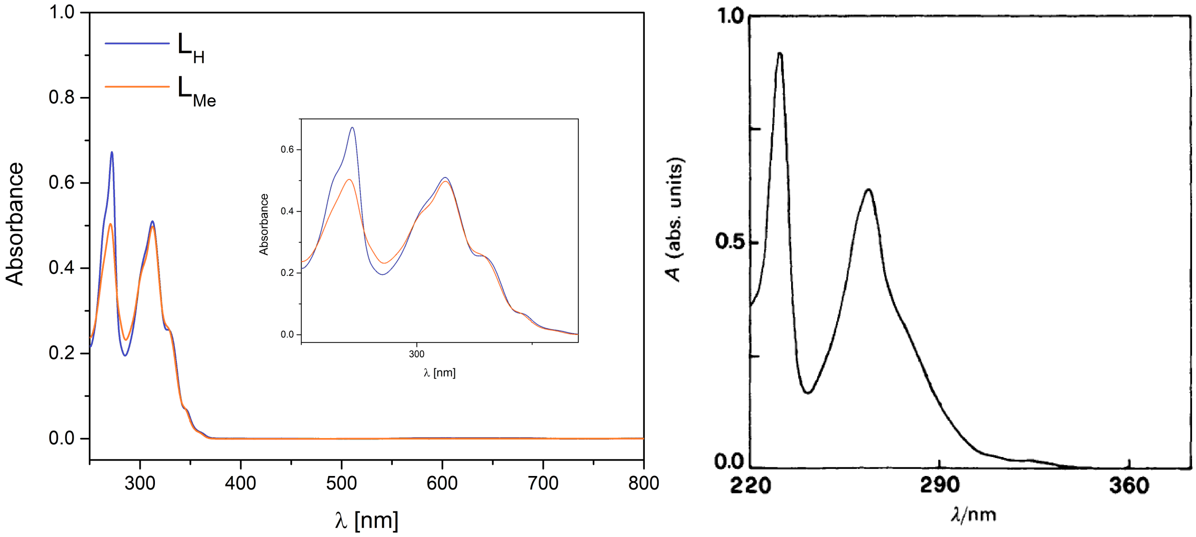

Figure 3.3: Room temperature UV-vis absorption spectra of **L**$_H$ and **L**$_{Me}$ in $CHCl_3$ (left, this work) and phen in CH_2Cl_2 (right).[89]

The low energy band is assigned to the spin-allowed π-π^* transition of the aromatic phenanthroline system. The shape of both absorption curves is near identical with the only significant difference being observed in the relative intensity of the high energy band. The high energy band in $\mathbf{L}_H$ shows a higher intensity in comparison to the π-π^* transition band. For $\mathbf{L}_{Me}$ the intensity of both bands are similar. This is most likely a consequence of the added electron donating effect of the dimethyl-pyrazole groups over the unsubstituted pyrazoles, resulting in a more efficient π-π^* transition of the phenanthroline chromophore. A comparable two band spectrum is observed for the unsubstituted phen,[89] as shown in figure 3.3 (right). In the parent molecule, the high energy band is even more pronounced over the low energy band compared to $\mathbf{L}_H$, confirming the trend that electron-donating substituents increase the intensity of the π-π^* band. Additionally a significant red-shift of the absorption bands is observed upon moving from the unsubstituted phen to $\mathbf{L}_H$ and $\mathbf{L}_{Me}$. The maximum of the low energy band for phen was reported at 264 nm. This translates to a red-shift of 49 nm and an energy difference of around 5930 cm^{-1} for the π-π^* transition, upon substitution with the pyrazole moieties. Such a red-shift has also been observed upon substitution of phen in the 2- and 9- position with other groups. For example a shift of the low energy band to 306 nm was observed for the diphenyl- and 323 nm for the dianisyl-substituted phen.[89]

The solid state photoluminescence properties of both $\mathbf{L}_H$ and $\mathbf{L}_{Me}$ were measured at room temperature. The excitation and emission spectra are shown in figure 3.4.

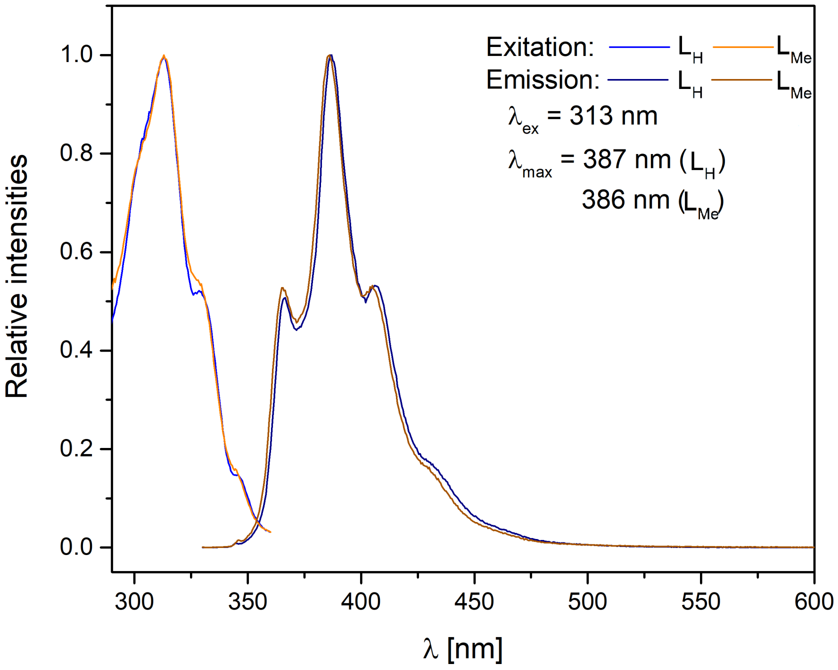

Figure 3.4: Room temperature excitation and emission spectra of $\mathbf{L}_H$ and $\mathbf{L}_{Me}$ in solid state.

The excitation spectra of both compounds show a maximum at 313 nm, matching the absorption band observed in the UV-vis spectrum collected in chloroform solution. The high energy band is not recorded, due to the absorption of the quartz sample holder employed in the spectrometer. Upon excitation at 313 nm, a fluorescent emission is observed for both compounds between 350 and 450 nm, with the maximum intensities found at $\lambda_{max} = 387$ nm and $\lambda_{max} = 386$ nm, for $\mathbf{L}_H$ and $\mathbf{L}_{Me}$, respectively. Both molecules show two additional emission peaks with lower intensities at 366 nm ($\mathbf{L}_H$)/ 365 nm ($\mathbf{L}_{Me}$) and 406 nm ($\mathbf{L}_H$)/ 405 nm ($\mathbf{L}_{Me}$), as well as a shoulder around 430 nm. The highly comparable features of both the absorption and luminescence spectra of $\mathbf{L}_H$ and $\mathbf{L}_{Me}$ prove, that the light-active site is solely the phen unit, with the pyrazole groups only indirectly influencing the properties through alteration of the electronic density. The additional methyl-groups on the pyrazole, however, only have a minor influence on the luminescent properties. The favourable energetic positions of the absorption and emission bands associated with the ligands could be used to prepare Ln(III) complexes that can show sensitized emission.

In solution, the C-N bond between the phen unit and the pyrazole groups can freely rotate. Assuming common distances of C-N and C-C bonds a flat configuration, as schematically depicted in figure 3.1, would lead to a N$\cdots$N distance between the two N-donors of the pyrazole groups of approx. 5.2 Å. The resulting N_4 pocket is quite well suited to accommodate a single trivalent rare earth ion. In comparison, the N_4 arrangement is relatively big for transition metals, which led to the octacoordinated iron(II) complex by Li *et al*, which is a rather uncommon coordination number for Fe(II) ions.[88] Employing rare earth nitrates as precursors, the nitrate anions can act as bidentate ligands to occupy the metal's coordination sphere, without introduction of unwanted X-H vibrations (X = C, N, O), see section 3.2 and 3.3.

3.2 Lanthanide complexes of L_H

Layering methanolic solutions of $Ln(NO_3)_3 \cdot$ x H_2O salts on top of chloroform solutions of $\mathbf{L}_H$ resulted in the complexation of the Lanthanide metal ions by the N_4 moiety of the ligand (see figure 3.5).

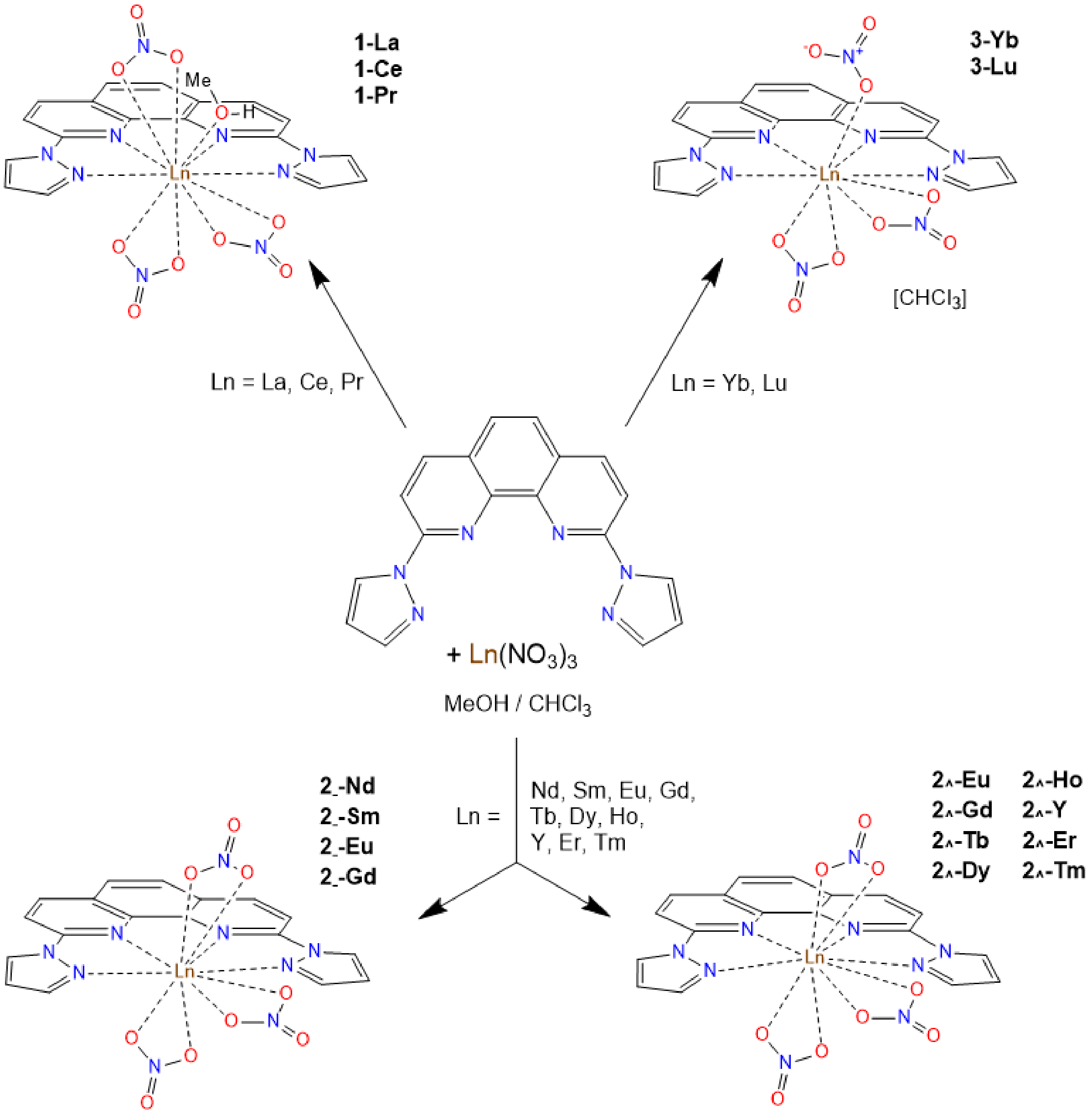

Figure 3.5: Preparation of Ln(III) complexes based on $\mathbf{L}_H$.

Starting with the lighter and bigger ions of the lanthanide series, lanthanum, cerium and praseodymium, the three complexes **1-La**, **1-Ce** and **1-Pr** of the general formula $[LnL_H(NO_3)_3MeOH]$ were obtained. All three complexes crystallize in the triclinic space group $P\bar{1}$ with two molecules in the unit cell. **1-Ce** and **1-Pr** are fully isostructural, as seen by the unit cell parameters given in table 3.1. **1-La** on the other hand, crystallizes in a different unit cell, although still triclinic.

Table 3.1: Unit cell parameters for **1-La**, **1-Ce** and **1-Pr**. Full crystallographic details are given in the appendix.

	1-La	**1-Ce**	**1-Pr**
space group	$P\bar{1}$	$P\bar{1}$	$P\bar{1}$
a [Å]	8.7676(4)	9.1606(5)	9.1399(4)
b [Å]	10.2763(5)	11.3285(6)	11.3179(5)
c [Å]	13.6794(7)	12.1041(6)	12.0778(6)
α [°]	98.328(4)	75.800(4)	75.835(4)
β [°]	98.634(4)	71.342(4)	71.410(4)
γ [°]	96.711(4)	82.471(4)	82.537(4)
V [Å^3]	1193.51(10)	1151.85(11)	1146.36(10)

Figure 3.6 shows the molecular structures of the complexes **1-Ln**. The structures consist of a single central Ln(III) ion, which is pincered by the $\mathbf{L}_H$ ligand. One of the pyrazole units is slightly tilted out of the plane in order to fit the metal ion. The charge balance as well as filling of the coordination sphere is achieved through coordination of three nitrate anions that all coordinate in a bidentate mode. The relative position of the nitrates with respect to the nitrogen-backbone can be described as lying on an orthogonal meridian, reminiscent of a mer-isomer of a prototypical octahedral MA_3B_3 complex.[35] Due to the big ionic radius of the early lanthanide ions, an additional solvent molecule, methanol, is coordinated to the central ion to fully occupy the coordination sphere. The methanol molecule is found on the nitrate meridian in between the nitrate anions. The resulting coordination sphere for **1-Ln** is, therefore, characterized as N_4O_7 with CN = 11.

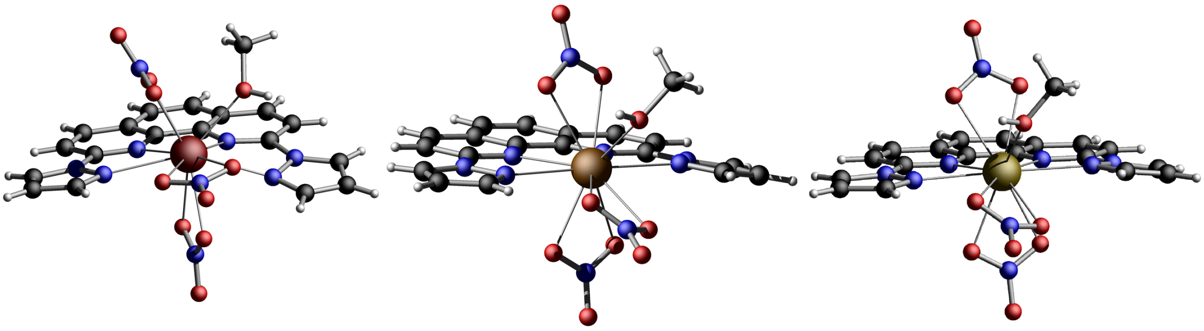

Figure 3.6: Molecular structures obtained from single-crystal X-ray diffraction studies of **1-Ln** (Ln = La, Ce, Pr from left to right).

The difference between **1-La** and **1-Ce**/ **1-Pr** is the orientation of both the methanol as well as the nitrates. While all three nitrate ligands are close to orthogonal with the meridian they are located on for **1-Ce** and **1-Pr**, two of the nitrates in **1-La** align with the meridian (compare figure 3.6, left). The methanolic hydrogen is found pointing away from the meridian in **1-La** and pointing towards it in **1-Ce** and **1-Pr**. Table 3.2 lists the bond lengths between the central metal ion and the nitrogen and oxygen donor atoms. N1 and N6 are the nitrogen-donors of the pyrazole groups, N2 and N3 are the Ns of the phenanthroline unit and O10 is the methanolic oxygen.

Table 3.2: Selected bond lengths for complexes **1-Ln** in Å.

Bond	**1-La**	**1-Ce**	**1-Pr**
Ln···N1	2.688(4)	2.637(3)	2.635(4)
Ln···N3	2.725(3)	2.674(4)	2.654(4)
Ln···N4	2.761(3)	2.696(4)	2.683(4)
Ln···N6	2.665(4)	2.657(3)	2.652(3)
Ln···O1	2.594(3)	2.707(4)	2.693(4)
Ln···O2	2.655(4)	2.671(4)	2.649(4)
Ln···O4	2.687(3)	2.636(4)	2.618(4)
Ln···O5	2.665(3)	2.612(4)	2.592(4)
Ln···O7	2.673(3)	2.569(3)	2.543(3)
Ln···O8	2.632(3)	2.645(3)	2.629(3)
Ln···O10	2.579(3)	2.592(3)	2.588(3)

In all three complexes the Ln···N distances towards the pyrazole-Ns are strictly shorter than the Ln···N distances with the nitrogens of the phen backbone. The average Ln···N distances decrease from 2.710 Å for **1-La** to 2.666 Å for **1-Ce** and 2.656 Å for **1-Pr**, matching the decreasing ionic radius of the lanthanide ions. Similarly a decrease is observed for the average Ln···O distances from 2.641 Å to 2.633 Å and 2.616 Å , for **1-La**, **1-Ce** and **1-Pr**, respectively. Generally, the observed Ln···O distance towards the methanol-O is shorter than the Ln···O distances obtained between the metal and the nitrate-O's. The decreasing ionic radius is also observed in the decreasing volume of the unit cells from 1193.51 $Å^3$ for **1-La** down to 1146.36 $Å^3$ for **1-Pr** (table 3.1). The powder X-ray diffraction patterns of the bulk samples of complexes **1-Ln** are shown in figure 3.7. It is evident, that the bulk samples contain only a single crystallographic species, matching the single crystal data discussed.

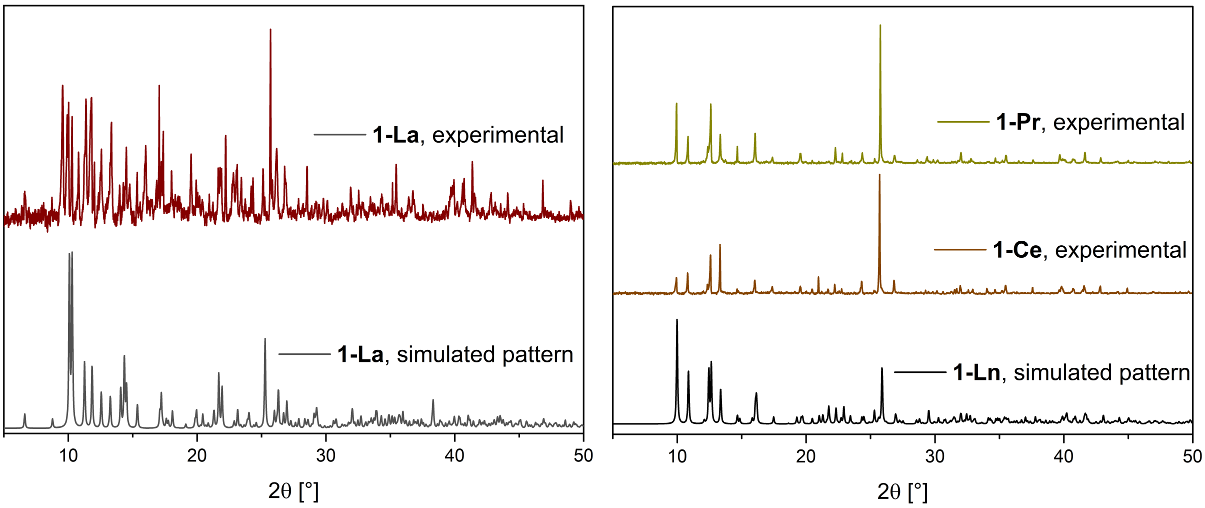

Figure 3.7: Comparison between the simulated pattern obtained from SC-XRD and experimental PXRD patterns for **1-Ln**.

As far as the other Ln(III) complexes are concerned, a shift of the molecular structure is observed upon switching from praseodymium to neodymium. All rare earth ion complexes of L_H starting from Nd to Tm (excluding Pm, due to its radioactivity) were obtained with a general molecular formula $[LnL_H(NO_3)_3]$ (**2-Ln**).

The most significant difference compared to the molecular structures of **1-Ln** is the missing solvent methanol. Due to the further decrease of the ionic radii, coordination of a methanol unit is no longer observed. This results in the complexes **2-Ln** being ten-coordinate complexes with a N_4O_6-coordination sphere. Besides, the general motif of three nitrates coordinating along an orthogonal meridian, found in **1-Ln**, remains. In depth analysis of the single crystal and powder X-ray diffraction data revealed two different substructures in **2-Ln**. The two different polymorphs of **2-Eu** and **2-Gd** are shown in figure 3.8. In both structures the nitrate ligands coordinate in the same fashion, where two nitrates are coordinated orthogonal to their meridian, similar to the nitrate coordination in complexes **1-Ce** and **1-Pr**. However, the third nitrate ligand is rotated by 90°, with both O-donors found on the meridian. The distinction of the polymorphs is based on the ligands' geometry. In one structure, the two pyrazole units are slightly rotated in the same direction, resulting in the Ln(III) ion sitting right in the center of the N_4-arrangement provided by the ligand (figure 3.8, top). In the structure of the second polymorph the pyrazole groups are rotated in opposing directions to one another, leading to an overall bent geometry of the ligand. Therefore, the Ln(III) ion sits on top of the bent ligand, slightly out of the N_4-arrangement (figure 3.8, bottom). Based on the resulting N-Ln-N arrangement of the pyrazoles' donor-N's the first polymorph of **2-Ln** is referred to as **$2_{\_}$-Ln** and the second one as **$2_{\wedge}$-Ln**.

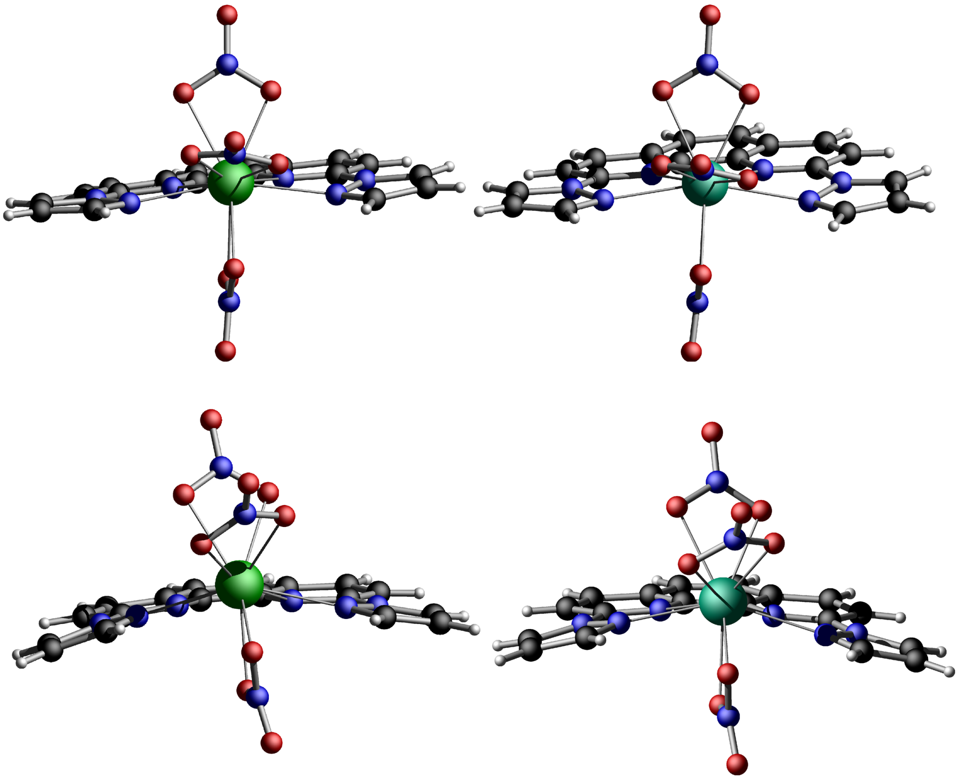

Figure 3.8: Molecular structures obtained from single-crystal X-ray diffraction studies of **2-Ln** (Top: **2**$_{-}$**-Eu**, **2**$_{-}$**-Gd**, Bottom: **2**$_{\wedge}$**-Eu**, **2**$_{\wedge}$**-Gd**).

As shown in figure 3.8, single crystals of both **2**$_{-}$**-Ln** and **2**$_{\wedge}$**-Ln** could be obtained from samples of **2-Eu** and **2-Gd**. The elements Eu and Gd were, however, the only elements for which both polymorphs were observed simultaneously. The larger ions Nd(III) and Sm(III) were exclusively found forming the N_4-centered polymorphs **2**$_{-}$**-Nd** and **2**$_{-}$**-Sm**, while the smaller ions were only found as **2**$_{\wedge}$**-Ln** (Ln = Tb, Dy, Ho, Y, Er, Tm).

Table 3.3: Unit cell parameters for **2**$_{-}$**-Ln**. Full crystallographic details are given in the appendix.

	2$_{-}$**-Nd**	**2**$_{-}$**-Sm**	**2**$_{-}$**-Eu**	**2**$_{-}$**-Gd**
space group	$P\bar{1}$	$P2_1/c$	$P2_1/c$	$P2_1/c$
a [Å]	10.7373(4)	11.1790(2)	11.1803(2)	11.1722(2)
b [Å]	11.3278(4)	10.79670(10)	10.8029(2)	10.8000(2)
c [Å]	17.9420(6)	18.0733(3)	18.0552(3)	18.0260(3)
α [°]	85.794(3)	90	90	90
β [°]	85.958(3)	94.3540(10)	94.264(2)	94.225(1)
γ [°]	87.736(3)	90	90	90
V [Å^3]	2169.70(13)	2175.08(6)	2174.66(7)	2169.10(7)

2_-Nd crystallized in the triclinic unit cell $P\bar{1}$ with four molecules in the unit cell, while **2_-Sm**, **2_-Eu** and **2_-Gd** are isostructural, crystallizing in the monoclinic space group $P2_1/c$ with four molecules in the unit cell. Despite the different crystallization behaviour of the neodymium analogue, refinement of the single crystal data revealed the geometry of **2-Nd** to match the ones found for **2_-Ln**, and consequentially the obtained compound is labelled **2_-Nd**. The molecular structures of **2_-Nd** and **2_-Sm** are given in figure 3.9, revealing the similarities with the structures found for **2_-Eu** and **2_-Gd** (figure 3.8, top).

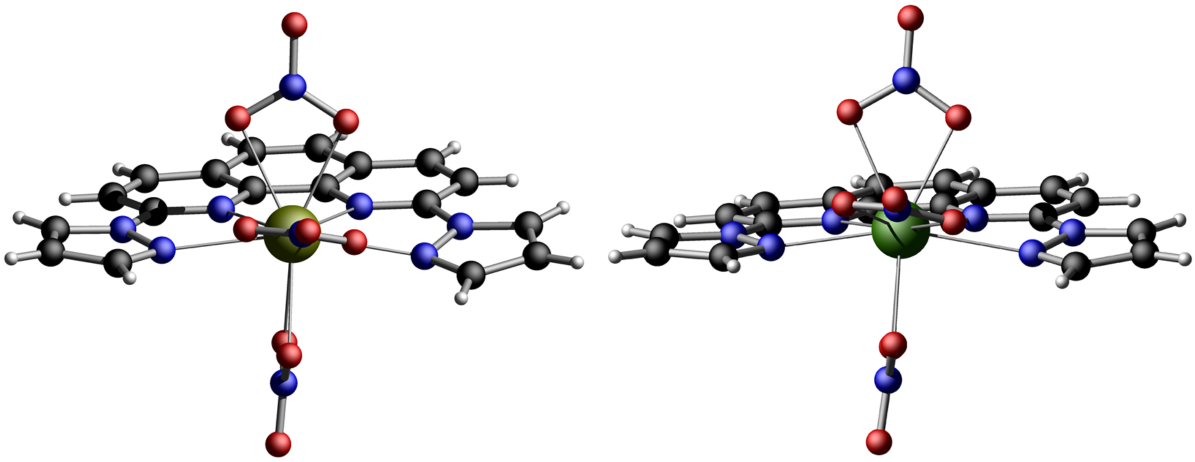

Figure 3.9: Molecular structures obtained from single-crystal X-ray diffraction studies of **2_-Nd** and **2_-Sm**.

The trend already observed for **1-Ln** of the Ln$\cdots$N bond lengths towards the phen-Ns being exclusively longer than the bond lengths towards the pyrazole-Ns is also observed in all complexes of **2_-Ln** (table 3.4). The average Ln$\cdots$N distances are 2.634 Å, 2.602 Å, 2.590 Å and 2.584 Å for **2_-Nd**, **2_-Sm**, **2_-Eu** and **2_-Gd** respectively, again decreasing as expected with increasing atomic number. The same is true for the average Ln$\cdots$O bond lengths, decreasing from 2.529 Å(**2_-Nd**), 2.507 Å(**2_-Sm**), 2.495 Å(**2_-Eu**) to 2.487 Å(**2_-Gd**).

Table 3.4: Selected bond lengths of complexes **2_-Ln** in Å.

Bond	**2_-Nd**	**2_-Sm**	**2_-Eu**	**2_-Gd**
Ln···N1	2.586(7)	2.545(2)	2.535(3)	2.525(3)
Ln···N3	2.647(7)	2.630(2)	2.614(3)	2.615(3)
Ln···N4	2.666(7)	2.631(2)	2.625(3)	2.614(3)
Ln···N6	2.636(8)	2.602(3)	2.587(3)	2.580(4)
Ln···O1	2.532(7)	2.444(3)	2.496(3)	2.486(3)
Ln···O2	2.511(7)	2.501(2)	2.487(3)	2.472(3)
Ln···O4	2.573(7)	2.564(3)	2.566(3)	2.571(3)
Ln···O5	2.563(6)	2.519(2)	2.501(3)	2.493(3)
Ln···O7	2.475(7)	2.502(2)	2.432(3)	2.421(3)
Ln···O8	2.518(6)	2.513(2)	2.488(3)	2.478(3)

The X-ray powder patterns of **2-Nd** and **2-Sm** are shown in figure 3.10. The experimental patterns do not show any reflections that would match with the simulated pattern obtained from single crystal data of **2**$_\wedge$**-Ln**, confirming that **2-Nd** and **2-Sm** form exclusively **2_-Nd** and **2_-Sm**.

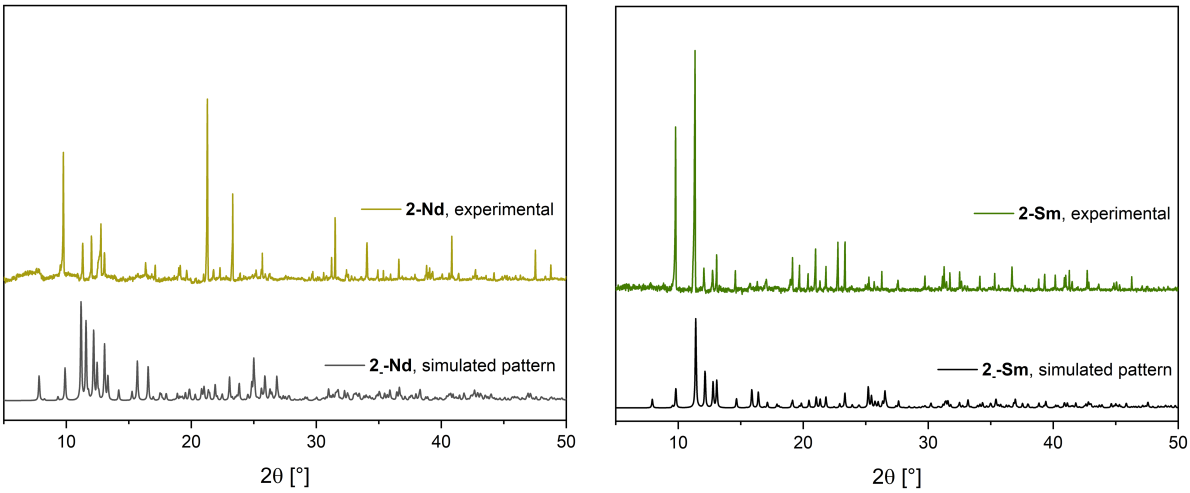

Figure 3.10: Comparison between the simulated pattern obtained from SC-XRD and experimental PXRD patterns for **2_-Nd** and **2_-Sm**.

The compounds **2**$_\wedge$**-Ln** (Ln = Y, Eu-Tm) are fully isostructural (figure 3.8 bottom and figure 3.11), crystallizing in the triclinic space group $P\bar{1}$ with two molecules per unit cell. Again, a steady decrease of the unit cell volume from 1077.12 Å^3 in **2**$_\wedge$**-Eu** down to 1063.66 Å^3 in **2**$_\wedge$**-Tm**, alongside the decreasing ionic radius is observed (table 3.5). Notably, an anomaly is observed between **2**$_\wedge$**-Tb** and **2**$_\wedge$**-Dy** with a minor increase in the determined unit cell volume, however, this might be linked to the standard uncertainties of the X-ray structure refinement.

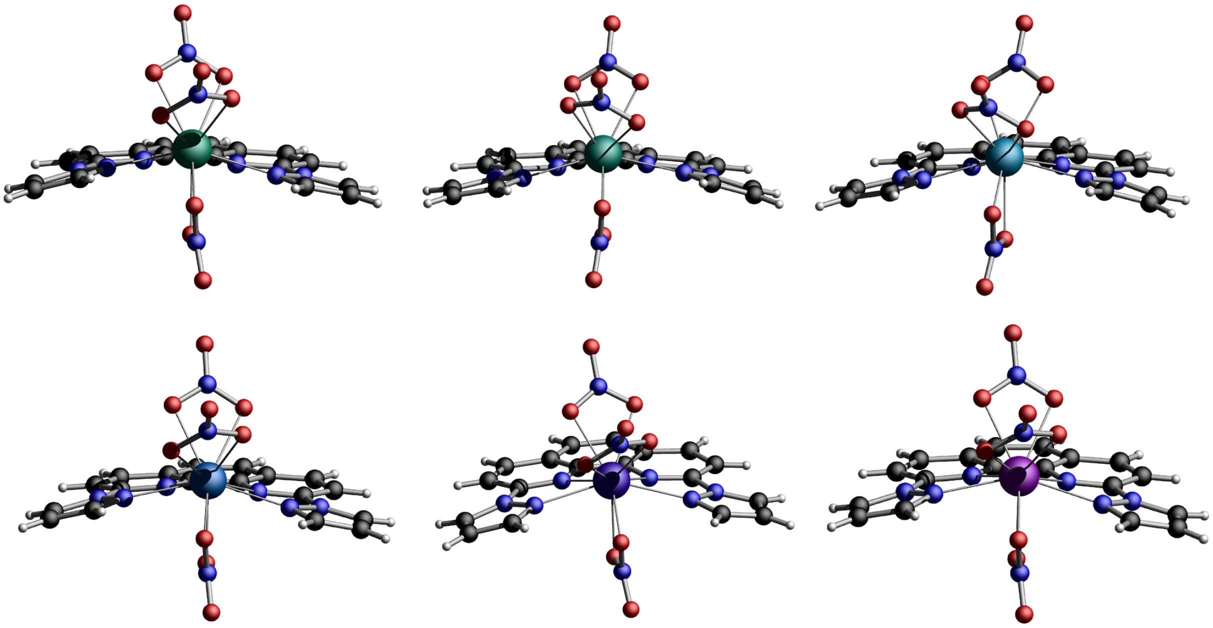

Figure 3.11: Single crystal molecular structures of $\mathbf{2}_{\wedge}$**-Ln** (Top: Ln = Tb, Dy, Ho, Bottom: Ln = Y, Er, Tm).

The average Ln···N distances found in $\mathbf{2}_{\wedge}$**-Ln** are 2.564 Å(Eu), 2.556 Å(Gd), 2.543 Å(Tb), 2.532 Å(Dy), 2.521 Å(Ho), 2.519 Å(Y), 2.508 Å(Er) and 2.498 Å(Tm). The average Ln···O bond lengths are 2.503 Å(Eu), 2.494 Å(Gd), 2.482 Å(Tb), 2.476 Å(Dy), 2.460 Å(Ho), 2.453 Å(Y), 2.451 Å(Er) and 2.442 Å(Tm), showing the expected decrease, with decreasing ionic radius. As the crystal systems, in which $\mathbf{2}_{-}$**-Ln** and $\mathbf{2}_{\wedge}$**-Ln** are obtained, differ, the unit cell volumes do not hold as a good metric for comparison. The average Ln···N distances observed in $\mathbf{2}_{\wedge}$**-Ln** (Ln = Eu, Gd) are about 0.3 Å shorter than the distances in $\mathbf{2}_{-}$**-Ln** (Ln = Eu, Gd). The ligand's N_4-coordination pocket is, therefore, smaller for $\mathbf{2}_{\wedge}$**-Ln** in respect to $\mathbf{2}_{-}$**-Ln**, which matches with the observation of the $\mathbf{2}_{\wedge}$**-Ln** polymorph being favoured for the smaller and heavier elements of the series. Interestingly, the larger coordination pocket provided by the organic ligand in $\mathbf{2}_{-}$**-Ln** and the therefore lowered electron donating effect of the nitrogen atoms, seems to be balanced out by the nitrates, which are moved closer to the central atom, characterized by approximately 0.08 Å shorter Ln···O bond lengths in $\mathbf{2}_{-}$**-Eu** and $\mathbf{2}_{-}$**-Gd** compared to $\mathbf{2}_{\wedge}$**-Eu** and $\mathbf{2}_{\wedge}$**-Gd**.

Table 3.5: Unit cell parameters for **2$_{\wedge}$-Ln**. Full crystallographic details are given in the appendix.

	2$_{\wedge}$-Eu	**2$_{\wedge}$-Gd**	**2$_{\wedge}$-Tb**	**2$_{\wedge}$-Dy**
space group	$P\bar{1}$	$P\bar{1}$	$P\bar{1}$	$P\bar{1}$
a [Å]	8.6450(5)	8.6368(5)	8.6133(4)	8.6024(6)
b [Å]	9.2078(5)	9.2186(4)	9.2356(5)	9.2462(5)
c [Å]	14.1581(8)	14.1407(7)	14.1183(6)	14.1380(9)
α [°]	78.383(4)	78.338(4)	78.283(4)	78.196(5)
β [°]	79.974(5)	79.922(4)	79.833(4)	79.701(6)
γ [°]	80.490(4)	80.374(4)	80.175(4)	79.939(5)
V [Å^3]	1077.12(11)	1075.42(10)	1071.79(9)	1071.82(12)
	2$_{\wedge}$-Ho	**2$_{\wedge}$-Y**	**2$_{\wedge}$-Er**	**2$_{\wedge}$-Tm**
space group	$P\bar{1}$	$P\bar{1}$	$P\bar{1}$	$P\bar{1}$
a [Å]	8.5891(5)	8.5916(4)	8.5812(5)	8.5742(5)
b [Å]	9.2549(6)	9.2518(5)	9.2609(4)	9.2729(6)
c [Å]	14.0807(7)	14.0736(8)	14.0753(8)	14.0458(9)
α [°]	78.163(5)	78.174(4)	78.157(4)	78.076(5)
β [°]	79.720(4)	79.586(4)	79.571(5)	79.644(5)
γ [°]	80.027(5)	79.929(4)	79.910(4)	79.883(5)
V [Å^3]	1067.01(11)	1065.80(10)	1065.53(10)	1063.66(12)

Table 3.6: Selected bond lengths for complexes **2$_{\wedge}$-Ln** in Å.

Bond	**2$_{\wedge}$-Eu**	**2$_{\wedge}$-Gd**	**2$_{\wedge}$-Tb**	**2$_{\wedge}$-Dy**	**2$_{\wedge}$-Ho**	**2$_{\wedge}$-Y**	**2$_{\wedge}$-Er**	**2$_{\wedge}$-Tm**
Ln$\cdots$N1	2.535(4)	2.540(3)	2.521(4)	2.521(4)	2.501(5)	2.490(1)	2.492(4)	2.479(6)
Ln$\cdots$N3	2.581(3)	2.586(2)	2.557(2)	2.568(4)	2.552(5)	2.525(1)	2.546(3)	2.535(6)
Ln$\cdots$N4	2.594(3)	2.569(2)	2.565(3)	2.535(4)	2.535(5)	2.557(1)	2.514(3)	2.514(5)
Ln$\cdots$N6	2.547(4)	2.527(3)	2.528(4)	2.502(4)	2.494(5)	2.503(1)	2.479(4)	2.465(6)
Ln$\cdots$O1	2.479(4)	2.464(3)	2.451(3)	2.447(5)	2.426(6)	2.415(2)	2.411(4)	2.430(6)
Ln$\cdots$O2	2.432(3)	2.416(3)	2.402(3)	2.394(5)	2.380(6)	2.376(1)	2.376(4)	2.544(7)
Ln$\cdots$O4	2.462(4)	2.548(2)	2.444(3)	2.532(4)	2.416(5)	2.525(1)	2.526(3)	2.534(6)
Ln$\cdots$O5	2.551(3)	2.454(3)	2.537(3)	2.440(4)	2.536(5)	2.414(1)	2.411(3)	2.389(6)
Ln$\cdots$O7	2.590(4)	2.494(3)	2.478(3)	2.569(4)	2.555(6)	2.544(1)	2.543(4)	2.370(6)
Ln$\cdots$O8	2.505(3)	2.585(3)	2.577(3)	2.473(5)	2.447(6)	2.445(1)	2.438(4)	2.386(7)

Another interesting metric worth discussing, are the observed N-Ln-N angles between the pyrazole-Ns of **2$_{\wedge}$-Ln**. Based on the observed structure of the Ln(III) ion sitting on top of the ligand (compare figure 3.8, bottom and figure 3.11), a decreasing N-Ln-N angle would be expected with increasing atomic number, as the smaller ions should move into the N_4 pocket more closely. In fact, a small decrease is observed from 149.62 in **2$_{\wedge}$-Eu** down to 148.70 in **2$_{\wedge}$-Tm** (table 3.7), however, the effect is rather small, with two observed anomalies between Ho/Y and Er/Tm. The X-ray powder diffraction patterns for the different samples of **2-Ln** (Ln = Y, Eu-Tm) are shown in figure 3.12. The patterns for Ln = Y, Tb-Tm confirm the exclusive formation of **2$_{\wedge}$-Ln**. The powder patterns recorded for **2-Eu** and **2-Gd** show patterns mainly matching with the simulated pattern of **2$_{\wedge}$-Ln**, leading to the assumption, that the percentage of **2$_{\wedge}$-Ln** obtained is higher than of **2$_{\_}$-Ln**, which is not quantitatively measurable in this way, as it might also be a consequence of e.g., lower crystallinity of the **2$_{\_}$-Ln** polymorph.

Table 3.7: Observed N-Ln-N angles in **2$_{\wedge}$-Ln**

Compound	N-Ln-N angle [°]
2$_{\wedge}$-Eu	149.62(12)
2$_{\wedge}$-Gd	149.46(9)
2$_{\wedge}$-Tb	149.17(12)
2$_{\wedge}$-Dy	148.84(15)
2$_{\wedge}$-Ho	148.65(19)
2$_{\wedge}$-Y	148.84(5)
2$_{\wedge}$-Er	148.57(12)
2$_{\wedge}$-Tm	148.70(2)

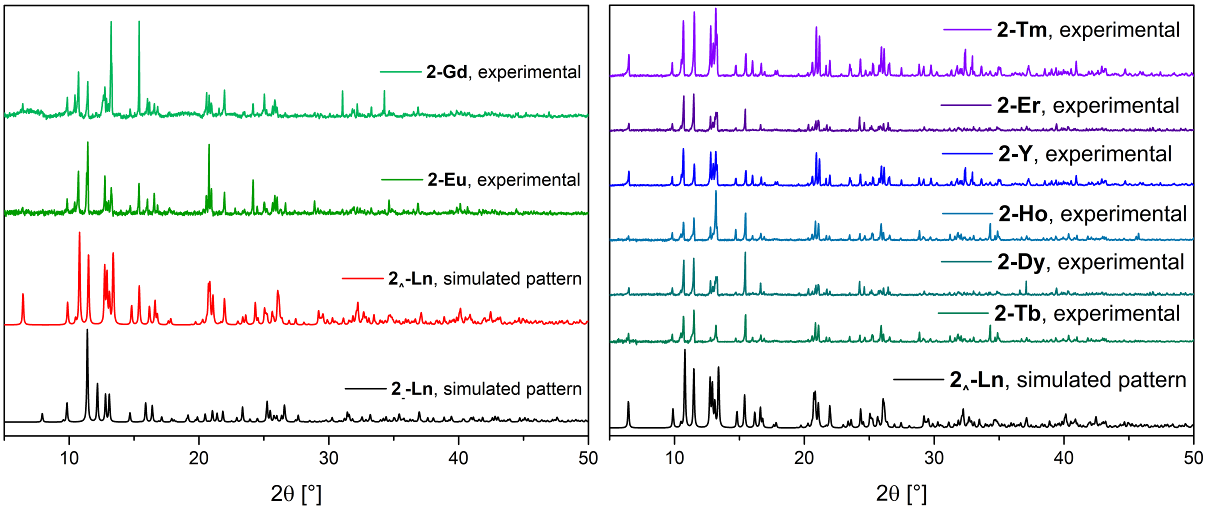

Figure 3.12: X-ray powder diffraction patterns of **2$_{\wedge}$-Ln**.

The two smallest and heaviest elements of the lanthanide series Yb and Lu are obtained as **3-Ln** (Ln = Yb, Lu) upon reaction of their nitrate salts with L_H. They both are isostructural, crystallizing in the monoclinic space group $C2/c$ (table 3.8), with eight molecules in the unit cell. Alongside, one chloroform solvent molecule is found in the crystal lattice per molecule, giving the general formula $[LnL_H(NO_3)_3]\cdot CHCl_3$ (Ln = Yb, Lu). Interestingly, the unit cell parameters a and β differ significantly from one another in **3-Yb** and **3-Lu**, as the observed orientation of the molceules in the unit cells differ. The molecular structures obtained from single crystal X-ray diffraction are shown in figure 3.13.

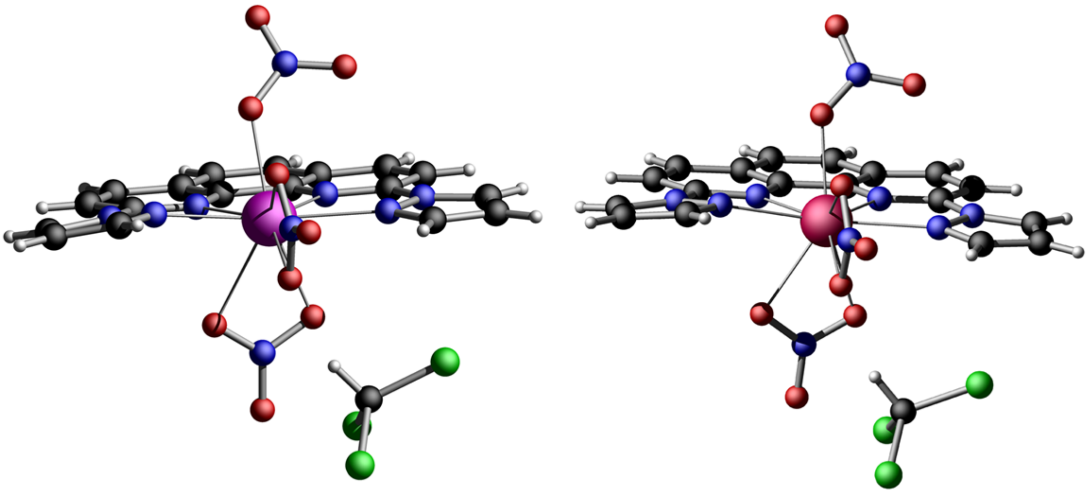

Figure 3.13: Molecular structures obtained from single-crystal X-ray diffraction studies of **3-Yb** (left) and **3-Lu** (right).

The observed molecular structures of **3-Ln** reveal a ligand geometry in which one of the pyrazole groups is slightly angled and the other one remains within the plane of the phen backbone, closer to what has also been observed in compounds **1-Ln** and **$2_{–}$-Ln**. This is interesting, as the smaller ionic radius would suggest the bent geometry, observed for **$2_{\wedge}$-Ln**, to be beneficial. Aside the co-crystallizing solvent chloroform, the major difference observed for **3-Ln** is in the coordination modes of the nitrate anions. While two of the nitrates coordinate, similar to the structures of **1-Ln** and **2-Ln**, in a bidentate fashion (one aligned with the nitrates' meridian, the other perpendicular to it), the third nitrate ligand coordinates in a monodentate mode, with only one oxygen donor forming a coordination bond with the Ln(III) ions. Therefore, compounds **3-Ln** are nonacoordinate complexes with a N_4O_5 coordination sphere.

Table 3.8: Unit cell parameters for **3-Ln**. Full crystallographic details are given in the appendix.

	3-Yb	**3-Lu**
space group	*C*2/*c*	*C*2/*c*
a [Å]	27.510(3)	31.7466(10)
b [Å]	12.7874(10)	12.8128(2)
c [Å]	15.7335(12)	15.7261(5)
α [°]	90	90
β [°]	115.168(6)	128.256(5)
γ [°]	90	90
V [Å^3]	5009.4(7)	5025.28(15)

As expected for Yb and Lu, the average Ln···N bond lengths in **3-Ln** are shorter than the distances observed for compounds **1-Ln** and **2-Ln** with 2.433 Å and 2.424 Å for **3-Yb** and **3-Lu**, respectively. Similarly, the average Ln···O bond lengths with 2.379 Å (**3-Yb**) and 2.382 Å (**3-Lu**) are also significantly shorter than the distances observed in **1-Ln** and **2-Ln**. Interestingly, and contradicting to **1-Ln** and **2-Ln**, the Ln···N distances towards the phen-Ns in the complexes **3-Yb** and **3-Lu** are shorter than the Ln···N distances towards the pyrazole-Ns. This observation represents a shift of the Ln(III) ion from a more outside-of-the-pocket to an inside-of-the-pocket coordination by the ligand. The Ln···O bond length between the central ion and the monodentate nitrate-O (O7) is approximately 0.1 Å shorter than the distances towards the bidentate nitrate donors, which is an effect of the electron density. As one of the donor atoms is removed from the coordination sphere, the remaining oxygen atom moves closer to the central ion in order to compensate the missing electron donating effect.

Table 3.9: Selected bond lengths for complexes **3-Ln** in Å.

Bond	**3-Yb**	**3-Lu**
Ln···N1	2.439(2)	2.440(4)
Ln···N3	2.415(2)	2.406(4)
Ln···N4	2.431(2)	2.425(4)
Ln···N6	2.446(2)	2.425(3)
Ln···O1	2.464(2)	2.469(3)
Ln···O2	2.384(2)	2.385(3)
Ln···O4	2.375(2)	2.380(4)
Ln···O5	2.374(2)	2.380(4)
Ln···O7	2.300(3)	2.298(3)

The measured powder diffraction patterns are shown in figure 3.14. The experimentally determined patterns show diffractions, that are not fully matching the pattern simulated using the single crystal refinement data, suggesting the possibility of a second polymorph. However, no single crystals of a second polymorph could be identified, despite the best efforts.

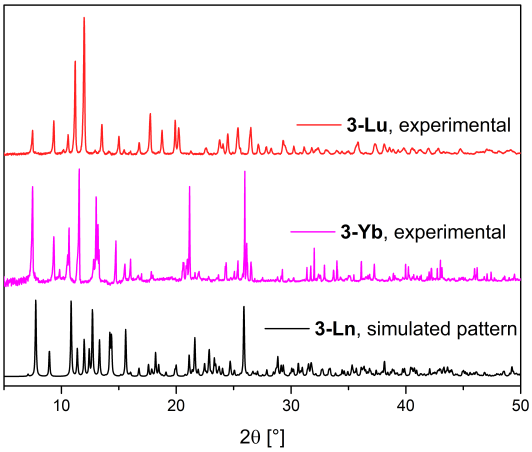

Figure 3.14: X-ray powder diffraction patterns for **3-Yb** and **3-Lu**.

3.3 Lanthanide complexes of L_{Me}

In a similar setup, the slow diffusion of REI nitrates into a chloroform solution of L_{Me} resulted in the formation of coordination compounds of yttrium and the full lanthanide series, excluding Pm (figure 3.15).

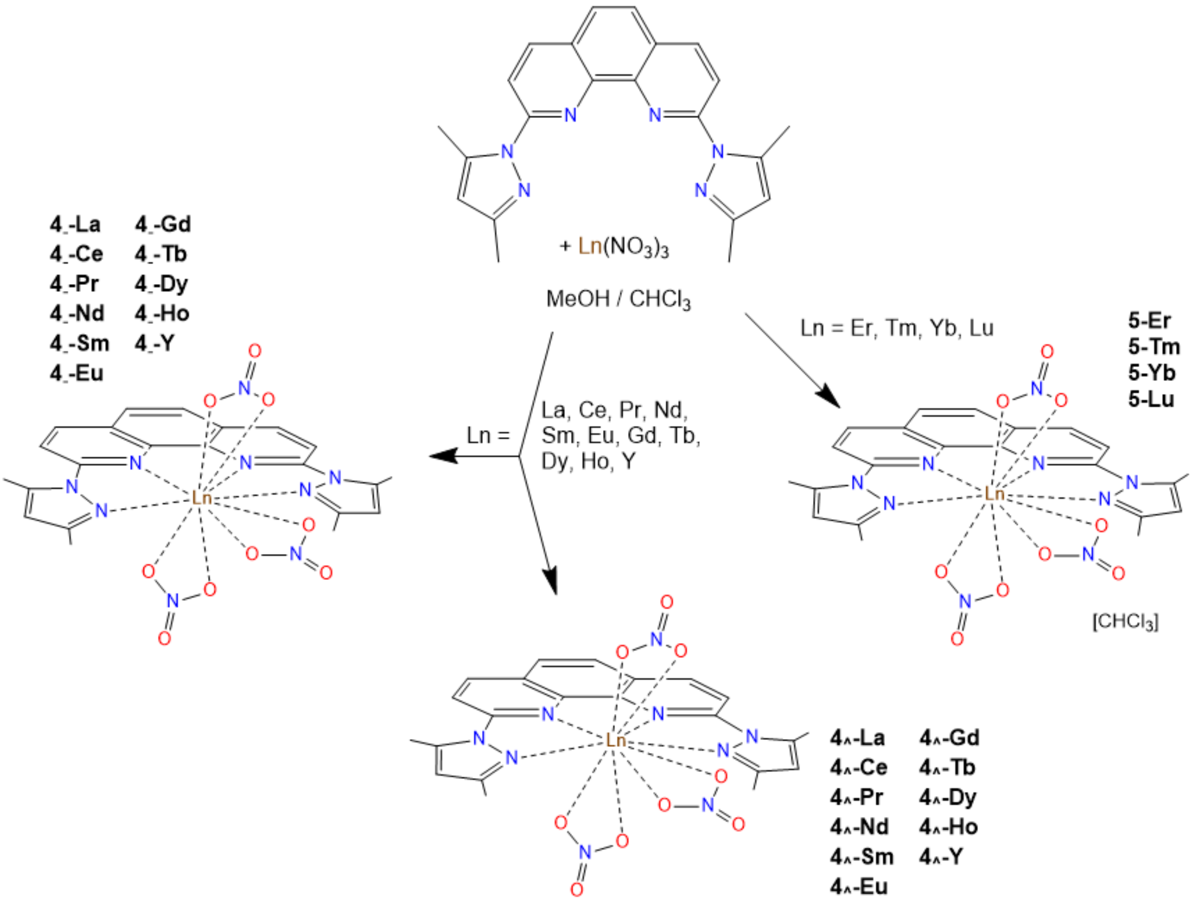

Figure 3.15: Preparation of Ln(III) complexes based on L_{Me}.

The L_{Me} complexes of the earlier lanthanide ions up to Ho including Y are characterized as compounds of the general formula $[LnL_{Me}(NO_3)_3]$ (**4-Ln**). Two different polymorphs were identified to be present in samples of **4-Ln**, similar to **2-Ln**. The single crystal structures of the two polymorphs in **4-Dy** are given in figure 3.16.

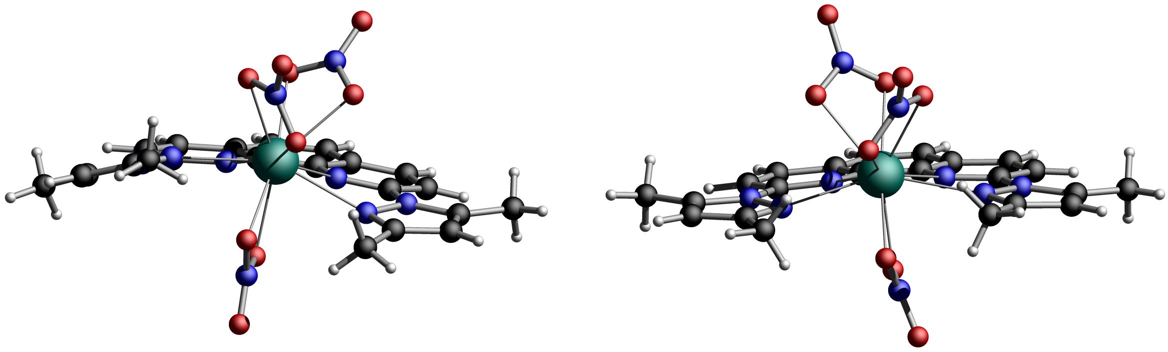

Figure 3.16: Molecular structures obtained from single-crystal X-ray diffraction studies of **$4_{\_}$-Dy** (left) and **$4_{\wedge}$-Dy** (right).

To keep a consistent terminology the two polymorphs are referred to as **$4_{\_}$-Ln** and **$4_{\wedge}$-Ln**, even though the resulting ligands' topologies are not properly matching a flat or angled structure that the labelling might imply. In fact, the coordination symmetry exerted in **$4_{\wedge}$-Ln** is closer to both polymorphs **$2_{\wedge}$-Ln** and **$2_{\_}$-Ln**, than that of **$4_{\_}$-Ln**, *vide infra*. Similar to the molecular structures of **$2_{\_}$-Ln**, the two dimethyl-pyrazole units are rotated around the corresponding C-N bond in the same direction. The added methyl-groups lead to a much stronger rotation compared to what has been observed for **$2_{\_}$-Ln** due to their increased sterical demand. The resulting coordination geometry exerted by the four N-donor atoms can be thought of as a small sector of a spiral or helix (compare figure 3.15, left). The two pyrazole rings of **$4_{\wedge}$-Ln** are rotated in opposing directions, again matching the structures of **$2_{\wedge}$-Ln**. Interestingly, in contrast to what is observed between **$2_{\_}$-Ln** and **$4_{\_}$-Ln**, the added sterical hinderance of the methyl-groups leads to less pronounced rotation in **$4_{\wedge}$-Ln** than in **$2_{\wedge}$-Ln**, as a stronger rotation would let the methyl-groups interfere with the coordination of the nitrate anions (compare figure 3.15, right). All **$4_{\_}$-Ln** complexes are isostructural, crystallizing in the monoclinic space group $P2_1/c$ with four molecules per unit cell (table 3.10, figure 3.16). Single crystals of **$4_{\_}$-Sm** and **$4_{\_}$-Tb** could not be picked out of multiple samples of **4-Sm** and **4-Tb** even after extensive search. The average Ln$\cdots$N bond lengths observed for the complexes **$4_{\_}$-Ln** are 2.650 Å (La), 2.625 Å (Ce), 2.608 Å (Pr), 2.593 Å (Nd), 2.556 Å (Eu), 2.546 Å (Gd), 2.525 Å (Dy), 2.512 Å (Ho) and 2.517 Å (Y) (table 3.11), decreasing along the series. Unlike for the non-methylated **2-Ln**, the distances between the central ion and the phenanthroline's Ns are not generally shorter or longer than the distances between the central ion and the Ns of the pyrazole group. The obtained average Ln$\cdots$O bond lengths in **$4_{\_}$-Ln** are 2.603 Å (La), 2.578 Å (Ce), 2.559 Å (Pr), 2.548 Å (Nd), 2.509 Å (Eu), 2.504 Å (Gd), 2.479 Å (Dy), 2.464 Å (Ho) and 2.465 Å (Y) (table 3.11).

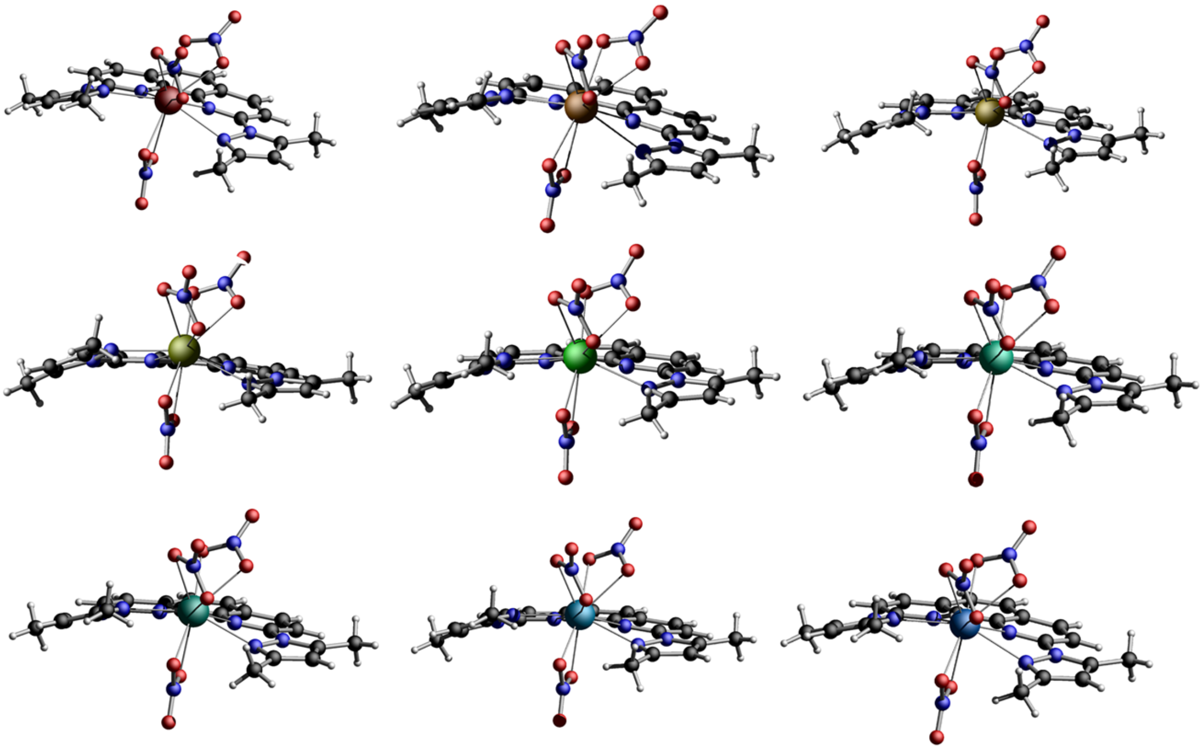

Figure 3.17: Single crystal molecular structures of **4_-Ln** (Top: La, Ce, Pr, Middle: Nd, Eu, Gd, Bottom: Dy, Ho, Y).

Table 3.10: Unit cell parameters for **4_-Ln**. Full crystallographic details are given in the appendix.

	4_-La	**4_-Ce**	**4_-Pr**	**4_-Nd**	**4_-Eu**
space group	$P2_1/c$	$P2_1/c$	$P2_1/c$	$P2_1/c$	$P2_1/c$
a [Å]	16.0914(11)	16.0829(3)	16.0644(3)	16.0758(4)	16.0264(3)
b [Å]	9.1256(4)	9.1322(1)	9.13000(10)	9.1447(2)	9.1482(1)
c [Å]	19.0568(10)	19.0036(4)	18.9428(3)	18.9290(5)	18.7882(3)
α [°]	90	90	90	90	90
β [°]	113.741(7)	113.732(2)	113.728(2)	113.755(3)	113.719(2)
γ [°]	90	90	90	90	90
V [Å^3]	2561.6(3)	2555.08(9)	2543.44(8)	2546.96(12)	2521.91(8)
	4_-Gd	**4_-Dy**	**4_-Ho**	**4_-Y**	
space group	$P2_1/c$	$P2_1/c$	$P2_1/c$	$P2_1/c$	
a [Å]	16.0174(7)	16.0735(4)	15.9752(3)	15.9930(4)	
b [Å]	9.1524(3)	9.2075(2)	9.1609(1)	9.1657(2)	
c [Å]	18.7586(8)	18.7592(5)	18.6683(3)	18.6673(4)	
α [°]	90	90	90	90	
β [°]	113.763(5)	113.785(3)	113.721(2)	113.709(3)	
γ [°]	90	90	90	90	
V [Å^3]	2516.8(2)	2540.50(12)	2501.24(8)	2505.43(11)	

Comparing the Ln···N and Ln···O distances of **4_-Ln** (Ln = Eu, Gd) with the distances observed for **2_-Ln** (Ln = Eu, Gd), it can be seen that the twisting of L_{Me} benefits the coordination of the REI, allowing for a more direct coordination characterized by shorter Ln···N distances of about 0.35 Å in **4_-Ln** (Ln = Eu, Gd). The closer coordination of the nitrogen donor atoms is linked with a weaker coordination of the nitrates oxygen donors, which show 0.14 Å longer Ln···O distances in **4_-Ln** (Ln = Eu, Gd), relative to **2_-Ln**.

Table 3.11: Selected bond lengths for complexes **4_-Ln** in Å.

Bond	**4_-La**	**4_-Ce**	**4_-Pr**	**4_-Nd**	**4_-Eu**
Ln···N1	2.634(7)	2.650(3)	2.594(3)	2.623(4)	2.585(3)
Ln···N3	2.666(7)	2.603(2)	2.613(3)	2.565(3)	2.528(2)
Ln···N4	2.629(5)	2.634(3)	2.587(2)	2.600(4)	2.561(3)
Ln···N6	2.670(7)	2.612(3)	2.637(3)	2.583(3)	2.551(3)
Ln···O1	2.587(6)	2.566(2)	2.557(2)	2.538(3)	2.495(3)
Ln···O2	2.590(7)	2.565(2)	2.593(2)	2.531(3)	2.496(3)
Ln···O4	2.588(6)	2.549(2)	2.579(3)	2.522(3)	2.478(3)
Ln···O5	2.622(7)	2.601(3)	2.527(2)	2.568(4)	2.538(3)
Ln···O7	2.594(6)	2.574(2)	2.545(2)	2.544(3)	2.546(3)
Ln···O8	2.636(6)	2.614(2)	2.552(2)	2.585(3)	2.501(2)
Bond	**4_-Gd**	**4_-Dy**	**4_-Ho**	**4_-Y**	
Ln···N1	2.539(6)	2.561(5)	2.510(4)	2.513(3)	
Ln···N3	2.546(6)	2.488(3)	2.515(4)	2.522(3)	
Ln···N4	2.519(5)	2.522(4)	2.474(3)	2.481(2)	
Ln···N6	2.580(7)	2.527(5)	2.547(4)	2.553(3)	
Ln···O1	2.482(6)	2.520(4)	2.446(3)	2.444(2)	
Ln···O2	2.490(5)	2.474(3)	2.456(3)	2.456(2)	
Ln···O4	2.474(5)	2.522(5)	2.430(3)	2.432(2)	
Ln···O5	2.535(6)	2.442(4)	2.497(4)	2.499(3)	
Ln···O7	2.498(4)	2.461(4)	2.452(3)	2.455(2)	
Ln···O8	2.545(6)	2.456(4)	2.503(4)	2.503(2)	

Similarly, the complexes **4**$_{\wedge}$**-Ln** (Ln = Y, La - Ho) are fully isostructural, crystallizing in the monoclinic space groups $P2_1/c$ and $P2_1/n$, with four molecules per unit cell (table 3.12, figure 3.18). The unit cell volumes are smoothly decreasing from 2548.82 Å^3 in **4**$_{\wedge}$**-La** to 2472.29 Å^3 in **4**$_{\wedge}$**-Y**. The average Ln···N bond lengths obtained for **4**$_{\wedge}$**-Ln** are 2.656 Å (La), 2.634 Å (Ce), 2.617 Å (Pr), 2.598 Å (Nd), 2.570 Å (Sm), 2.559 Å (Eu), 2.548 Å (Gd), 2.531 Å (Tb), 2.525 Å (Dy), 2.510 Å (Ho) and 2.509 Å (Y). The average Ln···O distances are 2.604 Å (La), 2.578 Å (Ce), 2.561 Å (Pr), 2.550 Å (Nd), 2.522

Å (Sm), 2.511 Å (Eu), 2.507 Å (Gd), 2.488 Å (Tb), 2.478 Å (Dy), 2.472 Å (Ho) and 2.470 Å (Y) (table 3.13).

Table 3.12: Unit cell parameters for **$4_\wedge$-Ln**. Full crystallographic details are given in the appendix.

	$4_\wedge$-La	**$4_\wedge$-Ce**	**$4_\wedge$-Pr**	**$4_\wedge$-Nd**	**$4_\wedge$-Sm**	**$4_\wedge$-Eu**
space group	$P2_1/c$	$P2_1/c$	$P2_1/c$	$P2_1/c$	$P2_1/n$	$P2_1/n$
a [Å]	7.7003(1)	7.70000(10)	7.7015(2)	7.7026(2)	7.68980(10)	7.6902(3)
b [Å]	19.7053(2)	19.6377(3)	19.5981(4)	19.5530(6)	19.4806(3)	19.4453(10)
c [Å]	17.2023(2)	17.1912(3)	17.1969(3)	17.1741(5)	17.1463(3)	17.1342(5)
α [°]	90	90	90	90	90	90
β [°]	102.452(1)	102.617(2)	102.762(2)	102.788(3)	102.853(2)	102.784(4)
γ [°]	90	90	90	90	90	90
V [Å^3]	2548.82(5)	2536.71(7)	2531.49(10)	2522.41(13)	2504.19(7)	2498.70(18)
	$4_\wedge$-Gd	**$4_\wedge$-Tb**	**$4_\wedge$-Dy**	**$4_\wedge$-Ho**	**$4_\wedge$-Y**	
space group	$P2_1/n$	$P2_1/n$	$P2_1/n$	$P2_1/n$	$P2_1/n$	
a [Å]	7.6891(2)	7.67940(10)	7.6785(2)	7.6797(2)	7.6712(2)	
b [Å]	19.4373(5)	19.3950(3)	19.3699(4)	19.3563(5)	19.3500(5)	
c [Å]	17.1118(3)	17.0916(2)	17.0746(4)	17.0572(4)	17.0643(4)	
α [°]	90	90	90	90	90	
β [°]	102.750(2)	102.643(2)	102.582(2)	102.596(2)	102.568(2)	
γ [°]	90	90	90	90	90	
V [Å^3]	2494.39(10)	2483.93(6)	2478.55(10)	2474.54(11)	2472.29(11)	

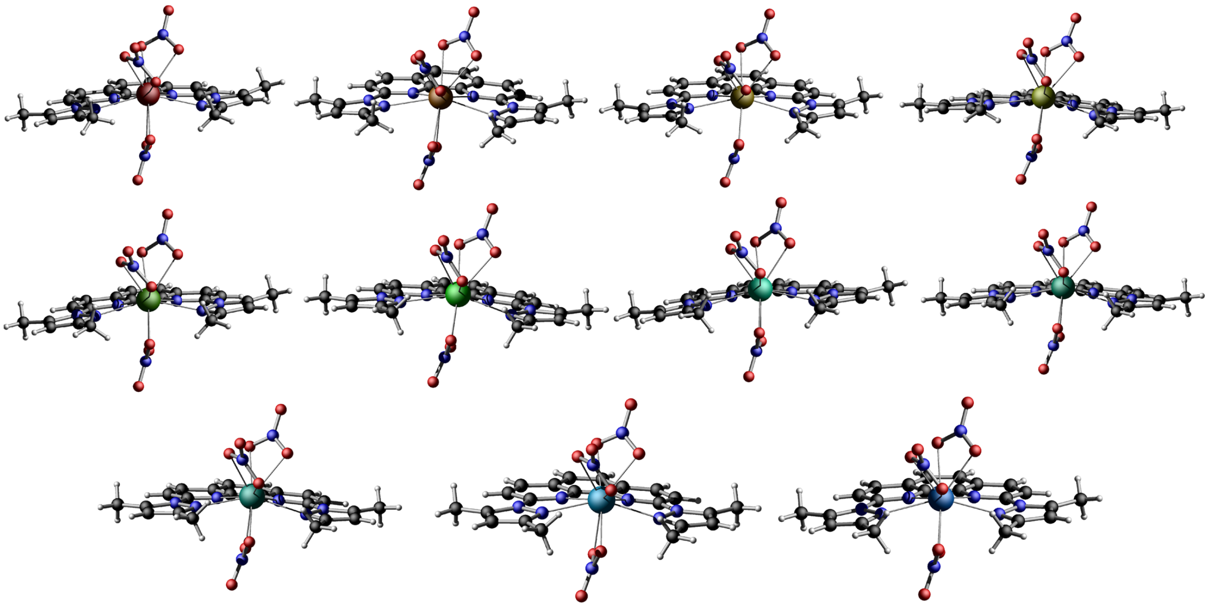

Figure 3.18: Single crystal molecular structures of **$4_\wedge$-Ln** (Top: La, Ce, Pr, Nd, Middle: Sm, Eu, Gd, Tb, Bottom: Dy, Ho, Y).

Within the series of **$4_{\wedge}$-Ln**-complexes the average bond lengths are decreasing as expected with the shrinking ionic radius. More interestingly, the average Ln$\cdots$N bond lengths of **$4_{\wedge}$-Ln** are slightly longer than in **4_{-}-Ln**, for the early Ln(III) ions, however, at Dy(III) the average Ln$\cdots$N distances are 2.525 Å in both **4_{-}-Dy** and **$4_{\wedge}$-Dy**. For the two smallest ions forming **4-Ln**, Ho(III) and Y(III), the Ln$\cdots$N bond lengths of **$4_{\wedge}$-Ln** are now shorter than in **4_{-}-Ln**. The average Ln$\cdots$O bond lengths remain on average 0.02 Å longer in **$4_{\wedge}$-Ln** over the full series of compounds.

Table 3.13: Selected bond lengths for complexes **$4_{\wedge}$-Ln** in Å.

Bond	**$4_{\wedge}$-La**	**$4_{\wedge}$-Ce**	**$4_{\wedge}$-Pr**	**$4_{\wedge}$-Nd**	**$4_{\wedge}$-Sm**	**$4_{\wedge}$-Eu**
Ln$\cdots$N1	2.666(2)	2.620(3)	2.634(3)	2.592(4)	2.596(3)	2.552(5)
Ln$\cdots$N3	2.685(2)	2.608(2)	2.640(3)	2.573(4)	2.585(3)	2.517(6)
Ln$\cdots$N4	2.631(2)	2.661(2)	2.589(3)	2.611(3)	2.534(3)	2.574(5)
Ln$\cdots$N6	2.640(2)	2.648(3)	2.606(3)	2.616(5)	2.563(3)	2.593(5)
Ln$\cdots$O1	2.565(2)	2.532(2)	2.517(3)	2.501(3)	2.473(3)	2.465(6)
Ln$\cdots$O2	2.601(2)	2.578(2)	2.554(3)	2.542(4)	2.513(3)	2.508(6)
Ln$\cdots$O4	2.623(2)	2.596(2)	2.576(3)	2.567(3)	2.529(4)	2.509(6)
Ln$\cdots$O5	2.602(2)	2.577(2)	2.565(3)	2.556(4)	2.531(4)	2.523(6)
Ln$\cdots$O7	2.599(2)	2.573(2)	2.557(3)	2.551(4)	2.514(4)	2.505(6)
Ln$\cdots$O8	2.636(2)	2.614(3)	2.597(3)	2.581(4)	2.569(4)	2.557(5)

Bond	**$4_{\wedge}$-Gd**	**$4_{\wedge}$-Tb**	**$4_{\wedge}$-Dy**	**$4_{\wedge}$-Ho**	**$4_{\wedge}$-Y**
Ln$\cdots$N1	2.542(3)	2.527(2)	2.525(4)	2.508(4)	2.552(4)
Ln$\cdots$N3	2.510(4)	2.489(3)	2.477(4)	2.471(4)	2.515(3)
Ln$\cdots$N4	2.558(3)	2.544(2)	2.537(5)	2.514(3)	2.464(4)
Ln$\cdots$N6	2.581(4)	2.565(3)	2.560(5)	2.546(4)	2.503(3)
Ln$\cdots$O1	2.560(4)	2.440(2)	2.426(4)	2.462(4)	2.419(4)
Ln$\cdots$O2	2.488(4)	2.485(2)	2.465(4)	2.423(4)	2.457(4)
Ln$\cdots$O4	2.523(4)	2.474(3)	2.495(5)	2.451(4)	2.446(4)
Ln$\cdots$O5	2.505(4)	2.507(2)	2.463(5)	2.497(4)	2.493(4)
Ln$\cdots$O7	2.501(4)	2.470(3)	2.547(4)	2.451(4)	2.454(4)
Ln$\cdots$O8	2.462(3)	2.550(3)	2.470(5)	2.547(4)	2.553(4)

The very minor differences observed in the bond lengths of **4_{-}-Ln** and **$4_{\wedge}$-Ln** are a good explanation to trends of complex formation observed. In **2_{-}-Ln** and **$2_{\wedge}$-Ln** the size of the coordination sphere significantly differed from one another, making **2_{-}-Ln** the more beneficial polymorph for the bigger, earlier ions and **$2_{\wedge}$-Ln** the better suited polymorph for the later, smaller ions. In **4_{-}-Ln** and **$4_{\wedge}$-Ln** however, the difference in size of the first coordination is very low, deeming neither polymorph more beneficial than the other, and yielding both polymorphs along the full series. The recorded powder X-ray diffraction patterns of the **4-Ln** series are shown in figure 3.19. It does appear, that the diffractions originating from **4$_{\_}$-Ln** become more intense towards the later ions of the series, but this might be a consequence of the crystallinity of the samples and is not a quantitative analysis.

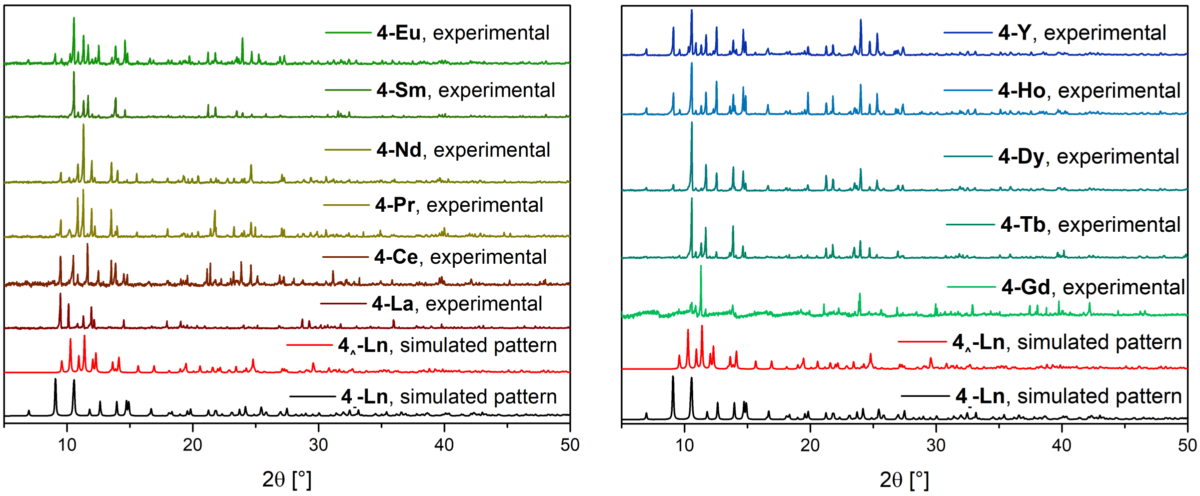

Figure 3.19: X-ray powder diffraction patterns for **4-Ln**.

The last compounds obtained from the reaction of Ln(III) nitrates with L$_{Me}$ are complexes **5-Ln** (Ln = Er, Tm, Yb, Lu) with a general formula [LnL$_{Me}$(NO$_3$)$_3$]·CHCl$_3$. The four complexes are isostructural, crystallizing in the triclinic space group $P\bar{1}$ with two molecules and two lattice solvent chloroforms per unit cell (table 3.14).

Table 3.14: Unit cell parameters for **5-Ln**. Full crystallographic details are given in the appendix.

	5-Er	**5-Tm**	**5-Yb**	**5-Lu**
space group	$P\bar{1}$	$P\bar{1}$	$P\bar{1}$	$P\bar{1}$
a [Å]	9.0664(5)	9.0494(4)	9.0530(5)	9.0497(6)
b [Å]	12.0587(6)	12.0382(5)	12.0223(6)	12.0207(10)
c [Å]	13.7208(8)	13.7144(4)	13.7124(7)	13.7156(12)
α [°]	75.550(5)	75.576(3)	75.616(5)	75.572(7)
β [°]	87.281(4)	87.269(3)	87.287(4)	87.223(6)
γ [°]	86.483(4)	86.409(3)	86.403(4)	86.362(6)
V [Å^3]	1449.09(14)	1443.30(10)	1442.02(13)	1441.2(2)

The molecular structures observed in **5-Ln** are very close to those of **4$_\wedge$-Ln** with no significant distortion of the ligands topology. The nitrate ions are also arranged similarly to **$4_\wedge$-Ln**, with one aligned on the meridian and the other two being tilted away from it. The effect of the small ionic radius causing a coordination of one nitrate as a monodentate ligand, as it has been the case in **3-Ln**, is not observed in **5-Ln**.

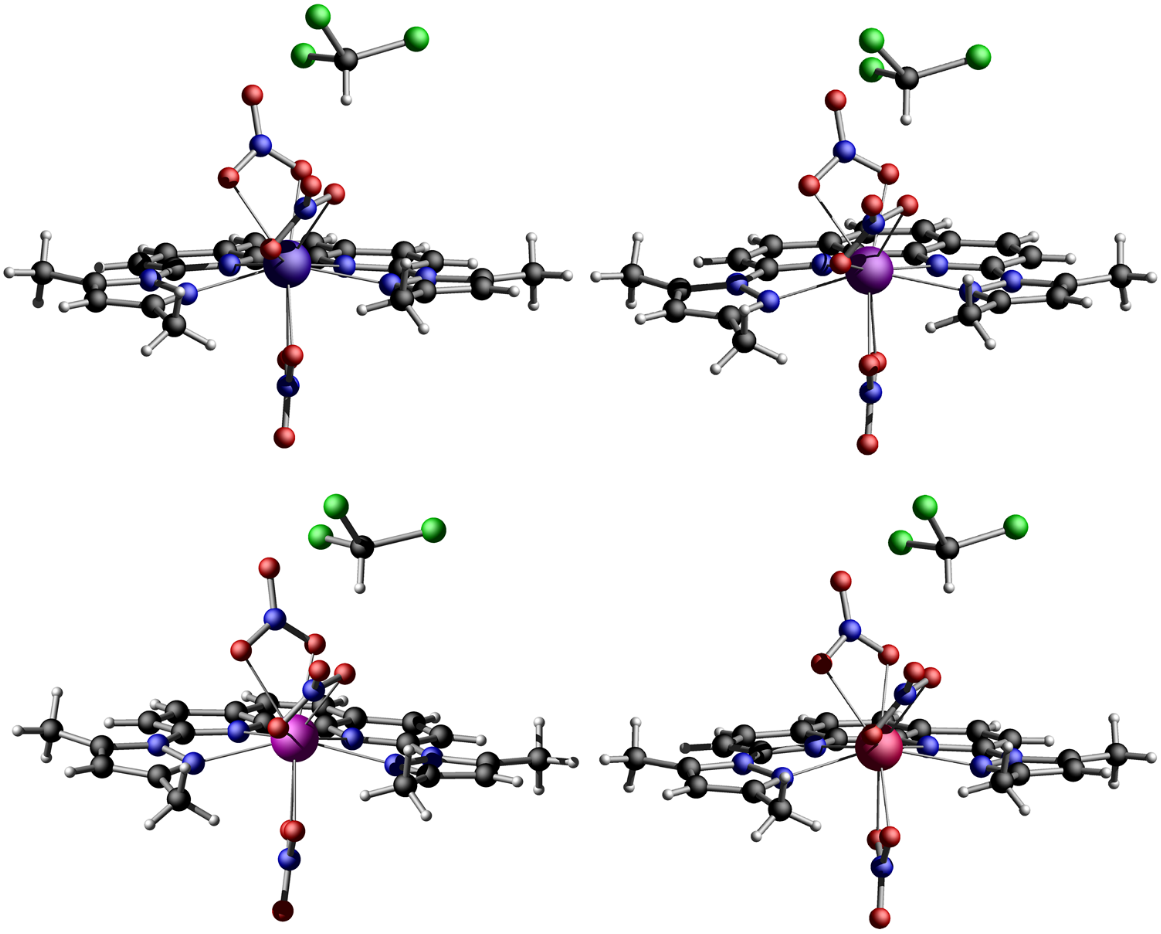

Figure 3.20: Single crystal molecular structures of **5-Ln** (Top: Er, Tm, Bottom: Yb, Lu).

The average Ln···N distances are 2.488 Å, 2.476 Å, 2.467 Åand 2.470 Å and the average Ln···O distances are 2.472 Å, 2.459 Å, 2.453 Å and 2.446 Å for **5-Er**, **5-Tm**, **5-Yb** and **5-Lu**, respectively. Comparing the bond lengths to the lengths observed in the **4-Ln**-analogues of the smallest ions Ho and Y, it is seen that the Ln···O distances remain the same between **4-Ho**/**4-Y** and **5-Er**, while the Ln···N distances decrease strongly by about 0.3 Å upon shifting from **4-Ln** to **5-Ln**. This can be interpreted as a tighter coordination of the ligand, while the nitrates' coordination remains mostly unchanged.

Table 3.15: Selected bond lengths for complexes **5-Ln** in Å.

Bond	**5-Er**	**5-Tm**	**5-Yb**	**5-Lu**
Ln···N1	2.497(4)	2.490(3)	2.486(4)	2.481(7)
Ln···N3	2.501(4)	2.491(3)	2.473(4)	2.428(8)
Ln···N4	2.450(4)	2.435(3)	2.424(5)	2.481(8)
Ln···N6	2.504(3)	2.487(2)	2.484(4)	2.490(7)
Ln···O1	2.518(4)	2.456(3)	2.461(3)	2.455(7)
Ln···O2	2.421(4)	2.468(2)	2.424(4)	2.412(7)
Ln···O4	2.481(3)	2.524(3)	2.387(4)	2.373(8)
Ln···O5	2.470(4)	2.404(3)	2.529(4)	2.528(8)
Ln···O7	2.454(4)	2.467(2)	2.467(3)	2.453(7)
Ln···O8	2.485(3)	2.435(3)	2.452(4)	2.456(7)

The powder X-ray diffraction patterns of the complexes are given in figure 3.21. It can be seen that all compounds are isostructural with matching diffraction patterns. However, the experimental data does reveal reflections that do not match with the simulated pattern, suggesting a possible second polymorph as already observed in the analogues of the lighter lanthanides. No other polymorph could be experimentally observed in single crystal measurements though.

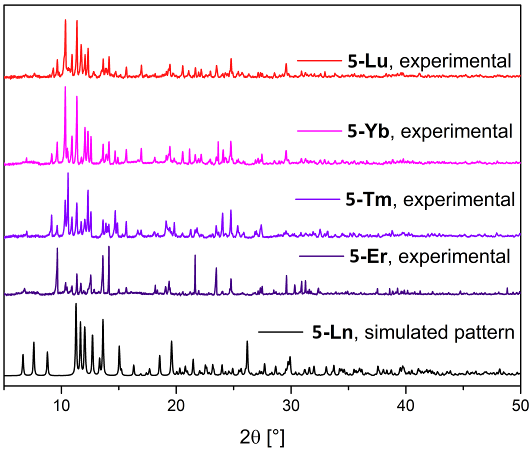

Figure 3.21: X-ray powder diffraction patterns for **5-Ln**.

3.4 Symmetry considerations

The discussed bond lengths of all compounds are visualized in figure 3.21. Despite the expected decrease seen when going from La to Lu, the most remarkable features are the differences observed between the complexes of L_H and L_{Me}. While the L_{Me}-containing compounds **4-Ln** and **5-Ln** show a steady decrease of both the Ln···N and Ln···O bond lengths without big jumps, even at the structural breakpoint between **4-Y** and **5-Er**, big leaps are observed at the breakpoint of the L_H-containing compounds. The added sterical demand of the methylated pyrazole units, therefore, created a more stable coordination behaviour across the lanthanide series.

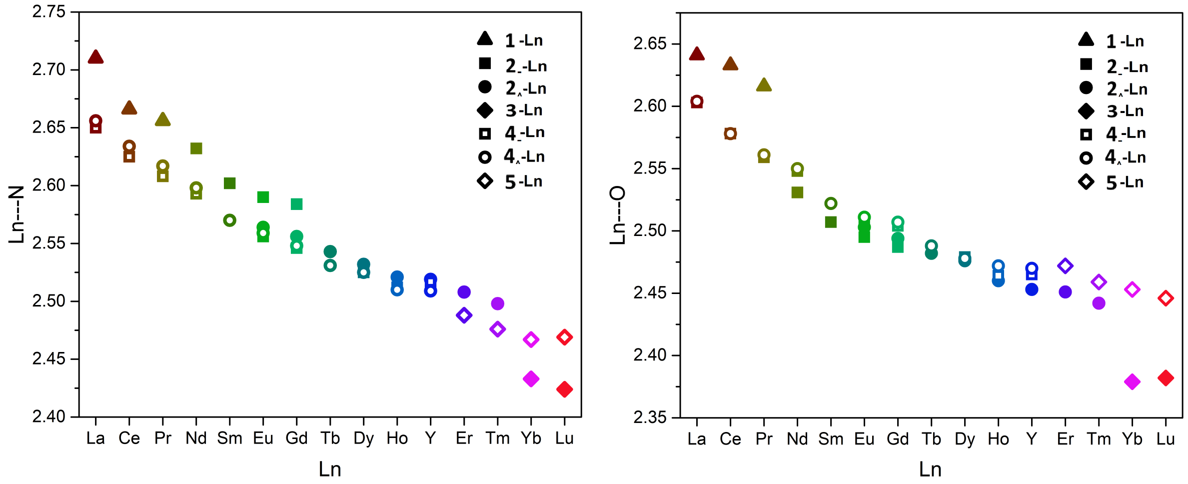

Figure 3.22: Average Ln···N (left) and Ln···O (right) bond lengths.

As previously discussed in section 2, both the photoluminescent and the magnetic properties of REI complexes are strongly influenced by symmetry of the first coordination sphere. Generally speaking, a highly symmetric coordination environment is beneficial in terms of magnetism, as it prevents mixing of the states and with that allows for slow relaxation between the states, by quenching efficient QTM.[82] For the observation of photoluminescence on the other hand, a low symmetry environment is often necessary, as certain transitions are spectroscopically forbidden and J-mixing allows their observation.[63] The symmetry of the coordination environments of the complexes **1-Ln** - **5-Ln** has been evaluated using continuous shape measures (CShM)[90] obtained from the Shape 2.1 software package.[91] The CShM value characterizes the deviation of a given geometry. In an idealized geometry, the CShM value is 1 and values higher than 1 represent distortion. As expected, the observed changes in bond lengths between the Ln(III)-analogues of either of the discussed complexes are not sufficient to change the coordination polyhedron, which best describes the coordination environment. In other words, within each set of complexes **1-Ln** - **5-Ln**, the coordination polyhedron is the same. Figures 3.22 - 3.28 show the coordination polyhedra for each complex.

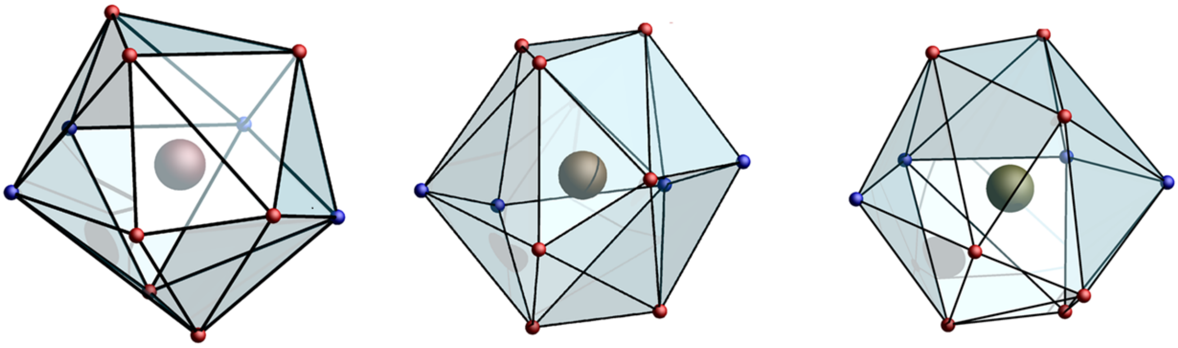

Figure 3.23: Coordination polyhedra for **1-Ln** (Ln = La, Ce, Pr).

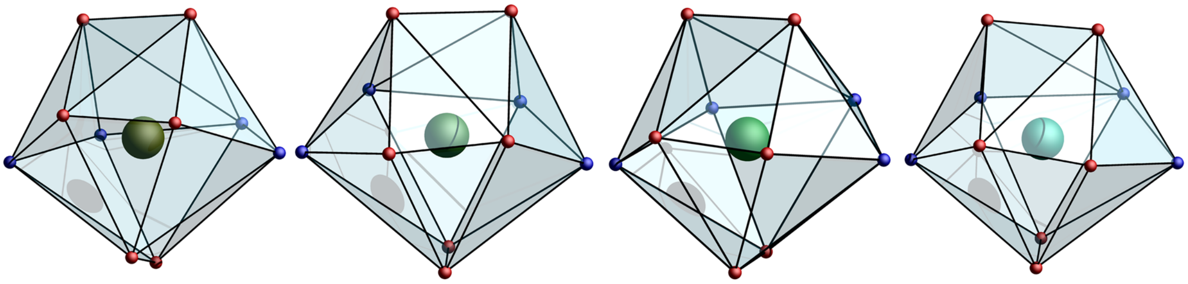

Figure 3.24: Coordination polyhedra for **2_-Ln** (Ln = Nd, Sm, Eu, Gd).

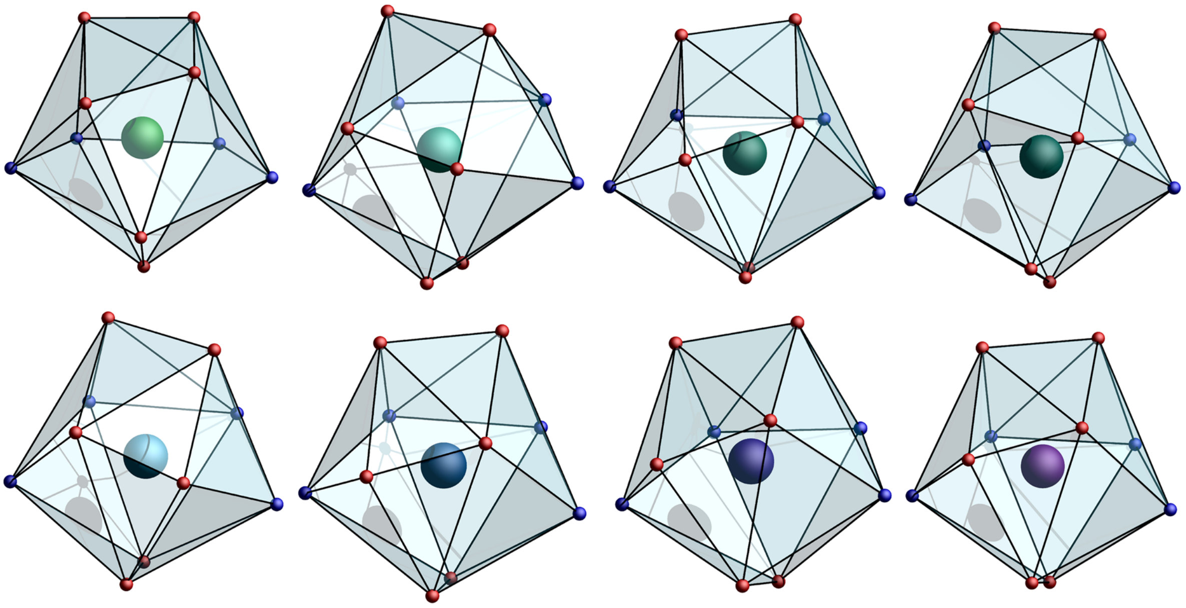

Figure 3.25: Coordination polyhedra for **$2_{\wedge}$-Ln** (Ln = Top: Eu, Gd, Tb, Dy, Bottom: Ho, Y, Er, Tm).

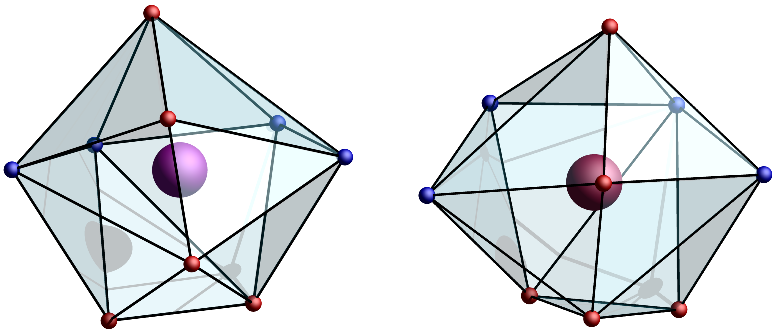

Figure 3.26: Coordination polyhedra for **3-Ln** (Ln = Yb, Lu).

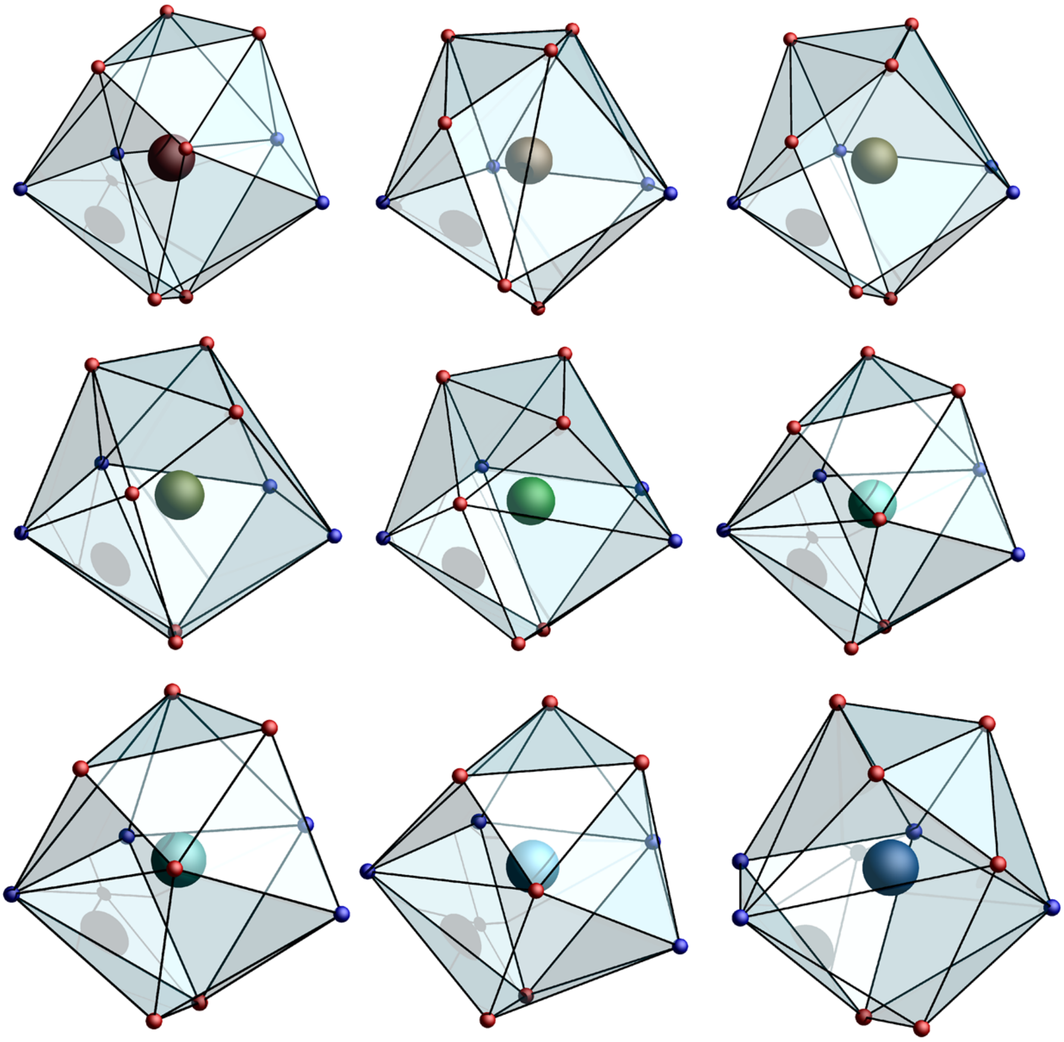

Figure 3.27: Coordination polyhedra for **4_-Ln** (Ln = Top: La, Ce, Pr, Middle: Nd, Eu, Gd, Bottom: Dy, Ho, Y).

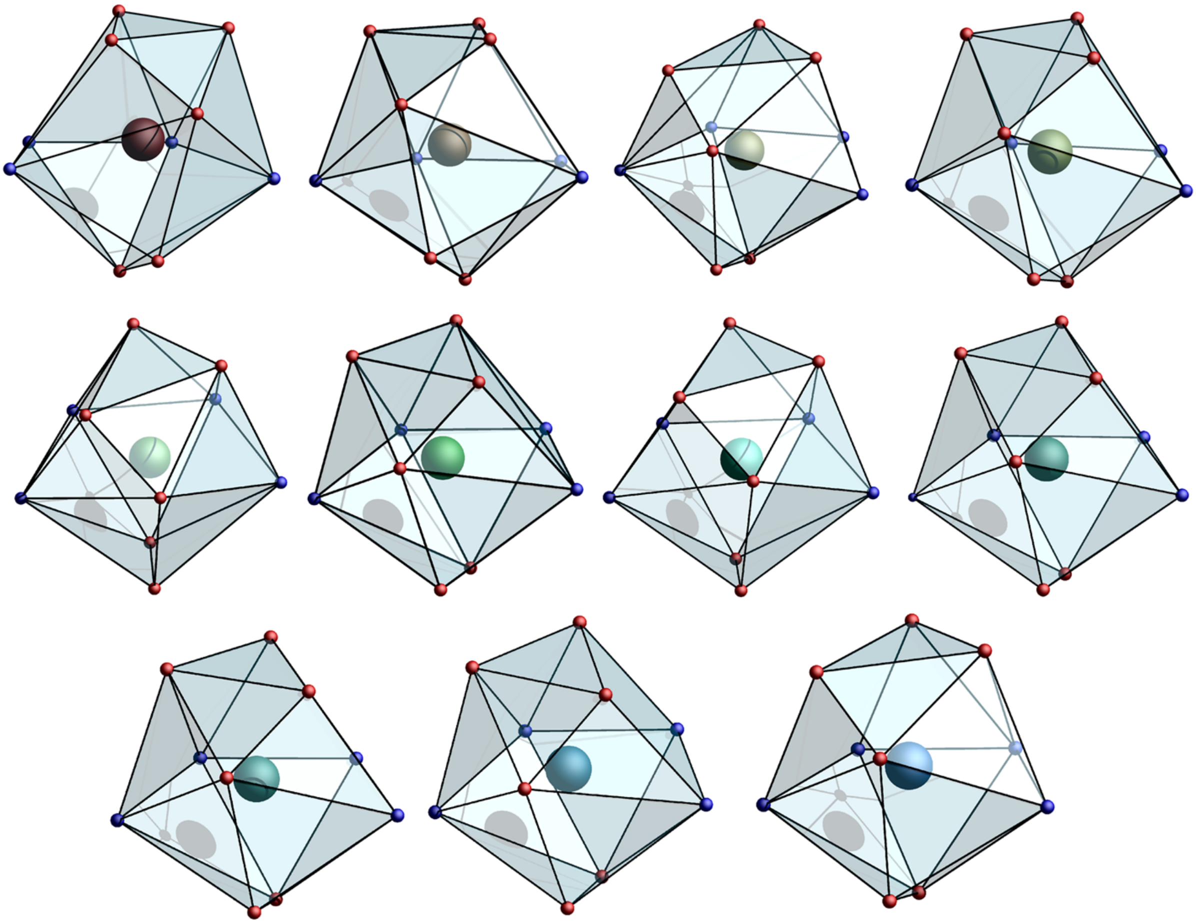

Figure 3.28: Coordination polyhedra for **4$_\wedge$-Ln** (Ln = Top: La, Ce, Pr, Nd, Middle: Sm, Eu, Gd, Tb, Bottom: Dy, Ho, Y).

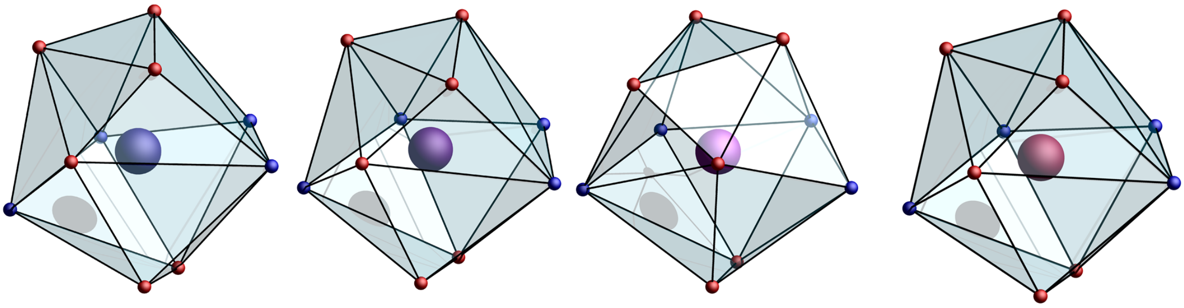

Figure 3.29: Coordination polyhedra for **5-Ln** (Ln = Er, Tm, Yb, Lu).

Complexes **1-Ln** show a coordination number of eleven, due to the additional solvent methanol acting as a monodentate ligand, *vide supra*. Their first coordination sphere is best described as a capped pentagonal antiprism with CShM values of 3.774, 4.283 and 4.274 for **1-La**, **1-Ce** and **1-Pr**, respectively. This polyhedron represents a fivefold C_{5v} symmetry, however, as the obtained CShM values are showing significant deviation from

1, the actual symmetry of the coordination environment is rather low. The ten-coordinate environment in the molecules of **2**$_{\_}$**-Ln** is best described as a tetradecahedron with twofold C_{2v} symmetry. The observed CShM values are between 1.548 (**2**$_{\_}$**-Nd** and **2**$_{\_}$**-Sm**) and 1.639 (**2**$_{\_}$**-Gd**), revealing that this description is reasonably accurate. Interestingly, the coordination polyhedron of the similarly ten-coordinate complexes of **2**$_{\wedge}$**-Ln** is best described as a sphenocorona, which shows the same twofold C_{2v} symmetry. The distortion represented by the CShM values is, however, considerably stronger with values between 3.247 (**2**$_{\wedge}$**-Tm**) and 3.520 (**2**$_{\wedge}$**-Eu**), resulting in an overall lower symmetry environment. The two complexes **3-Yb** and **3-Lu** are nonacoordinate molecules, as one nitrate acts only as a monodentate, rather than a bidentate ligand, *vide supra*. Their coordination environment is best described as a spherical tricapped trigonal prism with D_{3h} symmetry with CShM values of 1.865 and 1.792 for **3-Yb** and **3-Lu**, respectively. Showing D_{3h} symmetry and being characterized through values close to 1, the coordination environments of **3-Yb** and **3-Lu** are the highest symmetry environments observed in all compounds **1-Ln** - **5-Ln**.

All complexes obtained from using L_{Me} as a ligand are ten-coordinate complexes. As it was observed for the general structural diversity, as well as for the variation in bond lengths, the methylation of the ligand has led to less variation and a more stable coordination behaviour throughout the lanthanide series. A similar trend is observed when analysing the coordination polyhedra of the complexes **4**$_{\_}$**-Ln**, **4**$_{\wedge}$**-Ln** and **5-Ln**, which are all best described as a sphenocorona with C_{2v} symmetry. The highest symmetry is observed for the complexes of **4**$_{\_}$**-Ln** with CShM values between 2.358 (**4**$_{\_}$**-Y**) and 2.972 (**4**$_{\_}$**-La**), while the complexes of **4**$_{\wedge}$**-Ln** show the strongest distortion and with that the lowest symmetry with CShM values between 2.701 (**4**$_{\wedge}$**-Y**) and 3.263 (**4**$_{\wedge}$**-La**). The distortion of the coordination environment of **5-Ln** is an intermediate of what is observed for **4**$_{\_}$**-Ln** and **4**$_{\wedge}$**-Ln** with CShM values between 2.508 (**5-Er**) and 2.459 (**5-Lu**). A feature, which is observed for all configurations of the L_{Me} containing complexes, is an increasing symmetry characterized by decreasing CShM values with decreasing ionic radius of the central REI. Tables with full details of the continuous shape analysis are given in the appendix. It should be mentioned that the coordination observed in **2**$_{\wedge}$**-Ln** is closer to the coordination in **4**$_{\wedge}$**-Ln** than in **4**$_{\_}$**-Ln**. Similarly, the coordination environment of **2**$_{\_}$**-Ln** is also closer related to the coordination in **4**$_{\wedge}$**-Ln**, due to the strong twisting and the resulting pseudo-helical conformation of L_{Me} in **4**$_{\_}$**-Ln**.

It should be mentioned that, due to the twisting of the ligands, all obtained complexes show helical Δ/Λ chirality, crystallizing in 50:50 racemic mixtures. Measuring the magnetic and PL properties of the racemic bulk samples cannot reveal differences between the enantiomers.

4 Magnetic and photophysical characterizations

4.1 Magnetic and photophysical properties of the Gd-analogues

Gadolinium is the element found in the middle of the lanthanide series. The trivalent Gd ion's electron configuration is $4f^7$, meaning it has an exactly half filled 4f shell and with that an angular momentum of $L = 0$. As discussed in section 2, spin-orbit coupling is usually very strong for the elements of the lanthanide series. In Gadolinium however, the fully quenched orbital momentum results in isotropic spin-only behaviour of the electronic spins. As single molecule behaviour is a consequence of magnetic anisotropy, Gd(III) based SMMs are extremely rare.[92] In fact, nearly all reports on slow relaxation of Gd(III) systems are observed only for polynuclear compounds, where the slow relaxation results from the intramolecular coupling.[93–95] The few mononuclear Gd(III) based SMMs are complexes with a high local symmetry around the central ion.[96,97] The temperature dependent DC susceptibility behaviour of Gd(III) complexes is, however, a very useful tool in order to investigate intra- and intermolecular magnetic interactions. As there is no intrinsic anisotropy of the Gd(III) ion, any deviation from the ideal behaviour can be explained by magnetic interactions between Gd(III) ions, without having to consider contributions from the depopulation of Stark levels, that is observed in other Ln(III) compounds. The temperature dependency of the magnetic susceptibility was recorded for polycrystalline samples of **2-Gd** and **4-Gd**.

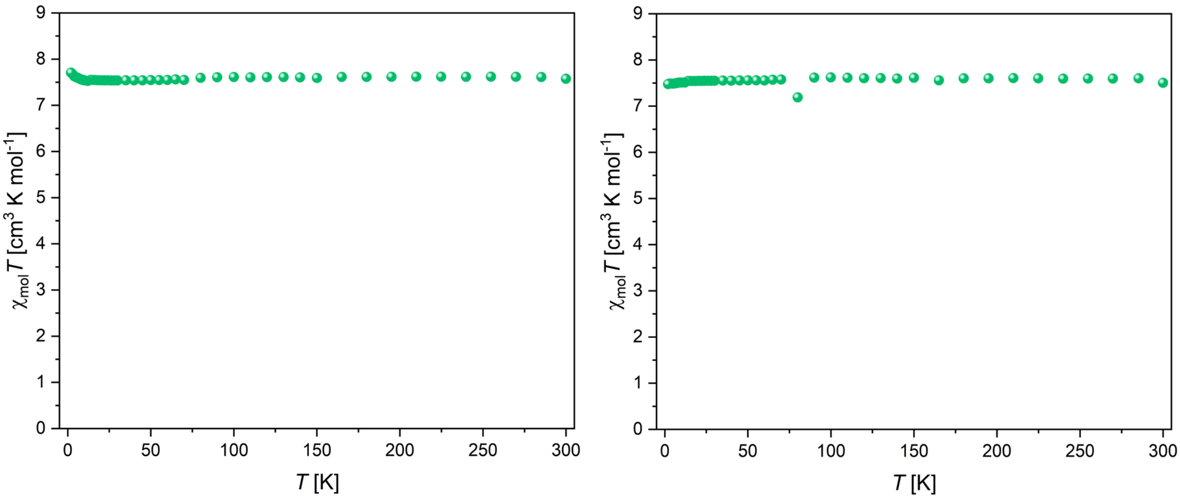

Figure 4.1: Temperature-product of the molar magnetic susceptibility vs. temperature for **2-Gd** (left) and **4-Gd** (right).

Both samples show a nearly T-independent behaviour of χT with room temperature values of 7.62 cm^3 K mol^{-1} and 7.51 cm^3 K mol^{-1}, for **2-Gd** and **4-Gd**, respectively. Upon cooling, no change is observed until reaching temperatures below 10 K. There, a weak upturn of χT is observed in **2-Gd**, while the values remain constant for **4-Gd**. The observed upturn is a consequence of small intermolecular ferromagnetic interactions. As the compounds are mononuclear complexes, intramolecular interactions can be ruled out and instead dipolar interactions are the basis of the observed behaviour. The shortest intermolecular Gd$\cdots$Gd distances observed are 7.569 Å, 8.126 Å, 7.689 Å and 8.804 Å for **2$_\wedge$-Gd**, **2$_-$-Gd**, **4$_\wedge$-Gd** and **4$_-$-Gd**, respectively. This observation of the lowest intermolecular Gd$\cdots$Gd distances being observed for **2$_\wedge$-Gd** is in line, with the upturn of χT being only observed for **2-Gd**. Employing equation 2.8, the strengths of the purely dipolar interactions J_{dip} are found to be 3.12 x 10^{-3} cm^{-1}, 2.52 x 10^{-3} cm^{-1}, 2.98 x 10^{-3} cm^{-1} and 1.27 x 10^{-3} cm^{-1} for **2$_\wedge$-Gd**, **2$_-$-Gd**, **4$_\wedge$-Gd** and **4$_-$-Gd**, respectively. The magnitude of the interactions are considerably small, matching the trend of being only noticeable at very low T.

In photoluminescence studies, Gd(III) compounds similarly can act as a neutral probe, as previously discussed in section 2. The ground state of the trivalent Gd ion is given as ^{8}S$_{7/2}$ and its first excited state is ^{6}P$_{7/2}$. The energy gap between those two states is typically in the order of 30000 cm^{-1} and with that bigger than the optical energy stored in the excited triplet state of organic antenna ligands. Therefore, the luminescence observed in Gd(III)-based compounds is solely occurring on the ligands site. With that Gd(III) complexes reveal the differences in PL behaviour of the pure ligand and the ligand in its coordinating form. Figure 4.2 shows the excitation and emission spectra recorded on solid state samples of **2-Gd** and **4-Gd** at 3 K.

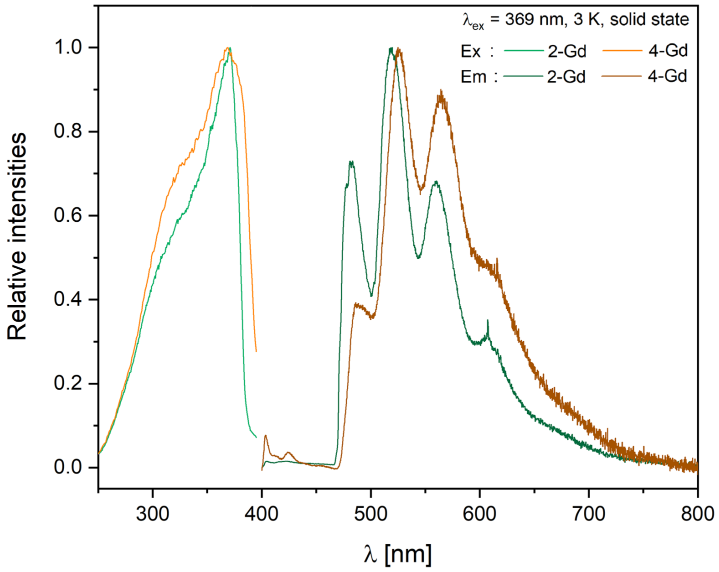

Figure 4.2: Solid state photoluminescence spectra of **2-Gd** and **4-Gd**.

The maximum excitation wavelengths λ_{ex} observed are found at 369 nm for both samples **2-Gd** and **4-Gd**. The shape of the excitation peak shows a shoulder at lower wavelengths, similar to the shape of the excitation spectra recorded for the pure ligands L_H and L_{Me} (compare figures 3.2, 3.3). The shoulder that has been observed at higher wavelengths in L_H and L_{Me} disappeared. Possibly this excitation was linked with a structural change of the ligands geometry, which is prevented by the coordinated Gd(III) ion. Upon the coordination of Gd(III) the observed excitation peaks are significantly red-shifted by 56 nm. In comparison, the introduction of Gd(III) into a hematoporphyrin, was reported to cause a red-shift of approx. 10 nm.[64] The emission spectra of **2-Gd** and **4-Gd** both reveal three separate emission peaks and a shoulder at higher wavelengths. The strongest emission peak is observed at a wavelength λ_{max} of 520 nm and 525 nm for **2-Gd** and **4-Gd**, respectively, corresponding to the excited state energies of 19231 cm^{-1} and 19048 cm^{-1}. The highest energy transitions are observed at 482 nm/ 20747 cm^{-1} and 487 nm/ 20534 cm^{-1} for **2-Gd** and **4-Gd**, respectively. The red-shift observed in the emission spectra is stronger in **4-Gd** than in **2-Gd** which matches the trends discussed previously in section 3. The average $Ln \cdots N$ distances in both polymorphs of **2-Gd** are longer than the distances observed in the polymorphs of **4-Gd** (compare figure 3.21). Due to the shorter bond lengths the effect of the Gd(III)'s electron density is stronger felt in the complexes of **4-Gd**, causing a more intense red-shift. Another interesting feature are the relative intensities observed in the emission spectrum. For **2-Gd**, the high and the low energy peak show approximately the same intensities of about 70% of the main emission peak's intensity. This matches the behaviour that has been observed in the fluorescence spectra of both of the pure ligands L_H and L_{Me} (compare figure 3.3). However, in the emission spectrum recorded for **4-Gd** the intensity of the high energy peak is significantly lowered to about 40%, while the low energy peak shows an increased intensity of about 90% of the maximum intensity. It appears that the non-radiative relaxation within the ligand's excited manifold from the high energy state into the low energy state is more efficient in **4-Gd** than in **2-Gd**, causing an increased contribution of the low energy emission. This might be a consequence of non-radiative relaxation being supported by additional vibrational modes of the methylgroup in close proximity to the phen moiety.

Despite the structural analysis revealing the presence of two different polymorphs in both **2-Gd** and **4-Gd**, an optical distinction between the polymorphs is not possible. The fluorescence peaks of the aromatic ligand system are not sharp enough to allow deconvolution of the emission peak envelopes. The only possible observation is in the high energy emission peak observed for **2-Gd**, where a small shoulder is observed that might be a result of the different ligand configurations in the two polymorphs. However, two separate peaks are not clearly identifiable.

4.2 Magnetic and photophysical properties of the Ce-analogues

The most abundant element of the lanthanides is cerium. It is also the lightest element of the series that has a paramagnetic Ln(III) ion, as La(III) has an empty 4f shell and is, therefore, diamagnetic. Since removal of a single extra electron creates an empty 4f shell, cerium can occur as a stable tetravalent ion. Therefore, cerium shows the most rich redoxchemistry among the lanthanides. However, no redox phenomena were observed for the compounds **1-Ce** and **4-Ce**. The $4f^1$ electron configuration of Ce(III) gives rise to a $^2F_{5/2}$ ground state. In literature, not much attention is usually paid to the magnetic properties of the earlier Ln(III) ions, as their ground states exhibit lower magnetic moments, due to the less than half-filled 4f-shell and the resulting total angular momentum being $J = L - S$ rather than $J = L + S$, observed for the later ions of the series. Nevertheless, with $S = 1/2$ and $J = 5/2$, Ce(III) is a Kramers ion, with intrinsically degenerate m_J-states, extremely beneficial for SMM behaviour as the degeneracy does not depend on the coordination environment. The static magnetic behaviour of the cerium compounds **1-Ce** and **4-Ce** was tested by cooling polycrystalline samples in an external field of 1000 Oe (figure 4.3).

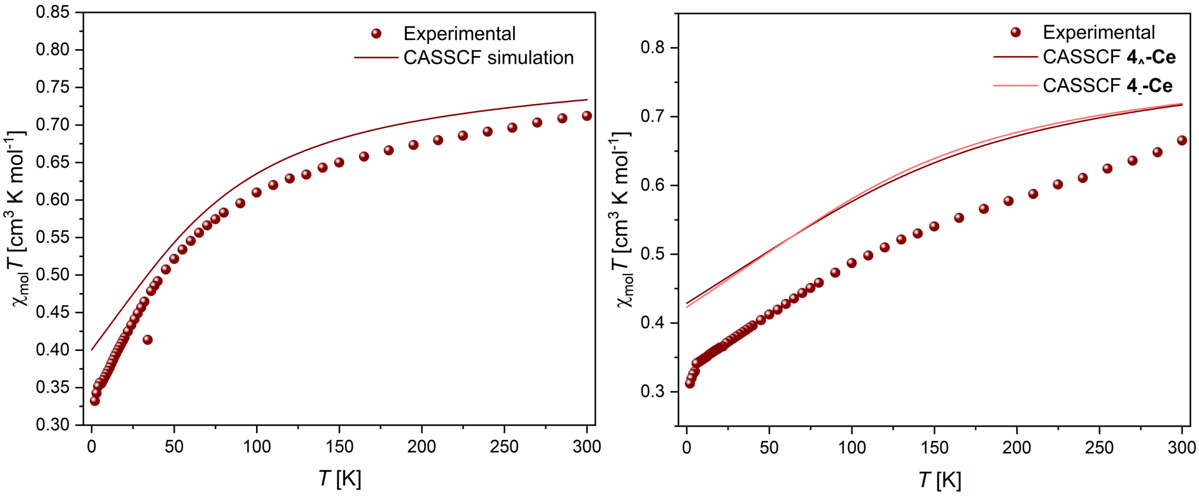

Figure 4.3: Temperature-product of the molar magnetic susceptibility vs. temperature of **1-Ce** (left) and **4-Ce** (right).

The theoretical room temperature values following Curie's law (equation 2.4, table 2.2) for any compound with a single Ce(III) ion is 0.8 cm^3 K mol^{-1}. The measured $\chi_{mol}T$ values were 0.72 cm^3 K mol^{-1} and 0.66 cm^3 K mol^{-1} for **1-Ce** and **4-Ce**, respectively. Interestingly, the CASSCF simulated susceptibilities are only 0.73 cm^3 K mol^{-1} at 300 K, and with that in reasonable agreement with the experiment. The overall T-dependence differs significantly between the two samples of **1-Ce** and **4-Ce**, as for **1-Ce** a steady decrease is observed down to about 0.60 cm^3 K mol^{-1} at 100 K, followed by an increasingly strong decrease down to 0.33 cm^3 K mol^{-1} at 2 K. For the sample of **4-Ce**, the decrease is more linear and while a stronger decrease is observable at temperatures below 100 K, the downturn is much less pronounced than in **1-Ce**. In both cases, even though the absolute values are lower than for the CASSCF simulated curves, the T-dependency matches the simulation reasonably well. The different curvatures of **1-Ce** and **4-Ce**, are a consequence of the different coordination environments of **1-Ce** and **4-Ce**. As described in sections 3.2 and 3.3, **1-Ce** is an eleven coordinate complex due to the coordination of a solvent methanol molecule, while the two polymorphs in **4-Ce** are both ten coordinate complexes. With such a significant change of the ligand field, different behaviour is expected.

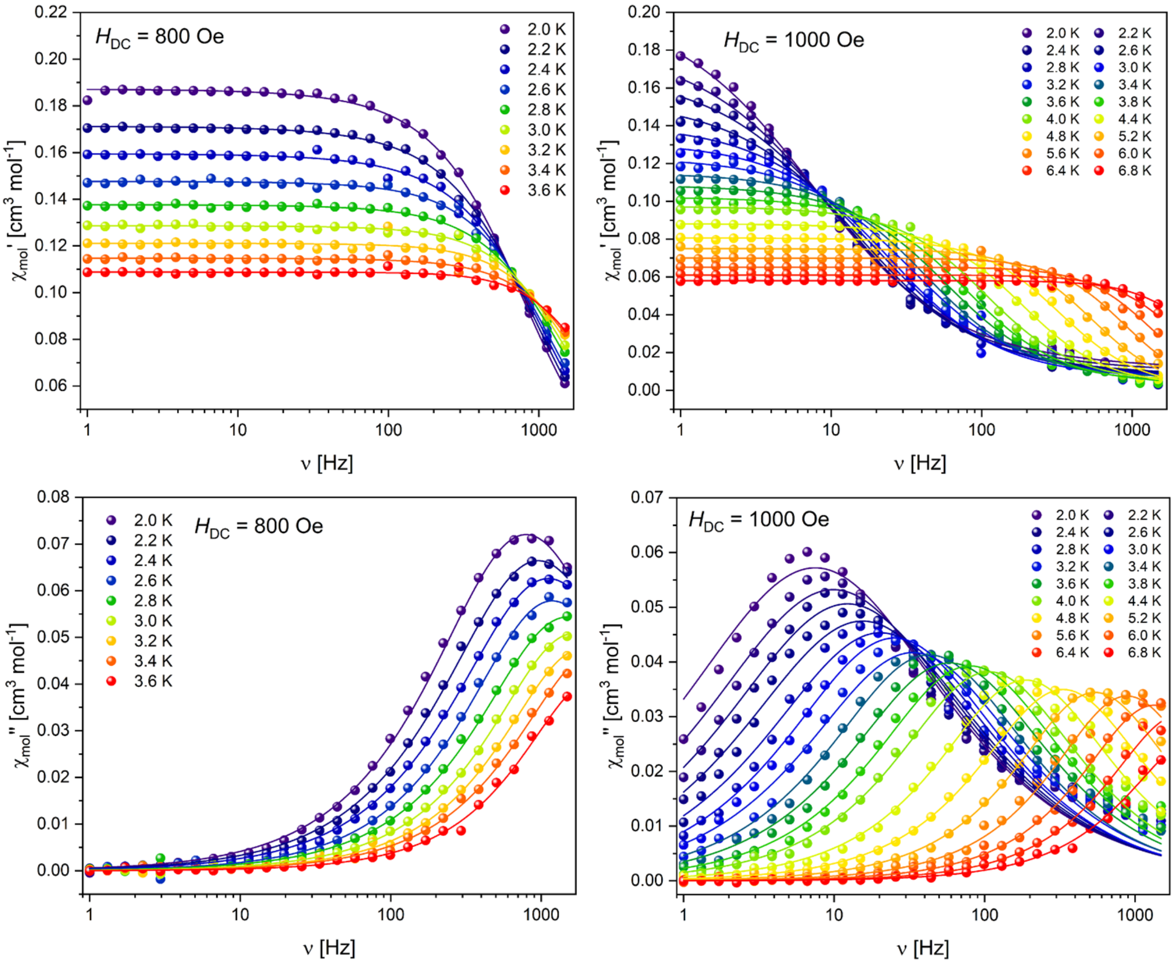

Figure 4.4: Frequency dependency of the in-phase (top) and out-of-phase (bottom) component of the magnetic susceptibility for **1-Ce** (left) and **4-Ce** (right). The solid lines are the best fits to a generalized Debeye model.

Alternating current (AC) susceptibility measurements were performed at different applied DC magnetic fields starting at the lowest temperature of 2 K. Neither sample showed any out-of-phase signals without an applied external field. This is common behaviour in low symmetry coordination complexes, due to efficient quantum tunnelling, supported by transverse components of the g-tensor. In fact, while the overall number of reported cerium-based SMMs is relatively low compared to other Ln(III) species, Ce(III) SMMs showing slow relaxation at zero field have not been reported in the literature.[92,98–100] Upon the application of an external field both samples of **1-Ce** and **4-Ce** revealed a frequency-dependent out-of-phase signal. The optimal fields found are 800 Oe and 1000 Oe for **1-Ce** and **4-Ce**, respectively. The frequency-dependent behaviour of the in-phase (χ') and out-of-phase (χ'') components of the magnetic susceptibility recorded at different temperatures for **1-Ce** and **4-Ce** are shown in figure 4.4. The data for **1-Ce** reveals a single maximum in the out-of-phase component alongside a decrease of the in-phase signal, as expected. The maximum is found at a high frequency around 900 Hz at the lowest possible temperature of 2 K. An immediate shift to higher frequencies is observed upon increasing the temperature, as there are no temperature-independent relaxation processes besides QTM, which is suppressed by the application of the external field. Already at 2.8 K the maximum has shifted to the highest observable frequency of 1500 Hz, however, the recorded data is shown up to 3.6 K, as reasonable fits to a generalized Debye model were still obtainable. The AC susceptibility data of **4-Ce** (figure 4.4, right) also is characterized by a single maximum in the out-of-phase component. The maximum is found at a significantly lower frequency of 7 Hz at 2 K, compared to **1-Ce**. With increasing temperature the maximum is slowly shifted to higher frequencies up to approximately 4 K, where the frequency shift starts becoming more pronounced. This behaviour is typically observed for low temperature relaxation dominated by Raman relaxation, followed by the Orbach regime at higher temperatures. The maximum is reaching the highest observable frequency of 1500 Hz at 6.0 K. Knowing about the presence of the two individual polymorphs **$4_{\wedge}$-Ce** and **4_{-}-Ce**, two distinct relaxations might be expected. The observation of only one maximum can either be explained by very comparable relaxation behaviours of the two polymorphs, leading to an overlapping and not distinguishable relaxation behaviour, or by one of the polymorphs showing very fast relaxation at frequencies, which are out of the observable frequency window. Using the information obtained from investigation of the relaxation dynamics of the later Ln's, *vide infra*, the second case of one polymorph being already out of the frequency window seems more likely. The electron distribution of the Ce(III) ion is characterized as an oblate shape (see section 2.2) and trends should, therefore, be comparable to other oblate ions like Nd(III) and Dy(III). On this basis, the relaxation observed in **4-Ce** is attributed to **$4_{\wedge}$-Ce**. The cole-cole plots for **1-Ce** and **4-Ce** are shown in figure 4.5. As the relaxation time of **1-Ce** is already too low to observe the full shape of the maximum at 2 K only broken semicircles are observed for **1-Ce**, suggesting a narrow distribution of relaxation processes, while the cole-cole plot of **4-Ce** suggests a wider distribution of active relaxation processes. This is further evidenced by investigation of the obtained α parameters of the fits to a generalized Debye model. The values of α found in **1-Ce** range in between 15% at low T, down to 1.6% at the highest measured temperature of 3.6 K. With that, the relaxation of **1-Ce** appears mainly via one type of relaxation at the highest observed temperature, while other processes seem to still be active at lower T. In **4-Ce** the obtained α parameters range from 32% at 2 K to 0.4% at 6.8 K. Those values clearly describe several active relaxation pathways, typical of the Raman regime, at low T, while the relaxation at elevated temperatures occurs only through a single process.

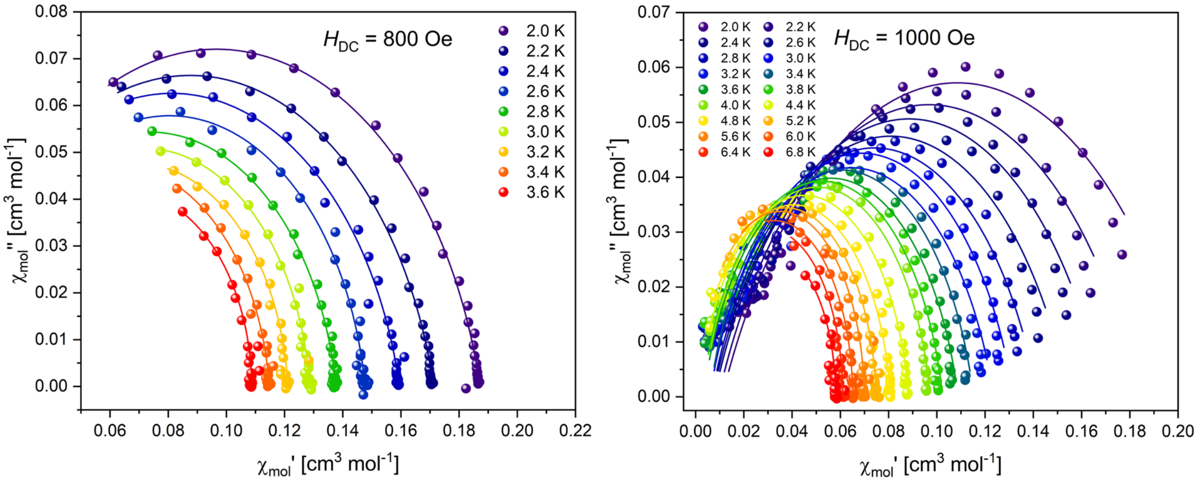

Figure 4.5: Cole-Cole plots for **1-Ce** (left) and **4-Ce** (right). The solid lines are the best fits to a generalized Debye model.

Using the relaxation times obtained from the best fits to the frequency dependent AC data, Arrhenius plots are obtained. The relaxation behaviour of **4-Ce** (figure 4.6, right) is well reproduced by fitting the relaxation time using a combination of Orbach and Raman relaxation (see equation 2.11). The best fit parameters gave $\tau_0 = 2.49$ x 10^{-7} s, $U_{eff} = 37.74$ K (26.24 cm^{-1}), C = 6.39 s K^{-n}, n = 2.86 for **4-Ce**. On the other hand, the relaxation behaviour of **1-Ce** is difficult to asses due to the small temperature window at which the out-of-phase signal can be observed. The Arrhenius plot of **1-Ce** (figure 4.5, left), appears to best match a linear behaviour as it is normally observed for the Orbach regime of relaxation. Performing a linear fit of the data, equivalent to a pure Orbach relaxation, gives $\tau_0 = 1.66$ x 10^{-5} s, $U_{eff} = 5.12$ K (3.56 cm^{-1}). However, the most likely case, as also evidenced by the strongly decreasing α parameter throughout the T-window, is that the observable relaxation data is at the intermediate regime between the Raman- and Orbach-dominated temperature regions.

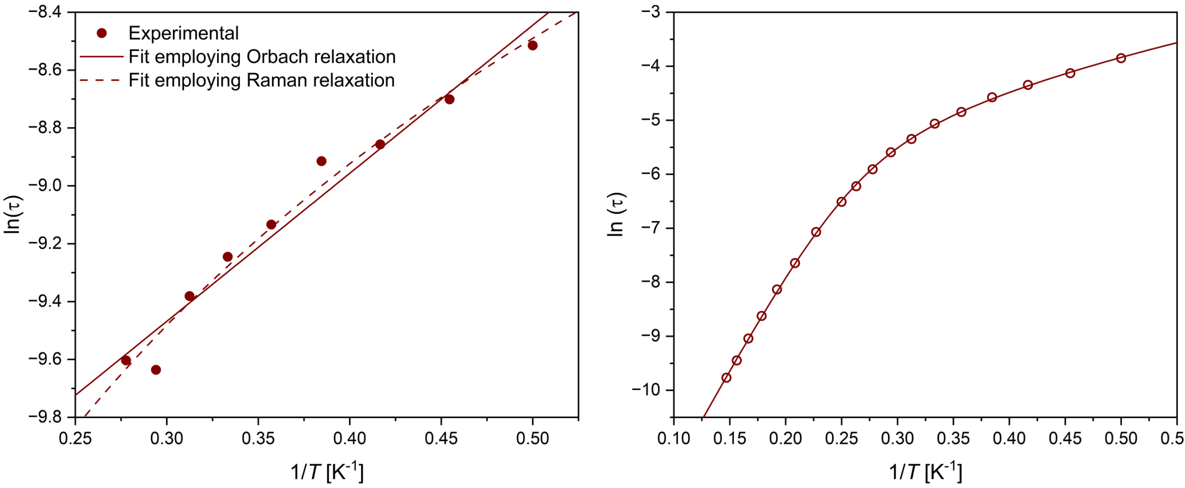

Figure 4.6: Arrhenius plot for **1-Ce** (left) and **4-Ce** (right).

A reasonable fit can also be obtained employing only Raman relaxation, giving C = 1266.67 s K^{-n}, n = 1.94. While both fits, do fit the experimental data reasonably well, the obtained parameters seem unrealistic, matching the assumption of being in the intermediate region between Raman and Orbach type relaxation. In fact, the τ_0 of **1-Ce** should be lower compared to **4-Ce** as the maximum is observed at higher frequencies, which is very likely a result of the coordinating methanol molecule. The hydroxy-group represents a source of O-H vibrations in very close proximity to the central Ce(III) ion, allowing fast Raman relaxation through the interaction with phonons. The obtained energy barrier of 37.74 K for **4-Ce** appears low in comparison to reported energy barriers of lanthanide based SMMs, which can reach values two order of magnitude higher. However, in respect to the energy barriers reported for Cerium single molecule magnets, the observed barrier height is considerably high.[92] In fact, the highest reported effective energy barrier in Ce(III) compounds is 44 K, reported for a diaza-18-crown-6 complex of Cerium.[100] For a better understanding of the properties *ab initio* CASSCF calculations were performed. The energy spectrum of Ce(III) is characterized by the $^2F_{5/2}$ ground multiplet, being split into three individual Kramers doublets through the effect of the ligand field. The obtained energy diagrams of **1-Ce**, **4$_\wedge$-Ce** and **4$_\_$-Ce** are given in figure 4.7. Following equation 2.20, an idealized strongly axial $|5/2\rangle$ ground state of Ce(III) would be characterized by $g_x = g_y = 0$ and $g_z = 4.286$. The performed CASSCF calculation yielded the ground state tensors of $g_x = 0.039$, $g_y = 0.333$ and $g_z = 3.563$ for **1-Ce**, $g_x = 0.984$, $g_y = 1.367$ and $g_z = 3.298$ for **4$_\wedge$-Ce** and $g_x = 0.916$, $g_y = 1.331$ and $g_z = 3.305$ for **4$_\_$-Ce** (see appendix). For all three complexes significant transverse components are observed, causing efficient QTM and explaining the absence of slow relaxation at zero field. The ground state doublet of all three molecules is described by a 87% $|5/2\rangle$ wavefunction with added component of lower m_J states.

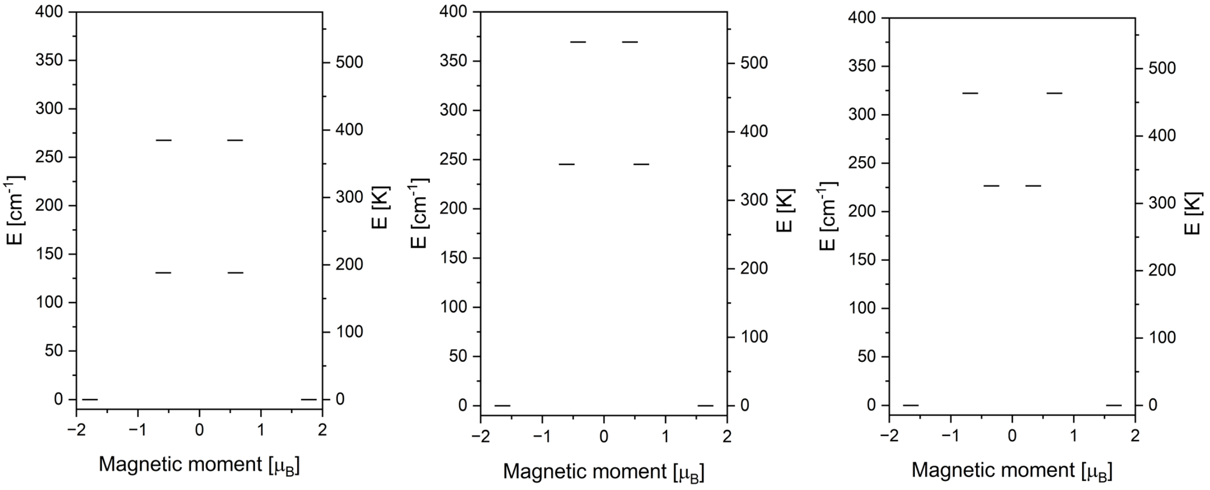

Figure 4.7: *Ab initio* energy diagram for **1-Ce**, **$4_{\wedge}$-Ce** and **$4_{\_}$-Ce**.

The excited states for **1-Ce** are found at 188.19 K (130.87 cm^{-1}) and 384.85 K (267.63 cm^{-1}). The energy separation observed for both calculated polymorphs of **4-Ce** is much higher with 352.57 K (245.18 cm^{-1}) and 531.27 K (369.45 cm^{-1}) for **$4_{\wedge}$-Ce** and 326.07 K (226.75 cm^{-1}) and 463.57 K (322.37 cm^{-1}) for **$4_{\_}$-Ce**. The energies found for the first excited Kramers doublets are much higher than the experimentally observed energy barrier, which suggests that magnetic relaxation is not occurring over-the-barrier via Orbach and TA-QTM processes but rather through virtual levels below the barrier. This observation is consistent with other *ab initio* studies of Ce(III) SMMs, where the calculated energy separation is an order of magnitude higher than the experimentally observed barrier.[98] Likely, this is a result of under-the-barrier relaxation.

4.3 Magnetic and photophysical properties of the Pr-analogues

As a non-Kramers ion with $J = 4$, Pr(III) compounds are not guaranteed to show degenerate m_J-states. Instead, the ligand field strongly influences the energetic finestructure. Similar to the other elements of the earlier half of the lanthanide series, Pr(III) compounds have been receiving much less attention than complexes of the later lanthanides. In order to get insights into the static magnetic properties of the Pr(III) complexes, the temperature-dependent magnetic susceptibilities have been recorded in an external field of 1000 Oe between 300 K and 2 K for **1-Pr** and **4-Pr**.

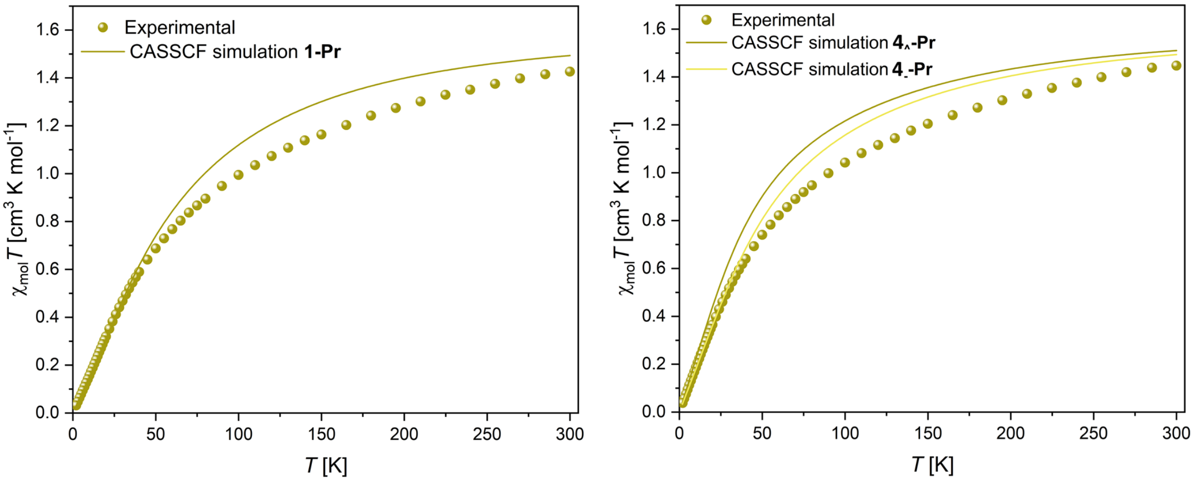

Figure 4.8: Temperature-product of the molar magnetic susceptibility vs. temperature of **1-Pr** (left) and **4-Pr** (right).

The experimentally determined room temperature values of **1-Pr** and **4-Pr** are 1.43 cm^3 K mol^{-1} and 1.45 cm^3 K mol^{-1}, respectively, in good agreement to the theoretically expected value of 1.60 cm^3 K mol^{-1}. Upon cooling the $\chi_{mol}T$ values decrease smoothly for both compounds, without any distinct features. At very low T, the observed values are approaching 0 cm^3 K mol^{-1}, which is also observed for other Pr(III) compounds in the literature.[101] The CASSCF simulated T-dependent behaviour matches the strength of the observed decrease, showing that the resulting low temperature value close to 0 cm^3 K mol^{-1} is not a consequence of antiferromagnetic coupling but an intrinsic property of the Pr(III) complex due to Stark depopulation. The dynamic magnetic behaviour of **1-Pr** and **4-Pr** was tested by performing AC susceptibility measurements, however, no out-of-phase signal was observed, at zero field. As described for the Ce(III) analogue, slow relaxation was only observed upon application of an external DC magnetic field, as QTM is too efficient at zero field for **1-Ce** and **4-Ce**. In **1-Pr** and **4-Pr**, the application of an external field did not lead to the observation of an $\chi''(\nu)$ signal. This can be explained by the low symmetry coordination of a non-Kramers ion. The low symmetry environment observed for the structures of **1-Ln** and **4-Ln** causes strong mixing of the m_J states, leading to efficient QTM in degenerate states of Kramers ions, and non-degeneracy of the states of a non-Kramers ion. Without the bistability of a degenerate ground state, SMM behaviour cannot be observed. In fact, slow relaxation of a Pr(III) based complex, has not been reported to date. To further validate this assumption, the energetic structure of **1-Pr** and **4-Pr** was analyzed using CASSCF calculations.

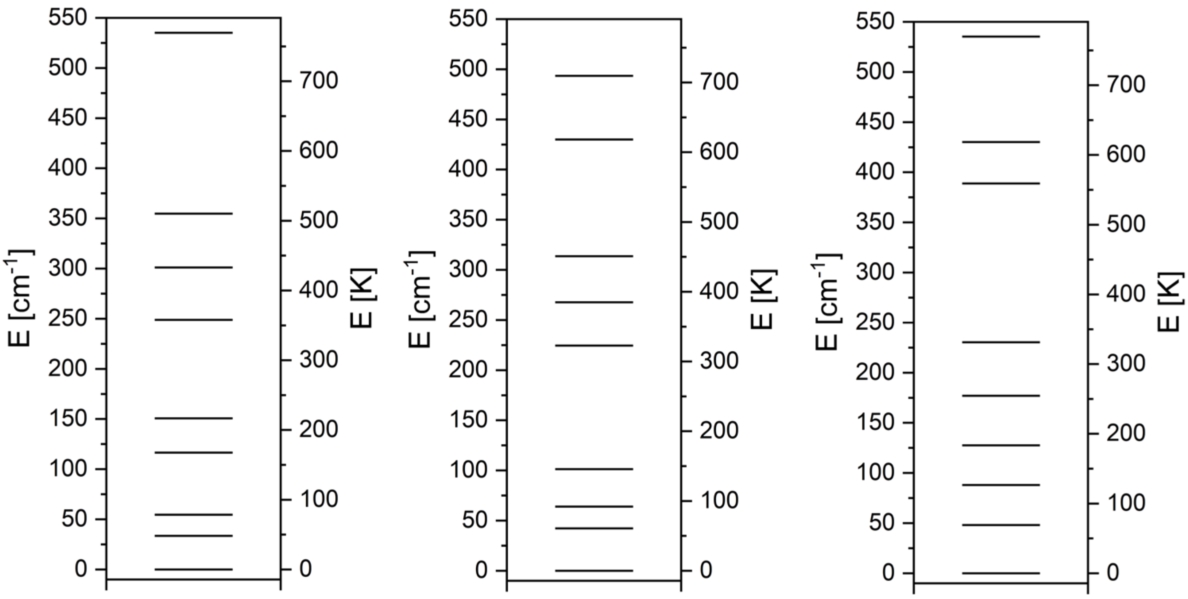

Figure 4.9: *Ab initio* energy diagram for **1-Pr**, **4**$_{\wedge}$**-Pr** and **4**$_{-}$**-Pr**.

The *ab initio* energies of the $J = 4$ multiplet for **1-Pr**, **4**$_{\wedge}$**-Pr** and **4**$_{-}$**-Pr** are shown in figure 4.9. For **1-Pr** and **4**$_{-}$**-Pr**, the observed energy splitting is in the range of 550 cm^{-1}, while for **4**$_{\wedge}$**-Pr** the highest excited state is found just below 500 cm^{-1}. The energies of the first excited state are 33.50 cm^{-1}, 42.19 cm^{-1} and 48.91 cm^{-1}, for **1-Pr**, **4**$_{\wedge}$**-Pr** and **4**$_{-}$**-Pr** respectively. This significant energy gap is perfectly in line with the absence of slow magnetic relaxation, even under the application of an external magnetic field.

Literature reports of Pr(III) sensitized emission, have shown emission peaks throughout the whole visible spectrum from 480 nm to 730 nm, with the most dominant emission usually being observed around 620 nm, corresponding to the $^3P_0 \rightarrow {}^3F_2$ transition.[102–104] PL measurement of crystalline samples of **1-Pr** and **4-Pr** at 3 K, did not yield any observable emission. The emission reported for molecular Pr(III) compounds is usually not very intense, compared to the photoemission of other trivalent lanthanide ions. Most likely, the Pr(III) centered emission is fully quenched through non-radiative decay channels.

4.4 Magnetic and photophysical properties of the Nd-analogues

Alloys of iron, boron and neodymium are used in material science to fabricate the strongest permanent magnets available.[28] The high magnetic coercivity of those materials is a result of the polarizability of the iron and the strong anisotropy of the neodymium. Interestingly, in molecular magnetism Nd is not very well researched, as it is among the early half of the lanthanide series, causing the lowest available J state to be the ground state obtained from SOC. However, the ground state of a Nd(III) ion is $^4I_{9/2}$ and with that it is the element with the highest magnetic moment among the first half of the Ln-series. Its J value of 9/2 is even higher than that of the much heavier Yb(III) with a ground state $J = 7/2$. Due to the lower gyromagnetic factor g_J, the observed magnetic moment of Nd(III) is, however, still lower than what is observed for Yb(III) (compare section 2.2). The samples of the Nd(III)-complexes of L_H and L_{Me}, **2-Nd** and **4-Nd** have been magnetically investigated. The DC susceptibilities recorded upon cooling the samples from 300 K to 2 K in an 1000 Oe strong applied DC field are given in figure 4.10.

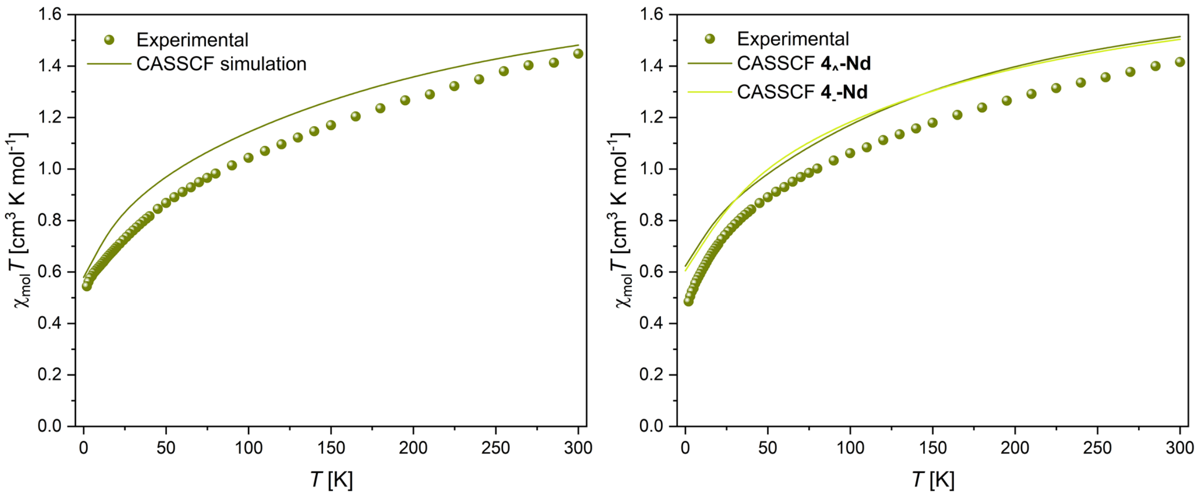

Figure 4.10: Temperature-product of the molar magnetic susceptibility vs. temperature of **2-Nd** (left) and **4-Nd** (right).

The experimentally determined $\chi_{mol}T$ values at 300 K are 1.45 cm^3 K mol^{-1} and 1.41 cm^3 K mol^{-1} for **2-Nd** and **4-Nd**, respectively. The theoretically expected room temperature value of a single Nd(III) ion is 1.64 cm^3 K mol^{-1}. Similar to what was observed in the Ce-analogues, the simulated room temperature values from CASSCF methods are 1.48 cm^3 K mol^{-1} for **2-Nd** and 1.51 cm^3 K mol^{-1} for both polymorphs **$4_\wedge$-Nd** and **$4_\_$-Nd**. Under that consideration, the experimentally obtained values are in reasonable agreement with what is expected. In contrast to the Ce-analogues, the two

Nd samples reveal almost similar T-dependencies, with a slowly decreasing $\chi_{mol}T$ and a slightly faster decrease below approximately 50 K, due to the depopulation of stark levels. The final $\chi_{mol}T$ observed at 2 K are 0.54 cm^3 K mol^{-1} for **2-Nd** and 0.48 cm^3 K mol^{-1} for **4-Nd**. The comparable nature of the $\chi_{mol}T$ vs. T curves is matching the close structural relation between **2-Ln** and **4-Ln**, other than comparison of **1-Ln** and **4-Ln** in the Ce(III) and Pr(III) cases (see sections 4.2 and 4.3). Dynamic studies were performed using AC susceptibility measurements at different frequencies and low temperatures.

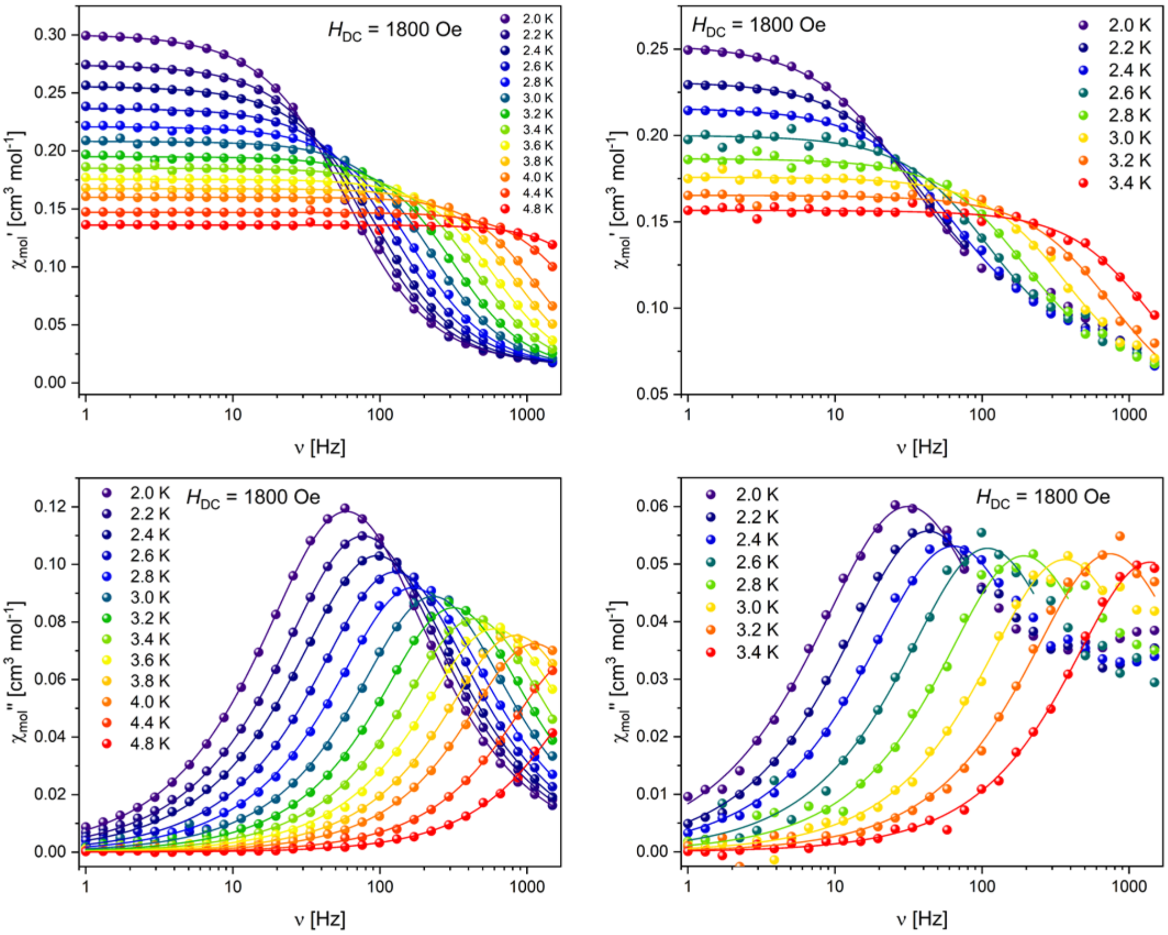

Figure 4.11: Frequency dependency of the in-phase (top) and out-of-phase (bottom) component of the magnetic susceptibility for **2-Nd** (left) and **4-Nd** (right). The solid lines are the best fits to a generalized Debye model.

In the absence of an external field, no slow relaxation was observable for both samples, very likely due to efficient QTM between the two states of opposing magnetisation. This has also been observed in literature reports of Nd(III)-based SMMs, where the majority of reported compounds are field-induced SMMs.[92,105] A clear signal in the out-of-phase component of the magnetic susceptibility is observed upon applying an external magnetic field. In both samples the lowest frequency for the maximum was observed at an optimal field of 1800 Oe. The AC data of **2-Nd** describes a symmetric maximum in the out-of-phase and a decrease of the in-phase signal. The maximum is observed at 60 Hz at 2 K, shifting to higher frequencies with T and reaching 1500 Hz at 4.4 Hz (figure 4.11, left). The temperature shift is less pronounced at low T, suggesting Raman relaxation to be the dominant process. On the other hand, the AC susceptibility recorded for **4-Nd** does not show a symmetric maximum. While only a single maximum is observed in the out-of-phase component, similar to **2-Nd**, the shape of the curve is highly asymmetric, with unexpectedly high χ'' values at high frequencies. As a consequence of the presence of the two polymorphs **$4_\wedge$-Nd** and **4_--Nd**, two maxima could be expected, as long as the relaxation dynamics are not overlapping. The asymmetric shape of the χ'' vs. T curve is most likely caused by a second maxima resulting from the slow relaxation of either of the polymorphs being found at frequencies above 1500 Hz outside of the measurable frequency window. The fully observable maximum is located around 15 Hz at 2 K and shifts to 1500 Hz at 3.4 K. The asymmetric shape of the maxima is observable up to about 3 K. This difference of the relaxation time between **4-Nd** and **4-Nd** is attributed to the methylation of the ligand from L_H in **2-Nd** to L_{Me} in **4-Nd**. The replacement of the hydrogen in the pyrazole's 3-position with a methyl-group, moves the closest C-H oscillator further away from the central Nd(III) ion, lowering the interaction with phonons and, therefore, increasing τ and shifting the maximum to slightly lower frequencies. The cole-cole plots for **2-Nd** and **4-Nd** are shown in figure 4.12, clearly showing the different symmetric and asymmetric behaviours of **2-Nd** and **4-Nd**.

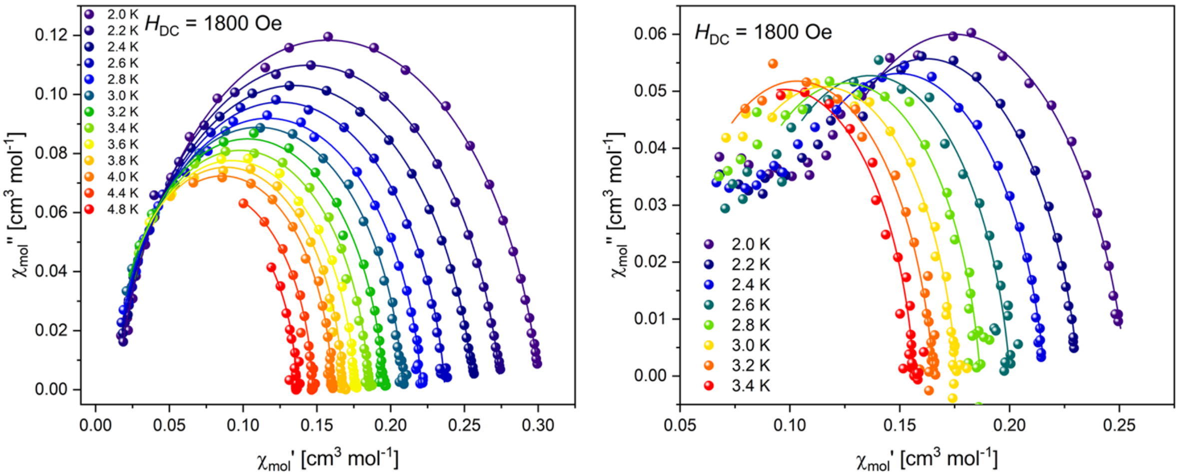

Figure 4.12: Cole-Cole plots for **2-Nd** (left) and **4-Nd** (right). The solid lines are the best fits to a generalized Debye model.

Fits to a generalized Debye model have been performed on the AC susceptibility data of **2-Nd** and **4-Nd**. Due to the discussed asymmetry of **4-Nd**, the fits were not performed over the full data range, but instead on an appropriate frequency window (see figures 4.11 and 4.12). The obtained α parameters for **2-Nd** decrease from 0.12 at 2 K to 0.01 at 4.8, clearly showing relaxation via a single process at elevated temperatures. For **4-Nd** the distribution of relaxation processes remains wider, characterized by α values between 0.17 and 0.10 over the course of the observed temperature range, which is expected considering an overlap of the relaxation of the two polymorphs. The temperature dependent relaxation times obtained of the best fits are given in the Arrhenius plot in figure 4.13. Both curves could be well modelled using equation 2.11, employing Raman and Orbach relaxation mechanisms, exclusively.

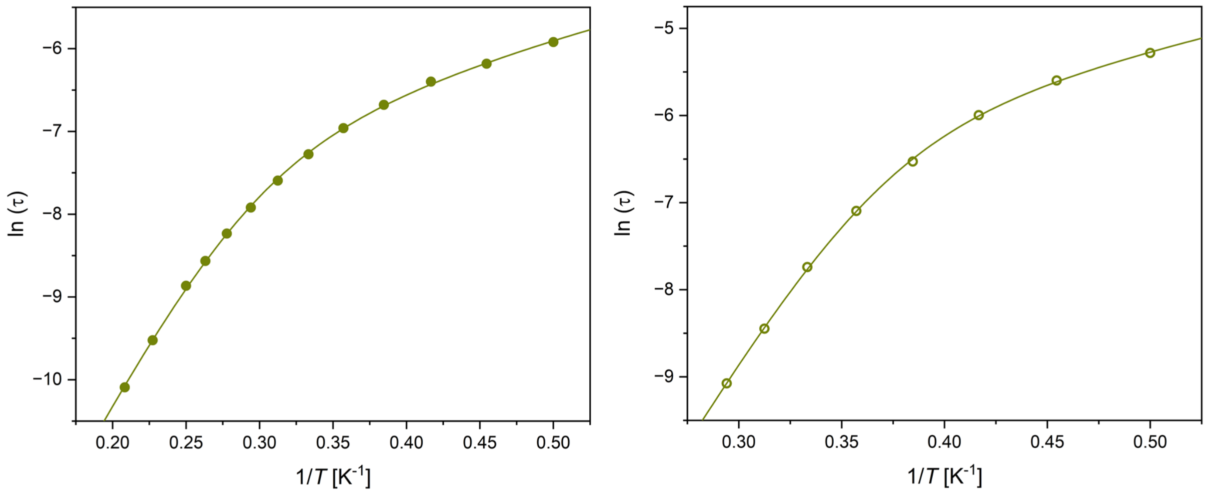

Figure 4.13: Arrhenius plot for **2-Nd** (left) and **4-Nd** (right).

The relaxation parameters obtained from the fitting procedure are $\tau_0 = 5.04$ x 10^{-8} s, $U_{eff} = 33.19$ K (23.08 cm^{-1}), C = 55.19 s K^{-n}, n = 2.73 for **2-Nd** and $\tau_0 = 1.38$ x 10^{-9} s, $U_{eff} = 38.93$ K (27.08 cm^{-1}), C = 22.07 s K^{-n}, n = 3.12 for **4-Nd**. As the relaxation dynamics of the observable maximum in **4-Nd** are comparable to those observed in **2-Nd**, the discussed relaxation of **4-Nd** is attributed to **4$_{\wedge}$-Nd** rather than **4$_{-}$-Nd**, based on the closer resemblance of the coordination environments. The obtained U_{eff} values compare well with values reported for Nd(III)-based SMMs in the literature, for which the energy barriers range mostly between 20 K and 40 K.[92,105] The highest observed energy barrier for Nd(III)-SMMs was reported for the Nd(III) analogue of the aforementioned diaza-18-crown-6 complex of Ce(III), with a value of 73 K.[100]

Ab initio CASSCF calculations were performed on the three molecules **2$_{-}$-Nd**, **4$_{\wedge}$-Nd** and **4$_{-}$-Nd**. The ligand field splits the $^4I_{9/2}$ ground state, yielding five Kramers doublets, visualized in figure 4.14.

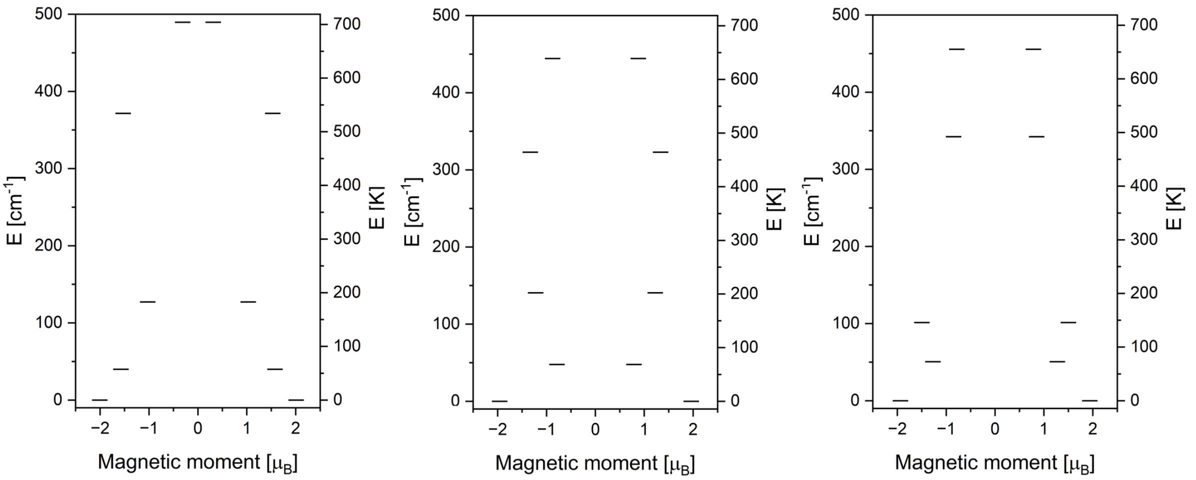

Figure 4.14: *Ab initio* energy diagram for **2**$_{\_}$**-Nd**, **4**$_{\wedge}$**-Nd** and **4**$_{\_}$**-Nd**.

Investigation of the obtained g-tensors and wavefunction compositions, reveal a very strong mixing of the states, with high transverse components of the g-tensor for all three calculated molecules. The individual components of the g-tensors are $\mathrm{g}_x = 0.852$, $\mathrm{g}_y = 1.270$ and $\mathrm{g}_z = 4.024$; $\mathrm{g}_x = 0.936$, $\mathrm{g}_y = 1.903$ and $\mathrm{g}_z = 3.928$; $\mathrm{g}_x = 1.163$, $\mathrm{g}_y = 1.713$ and $\mathrm{g}_z = 3.882$ for the ground state doublets of **2**$_{\_}$**-Nd**, **4**$_{\wedge}$**-Nd** and **4**$_{\_}$**-Nd**, respectively. A pure and highly axial $|9/2\rangle$ ground state doublet for Nd(III) would be characterized by $\mathrm{g}_x = \mathrm{g}_y = 0$ and $\mathrm{g}_z = 6.55$, showing how intensely the admixing of other states is for the calculated complexes. The strong mixing is caused by the low symmetry of the ligand field and is in good agreement with the missing slow magnetic relaxation without the application of external fields. The calculated energy gaps towards the first excited KDs are 57.39 K (39.91 cm^{-1}) for **2**$_{\_}$**-Nd**, 68.49 K (47.63 cm^{-1}) for **4**$_{\wedge}$**-Nd** and 72.63 K (50.51 cm^{-1}) for **4**$_{\_}$**-Nd**. In both cases, the *ab initio* energy separations towards the first excited state are higher than the experimentally obtained relaxation barriers. The comparison between the **2-Nd** and **4-Nd** reveals that the CASSCF energies overestimate the barrier in both cases by a factor of 1.7.

The low temperature photoluminescence of **2-Nd** and **4-Nd** has been recorded upon excitation at 369 nm. Nd(III) typically shows three emission lines in the near IR region between 850 nm and 1500 nm, linked to the three transitions into the lowest SOC states $^4\mathrm{F}_{3/2} \rightarrow {}^4\mathrm{I}_{9/2}$, $^4\mathrm{F}_{3/2} \rightarrow {}^4\mathrm{I}_{11/2}$ and $^4\mathrm{F}_{3/2} \rightarrow {}^4\mathrm{I}_{13/2}$.[60,106,107] Interestingly for both samples **2-Nd** and **4-Nd** the highest energy transition, $^4\mathrm{F}_{3/2} \rightarrow {}^4\mathrm{I}_{9/2}$, that would usually be observed between 880 nm and 910 nm, is extremely weak. The $^4\mathrm{F}_{3/2} \rightarrow {}^4\mathrm{I}_{11/2}$ with $\Delta J = 4$ is the most intensely observed line in the emission spectra due to the selection rules of induced electric dipole transitions, which is common among reported Nd(III) compounds. The experimental branching ratios β_{exp} are 5.26 %, 65.12 % and 29.62 % for $^4\mathrm{F}_{3/2} \rightarrow$

$^4I_{9/2}$, $^4F_{3/2} \rightarrow {}^4I_{11/2}$ and $^4F_{3/2} \rightarrow {}^4I_{13/2}$ in **2-Nd**, respectively. For **4-Nd**, the obtained branching ratios are 7.86%, 66.59% and 25.55%.

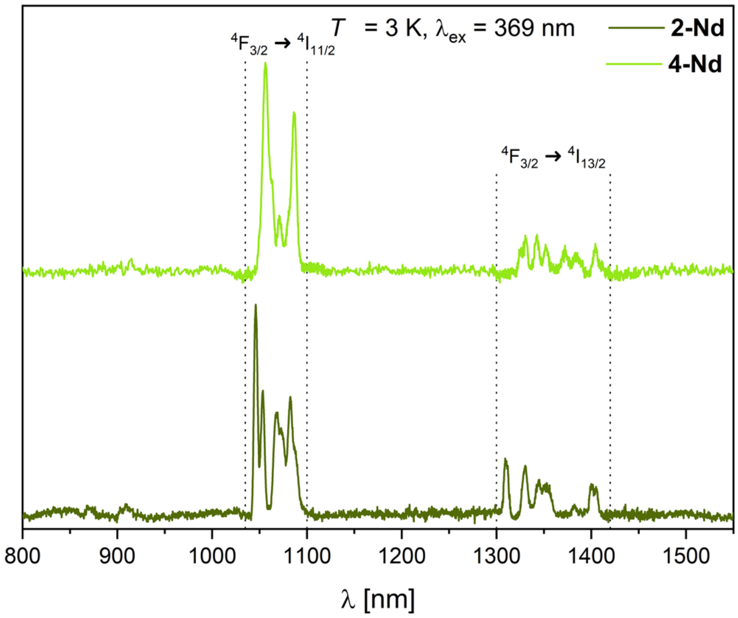

Figure 4.15: Emission spectra recorded at 3 K with $\lambda_{ex} = 369$ nm for **2-Nd** and **4-Nd**.

As expected for a Nd(III) ion in a low symmetry environment the finestructure of the $^4F_{3/2} \rightarrow {}^4I_{11/2}$ transition reveals six individual emission lines, while seven lines are observed for the $^4F_{3/2} \rightarrow {}^4I_{13/2}$ transition for **2-Nd**. The emission lines of the $^4F_{3/2} \rightarrow {}^4I_{9/2}$ cannot be resolved due to the low intensity. The peak positions found by deconvolution analysis are given in table 4.1. Interestingly, the transitions for **4-Nd** observed in the spectrum can also be properly modelled using six and seven separate peaks (figure 4.16, right), even though more peaks would be expected given the overlap of the two polymorphs **4$_\wedge$-Nd** and **4$_{\_}$-Nd**. As it is obtained from the CASSCF calculations, the energy spectrum of the ground state multiplet is comparable for **4$_\wedge$-Nd** and **4$_{\_}$-Nd**, with the three lowest KDs found within approximately 150 cm^{-1} and two higher excited KDs between 300 cm^{-1} and 500 cm^{-1}. It is likely, that the energy splitting of the SOC states $^4I_{11/2}$ and $^4I_{13/2}$ show a similar behaviour with comparable energies between **4$_\wedge$-Nd** and **4$_{\_}$-Nd**, which overlap in the emission spectrum. The peak positions obtained from deconvolution analysis can be converted to the energy separation between the $^4F_{3/2}$ excited state and the final state after relaxation. Table 4.1 shows the peak positions and the related energies in relation, using the highest energy emission line of each transition as a zero energy reference. Since the emission peaks corresponding to the $^4F_{3/2} \rightarrow {}^4I_{9/2}$ transition can not be observed with sufficient intensity, a correlation between PL and SMM characteristics cannot be established.

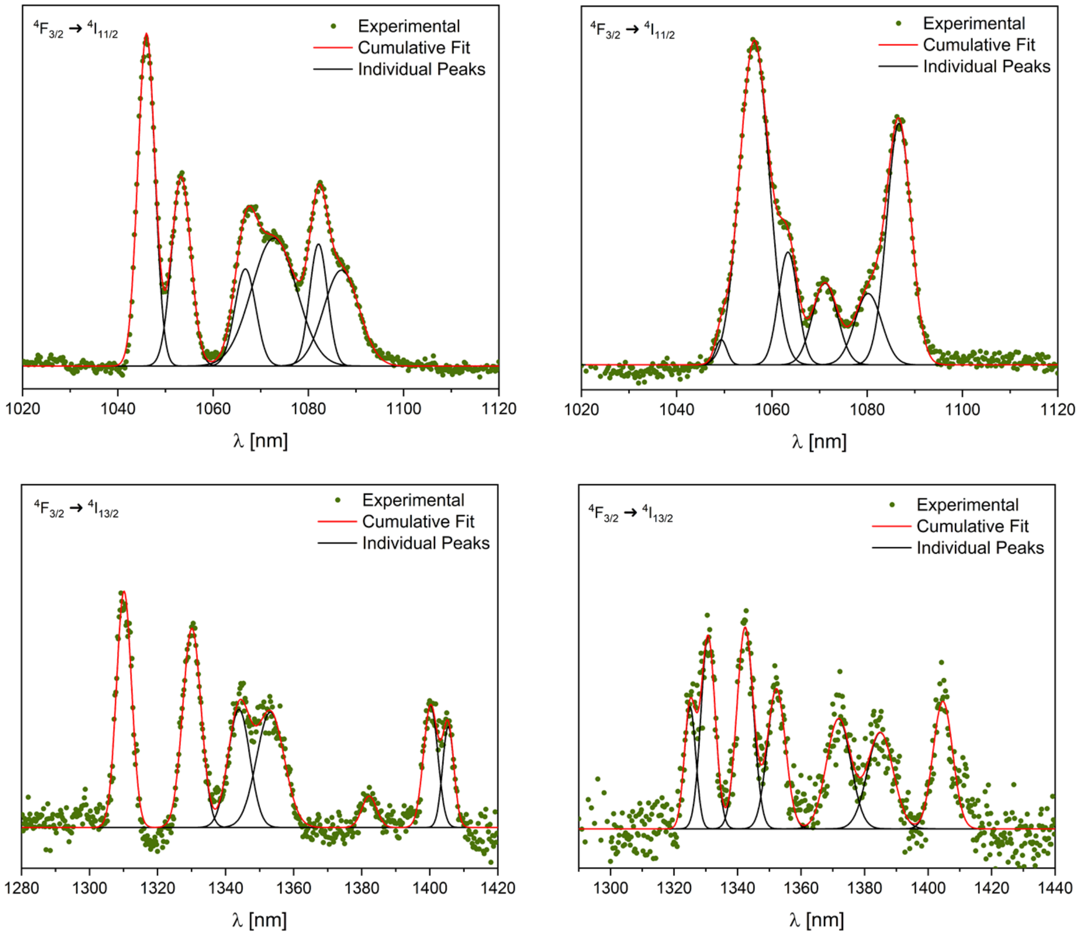

Figure 4.16: Peak deconvolution of the $^4F_{3/2} \rightarrow {}^4I_{11/2}$ (top) and $^4F_{3/2} \rightarrow {}^4I_{13/2}$ transitions (bottom) for **2-Nd** (left) and **4-Nd** (right).

Table 4.1: Experimental peak positions obtained from peak deconvolution for **2-Nd** and **4-Nd**. The energetically lowest doublet state is given as the absolute value of the transition, all other energies are given as relative values.

peak	**2-Nd**		**4-Nd**	
$^4F_{3/2} \rightarrow {}^4I_{11/2}$	peak position [nm]	energy [cm^{-1}]	peak position [nm]	energy [cm^{-1}]
1	1046.01	9560.14	1049.35	9529.71
2	1053.31	52.58	1056.30	62.70
3	1066.77	116.89	1063.38	125.73
4	1072.80	138.54	1071.14	193.86
5	1082.14	188.40	1080.20	272.17
6	1086.95	253.04	1086.67	327.28
$^4F_{3/2} \rightarrow {}^4I_{13/2}$	peak position [nm]	energy [cm^{-1}]	peak position [nm]	energy [cm^{-1}]
1	1310.15	7632.71	1325.01	7547.11
2	1330.10	114.48	1330.73	32.44
3	1343.93	191.85	1342.37	97.60
4	1353.16	242.60	1352.27	152.14
5	1382.23	398.02	1371.80	257.42
6	1400.26	491.18	1385.07	327.26
7	1405.43	517.45	1404.72	428.25

4.5 Magnetic and photophysical properties of the Sm-analogues

Despite being a Kramers ion with $J = 5/2$, which is very beneficial for the synthesis of single molecule magnets, coordination compounds of Sm(III) ions are not very well researched, in terms of their magnetism, as the magnetic moment exerted of Sm(III) is the lowest out of the non-diamagnetic lanthanides. Samples of **2-Sm** and **4-Sm** have been measured for their DC magnetic response in an external field of 1000 Oe. Due to the weak magnetic moment (0.09 cm^3 K mol^{-1}, expected from Curie's law), centering issues of the magnetometer prevented proper measurements cooling down from 300 K to 2 K. Instead, the samples had to be centered at low T, where the paramagnetic response already outweighs the diamagnetic contributions of the sample and the sample holder. The temperature dependent susceptibilities are, therefore, recorded upon cooling the sample to 2 K in an external field of 1000 Oe starting at 55 K and 24 K for **2-Sm** and **4-Sm**, respectively.

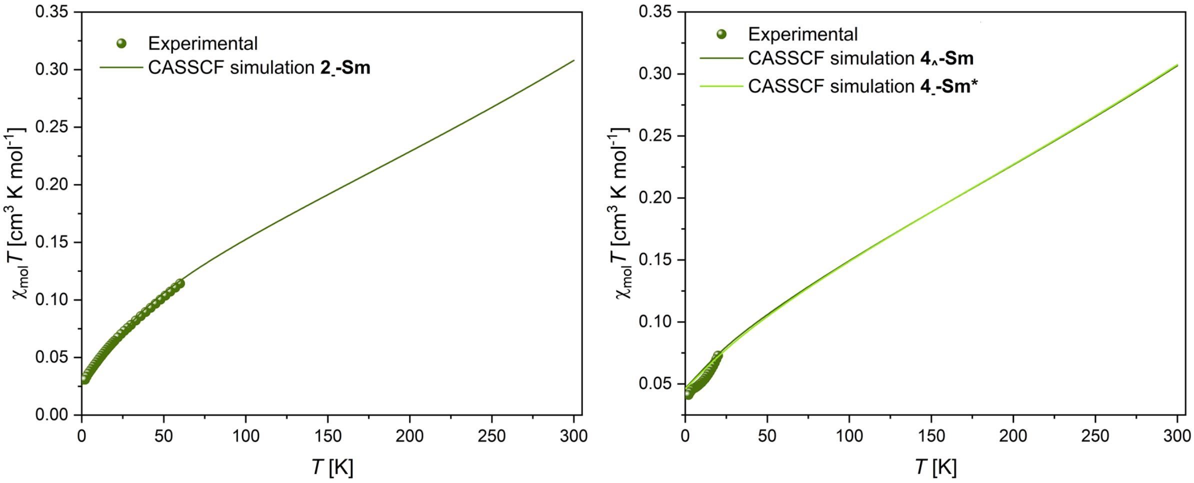

Figure 4.17: Temperature-product of the molar magnetic susceptibility vs. temperature of **2-Sm** (left) and **4-Sm** (right).

Classical validation of the experimental data using the observed room temperature $\chi_{mol}T$ values is not applicable. However, plotting of the experimental data alongside the simulated behaviour from *ab initio* CASSCF calculations, reveals a good agreement between the experiment and what is expected. The final $\chi_{mol}T$ values recorded at 2 K are 0.031 and 0.041 cm^3 K mol^{-1}, for **2-Sm** and **4-Sm**, respectively. Testing the dynamic behaviour of **2-Sm** and **4-Sm**, did not reveal an out-of-phase signal, irrespective of the application of an external field. This observation is interesting, as slow magnetic relaxation has been observed for all other analogues of Kramers ions under the application of an external field. Especially since the Er(III)-analogues showed SMM behaviour (see section

4.9), slow relaxation is also expected for Sm(III), as Sm(III) is also characterized by a prolate electron distribution, similar to Er(III). A possible explanation, could again be the small magnetic moment. The intensities of the out-of-phase signals observed for the complexes for the other lanthanides, are generally low, even for the highly magnetic ions Dy(III) and Er(III). In case of Sm(III), it is a possibility that a very weak out-of-phase signal is not be observed due to the intensity relative to the noise of the measurement. In order to gain deeper understanding of the compounds **2-Sm** and **4-Sm**, CASSCF calculations have been performed.

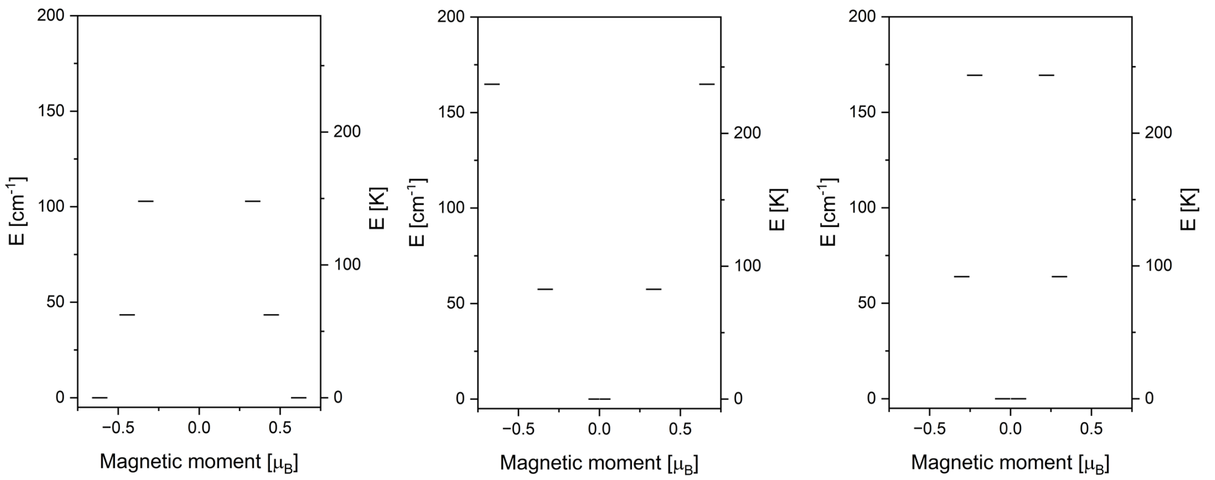

Figure 4.18: *Ab initio* energy diagram for **2$_{-}$-Sm**, **4$_{\wedge}$-Sm** and **4$_{-}$-Sm***.

As no single crystal structure of **4$_{-}$-Sm** has been obtained, the simulation was carried out on **4$_{-}$-Sm***, using the structural information of the closest analogue **4$_{-}$-Eu**, replacing the Eu(III) ion with Sm(III). The results of the calculation for **2$_{-}$-Sm** show a ground state doublet characterized mainly as m$_J$ = 5/2, with strong admixing of 1/2 and 3/2. The g-tensor is showing strong transverse components with g$_x$ = 0.144, g$_y$ = 0.368 and g$_z$ = 0.819. A pure m$_J$ = 5/2 with high axiality would give g$_x$ = g$_y$ = 0 and g$_z$ = 1.429. The high amount of observed mixing of the m$_J$-states, suggests that slow magnetic relaxation is not observable at zero field, due to QTM events. The absence of a frequency-dependent χ''_{mol} signal under the effect of an applied field, is therefore likely a consequence of the weak moment for **2-Sm**. For both polymorphs **4$_{\wedge}$-Sm** and **4$_{-}$-Sm***, the calculated energy diagram reveals that the ground state doublet is mainly a m$_J$ = 1/2 state, with g$_x$ = 1.048, g$_y$ = 0.627 and g$_z$ = 0.010 and g$_x$ = 1.029, g$_y$ = 0.636 and g$_z$ = 0.098, for **4$_{\wedge}$-Sm** and **4$_{-}$-Sm*** respectively. This feature explains the absence of slow relaxation for **4-Sm**, as the magnetization within a m$_J$ = ± 1/2 doublet is essentially, free to flip. The energies of the excited KD states are 62.44 K (43.42 cm^{-1}) and 147.91 K (102.86 cm^{-1}), 82.70 K (57.51 cm^{-1}) and 237.04 K (164.84 cm^{-1}) and 91.90 K (63.91 cm^{-1}) and 243.60 K

(169.40 cm^{-1}), for **2$_{\_}$-Sm**, **4$_{\wedge}$-Sm** and **4$_{\_}$-Sm***, respectively.

The energetic structure of **2-Sm** and **4-Sm** can be further experimentally tested using photoluminescence measurements. Under excitation at 369 nm, the PL emission of **2-Sm** and **4-Sm** has been recorded at 3 K.

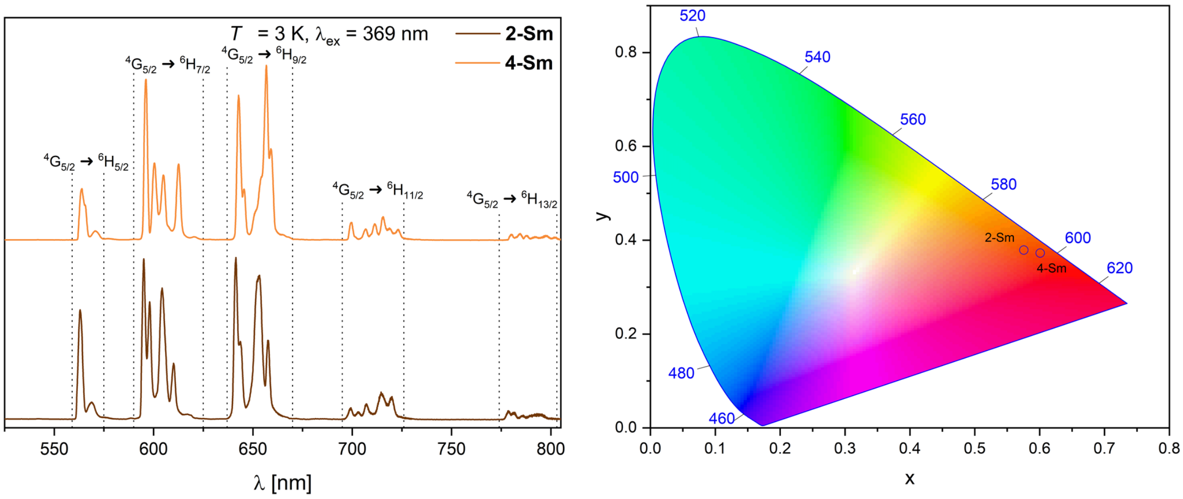

Figure 4.19: Emission spectra recorded at 3 K with $\lambda_{ex} = 369$ nm for **2-Sm** and **4-Sm** (left) and chromaticity diagram (right).

When excited with UV light, the samples of **2-Sm** and **4-Sm** show an orange/red luminescence. As shown in figure 4.19 (left), the emission is characterized by five emission bands, corresponding to the $^4G_{5/2} \rightarrow {}^6H_J$ transitions of Sm(III), where $J = 5/2$, 7/2, 9/2, 11/2 and 13/2.[108–110] The experimentally determined branching ratios for **2-Sm** between the transitions are 10.81%, 36.14%, 41.48%, 8.86% and 2.72%, for $J = 5/2$, 7/2, 9/2, 11/2 and 13/2, respectively. For **4-Sm** the obtained ratios are 7.73%, 34.34%, 46.13%, 8.96% and 2.84%, respectively. The colour of the emitted light is more towards the orange region for **2-Sm**, while **4-Sm** emits more in the red region (see figure 4.19, right), as the branching into the $J = 11/2$ and 13/2 transitions is higher for **4-Sm**. The $^4G_{5/2} \rightarrow {}^6H_{9/2}$ transition of Sm(III) is a hypersensitive transition, strongly dependent on the symmetry of the coordination environment, while the higher energy $^4G_{5/2} \rightarrow {}^6H_{5/2}$ and $^4G_{5/2} \rightarrow {}^6H_{7/2}$ transitions are both magnetic dipole transitions, less influenced by the chemical surrounding.[110] The considerably higher branching ratio for the $^4G_{5/2} \rightarrow {}^6H_{9/2}$ of 46.13% in **4-Sm** over 41.48% in **2-Sm**, suggests higher symmetry of **2-Sm**. This is in very good agreement with the determined CShM values of 1.548 (C_{2v}) and 2.874 (C_{2v}), for **2$_{\_}$-Sm** and **4$_{\wedge}$-Sm** respectively. Peak deconvolution analysis was performed with OriginPro, to obtain the positions of the emission lines and with that an experimental avenue to the energy splitting of the SO-coupled multiplets.

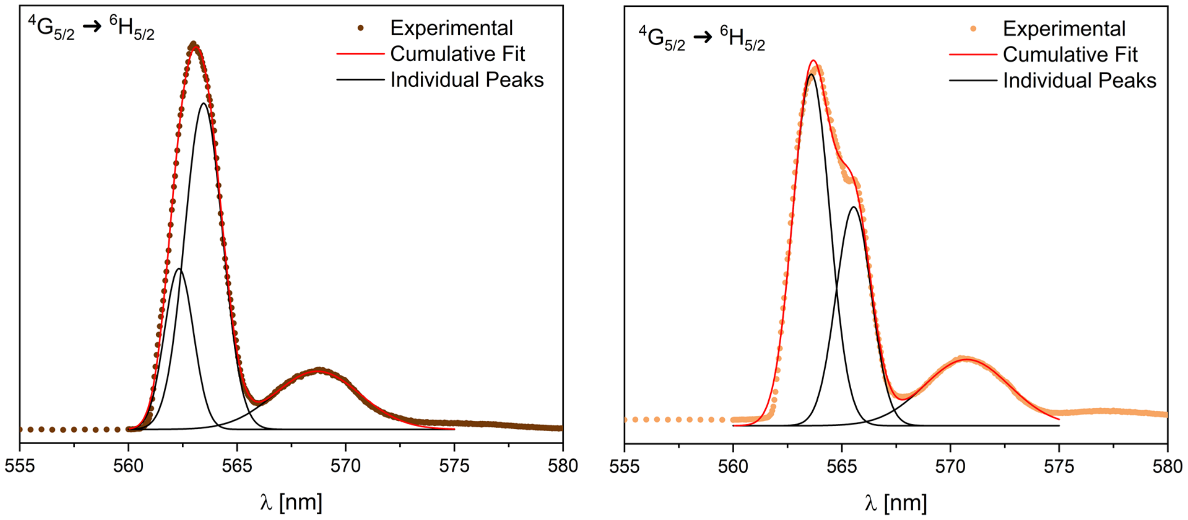

Figure 4.20: Peak deconvolution of the $^4G_{5/2} \rightarrow {}^6H_{5/2}$ transition for **2-Sm** (left) and **4-Sm** (right).

The highest energy $^4G_{5/2} \rightarrow {}^6H_{5/2}$ transition was fit with a good agreement using three emission lines, as it is expected for a $J = 5/2$ state, split into three KD states. The emission lines were found at 562.33 nm, 563.46 nm and 568.69 nm for **2-Sm**. The peak at 562.33 nm corresponds to relaxation into the ground state doublet. With that, the energy gap between $^6H_{5/2}$ and $^4G_{5/2}$ is found at 17783.31 cm^{-1}. Relative to that, the second and third peak correspond to the first and second excited doublet state, at 35.88 cm^{-1} and 199.10 cm^{-1}, respectively. For **4-Sm**, the peaks are found at 563.595 nm, 565.547 nm and 570.752 nm, which translate to relative energies of 0 cm^{-1}, 61.24 cm^{-1} and 222.49 cm^{-1}, respectively. The energy separation towards $^4G_{5/2}$ is 17743.24 cm^{-1}. The obtained results show that the experimentally observed energy gaps are higher than the energy levels predicted via CASSCF calculations. This is matching the trend observed in the analogue complexes of the other lanthanides. Deconvolution of the emission bands, has also been performed for the transitions up to $J = 11/2$. As expected the $^4G_{5/2} \rightarrow {}^6H_{7/2}$ transition, was well reproduced using four individual emission lines for both **2-Sm** and **4-Sm**. For **2-Sm**, the transitions $^4G_{5/2} \rightarrow {}^6H_{9/2}$ and $^4G_{5/2} \rightarrow {}^6H_{11/2}$ could be analysed using the expected amount of five and six peaks, although a broad emission was added in the fitting procedure, to account for a high background. For **4-Sm**, seven and nine individual lines were necessary to obtain a satisfying result. One peak employed for $^4G_{5/2} \rightarrow {}^6H_{9/2}$, was to account for a high background, similar to **2-Sm**. The added peaks that were needed in the fitting procedure, confirm the presence of **4$_{\_}$-Sm**, although in considerably small amounts. The low intensities of three of the peaks, allow to match the six intense peaks with **4$_{\wedge}$-Sm**. The peak deconvolution and the obtained energies are presented in figure 4.21 and table 4.2. For the $^4G_{5/2} \rightarrow {}^6H_{11/2}$ transition of **4-Sm** only the peaks that are correlated to **4**$_\Lambda$**-Sm** are presented.

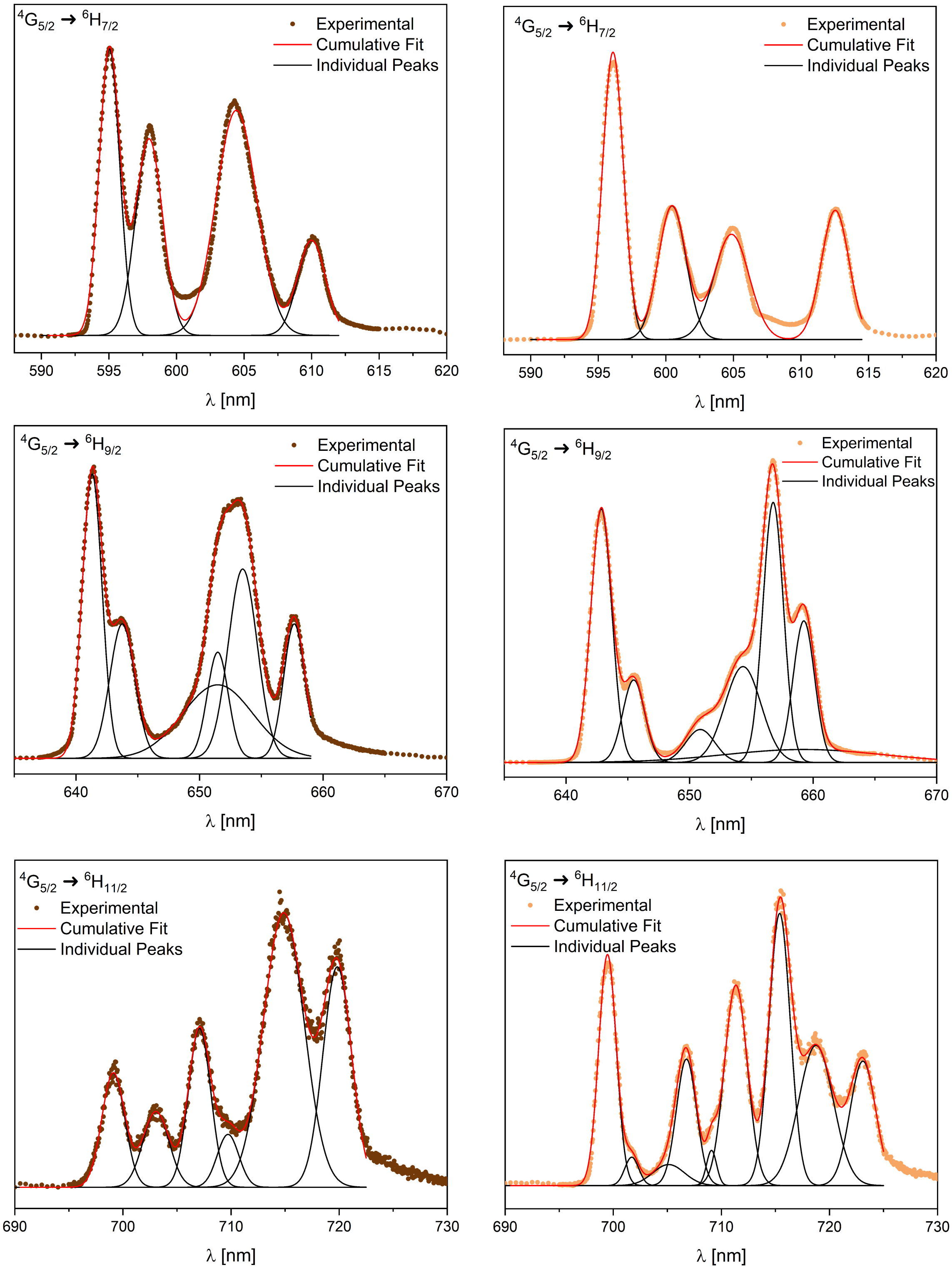

Figure 4.21: Peak deconvolution of the $^4G_{5/2} \rightarrow {}^6H_J$, $J = 7/2, 9/2, 11/2$ transitions for **2-Sm** (left) and **4-Sm** (right).

Table 4.2: Experimental peak positions obtained from peak deconvolution for **2-Sm** and **4-Sm**. The energetically lowest doublet state is given as the absolute value of the transition, all other energies are given as relative values.

peak	**2-Sm**		**4-Sm**	
$^4G_{5/2} \rightarrow {}^6H_{7/2}$	peak position [nm]	energy [cm^{-1}]	peak position [nm]	energy [cm^{-1}]
1	595.04	16805.65	596.09	16776.02
2	597.97	82.49	600.47	122.26
3	604.43	261.14	604.86	243.32
4	610.01	412.42	612.54	450.45
$^4G_{5/2} \rightarrow {}^6H_{9/2}$	peak position [nm]	energy [cm^{-1}]	peak position [nm]	energy [cm^{-1}]
1	641.31	15593.18	642.86	15555.61
2	643.75	59.10	645.48	63.14
3	651.47	234.37	650.87	191.51
4	653.49	290.82	654.32	272.64
5	657.67	387.92	656.76	329.44
6			659.25	386.81
$^4G_{5/2} \rightarrow {}^6H_{11/2}$	peak position [nm]	energy [cm^{-1}]	peak position [nm]	energy [cm^{-1}]
1	699.11	14303.90	699.468	14296.58
2	703.06	80.38	706.77	147.71
3	707.09	161.35	711.343	238.66
4	709.72	213.86	715.39	318.21
5	714.87	315.30	718.75	383.61
6	719.83	411.67	723.09	467.08

4.6 Magnetic and photophysical properties of the Tb-analogues

As mentioned before, and as also evidenced by the observations reported in chapter 4.3, generally non-Kramers ions are less likely to exhibit SMM behaviour, due to the bistability of the ground state not being an intrinsic feature. Tb(III) is the most studied non-Kramers ion in molecular magnetism, based on the discovery of lanthanide based SMM behaviour in $TbPc_2$ and many following studies.[55,111,112] The DC magnetic behaviour is shown in figure 4.22. It was measured upon cooling polycrystalline samples of **2-Tb** and **4-Tb** from 300 K to 2 K in an external field of 1000 Oe.

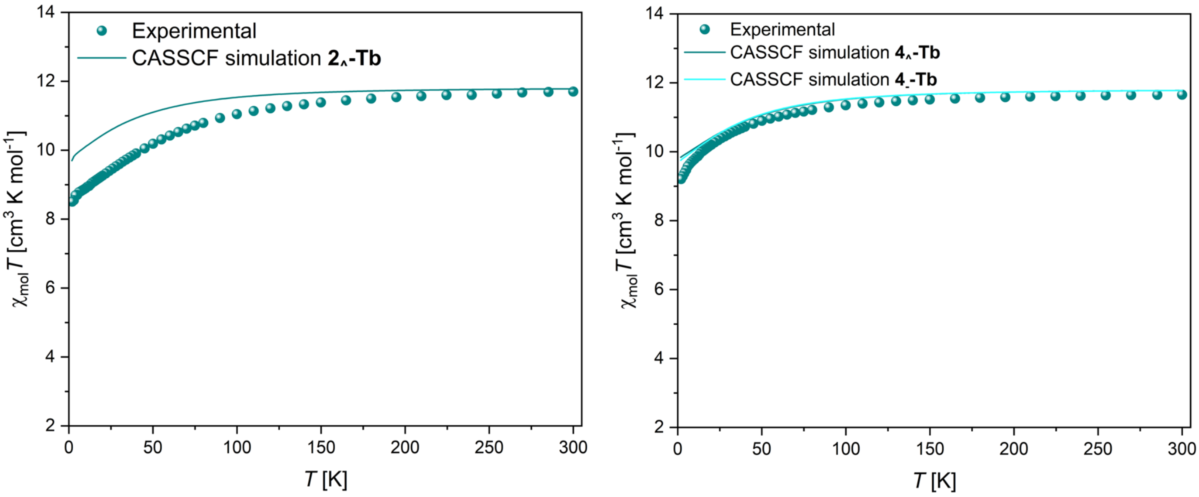

Figure 4.22: Temperature-product of the molar magnetic susceptibility vs. temperature for **2-Tb** (left) and **4-Tb** (right).

The observed values at 300 K are 11.70 cm^3 K mol^{-1} for **2-Tb** and 11.65 cm^3 K mol^{-1} for **4-Tb**, respectively, in good agreement with the theoretical value of 11.82 cm^3 K mol^{-1} for a single Tb(III) ion with $J = 6$ and $g_J = 3/2$. The experimental $\chi_{mol}T$ remains nearly temperature-independent down to approximately 100 K where it starts slowly decreasing until it reaches 8.46 cm^3 K mol^{-1} and 9.12 cm^3 K mol^{-1}, at 2 K, for **2-Tb** and **4-Tb**, respectively. The observed decrease nicely matches the simulation obtained via CASSCF methods for **4-Tb**. For **2-Tb** the experimental value drops considerably stronger than the simulation, possibly mediated by weak intermolecular antiferromagnetic interactions. This being only observed for **2-Tb** and not for **4-Tb**, matches the shortest metal-metal distances observed in the crystal structures of **2-Ln** being 0.12 Å shorter than those observed for **4-Ln**, as well as what has been observed for the isotropic Gd-analogues. It should be noted, however, that interactions have not been observed for the later analogues of Dy(III), Ho(III) and Er(III). As mentioned above, Tb(III) is not a Kramers ion and with that the observation of slow magnetic relaxation is less likely compared to analogues of Kramers ions. The dynamic magnetic behaviour was tested using AC susceptibility measurement techniques at low T. As expected, and matching what has been observed in the other lanthanides analogues, no out-of-phase signal was observed without the application of an external field. With the application of an external DC field, a weak signal has been observed, as shown in figure 4.23.

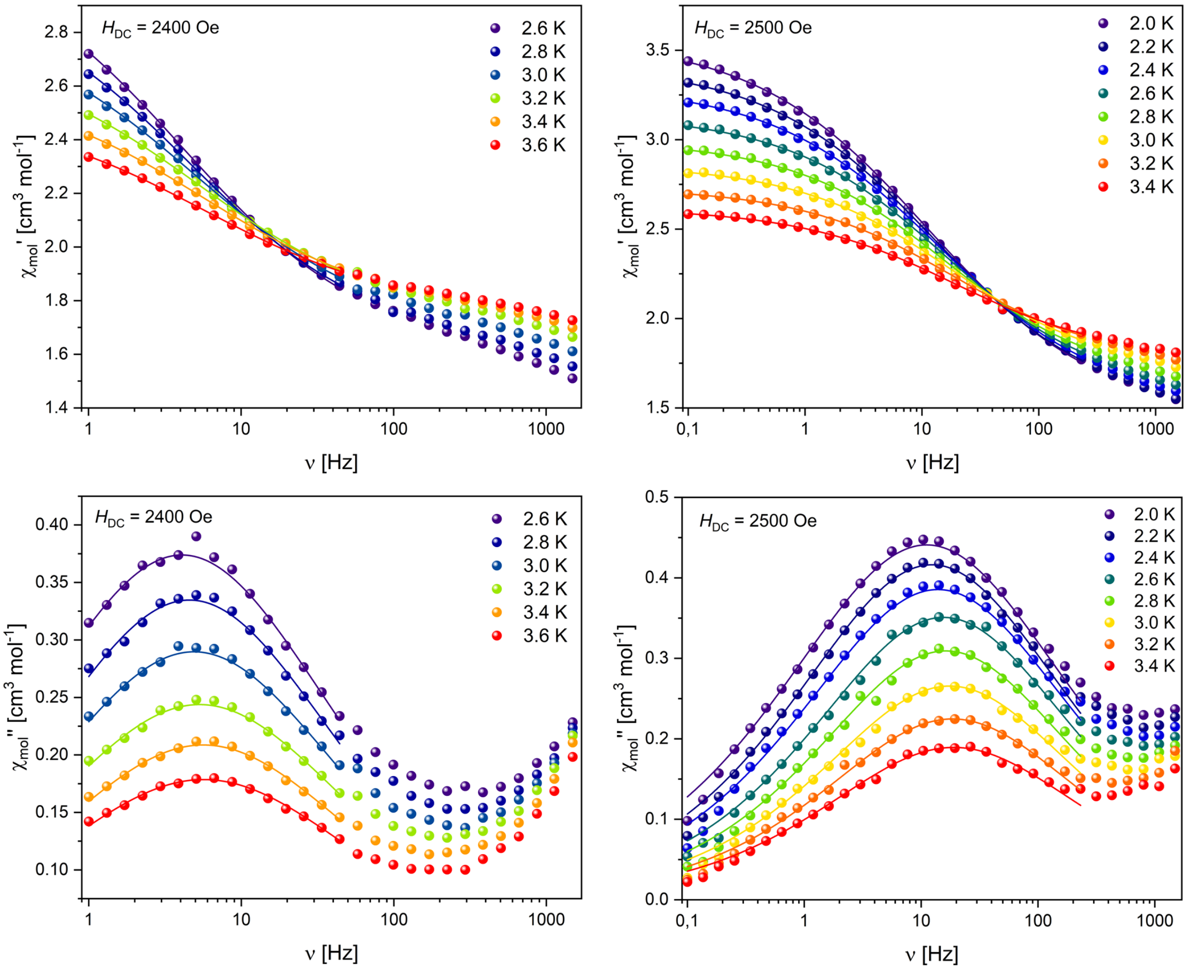

Figure 4.23: Frequency dependency of the in-phase (top) and out-of-phase (bottom) component of the magnetic susceptibility for **2-Tb** (left) and **4-Tb** (right). The solid lines are the best fits to a generalized Debye model.

The optimal DC fields have been found to be 2400 Oe and 2500 Oe, for **2-Tb** and **4-Tb**, respectively. It should be stated that the applied fields are comparably stronger than the optimal fields that have been found for the other lanthanide analogues. The observed signals are found around 4 Hz for **2-Tb** and 10 Hz for **4-Tb**, respectively. Upon increasing temperature the typical shift towards higher frequencies is almost not observable, but the signal quickly vanishes. Reasonable fits of the data were only obtainable up to 3.6 K and 3.4 K, for **2-Tb** and **4-Tb**, respectively. Both samples reveal a second increase in the out-of-phase component outside of the frequency window, which might be related to the polymorphs of the molecule. Interestingly, a second crystallographic polymorph of **2-Tb** has not been observed, however, since Tb is at the breakpoint between the polymorphs **2$_{\_}$-Ln** and **2$_{\wedge}$-Ln** which have both been observed for **2-Gd**, a small contribution of **2$_{\_}$-Tb** appears reasonable. It should be noted, that this is not a proof, since the combination of the strong applied field and the weak intensity of the signal, might also be interpreted as an artifact of the measurement. The Cole-Cole plots are given in figure 4.24.

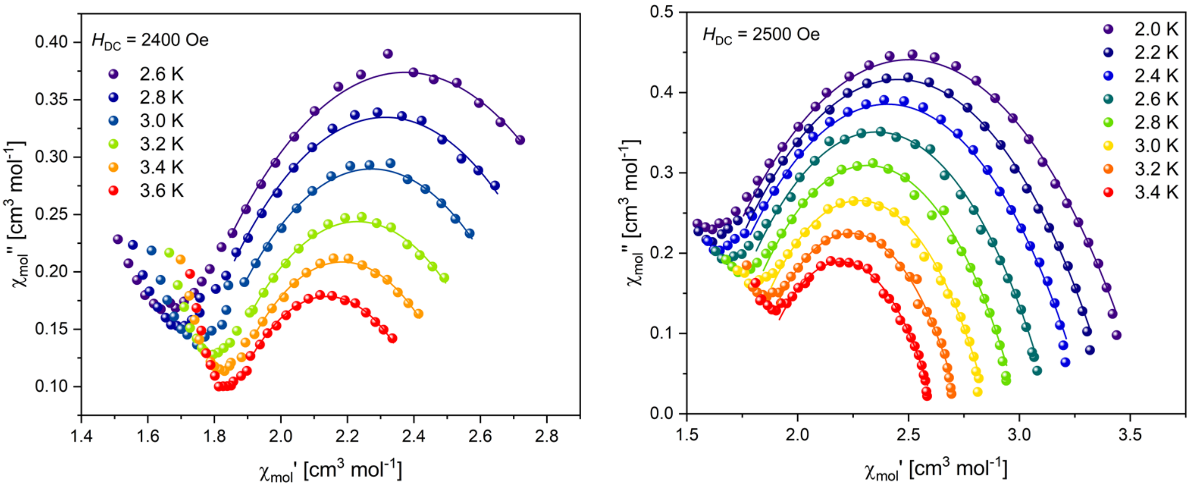

Figure 4.24: Cole-Cole plots for **2-Tb** (left) and **4-Tb** (right). The solid lines are the best fits to a generalized Debye model.

The shape of the Cole-Cole plots emphasizes, the second maximum appearing, as well as a broad distribution of relaxation processes. The distribution is further characterized by the α parameters of the best Debye fits, ranging between 45% and 43% for **2-Tb** and 51% and 46% for **4-Tb**, respectively, over the whole temperature-range. The high values observed for α over the whole temperature range match the absence of frequency shift typical for over-the-barrier type relaxation being observable in the AC data. The obtained relaxation times were fit using a linear fit. The linear fits match the data reasonably well, however, the amount of data points is very low in order to fully validate the fits. Performing a linear fit of $\ln(\tau)$ vs. $1/T$ represents Orbach-type relaxation, which is not expected based on the observed behaviour. Fits, employing the classical treatment of Raman relaxation as described in equation 2.11, did not yield good agreement. In the literature, there has been a discussion to perform fits of Raman relaxation, using a second exponential term, mathematically identical to the treatment of Orbach relaxation, as the CT^{-n} is purely phenomenological.[113] Therefore, the best interpretation of the relaxation data appears to be, assuming the obtained parameters correspond to Raman relaxation.

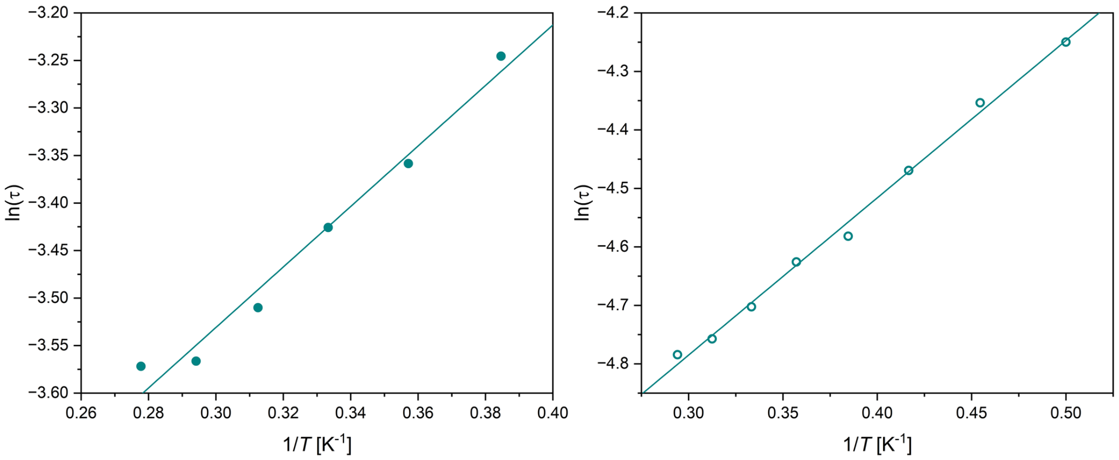

Figure 4.25: Temperature-dependent relaxation times for **2-Tb** (left) and **4-Tb** (right).

Using this, the fits yielded τ_{Raman} = 1.12 x 10^{-2} s, U_{eff} = 3.18 K (2.21 cm^{-1}) and τ_{Raman} = 3.73 x 10^{-3} s, U_{eff} = 2.69 K (1.87 cm^{-1}), for **2-Tb** and **4-Tb** respectively. The obtained values of the effective energy barrier are far below what has been reported for Tb(III) SMMs showing Orbach type relaxation, as expected. Through *ab initio* CASSCF calculations, the electronic finestructure of the $^7F_6$ ground state was further characterized. As no single crystals of **4$_{-}$-Tb** have been observed, the presented calculations were performed on the crystal structure of the closest analogue **4$_{-}$-Dy**, replacing the Dy(III) with Tb(III).

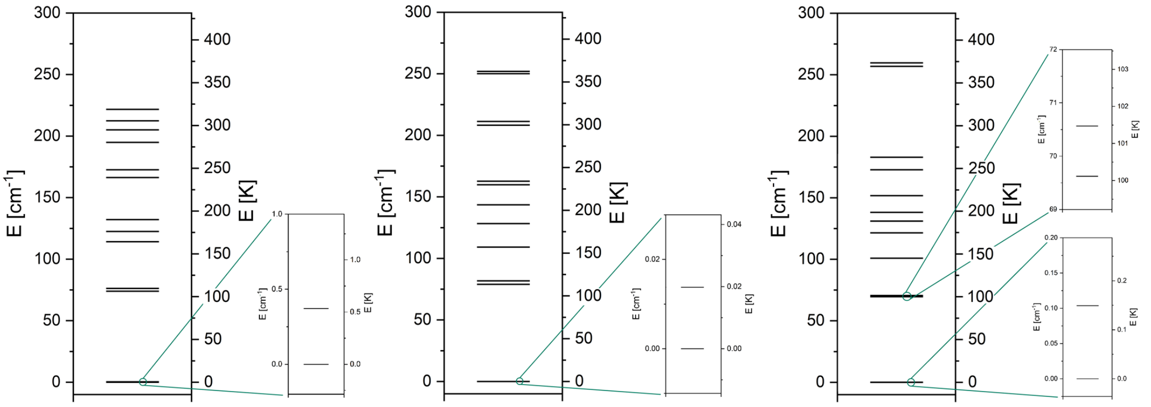

Figure 4.26: *Ab initio* energy diagrams for **2$_{\wedge}$-Tb**, **4$_{\wedge}$-Tb** and **4$_{-}$-Tb**.

As expected for a non-Kramers ion in a low symmetry coordination environment, the m_J-states do not give doublet states but are split over an energy range of 225 cm^{-1} (324 K) for **2$_{\wedge}$-Tb** and 260 cm^{-1} (374 K) for the two polymorphs of **4-Tb**. However, the two lowest lying state of each complex give rise to a pseudo-doublet ground state with calculated energy separations of 0.37 cm^{-1} (0.53 K), 0.01 cm^{-1} (0.01 K) and 0.10 cm^{-1} (0.14 K), for **$2_{\wedge}$-Tb**, **$4_{\wedge}$-Tb** and **$4_{\_}$-Tb** respectively. The pseudo-doublet ground state results in magnetic bistability, which is observed in the AC susceptibility data. It is interesting to observe slow magnetic relaxation in a doublet state that is separated by 0.37 cm^{-1} (**2-Tb**), as the energy gap within the pseudo doublet of reported Tb(III) SMMs is generally lower.

Complexes of Tb(III) ions with optically active ligands, typically show strong sensitized Tb(III) centered emission.[46,114,115] Photoluminescence studies have been performed at 3 K on samples of **2-Tb** and **4-Tb**.

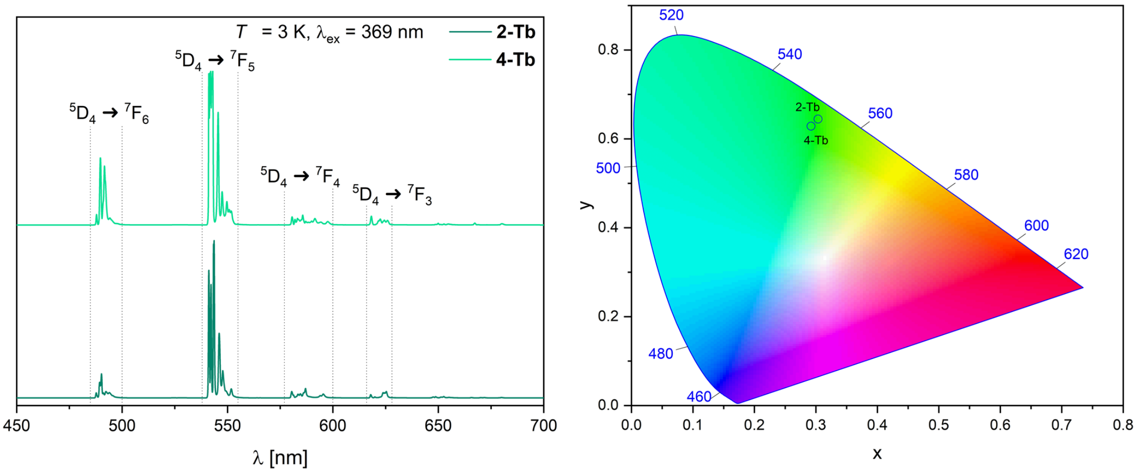

Figure 4.27: Emission spectra recorded at 3 K with $\lambda_{ex} = 369$ nm for **2-Tb** and **4-Tb** (left) and chromaticity diagram (right).

Under excitation at 369 nm, as derived from the Gd-analogue, strong emission bands are observed in the visible spectrum. The observed bands are found between 480 nm and 500 nm, 530 nm and 560 nm, 575 nm and 600 nm and between 615 nm and 630 nm, corresponding to the $^5D_4 \rightarrow {}^7F_6$, $^5D_4 \rightarrow {}^7F_5$, $^5D_4 \rightarrow {}^7F_4$ and $^5D_4 \rightarrow {}^7F_3$ transitions, respectively. A few extremely weak signals are observable between 650 nm and 700 nm, which are related to the $^5D_4 \rightarrow {}^7F_2$ transition. The emission of both samples is dominated by the green magnetic dipole transition $^5D_4 \rightarrow {}^7F_5$. The branching ratios found for the four transitions from high energy to low energy are 11.45%, 75.00%, 9.24% and 4.31% for **2-Tb** and 20.25%, 66.99%, 8.67% and 4.09% for **4-Tb**, respectively. For **4-Tb**, the branching ratio into the $^5D_4 \rightarrow {}^7F_6$ transition is higher compared to **2-Tb**, which is also reflected in the chromaticity coordinates being shifted slightly towards the blue region. The overall emission colour remains green for both compounds. Both the $^5D_4 \rightarrow {}^7F_6$ and $^5D_4 \rightarrow {}^7F_5$ transitions are elctric dipole transitions, which are strongly influenced by the ligand field. It has been reported that the green $^5D_4 \rightarrow {}^7F_5$ transition is very sensitive to asymmetry as well as covalency of the bonding.[114] In **2-Tb**, the green transition around 550 nm shows a significantly higher relative intensity, to what is observed for **4-Tb**. This suggests a lower coordination symmetry of **2-Tb** compared to **4-Tb**, which is in good agreement with the calculated CShM values for $\mathbf{2_\Lambda}$**-Tb** and $\mathbf{4_\Lambda}$**-Tb** of 3.429 and 2.750, respectively, both describing C_{2v} symmetry. A similar behaviour has been observed for the Dy(III) analogue, *vide infra*. Performing peak deconvolution using OriginPro on the high resolution spectra, it is possible to obtain the positions of the individual emission lines, within each transition band. As the lines originate from the m_J-states of the multiplet, the peak deconvolution provides a direct insight into the energy spectrum.

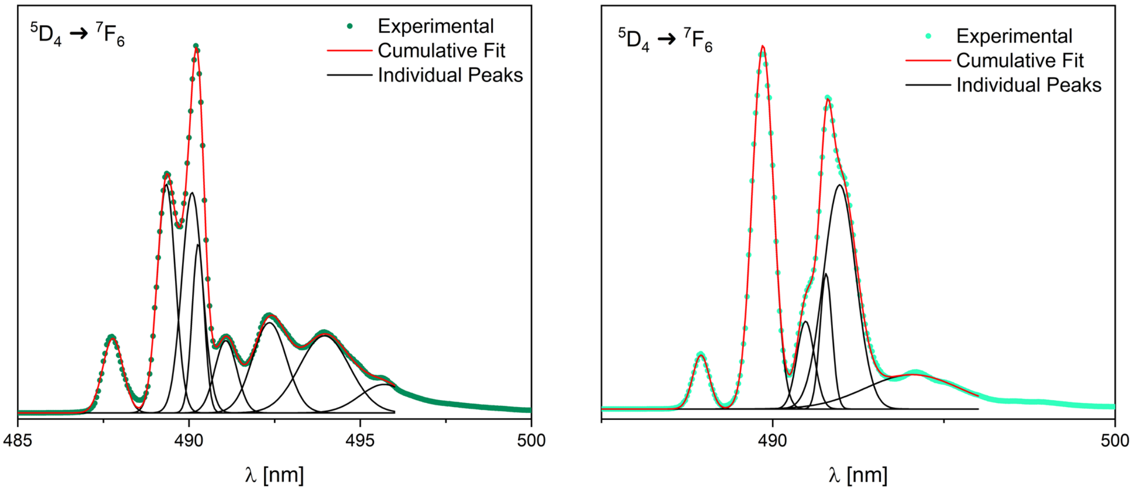

Figure 4.28: Peak deconvolution of the $^5D_4 \rightarrow {}^7F_6$ transition for **2-Tb** (left) and **4-Tb** (right).

For **2-Tb**, a good fit to the experimental spectrum was obtained, using eight individual emission lines. As shown in figure 4.28, proper fits of the low energy emission, coming from the highest excited states, couldn't be achieved. For a non-Kramers ion with $J = 6$, $2J + 1 = 13$ individual lines would be expected. Using the information gained via CASSCF calculations, the number of observable lines is likely to decrease to eleven, as the ground and first excited state, as well as the second and third excited states are to close in energy, to be resolved in the spectrum. The individual peaks obtained by the fitting procedure were found at 487.78 nm, 489.34 nm, 490.09 nm, 490.27 nm, 491.07 nm, 492.35 nm, 493.956 nm and 495.70 nm, respectively. The highest energy emission at 487.78 nm corresponds to an energy difference between the ground state of the excited $^5D_4$ multiplet and the ground state $^7F_6$ multiplet of 20501.21 cm^{-1}. Using this line as a reference, the relative positions of the other peaks translate to excited state energies of 65.40 cm^{-1}, 96.72 cm^{-1}, 104.21 cm^{-1}, 137.68 cm^{-1}, 190.34 cm^{-1}, 256.50 cm^{-1} and 327.72 cm^{-1}, respectively. By following the order and energy spacing of the calculated excited state energies, the experimentally determined emission lines can be linked with the excited states to which they correspond. The highest energy emission is obviously related to the ground state pseudo-doublet state at a relative energy of 0 cm^{-1} and 0.37 cm^{-1}, while the second line is related to the second and third excited state, calculated at 73.94 cm^{-1} and 76.28 cm^{-1}, respectively. The following two emission lines, are strongly overlapping in the PL spectrum, causing the most intense emission line within the transition band. While a good fit was obtained employing two individual lines, their origin is likely linked to the three states with even energy spacing, calculated between 114 cm^{-1} and 132 cm^{-1}. The following emission line at 137.68 cm^{-1} could be an overlap of the two states calculated at 166.37 cm^{-1} and 172.62 cm^{-1}, where the energy difference is below 10 cm^{-1}, and therefore, difficult to resolve in the spectrum. The remaining three lines are resulting from the four highest excited states. The experimentally determined energies and the energies of the most likely calculated equivalents are summarized in table 4.3.

Table 4.3: Relative energies of the emission lines obtained from peak deconvolution of PL data of **2-Tb** and energies from CASSCF calculations for **2**$_\Lambda$**-Tb** in cm^{-1}.

Peak	Experimental PL	*Ab initio* CASSCF
1	0	0.00, 0.37
2	65.40	73.94, 76.28
3	96.72	114.22, 122.49
4	104.21	132.18
5	137.68	166.37, 172.62
6	190.34	194.92
7	256.50	205.04
8	327.72	212.43, 221.71

A similar procedure was applied to process the data of **4-Tb**. As suggested by the powder diffraction data, and as no single crystal of **4**$_\Delta$**-Tb** has been experimentally confirmed, the sample of **4-Tb** is believed to contain mainly **4**$_\Lambda$**-Tb**, therefore, the calculated energy spectrum of **4**$_\Lambda$**-Tb** is used as a lone comparison. The ^{5}D$_4$ → ^{7}F$_6$ transition was fit using six individual lines, however, the lowest energy transition appears to be an overlap of two lines, that couldn't be resolved during the deconvolution process. By using the energy of the emission observed at the lowest wavelength again as a reference point, the relative energies of the other emission peaks are determined. The highest energy emission is observed at 487.91 nm, corresponding to an energy gap towards the excited multiplet of 20495.79 cm^{-1} and originating from relaxation into the pseudo-doublet ground-state. The second emission line is found at 489.71 nm (75.67 cm^{-1}) related to the second and third excited states at calculated energies of 78.94 cm^{-1} and 81.75 cm^{-1}. The two overlapping emission lines at 490.96 nm (127.54 cm^{-1}) and 491.56 nm (152.27 cm^{-1}) are very likely related to the three excited states which were calculated between 109.18 cm^{-1} and 143.59 cm^{-1}, while the peak at 491.96 nm (168.77 cm^{-1}) corresponds to the two states of very close energy at 159.85 cm^{-1} and 162.71 cm^{-1}, respectively. The last very broad emission line, which is believed to be not properly deconvoluted, is matched with the four highest excited states, that are forming two pseudo-doublets. The position, energies and corresponding *ab initio* calculated energies of the states are given in table 4.4.

Table 4.4: Relative energies of the emission lines obtained from peak deconvolution of PL data of **4-Tb** and energies from CASSCF calculations for **4$_{\Lambda}$-Tb** in cm^{-1}.

Peak	Experimental PL	*Ab initio* CASSCF
1	0	0.00, 0.01
2	75.67	78.94, 81.75
3	127.54	109.19
4	152.27	128.31, 143.59
5	168.77	159.85, 162.71
6	256.16	208.27, 211.30, 250.11, 251.95

Interestingly, for both **2-Tb** and **4-Tb**, especially for the higher excited states, the CASSCF-obtained energies are underestimating the experimentally observed energy splitting. However, for the lower excited states, the overall magnitude of the calculated energies is in reasonable agreement with the measurement. Comparison to the energy barrier obtained from magnetic AC susceptibility measurements is not possible, as the observed relaxation is not an over-the-barrier type relaxation, *vide supra*. Peak deconvolution has been performed for the lower energy transitions as well. The $^5D_4 \rightarrow {}^7F_5$ transition could be deconvoluted using eight and ten individual peaks, for **2-Tb** and **4-Tb** respectively. The $^5D_4 \rightarrow {}^7F_4$ and $^5D_4 \rightarrow {}^7F_3$ transitions have been fit employing nine and six lines for **2-Tb** and twelve and six lines for **4-Tb**, respectively. The amount of lines, that had to be employed for a good fit, exceeds the amount of theoretically possible lines for $^5D_4 \rightarrow {}^7F_4$ of **4-Tb**, where twelve peaks were employed, but ligand field splitting can only result in 9 individual states. This might be an observable effect of the second polymorph, giving rise to some of the weaker emission lines. In the other transitions, this polymorph could be covered by the emission of **4$_{\Lambda}$-Tb**, which is believed to be the main component. The peak deconvolution and the obtained energies are presented in figure 4.29 and table 4.5.

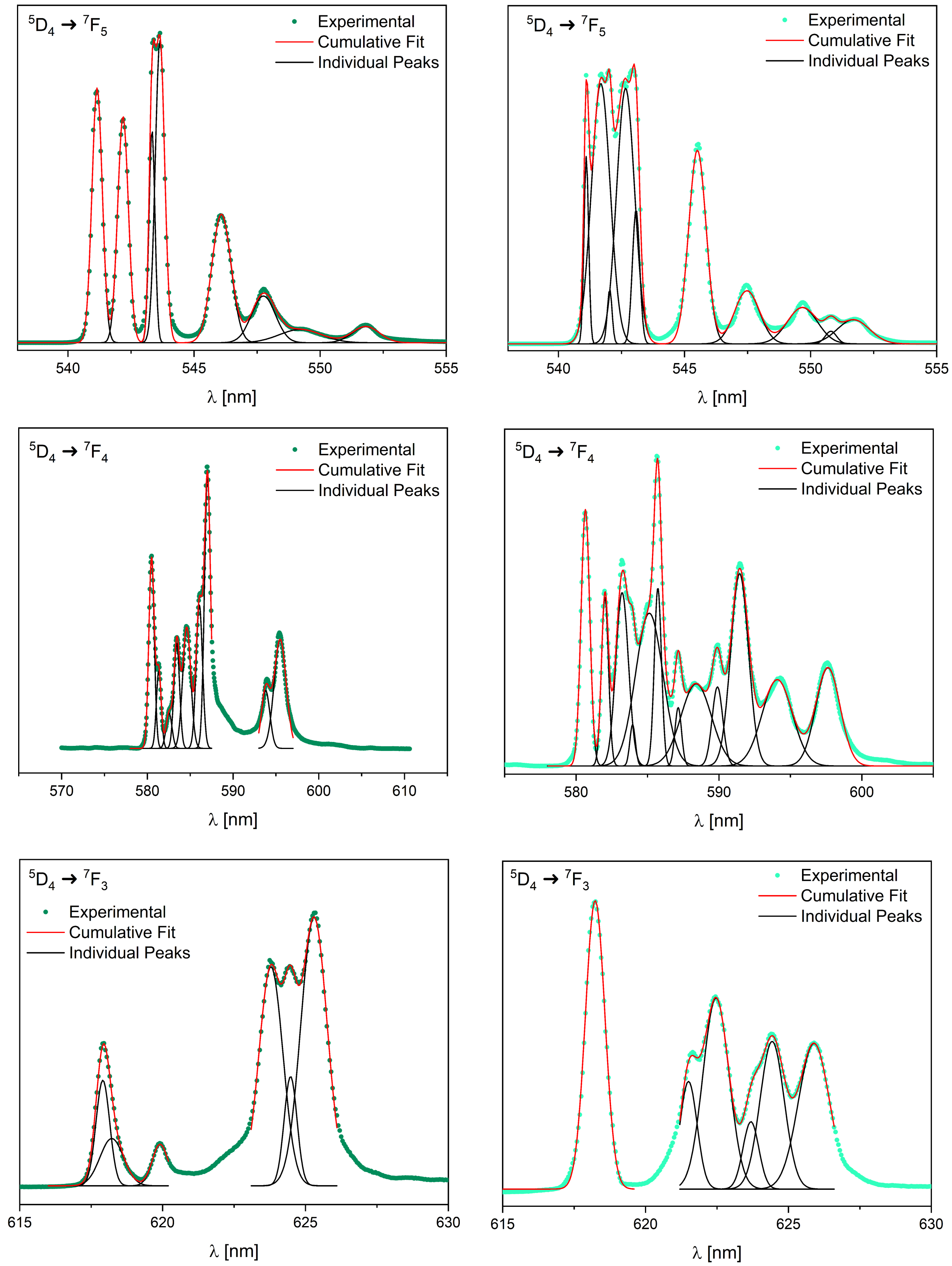

Figure 4.29: Peak deconvolution of the $^5D_4 \rightarrow {}^7F_J$, $J = 5, 4, 3$ transitions for **2-Tb** (left) and **4-Tb** (right).

Table 4.5: Experimental peak positions obtained from peak deconvolution for **2-Tb** and **4-Tb**. The energetically lowest doublet state is given as the absolute value of the transition, all other energies are given as relative values.

peak	**2-Tb**		**4-Tb**	
$^5D_4 \rightarrow {}^7F_5$	peak position [nm]	energy [cm^{-1}]	peak position [nm]	energy [cm^{-1}]
1	541.16	18478.99	541.10	18480.74
2	542.18	35.00	541.68	19.62
3	543.33	74.01	542.03	31.61
4	543.65	84.71	542.66	53.06
5	546.09	166.83	543.08	67.11
6	547.75	222.56	545.51	149.26
7	549.22	271.39	547.48	215.16
8	551.82	356.98	549.67	288.10
9			550.80	325.46
10			551.67	354.81
$^5D_4 \rightarrow {}^7F_4$	peak position [nm]	energy [cm^{-1}]	peak position [nm]	energy [cm^{-1}]
1	580.49	17226.77	580.66	17221.93
2	581.34	25.04	582.02	40.45
3	582.53	60.33	583.22	75.83
4	583.43	86.81	583.96	97.35
5	584.60	120.97	585.12	131.48
6	586.06	163.78	585.73	149.10
7	587.02	191.63	587.15	190.48
8	593.80	386.08	588.41	227.43
9	595.49	433.96	589.90	269.90
10			591.45	314.24
11			594.08	389.21
12			597.63	489.11
$^5D_4 \rightarrow {}^7F_3$	peak position [nm]	energy [cm^{-1}]	peak position [nm]	energy [cm^{-1}]
1	617.91	16183.61	618.24	16175.03
2	618.22	8.17	621.50	85.00
3	619.91	52.34	622.47	109.89
4	623.79	152.60	623.69	141.34
5	624.48	170.24	624.43	160.40
6	625.30	191.24	625.90	197.91

4.7 Magnetic and photophysical properties of the Dy-analogues

The most successfully employed Ln(III) ion in molecular magnetism is undoubtedly Dy(III), due to its highly magnetic ($J = 15/2$) and anisotropic ground state. As Dy(III) is also a Kramers ion, the bistability of the ground state is guaranteed. As shown in section 2, the record holding SMMs in terms of their effective energy barrier have been Dy(III)-based compounds for a long time.[57–59] The temperature dependent DC susceptibility has been recorded upon cooling samples of **2-Dy** and **4-Dy** from 300 K to 2 K in an external magnetic field of 1000 Oe (figure 4.30).

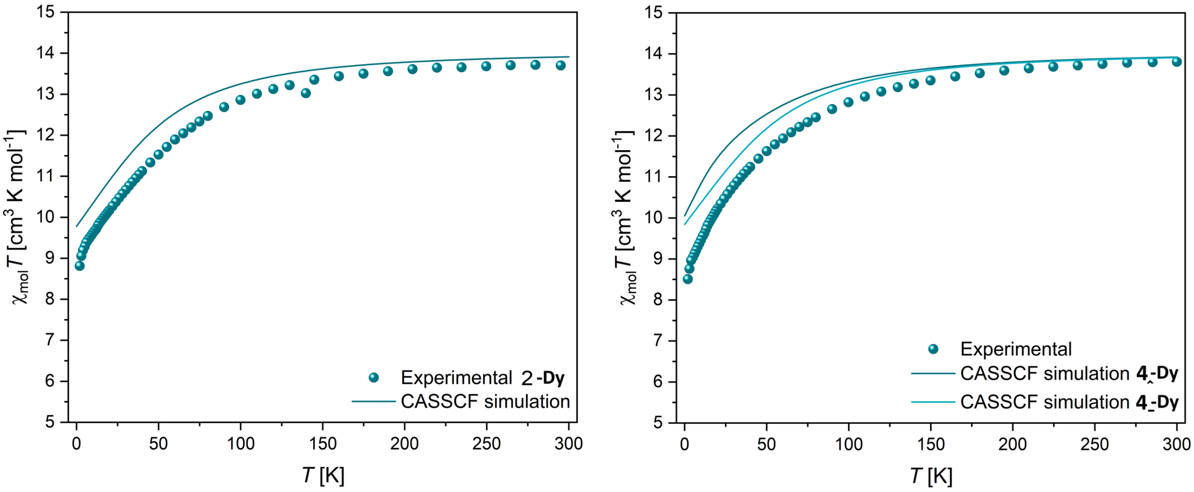

Figure 4.30: Temperature-product of the molar magnetic susceptibility vs. temperature for **2-Dy** (left) and **4-Dy** (right).

The room temperature $\chi_{mol}T$ value for **2-Dy** was found at 13.70 cm^3 K mol^{-1} and 13.80 cm^3 K mol^{-1} for **4-Dy**. Both values are in reasonable agreement to the theoretical value expected for a single Dy(III) ion of 14.17 cm^3 K mol^{-1}. The temperature dependence is characterized by a smooth decrease upon cooling related to the depopulation of the Stark levels, without any sudden drops that would suggest intermolecular magnetic coupling for both samples of **2-Dy** and **4-Dy**. The CASSCF simulated susceptibilities for **2_--Dy**, **4_--Dy** and **$4_\wedge$-Dy** are multiplied by a small correction factor in order to better match the slightly lower observed room temperature values. The temperature dependent behaviour shows a similar trend as the experimentally determined data, as it should be the case for a mononuclear compound, where intramolecular interactions cannot be observed. The dynamic magnetic relaxation behaviour has been studied using AC susceptibility techniques as described in section 2. Without the application of an external field, neither of the samples showed any out-of-phase signal, which can be qualitatively explained by the low symmetry environment around the Dy(III) discussed previously in section 3. Low symmetry enhances QTM, therefore, allowing efficient magnetic relaxation between the two orientations of the ground state doublet. Upon the application of an external magnetic field, slow relaxation was observed in both samples. The optimal fields for the relaxation were determined to be 1200 Oe for **2-Dy** and 700 Oe for **4-Dy**. Figure 4.31 shows the frequency dependent in-phase and out-of-phase components of the magnetic susceptibility for the samples of **2-Dy** and **4-Dy**.

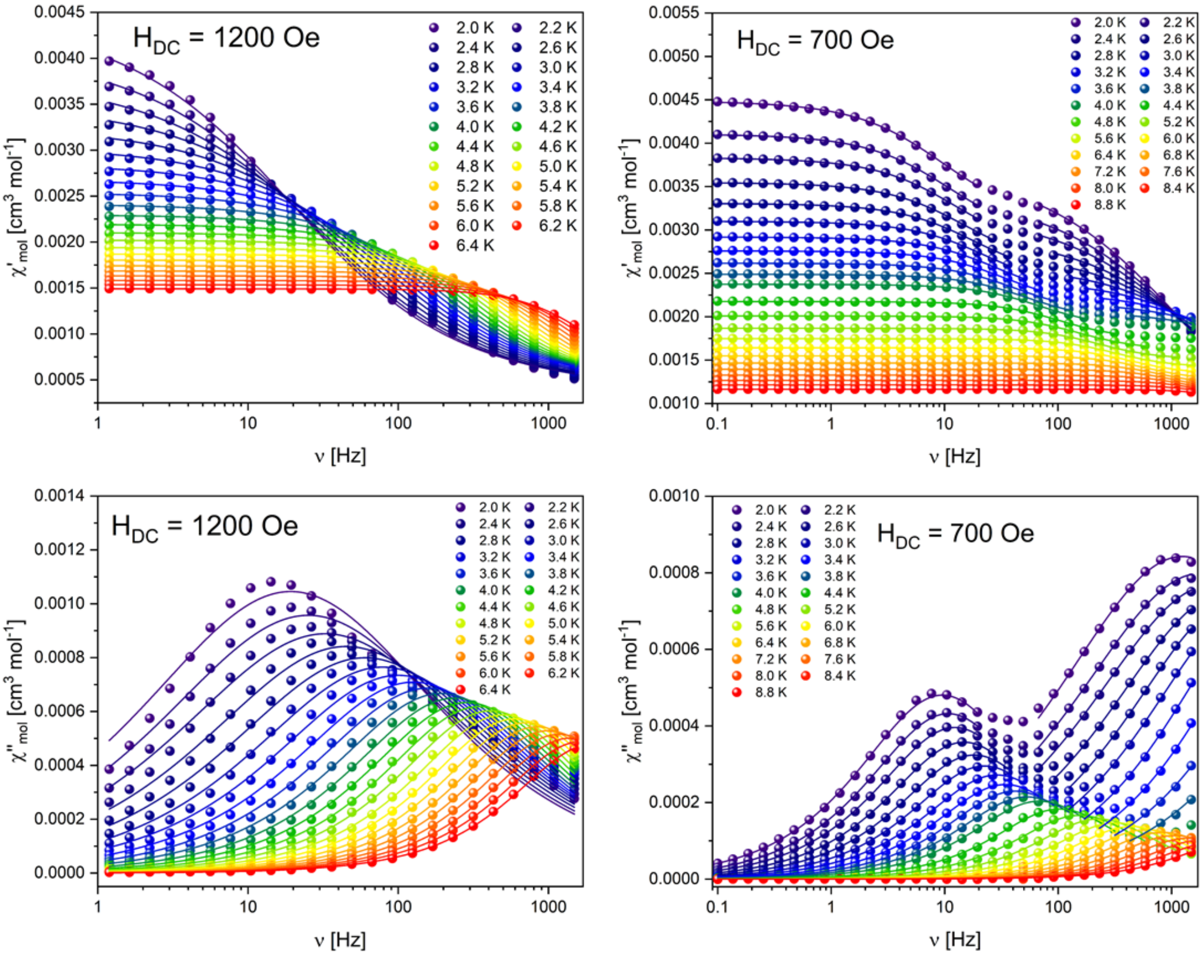

Figure 4.31: Frequency dependency of the in-phase (top) and out-of-phase (bottom) components of the magnetic susceptibility for **2-Dy** (left) and **4-Dy** (right). The solid lines are the best fits to a generalized Debye model.

A single maximum in the out-of-phase component alongside a decrease of the in-phase component is observed for **2-Dy** (figure 4.31, left). At the lowest measured temperature of 2 K, the maximum is observed around an AC frequency of 15 Hz. Upon increasing the temperature the maximum is shifting to higher frequencies while a decreasing intensity of the signal is also observed. The shifting nature of the out-of-phase signal with temperature is a clear sign of SMM behaviour. The maximum is observed close to the highest observable frequency of 1500 Hz at 6.4 K. The gathered AC data of **4-Dy** reveals two maxima in the χ'' vs. ν plot. The first of the maxima is observed at around 10 Hz at 2 K, shifting to higher frequencies with increasing T and reaching 1500 Hz around 8 K. The second maximum is found at significantly higher frequencies of around 1000 Hz at 2 K. The real maximum is no longer observable already at temperatures above 2.4 K, however, the increasing signal still allowed modelling up to 3.8 K. The two maxima observed are matching the expectation of having the sample be a mixture of the two structurally independent polymorphs **4**$_{-}$**-Dy** and **4**$_{\wedge}$**-Dy** (see section 3.3). As the SMM properties are closely linked to the molecular structure, observable differences between **4**$_{-}$**-Dy** and **4**$_{\wedge}$**-Dy** are expected. As the overall relaxation behaviour of the first maximum is very comparable to that observed in **2-Dy**, it is likely to be correlated to the polymorph **4**$_{\wedge}$**-Dy**, as the closer structural resemblance between **4**$_{\wedge}$**-Dy** and **2**$_{\wedge}$**-Dy** over **4**$_{-}$**-Dy** and **2**$_{\wedge}$**-Dy** could lead to similar relaxation mechanisms. However, further analysis using other methods is necessary to fully validate this assumption. In order to quantitatively assess the SMM properties, the in-phase and out-of-phase data were simultaneously fitted to a generalized Debye model (equations 2.9, 2.10). For **2-Dy** the full frequency range was employed in a single model, while fits of the data of **4-Dy** were performed using two separate frequency ranges, matching the individual maxima. The best fit functions are presented as solid lines in figure 4.31 and the obtained best fit parameters are given in the appendix.

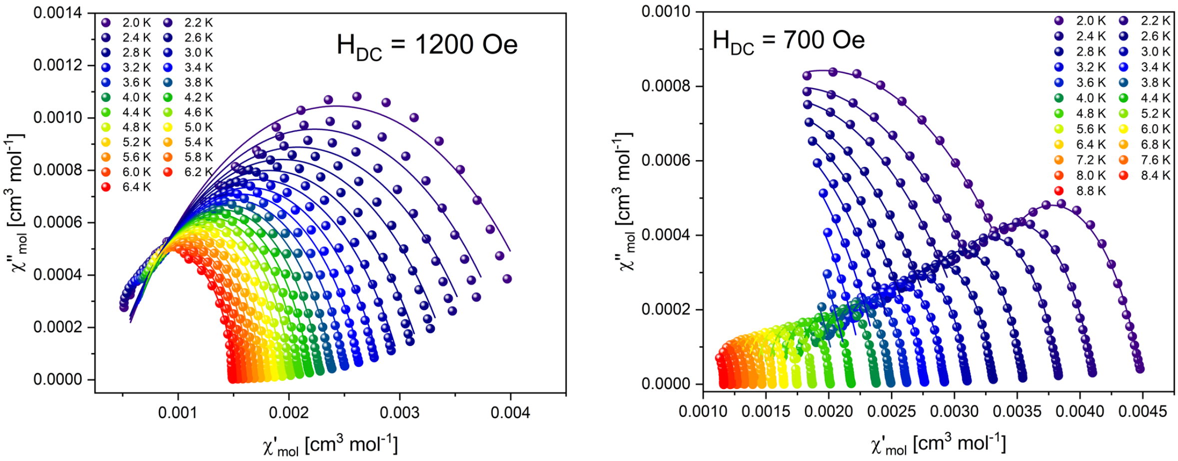

Figure 4.32: Cole-Cole plots for **2-Dy** (left) and **4-Dy** (right). The solid lines are the best fits to a generalized Debye model.

The obtained α values decrease with T, which is a typical behaviour, as the high temperature relaxation is dominated by the Orbach process (see section 2.2). The α values observed at 2 K are 0.4 for **2-Dy** and 0.24 and 0.44 for the two maxima of **4-**

Dy, respectively. The values make it apparent that significant contributions of Raman relaxation are present in the overall relaxation behaviour of the complexes. This is also confirmed by the curvature of the cole-cole data presented in figure 4.32. Arrhenius analysis has been performed on the temperature dependent τ values obtained employing equation 2.11. Good fits of the relaxation data were obtained employing Orbach, Raman and direct relaxation terms for **2-Dy** and the first maximum of **4-Dy**, while only Orbach and Raman terms were sufficient to model the data of the second maximum in **4-Dy** (figure 4.33).

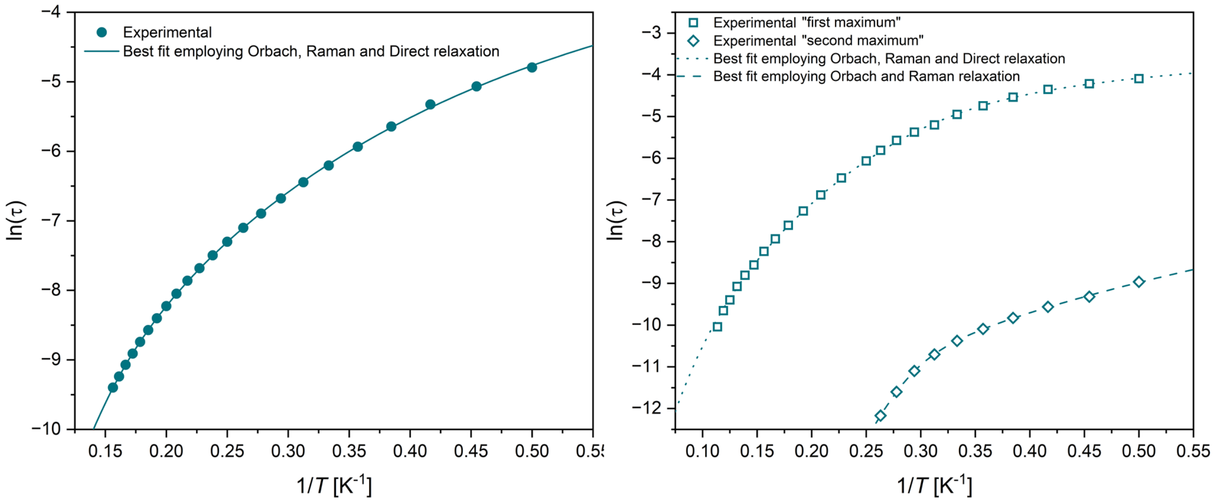

Figure 4.33: Arrhenius plots for **2-Dy** (left) and **4-Dy** (right).

The best fits yielded the relaxation parameters τ_0 = 1.00 x 10^{-8} s, U_{eff} = 68.71 K (47.76 cm^{-1}), C = 4.58 s K^{-n}, n = 4.13 and A = 18.65 s K^{-1} for **2-Dy**. Fittings of the two maxima of **4-Dy** gave τ_0 = 2.80 x 10^{-5} s, U_{eff} = 21.99 K (15.28 cm^{-1}), C = 6.18 x 10^{-2} s K^{-n}, n = 5.72, A = 27.69 s K^{-1} and τ_0 = 2.29 x 10^{-12} s, U_{eff} = 57.14 K (39.71 cm^{-1}), C = 831.59 s K^{-n}, n = 3.25. Interestingly, the obtained energy barrier is higher for the second maximum, despite it being only observable at lower temperatures, which is a consequence of the very small τ_0 observed. In all three complexes, the observed effective energy barriers are rather small in respect to what has been observed for Dy(III)-based SMMs featuring axial ligand fields. This is again a direct consequence of the low symmetry environment which is not ideal for stabilizing the m_J states of the central Dy(III) ion. Further insights into the electronic structure of the complexes **$2_\wedge$-Dy**, **$4_\wedge$-Dy** and **4_--Dy** were gained by performing *ab initio* CASSCF calculations employing 9 electrons in seven active orbitals (full details are given in the appendix). Figure 4.34 shows the energy diagrams obtained for the different complexes **$2_\wedge$-Dy**, **$4_\wedge$-Dy** and **4_--Dy**.

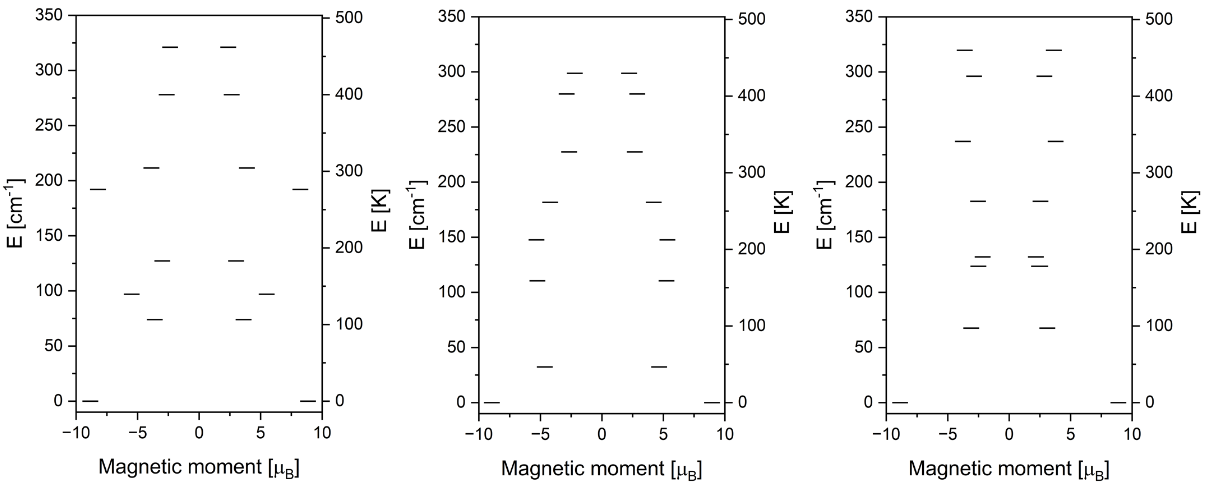

Figure 4.34: *Ab initio* energy diagrams for **2**$_{\wedge}$**-Dy**, **4**$_{\wedge}$**-Dy** and **4**$_{-}$**-Dy**.

The degeneracy of each m$_J$ state is an intrinsic property of Dy, as it is a Kramers ion with half-integer spin. Considering the $J = 15/2$ ground state the effective g-tensor is 20. A highly axial ground state, beneficial for SMM behaviour is, therefore, characterized with g$_x$ = g$_y$ = 0 and g$_z$ = 20. The ground state g-tensors found are g$_x$ = 0.11, g$_y$ = 0.24, g$_z$ = 17.68 for **2**$_{\wedge}$**-Dy**, g$_x$ = 0.46, g$_y$ = 1.22, g$_z$ = 17.88 for **4**$_{\wedge}$**-Dy** and g$_x$ = 0.28, g$_y$ = 0.48, g$_z$ = 17.73 for **4**$_{-}$**-Dy**. As expected from the quenching of the slow magnetic relaxation at zero field, the g-tensors represent strong m$_J$ mixing of the wavefunction, leading to efficient QTM in all three complexes. The energies of the first excited KD states are calculated at 106.36 K (73.92 cm^{-1}), 46.50 K (32.32 cm^{-1}) and 97.20 K (67.56 cm^{-1}) for **2**$_{\wedge}$**-Dy**, **4**$_{\wedge}$**-Dy** and **4**$_{-}$**-Dy**, respectively. All calculated energies of the excited states are considerably higher than the experimentally determined energy barriers. Very likely, this is due to the multitude of relaxation processes active, resulting in an overall lowered observed energy barrier. While the calculated energy gap between the ground state and the first excited state does not precisely represent the experimental results, the trend between all three complexes do match the experiment. Both the calculated energy gap of **2**$_{\wedge}$**-Dy** and the experimental effective energy barrier of **2-Dy** are highest among the three Dy-complexes. Similarly, both the calculation and the experiment yield one value of the two polymorphs in **4-Dy** close to and one significantly lower than the value of **2-Dy**. Using this information gained from the *ab initio* calculation, the low frequency maximum observed in the AC susceptibility can be correlated to **4**$_{-}$**-Dy** and the high frequency maximum to **4**$_{\wedge}$**-Dy**. With that, the calculation confirms the above mentioned qualitative assumption based on the comparable frequency dependency of the relaxation.

As the substituted phen ligand acts as an antenna for Dy(III) photoluminescence measurements on polycrystalline samples of **2-Dy** and **4-Dy** were performed at 3 K. The optimal excitation wavelength was found at 369 nm, matching what has been observed for the purely ligand based luminescence in the Gd-analogues.

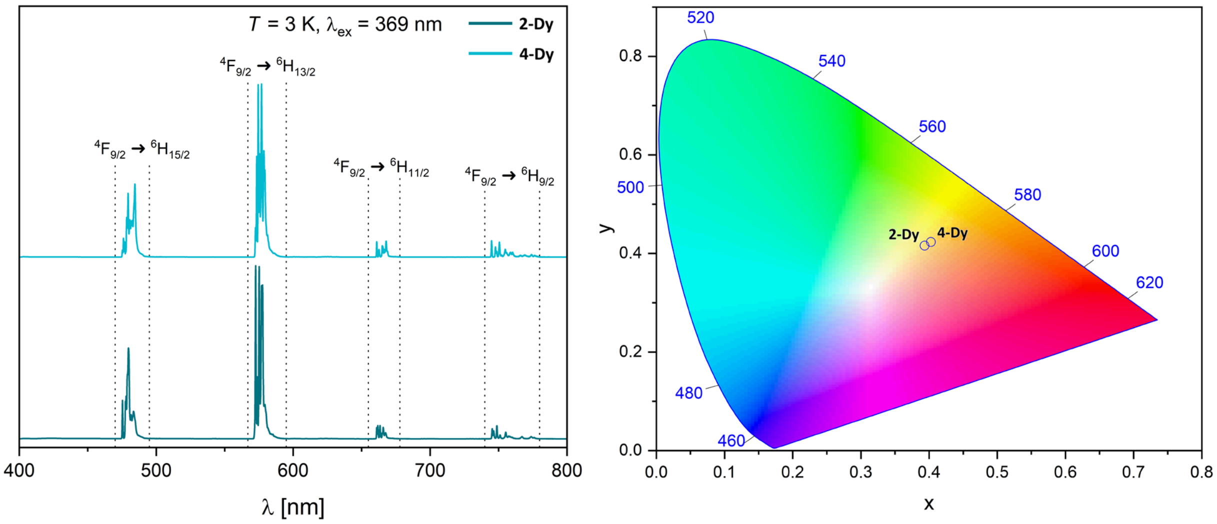

Figure 4.35: Emission spectra recorded at 3 K with $\lambda_{ex} = 369$ nm for **2-Dy** and **4-Dy** (left) and chromaticity diagram (right).

The photoemission of Dy(III) is based on the $^4F_{9/2} \rightarrow {}^6H_J$ transitions. The recorded spectra shown in figure 4.35 (left) reveal the four highest energy transitions within that ^6H_J multiplet. The transitions are observed between 470 nm and 490 nm, 560 nm and 590 nm, 655 nm and 670 nm and finally 740 nm and 780 nm, for the $^4F_{9/2} \rightarrow {}^6H_J$ transitions $J = 15/2$, $13/2$, $11/2$ and $9/2$, respectively. The highest intensity transition in both spectra is the $^4F_{9/2} \rightarrow {}^6H_{13/2}$ transition, followed by the $^4F_{9/2} \rightarrow {}^6H_{15/2}$ transition. Both transitions to the $J = 11/2$ and $J = 9/2$ manifold are significantly lower in intensity. The intensity ratio of the blue $^4F_{9/2} \rightarrow {}^6H_{15/2}$ and yellow $^4F_{9/2} \rightarrow {}^6H_{13/2}$ transition is a consequence of the low symmetry coordination environment. It has been observed in the literature that in low symmetry Dy(III) compounds the yellow transition is dominant, while the blue transition becomes dominant in compounds with high local symmetry around the Dy(III) ion.[116,117] This is due to the nature of the given transitions. The yellow $^4F_{9/2} \rightarrow {}^6H_{13/2}$ transition is a forced electric dipole transition, which is strongly influenced by the ligand field and enhanced by low symmetry, due to J-mixing. The blue $^4F_{9/2} \rightarrow {}^6H_{15/2}$ transition on the other hand is a magnetic dipole transition and much less sensitive to the coordination environment. This can be analysed using the experimentally determined branching ratios of 30.62%, 59.55%, 4.45% and 5.38% for the respective $^4F_{9/2} \rightarrow {}^6H_{15/2}$, $^4F_{9/2} \rightarrow {}^6H_{13/2}$, $^4F_{9/2} \rightarrow {}^6H_{11/2}$ and $^4F_{9/2} \rightarrow {}^6H_{9/2}$ transitions in **2-Dy**. The relative contribution of the yellow $^4F_{9/2} \rightarrow {}^6H_{13/2}$ transition in **4-Dy** is lower, while the branching of the blue $^4F_{9/2} \rightarrow {}^6H_{15/2}$ transition remains constant with 30.53%, 57.57%, 4.64% and 7.27% for the four transitions. In other words, the ratio between the blue and yellow transition is slightly higher for **4-Dy** than for **2-Dy**. As mentioned before, this suggests a higher symmetry of **4-Dy**, which is in line with the shape analysis performed on the crystal structure data, giving CShM values of 2.732 and 2.472 for **4**$_{\wedge}$**-Dy** and **4**$_{-}$**-Dy** and 3.382 for **2**$_{\wedge}$**-Dy**, respectively. Interestingly, in the chromaticity data shown in figure 4.35 (right), **2-Dy** appears to have a stronger contribution of the blue transition, as it is characterized by lower x and y values. However, this is a consequence of the stronger contribution of the red $^4F_{9/2} \rightarrow {}^6H_{9/2}$ transition in **4-Dy**. Due to the high resolution of the spectrum and the low temperature of the measurement, within each $^4F_{9/2} \rightarrow {}^6H_J$ transition individual peaks resulting from the ligand field splitting of the m_J-manifold are observable. Deconvolution of the spectrum, therefore, gives direct access to the energy splitting of the multiplet states. Peak deconvolution was performed on the PL emission spectrum using OriginPro.

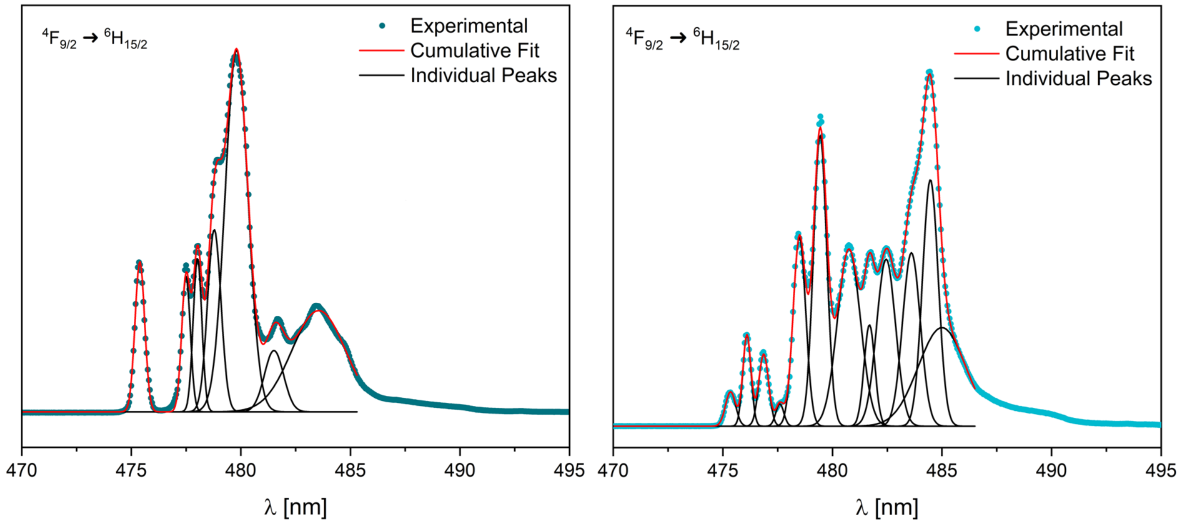

Figure 4.36: Peak deconvolution of the $^4F_{9/2} \rightarrow {}^6H_{15/2}$ transition for **2-Dy** (left) and **4-Dy** (right).

The recorded spectrum of **2-Dy** consists of six clearly recognizable peaks between 474 nm and 482 nm. A broader peak with a narrow feature overlayed is observed between 482 nm and 485 nm. A good fit was obtained employing an overlap of seven individual peaks, nicely recreating the behaviour up to 482 nm (figure 4.36, left). The broad peak mentioned is reasonably recreated using a single emission line, however, a good fit using two overlapping peaks could not be obtained. Nevertheless, assuming the peak between 482 nm and 485 nm is an overlap of two emission lines, the transition is accurately represented by eight individual lines, as it is expected for a $J = 15/2$ state being split into eight Kramers doublets. The highest energy peak, which corresponds to the transition into the ground state doublet is found at 475.388 nm, which translates to a separation between the $^6H_{15/2}$ ground state and the $^4F_{9/2}$ excited state of 21035.449 cm^{-1}. The energy separation between those two states obtained from the CASSCF calculation was found at a significantly higher value of 24537.86 cm^{-1}. However, it has been previously reported that CASSCF methods fall short in accurately predicting the energy of such highly excited states. In order to compare the experimental and ab initio energy levels, the high energy emission line at 475.388 nm (21035.449 cm^{-1}) is used as a reference for the zero energy ground state and the energies of the excited Kramers doublets can be obtained, by evaluating the spacing in between the lines. The positions of the seven individual peaks obtained from the deconvolution process for **2-Dy** are 475.388 nm, 477.496 nm, 478.021 nm, 478.784 nm, 479.801 nm, 481.510 nm and 483.552 nm, corresponding to relative energies of the Kramers doublets of 0 cm^{-1}, 92.865 cm^{-1}, 115.866 cm^{-1}, 149.204 cm^{-1}, 193.475 cm^{-1}, 267.448 cm^{-1} and 355.150 cm^{-1}.

Table 4.6: Relative energies of the emission lines obtained from peak deconvolution of PL data of **2-Dy** and KD energies from CASSCF calculations for **2_Λ-Dy** in cm^{-1}.

Peak	Experimental PL	*Ab initio* CASSCF
1	0	0
2	92.87	73.92
3	115.87	96.98
4	149.20	127.20
5	193.48	192.06
6	267.45	211.44
7	355.15	278.00, 321.09

As the spectrum consists of eight emission lines (seven resolved lines), the individual transitions can be easily matched with the respective Kramers doublets of the complex. Comparison of the spectroscopically obtained and calculated energy splitting of the $^6H_{15/2}$ multiplet, reveals that the calculated energies are generally underestimating the experimentally obtained values. The energy difference between the calculated and measured states increases with increasing energy from approx. 20 cm^{-1} for KDs 2, 3 and 4 up to more than 50 cm^{-1} for KDs 6 and 7. Interestingly, the calculated energy of KD 5 is very close to the experimentally determined energy (table 4.6), contradicting what is observed for the other states. This is possibly a consequence of the states wavefunction, as KD 5 is strongly anisotropic, mainly characterized by components of $|15/2\rangle$ (see appendix).

The deconvolution and interpretation of the PL emission spectrum of **4-Dy** is more challenging, due to the presence of the two polymorphs **4$_{\wedge}$-Dy** and **4$_{-}$-Dy**. The individual peaks of the transition are observed between 475 nm and 487 nm and a good fit was achieved by modelling with twelve distinct emission peaks (figure 4.36, right). Having two polymorphs and with that two different Dy(III)-complexes, 16 emission lines are expected, meaning some transitions are not resolved in the spectrum. The highest energy transition for **4-Dy** is found at 475.351 nm, close to the peak at 475.388 found in **2-Dy**, while the second highest transition is observed at 476.099 nm. As the separation towards the excited $^4F_{9/2}$ state is near independent of the chemical environment, a separation of approx. 0.75 nm between the two emission lines is too high to be the result of the two zero-line transitions of **4$_{\wedge}$-Dy** and **4$_{-}$-Dy**. Instead, the more likely interpretation is that the peak at 475.351 nm is an overlap of the two high energy transitions of the polymorphs, that cannot be resolved by the spectrometer. The peak position of 475.351 nm corresponds to an $^4F_{9/2}$ energy of 21037.076 cm^{-1}. The CASSCF energies of the $^4F_{9/2}$ state are 24536.32 cm^{-1} and 24544.95 cm^{-1} for **4$_{\wedge}$-Dy** and **4$_{-}$-Dy**, respectively, being very comparable to what has been observed in **2-Dy**. The peak positions obtained from deconvolution of the experimental data are 475.351 nm, 476.099 nm, 476.863 nm, 477.597 nm, 478.493 nm, 479.435 nm, 480.752 nm, 481.687 nm, 482.449 nm, 483.606 nm, 484.471 nm and 485.000 nm, respectively. Employing the transitions at 475.351 nm as the zero energy reference for both polymorphs, the peak positions correspond to relative energies of the Kramers doublets of 0 cm^{-1}, 33.051 cm^{-1}, 66.702 cm^{-1}, 98.931 cm^{-1}, 138.139 cm^{-1}, 179.201 cm^{-1}, 236.341 cm^{-1}, 276.717 cm^{-1}, 309.507 cm^{-1}, 359.096 cm^{-1}, 396.016 cm^{-1} and 418.529 cm^{-1}, respectively. As seen for **2-Dy**, the CASSCF calculated energies are not necessarily accurately matching the experimentally derived energies. Nevertheless, the CASSCF calculations should be comparable to each other, allowing to match the experimentally observed emissions to the two polymorphs by following the order of the two calculated energy spectra. The first emission lines at 33.051 cm^{-1} and 66.702 cm^{-1} can be related to the first excited states of **4$_{\wedge}$-Dy** and **4$_{-}$-Dy**, respectively which are calculated at 32.32 cm^{-1} and 66.56 cm^{-1}. The next peak at 98.93 cm^{-1} corresponds to the second excited doublet of **4$_{\wedge}$-Dy** at 110.40 cm^{-1}. Both KD 3 and 4, which are very close in energy (< 10 cm^{-1}), of **4$_{-}$-Dy** are attributed to the emission line observed at 138.14 cm^{-1}. The following transition is observed at 179.20 cm^{-1}, which would nicely match the calculated energies of KD 5 of both **4$_{\wedge}$-Dy** and **4$_{-}$-Dy**, however, leaving KD 4 of **4$_{\wedge}$-Dy** unmatched. Therefore, this transition is attributed to KD 4 of **4$_{\wedge}$-Dy**, which seems to be the more likely interpretation. The experimentally observed peak at 396.02 cm^{-1} is similarly attributed to an overlap between KD 7 of **4$_{\wedge}$-Dy** and KD 8 of **4$_{-}$-Dy**. The observed emissions and the responsible KDs are given in table 4.7.

Table 4.7: Relative energies of the emission lines obtained from peak deconvolution of PL data of **4-Dy** and KD energies from CASSCF calculations for **4**$_{\wedge}$**-Dy** and **4**$_{-}$**-Dy** in cm^{-1}.

Peak	Experimental PL	*Ab initio* CASSCF **4**$_{\wedge}$**-Dy**	*Ab initio* CASSCF **4**$_{-}$**-Dy**
1	0	0	0
2	33.05	32.32	
3	66.70		67.56
4	98.93	110.49	
5	138.14		123.59, 132.15
6	179.20	147.64	
7	236.34	181.68	182.70
8	276.72	227.43	
9	309.51		237.04
10	359.10	279.94	
11	396.02	298.74	296.21
12	418.53		319.70

A similar trend is observed as it has been the case for **2-Dy**, where the calculated energies are significantly underestimated relative to the experimentally observed energies of the higher excited doublets. At low energies the calculated energies compare well with the spectroscopically determined values. Interestingly, while the comparison between the effective energy barrier to magnetic relaxation and the energy gap already revealed that the relaxation occurs below the energy of the first excited state, the spectroscopic analysis reveals an even bigger difference between the effective energy barrier and the energy of the first excited Kramers doublet. Therefore, the magnetic relaxation is shown to occur mainly under the barrier, which is allowed due to the low symmetry around the Dy(III) ion.

4.8 Magnetic and photophysical properties of the Ho-analogues

The lanthanide with the highest observed total angular momentum $J = 8$ is Ho(III). It is also the lanthanide ion exerting the second highest magnetic moment after Dy(III). Several single-molecule magnets of Ho(III) have been reported with a wide range of observed energy barriers.[92,118] The magnetic response of **2-Ho** and **4-Ho** was tested upon cooling from 300 K to 2 K in an applied magnetic field of 1000 Oe.

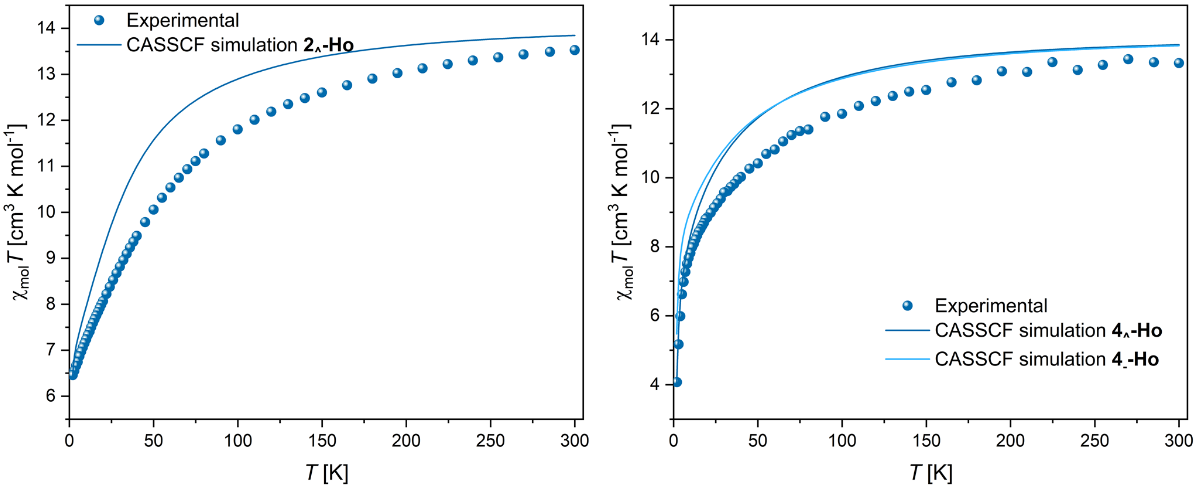

Figure 4.37: Temperature-product of the molar magnetic susceptibility vs. temperature for **2-Ho** (left) and **4-Ho** (right).

The recorded $\chi_{mol}T$ values at room temperature are 13.53 and 13.33 cm^3 K mol^{-1}, for **2-Ho** and **4-Ho**, respectively. Both values compare well with the theoretical value of 14.07 cm^3 K mol^{-1} expected for a single Ho(III) ion. Similar to the analogue complexes reported in this thesis, the *ab initio* simulation of the magnetic susceptibility, predicts a slightly lower room temperature value than the value predicted using Curie's law, of 13.8 cm^3 K mol^{-1} for all three calculated complexes **$\mathbf{2}_{\wedge}$-Ho**, **$\mathbf{4}_{\wedge}$-Ho** and **$\mathbf{4}_{\_}$-Ho**. The experimentally determined room temperature values are in good agreement with the simulated ones. Upon cooling, the values decrease smoothly without distinct features and the curvature, matches with the CASSCF simulation. Interestingly, the final $\chi_{mol}T$ value at 2 K for **2-Ho** is 6.47 cm^3 K mol^{-1}, which is significantly higher than 4.02 cm^3 K mol^{-1} that has been observed for **4-Ho**. The stronger decrease for **4-Ho** is, however, also recreated by the simulation, signalling that it is a consequence of depopulation of the Stark levels and not related to intermolecular coupling. Performing dynamic AC susceptibility studies, no out-of-phase signal was observed for any of the samples **2-Ho** and **4-Ho**. Also the application of an external field, did not result in an observable χ'' signal. Ho(III) is a non-Kramers ion, meaning the degeneracy of the m$_J$-states of opposing magnetization is not an intrinsic feature. Similar to what has been observed in the Pr(III)-based complexes **1-Pr** and **4-Pr**, the absence of any observable slow relaxation is most likely a result of a non degenerate ground state. In order to further confirm this hypothesis, the *ab initio* CASSCF calculations were carried out. The obtained energies of the ground state multiplets are given in figure 4.38.

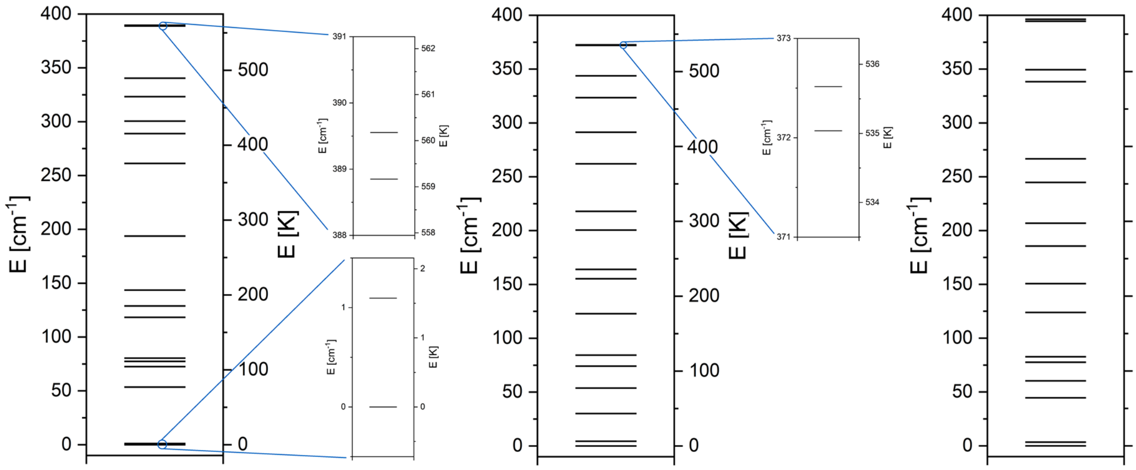

Figure 4.38: *Ab initio* energy diagram for **2$_{\wedge}$-Ho**, **4$_{\wedge}$-Ho** and **4$_{-}$-Ho**.

For all three complexes the observed energies of the whole multiplet span an energy close to 400 cm^{-1} (575 K). The first excited states are found at 1.10 cm^{-1} (1.58 K), 4.37 cm^{-1} (6.28 K) and 3.47 cm^{-1} (4.99 K), for **2$_{\wedge}$-Ho**, **4$_{\wedge}$-Ho** and **4$_{-}$-Ho**, respectively. This is interesting, as the two lowest m$_J$-states are much closer in energy as observed for example in **1-Pr** and **4-Pr**. Nevertheless, the energy gap between the two states is still significantly higher than for the pseudo-degenerate states of the Tb analogue **2-Tb** and **4-Tb**, where slow relaxation was observed. Especially the case of **2-Ho** is interesting, as the energy gap of 1.58 K is lower than the ambient temperature of 2 K. However, it appears, that the energy gap is still too high for the two states acting as a pseudo doublet, which can result in slow magnetic relaxation.

The samples of **2-Ho** and **4-Ho** have been tested for their photoluminescence properties at 3 K. Similar to what has been observed in the Pr(III)-analogue, Ho(III)-centered sensitized emission was not observed.

4.9 Magnetic and photophysical properties of the Er-analogues

Next to dysprosium-based compounds, Er(III) ions are among the most employed ions for synthesis of single-molecule magnets. Trivalent erbium ions posses the same total angular momentum as dysprosium ions of $J = 15/2$, however, their observed magnetic moment is lower than that of the ions Tb(III), Dy(III) and Ho(III), due to the lower gyromagnetic constant $g_J = 6/5$ of erbium. The shape of the electron density distribution is strongly prolate for Er(III), as discussed in section 2.2, therefore, equatorial ligand arrangements are beneficial for the observation of high energy barriers to slow magnetic relaxation.[56,119,120] Interestingly, since Dy(III)'s electron density distribution is characterized as oblate, often the Er(III) analogue of a high performance Dy(III)-SMM reveals a low energy barrier and vice versa. As a Kramers ion, Er(III) is guaranteed to possess doubly degenerate m_J states, resulting in the observation of slow relaxation being highly likely. The static DC magnetic response of the samples **2-Er** and **5-Er** was studied in the temperature range of 300 K to 2 K in an external field of 1000 Oe. The T-dependent $\chi_{mol}T$ is given in figure 4.39.

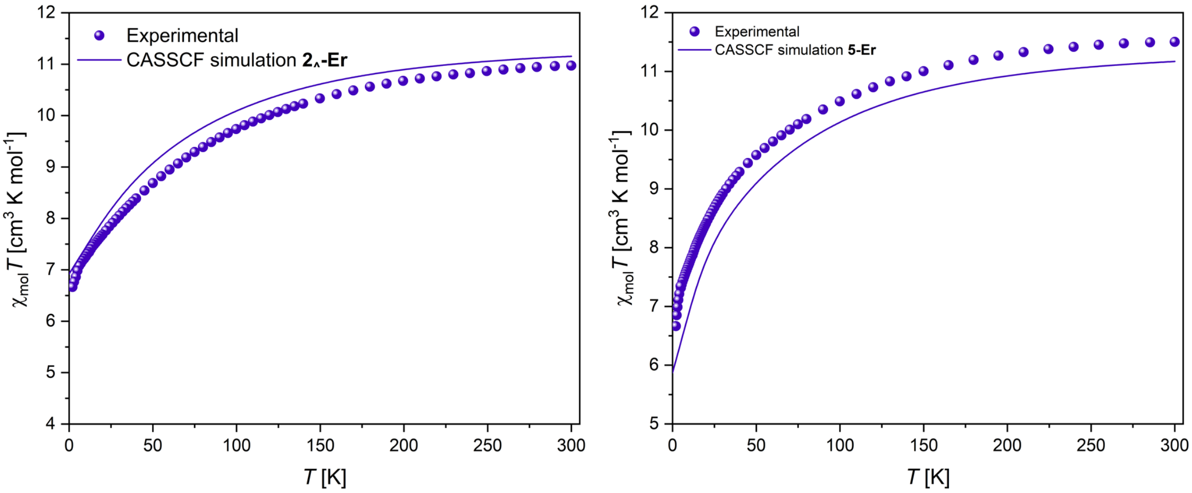

Figure 4.39: Temperature-product of the molar magnetic susceptibility vs. temperature for **2-Er** (left) and **5-Er** (right).

At room temperature the observed $\chi_{mol}T$ value is 10.97 cm^3 K mol^{-1} and 11.50 cm^3 K mol^{-1} for **2-Er** and **5-Er**, respectively. Both values are in good agreement with the theoretical value of 11.48 cm^3 K mol^{-1} for a single Er(III) ion. Simulations of the temperature dependency of $\chi_{mol}T$ obtained from CASSCF methods, predict slightly lower room temperature values around 11.00 cm^3 K mol^{-1}, which is in even better agreement with what is observed for **2-Er**. The observed value of **5-Er** being higher than the simulated value is most likely caused by solvent loss. As the structure of **5-Ln** revealed a single chloroform molecule that co-crystallizes as a lattice solvent. Loss of the lattice solvent upon drying would have resulted in the observation of a high $\chi_{mol}T$ value. Both samples show a smooth decrease of $\chi_{mol}T$ when cooling down, matching the simulated trends. No intermolecular interactions can be deduced, as the simulated and experimental shapes of the temperature-dependent curves compare well with one another. Testing the dynamic behaviour through AC susceptibility measurements, neither **2-Er** nor **5-Er** showed any signal in the out-of-phase component of the susceptibility that could be linked to slow magnetic relaxation. Under the application of an external field, a signal appeared and the optimal field was found to be 1000 Oe for **2-Er** and 1400 Oe for **5-Er**, respectively. The absence of any signal at zero field suggests efficient quantum tunnelling with the ground state Kramers doublet, allowing fast relaxation and, therefore, quenching zero-field SMM behaviour. The frequency-dependent in-phase and out-of-phase components of **2-Er** and **5-Er** are given in figure 4.40.

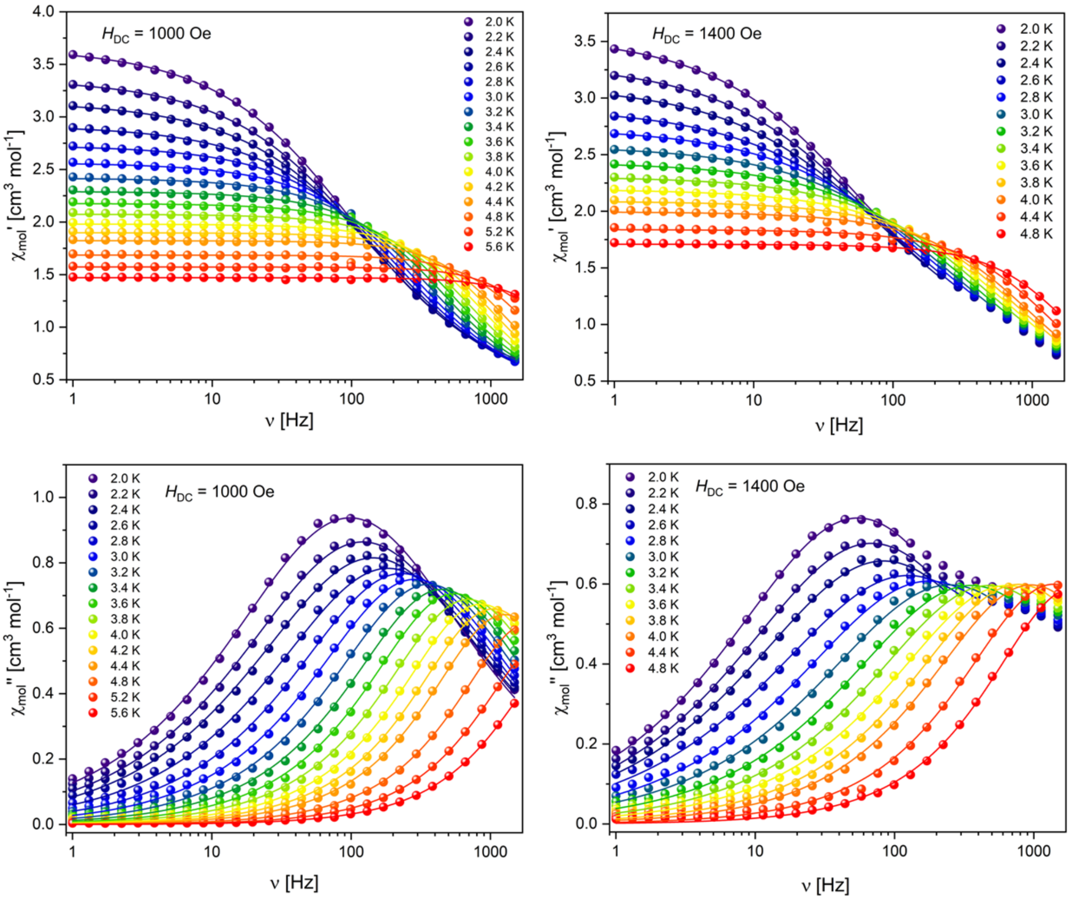

Figure 4.40: Frequency dependency of the in-phase (top) and out-of-phase (bottom) components of the magnetic susceptibility for **2-Er** (left) and **5-Er** (right). The solid lines are the best fits to a generalized Debye model.

Both samples reveal a single maximum in the out-of-phase component. For **2-Er** the χ'' maximum is observed around 100 Hz at the lowest temperature of 2 K. It decreases in intensity and slowly shifts to higher frequencies until 3 K, where the frequency shift gets more pronounced. This behaviour is typical for magnetic relaxation, that is dominated by Raman processes at low T and over-the-barrier and TA-QTM relaxation at higher T. At 4.8 K the maximum is observed at the highest observable frequency of 1500 Hz, however, good fits of the experimental data were obtained up to 5.6 K. Similarly, the experimental data of **5-Er** also reveals a single maximum located around 60 Hz at 2 K. The behaviour upon heating to higher temperatures is similar to **2-Er** with a slow frequency shift up to 2.8 K, signalling dominant Raman relaxation, and a stronger frequency shift starting at 3 K, suggesting Orbach-type relaxation. At 4.4 K the maximum is found at 1500 Hz and fits have been performed until 4.8 K. While the out-of-phase signal observed for **2-Er** is symmetric along the frequency axis, the data for **5-Er** decreases asymmetrically at higher frequencies. This is also visualized in the Cole-Cole plots for **2-Er** and **5-Er**, shown in figure 4.41.

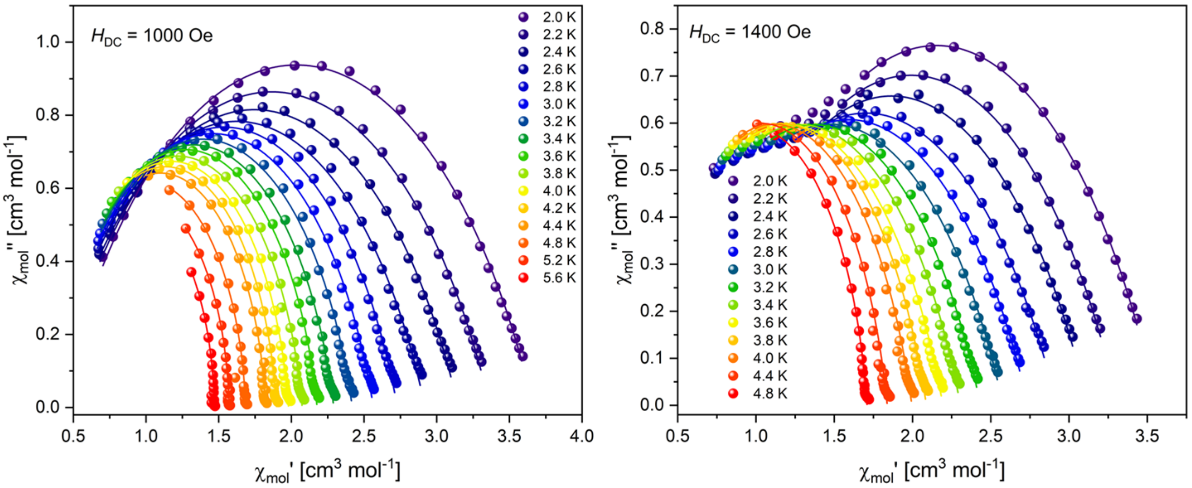

Figure 4.41: Cole-Cole plots for **2-Er** (left) and **5-Er** (right). The solid lines are the best fits to a generalized Debye model.

The same type of asymmetric behaviour has been observed for the neodymium complex of L_{Me}, **4-Nd**, while a second maximum has been observed for the dysprosium analogue, **4-Dy**. In **4-Dy** the two maxima can be analysed individually and, using that information alongside further *ab initio* characterization, be assigned to the two polymorphs **$4_{\wedge}$-Dy** and **4_{-}-Dy** (see section 4.7). Two polymorphs have also been observed in **4-Nd**, suggesting the asymmetric behaviour is a result of a second maximum outside of the frequency range, which is caused by one of the polymorphs (see section 4.4). Single-crystal measurements of **5-Er** have only resulted in the observation of a single molecular structure and arrangement. However, as mentioned previously, the powder diffraction patterns measured for several samples of **5-Ln** reveal reflections, that are not matching the simulated pattern for **5-Ln**. A second polymorph is, therefore, likely the origin of the asymmetric out-of-phase data observed for **5-Er**. Fits of the AC susceptibilities of **2-Er** and **5-Er** to a generalized Debye model have been performed. The α parameters obtained for **2-Er** range between 34% at 2 K and 3% at 5.6 K and for **5-Er** between 37% at 2 K and 13% at 4.8 K. The decrease in both cases indicates the onset of active Raman relaxation at low T.

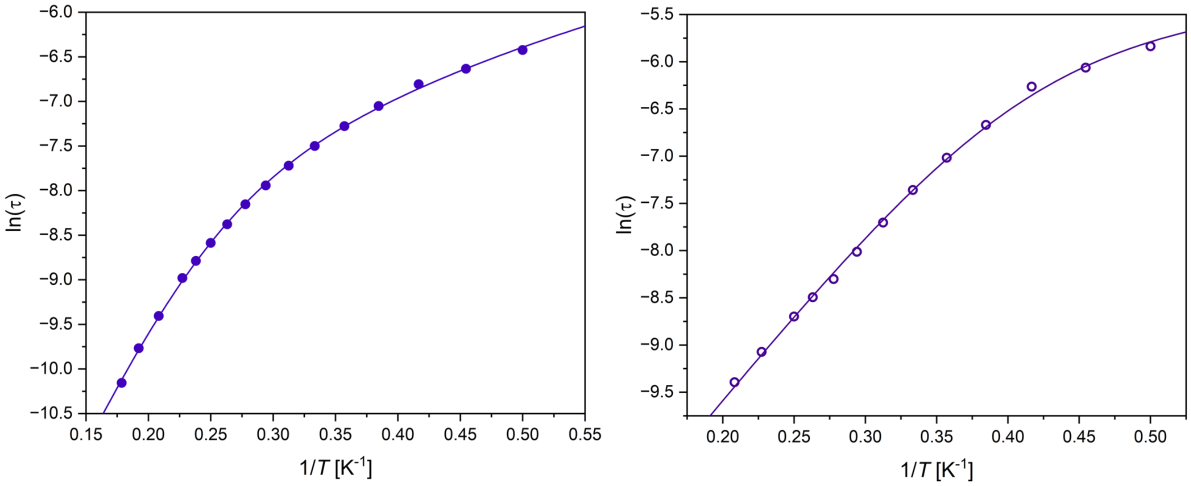

Figure 4.42: Arrhenius plots for **2-Er** (left) and **5-Er** (right).

The temperature-dependent relaxation times for **2-Er** were fitted obtaining good agreements employing Raman and Orbach relaxation processes. The best fits for **5-Er** were obtained using a combination of Direct and Raman relaxation. The best fit parameters for **2-Er** were $\tau_0 = 2.75 \text{ x } 10^{-7}$ s, $U_{eff} = 29.96$ K (20.83 cm^{-1}), C = 107.48 s K^{-n} and n = 2.47, while for **5-Er** $\tau_0 = 1.73 \text{ x } 10^{-6}$ s, $U_{eff} = 18.62$ K (12.95 cm^{-1}), A = 137.37 s K^{-1}. As it can be seen in figure 4.42 (right), the relaxation data for **5-Er** reveals only a small contribution of non-linear behaviour at low T. The choice of direct relaxation for the fitting procedure was based on test results employing Raman relaxation, which gave n parameters as low as 1, therefore, describing direct processes. It is possible, however, that the correct description would be Raman relaxation and good agreements might be obtainable, going to lower T, to obtain a wider range of datapoints for the fitting procedure. Both observed relaxation barriers are low when compared to other Er(III) SMMs reported in the literature,[119,120] most likely as a result of the low symmetry coordination environment around the erbium ion. Using *ab initio* CASSCF calculations, additional information about energetic structure of the ground state multiplet was gathered.

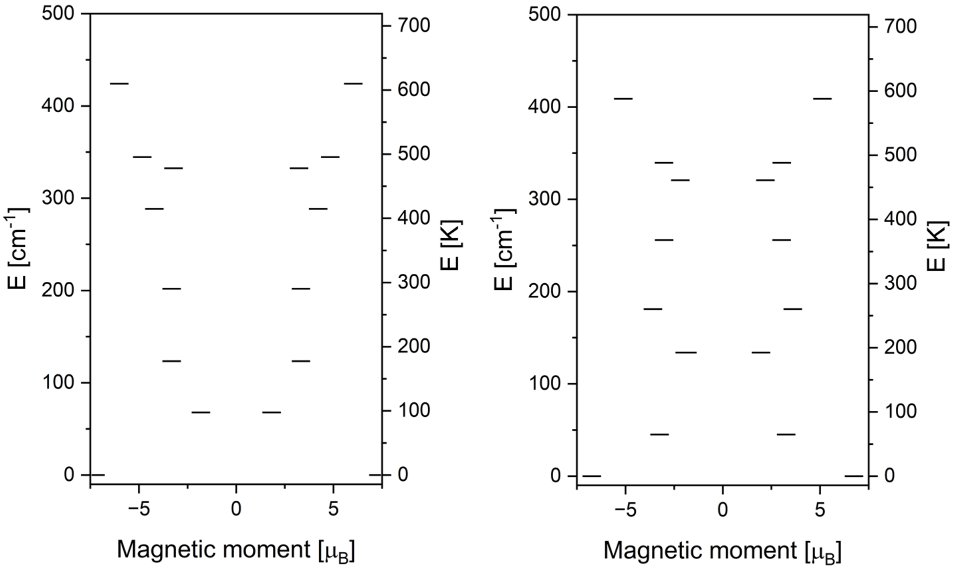

Figure 4.43: *Ab initio* energy diagram for **$2_\wedge$-Er** and **5-Er**.

Applying an effective spin half formalism for Er(III), with $J = 15/2$ and $g_J = 6/5$, gives an effective g-tensor with $g_x = g_y = 0$ and $g_z = 18$, in case of an idealized anisotropic $m_J = 15/2$ ground state doublet. The ground state doublet calculated for **$2_\wedge$-Er** is characterized with $g_x = 0.48$, $g_y = 0.76$ and $g_z = 14.85$, showing non-negligible transverse components of the g-tensor. Interestingly, the ground state's wavefunction is mainly $m_J = 13/2$, with admixing of other states (compare appendix), suggesting the coordination environment is not well suited for Er(III). For **5-Er** $g_x = 1.60$, $g_y = 1.86$ and $g_z = 13.48$ was found, showing even stronger transverse components than **$2_\wedge$-Er**. While the main component of the ground state's wavefunction for **5-Er** is $m_J = 15/2$, very strong admixing ($> 50\%$) is observed (compare appendix). The high transverse g_x and g_y components for **$2_\wedge$-Er** and **5-Er** are in good agreement with the absence of slow magnetic relaxation without the application of an external field, as transverse field promote quantum tunnelling between the two degenerate states of opposite magnetization. The calculated energies of the first excited doublet state are 97.68 K (67.93 cm^{-1}) and 64.93 K (43.15 cm^{-1}), for **$2_\wedge$-Er** and **5-Er**, respectively. Similar to what has been observed for the complexes of some of the other lanthanides, *vide supra*, the energy gap obtained from the calculation is significantly higher than the experimentally determined effective energy barrier. However, the *ab initio* predicted ratio between the barrier of **2-Er** and **5-Er** of 1.5 compares well to what was experimentally observed with 1.6.

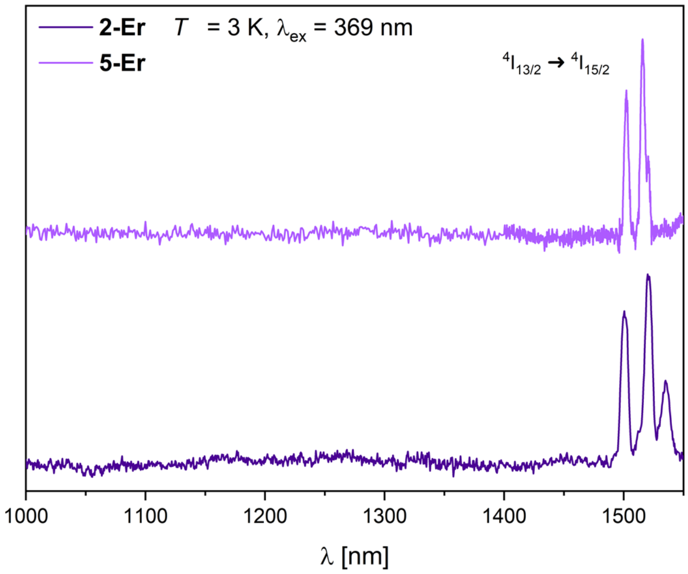

Figure 4.44: Emission spectra recorded at 3 K with $\lambda_{ex} = 369$ nm for **2-Er** and **5-Er**.

Photoluminescence measurements of **2-Er** and **5-Er** at 3 K revealed PL emission in the IR-region above 1490 nm.[77,121,122] This emission corresponds to the $^4I_{13/2} \rightarrow {}^4I_{15/2}$ transition of Er(III). The full emission band is not observable, due to the limitation of the detector's wavelength range to a maximum wavelength of 1550 nm. For both **2-Er** and **5-Er**, three individual emission lines are observed below the cutoff wavelength, allowing peak deconvolution analysis using OriginPro. Both spectra yield good fits employing three emission lines, as shown in figure 4.45.

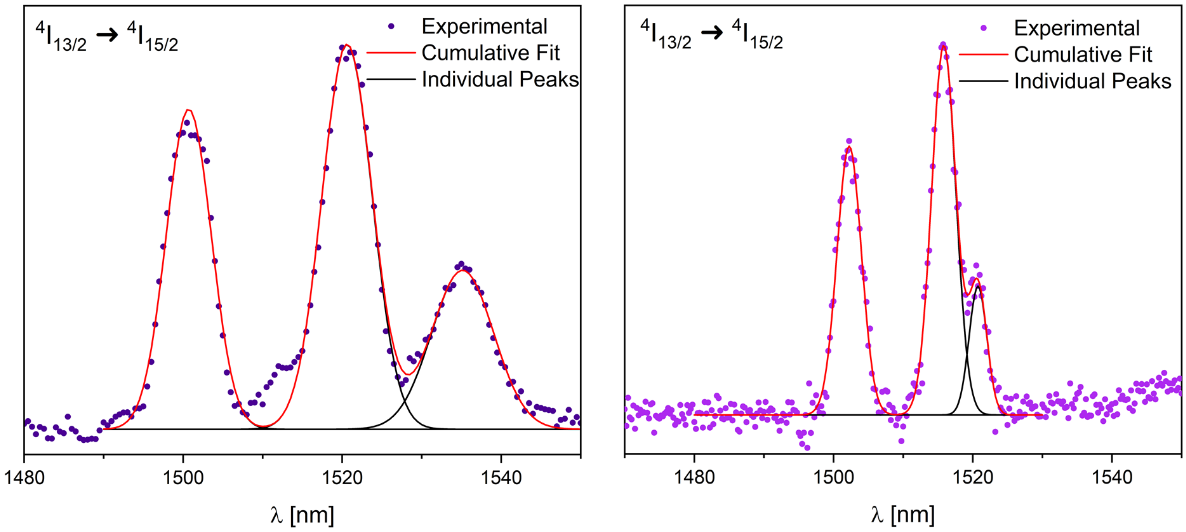

Figure 4.45: Peak deconvolution of the $^4I_{13/2} \rightarrow {}^4I_{15/2}$ transition for **2-Er** (left) and **5-Er** (right).

The highest energy emission line has been found at 1500.71 nm and 1502.25 nm, for **2-Er** and **5-Er** respectively. The peak positions translate to an energy gap between the $^4I_{15/2}$ and $^4I_{13/2}$ states of 6663.52 cm^{-1} and 6656.68 cm^{-1}, respectively. As the highest energy transition is linked to the ground state doublet, the two emission peaks observed at lower energies correspond to the first and second excited Kramers doublet. For **2-Er** the deconvolution gave the peak positions 1520.62 nm and 1535.14 nm, which translates to an energy separation of 87.24 cm^{-1} and 149.47 cm^{-1}. For **5-Er**, the determined peaks are found at 1515.83 nm and 1520.74 nm, corresponding to energies of the excited KDs of 59.64 cm^{-1} and 80.95 cm^{-1}. Interestingly, the *ab initio* energies of the first excited Kramers doublets, underestimate the experimentally observed energy, which is in line with what has been observed for the complexes of other lanthanides discussed in this thesis. For the second excited state, however, the calculation of **5-Er** overestimates the energy by more than 50 cm^{-1}, while for **2-Er**, the calculated energy is still underestimating the experiment. A sudden shift in a trend like this appears unlikely, instead the third peak observed in the emission spectrum of **5-Er**, is likely a result of a second polymorph, as it it also suggested by PXRD and SQUID measurements. The emission peak corresponding to the third excited state of **5-Er** is found at higher wavelengths, which would match the calculated energy, assuming an underestimation, as generally observed.

4.10 Magnetic and photophysical properties of the Tm-analogues

As thulium is the rarest of the REE, studies of Tm(III) complexes are also not commonly reported in the literature. The ground state resulting from SOC for Tm(III) is $^4H_6$, with a gyromagnetic constant of $g_J = 7/6$. With that Tm(III) exhibits a relatively strong magnetic moment, however, due to the non-Kramers nature of trivalent thulium ions, reports of Tm(III)-based SMMs are rare.[92,105] The temperature dependence of the magnetic susceptibilities of **2-Tm** and **5-Tm** was measured in an external field of 1000 Oe upon cooling the samples from room temperature to 2 K. Figure 4.46 shows the recorded behaviour.

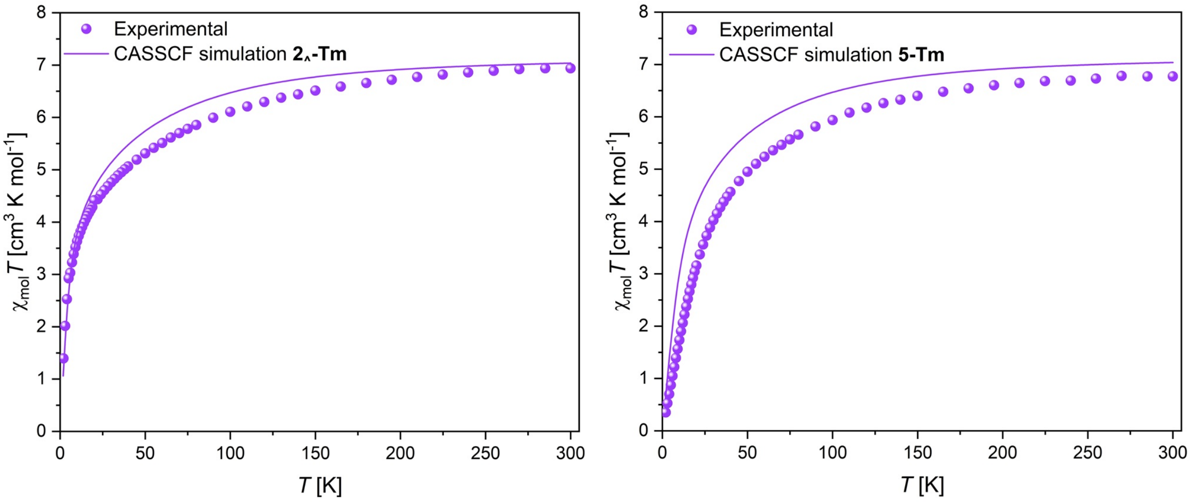

Figure 4.46: Temperature-product of the molar magnetic susceptibility vs. temperature for **2-Tm** (left) and **5-Tm** (right).

At room temperature the $\chi_{mol}T$ values have been found at 6.94 cm^3 K mol^{-1} for **2-Tm** and 6.77 cm^3 K mol^{-1} for **5-Tm**, respectively. Both values are in good agreement with the value predicted by Curie's law of 7.17 cm^3 K mol^{-1} for a single Tm(III) ion. Upon cooling, the observed $\chi_{mol}T$ values decrease increasingly strong reaching the lowest value of 1.41 cm^3 K mol^{-1} and 0.33 cm^3 K mol^{-1} at 2 K, for **2-Tm** and **5-Tm**, respectively. Generally, $\chi_{mol}T$ values close to zero can suggest the presence on antiferromagnetic interactions between neighbouring Ln(III) ions. For both samples, the experimentally determined behaviour is in good agreement with the simulations obtained from *ab initio* CASSCF calculations, especially in the low temperature region. Therefore, the strong decrease of the experimental $\chi_{mol}T$ value can be assigned fully to the intrinsic depopulation of Stark levels without any measurable contribution of magnetic coupling. In order to probe the samples for SMM characteristics, dynamic AC susceptibility measurements have been performed. Neither sample revealed an observable signal in $\chi''_{mol}(\nu)$ at zero field, as well as under the application of an external magnetic field. As described in section 3, the coordination that is exerted by the pyrazole-substituted phenanthroline and the three nitrate ligands is highly asymmetric. With that, the ZFS induced by the ligand field is unlikely to yield degeneracy of the ground state, as it is not a guaranteed property, similar to Kramers ions. To further validate this assumption, CASSCF calculations have been performed on the molecular structures of **2_Λ-Tm** and **5-Tm**. The energy splitting of the spin-orbit coupled ground state is shown in figure 4.47.

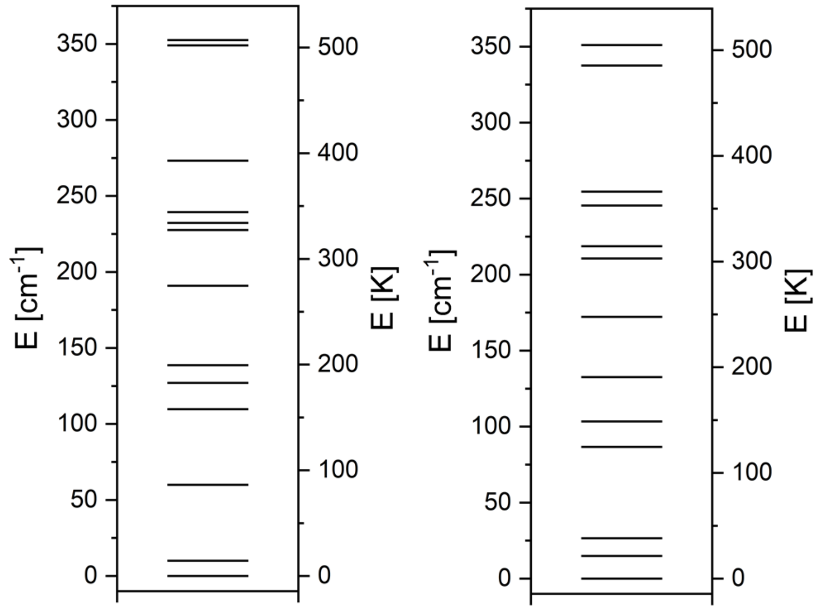

Figure 4.47: *Ab initio* energy diagram for **2_Λ-Tm** and **5-Tm**.

Matching the expectations derived from magnetic measurements, no pseudo degeneracy of the ground state is observed for either complex **2_Λ-Tm** or **5-Tm**. The energy splitting observed between the ground state and the first excited state are 9.98 cm^{-1} (14.35 K) for **2_Λ-Tm** and 14.97 cm^{-1} (21.53 K) for **5-Tm**, respectively. The whole multiplet is split across an energy range of approximately 350 cm^{-1} (500 K), for both complexes (figure 4.47). Based on the information obtained from the Tb(III) and Ho(III) analogues, an energy gap > 1 cm^{-1} between the ground and first excited state appears to be too high for the observation of slow relaxation, therefore, the calculated energy states agree well with the experimental results.

Photoluminescence measurements of the microcrystalline samples **2-Tm** and **5-Tm** were performed at 3 K, using excitation at $\lambda_{ex} = 369$ nm. The recorded emission spectra are given in figure 4.48 (left).

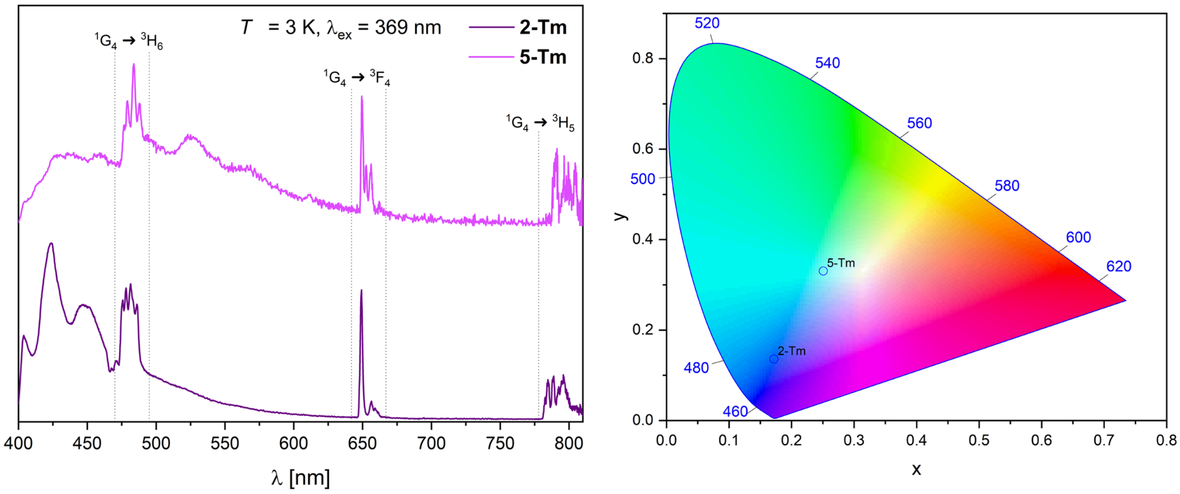

Figure 4.48: Emission spectra recorded at 3 K with $\lambda_{ex} = 369$ nm for **2-Tm** and **5-Tm** (left) and chromaticity diagram (right).

Each recorded emission spectrum reveals three characteristic bands around 480 nm, 650 nm and 790 nm. The bands correspond to the $^1G_4 \rightarrow {}^3H_6$, $^1G_4 \rightarrow {}^3F_4$ and $^1G_4 \rightarrow {}^3H_5$ transitions of Tm(III), respectively.[123] For **2-Tm**, the experimentally determined branching ratios are 45.27%, 19.67% and 35.05%, for $^1G_4 \rightarrow {}^3H_6$, $^1G_4 \rightarrow {}^3F_4$ and $^1G_4 \rightarrow {}^3H_5$, respectively. Interestingly, while the blue $^1G_4 \rightarrow {}^3H_6$ transition is dominant for **2-Tm**, for **5-Tm** the red $^1G_4 \rightarrow {}^3H_5$ transition is dominant with a branching ratio of 43.72%. For the $^1G_4 \rightarrow {}^3H_6$ and $^1G_4 \rightarrow {}^3F_4$ transitions in **5-Tm**, branching ratios of 35.52% and 20.77% were obtained. All three observed transitions are electric dipole transitions and it has been shown, that the ratio between the blue $^1G_4 \rightarrow {}^3H_6$ and the red $^1G_4 \rightarrow {}^3H_5$ transitions increases with lower symmetry.[124,125] This is in good agreement with the calculated CShM values of 3.247 (C_{2v}) for **$2_{\wedge}$-Tm** and 2.483 (C_{2v}) for **5-Tm**. Despite the Tm(III) centered emission, relatively strong ligand emission is also observed for **2-Tm**, less for **5-Tm**. The higher branching into the blue transition as well as the observed ligands fluorescence shift the emission colour of **2-Tm** strongly into the blue region, while the emission colour observed for **5-Tm** is better characterized between cyan and white (figure 4.48, right). Performing peak deconvolution analysis using OriginPro, single emission lines corresponding to each m_J-states can be obtained. The highest energy $^1G_4 \rightarrow {}^3H_6$ transition can be simulated employing ten individual lines for **2-Tm**. Interestingly, for **5-Tm**, the recorded data only allows deconvolution into four separate peaks. Considering the coordination sphere's low symmetry, up to 13 lines can be observed. The position of the highest energy peak corresponds to the energy gap between the observed energy difference between the $^1G_4$ excited and the $^3H_6$ ground state. The energies found are 21111.15 cm^{-1} and 20993.82 cm^{-1}, for **2-Tm** and **5-Tm**, respectively. The energy range of the zero field split ground multiplet correspond to the energy difference of the two outermost peaks of the deconvolution procedure, which is obtained as 620.53 cm^{-1} for **2-Tm** and 496.37 cm^{-1} for **5-Tm**, respectively. The experimentally determined energy ranges are significantly higher than the predicted ranges from CASSCF calculations of 352.63 cm^{-1} and 351.10 cm^{-1}, for **2-Tm** and **5-Tm**, respectively. This observation is in good agreement with what has been observed for the complexes of the other lanthanides of the series. The obtained peak positions and energies obtained from peak deconvolution analysis are shown in figure 4.49 and table 4.8.

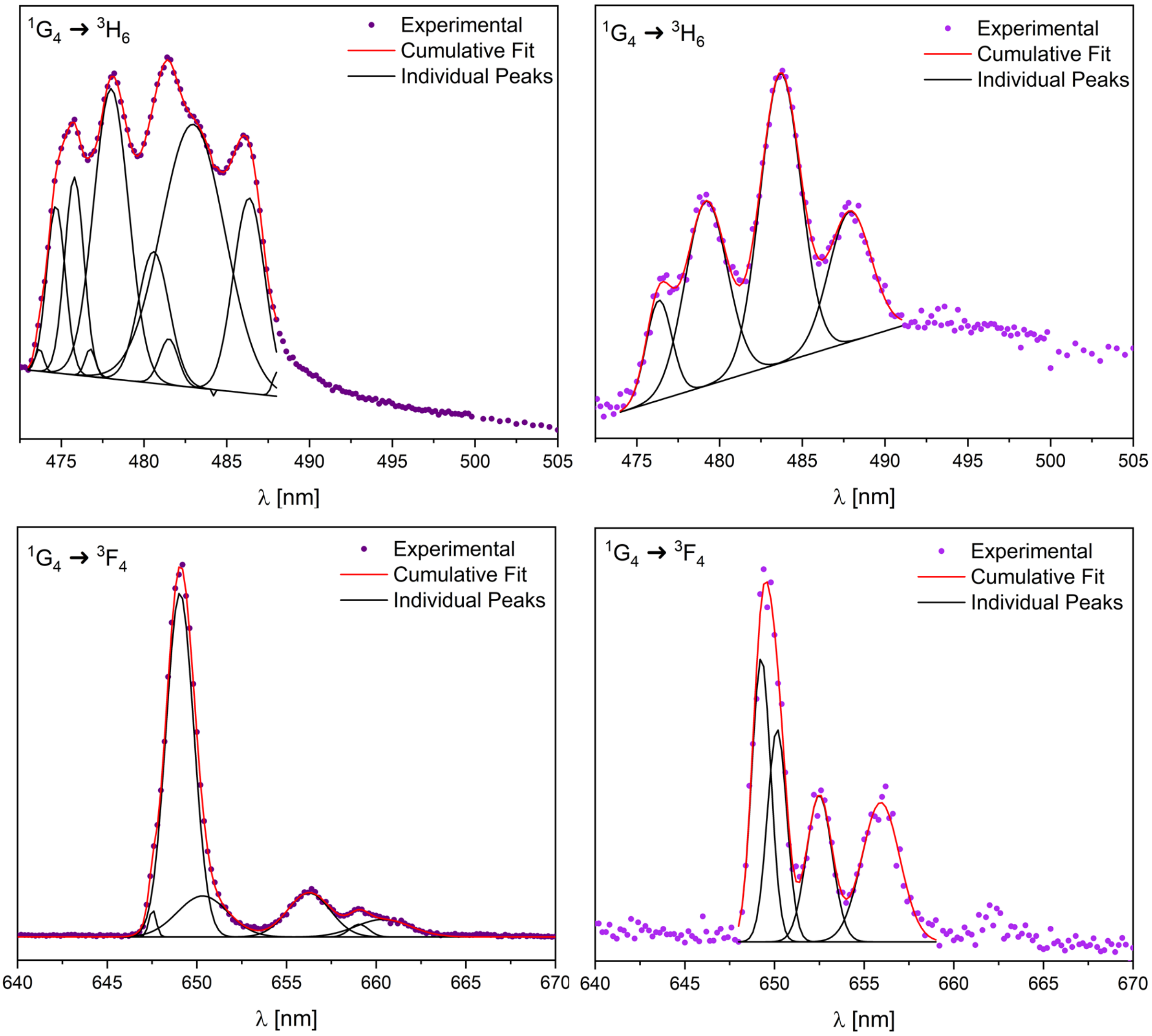

Figure 4.49: Peak deconvolution of the $^1G_4 \rightarrow ^3H_6$ and $^1G_4 \rightarrow ^3F_4$ transitions for **2-Tm** (left) and **5-Tm** (right).

Table 4.8: Experimental peak positions obtained from peak deconvolution for **2-Tm** and **5-Tm**. The energetically lowest state is given as the absolute value of the transition, all other energies are given as relative values.

peak	**2-Tm**		**5-Tm**	
$^1G_4 \rightarrow ^3H_6$	peak position [nm]	energy [cm^{-1}]	peak position [nm]	energy [cm^{-1}]
1	473.68	21111.15	476.33	20993.82
2	474.68	44.16	479.18	124.96
3	475.79	93.30	483.68	318.85
4	476.75	135.71	487.87	496.37
5	478.01	191.20		
6	480.58	302.98		
7	481.50	342.89		
8	482.96	405.67		
9	486.36	550.07		
10	488.03	620.53		
$^1G_4 \rightarrow ^3F_4$	peak position [nm]	energy [cm^{-1}]	peak position [nm]	energy [cm^{-1}]
1	647.53	15443.32	649.26	15402.06
2	649.05	36.30	650.15	20.88
3	650.33	66.41	652.50	76.33
4	656.24	205.06	655.93	156.48
5	659.05	269.98		
6	660.39	300.79		

4.11 Magnetic and photophysical properties of the Yb-analogues

The heaviest element of the lanthanides with a paramagnetic trivalent ion is ytterbium, with the $^2F_{7/2}$ ground state of Yb(III). Coordination complexes of Yb(III) have been reported to show slow magnetic relaxation as well as photoluminescent emission in the IR-region of the electromagnetic spectrum.[92,105,126] The temperature dependency of the magnetic response of samples of **3-Yb** and **5-Yb** has been measured in an external magnetic field of 1000 Oe upon cooling from room temperature to 2 K.

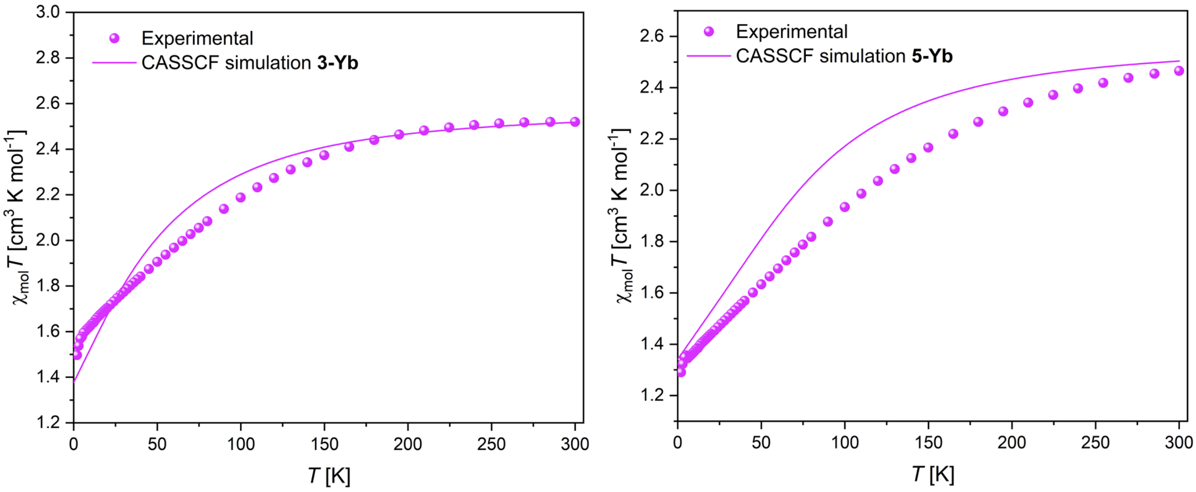

Figure 4.50: Temperature-product of the molar magnetic susceptibility vs. temperature for **3-Yb** (left) and **5-Yb** (right).

The obtained values of $\chi_{mol}T$ at 300 K are 2.52 cm^3 K mol^{-1} and 2.47 cm^3 K mol^{-1}, for **3-Yb** and **5-Yb**, respectively. Both are in very good agreement with the theoretically expected value of 2.57 cm^3 K mol^{-1} for a single Yb(III) ion at 300 K. The T-dependency of both samples is characterized by an almost horizontal behaviour down to 200 K, followed by a very steady decrease. A small drop is observed at 4 K, possibly due to weak intermolecular antiferromagnetic interactions. Comparison of the recorded behaviour to *ab initio* simulations of the susceptibility, shows an earlier, more steady decrease of the experimental data, while the low temperature and room temperature values are matching nicely. This gradual type of decrease has been reported for other Yb(III)-based compounds.[127] As it has been observed for the samples of the other Kramers ion complexes (except **2-Sm** and **4-Sm**), no out-of-phase signal was observed in the absence of an external magnetic field, but slow relaxation is observed once an external field is applied. The optimal fields were found at 1400 Oe, for both **3-Yb** and **5-Yb**. The in-phase and out-of-phase components of the magnetic susceptibility recorded at different temperatures are given in figure 4.51.

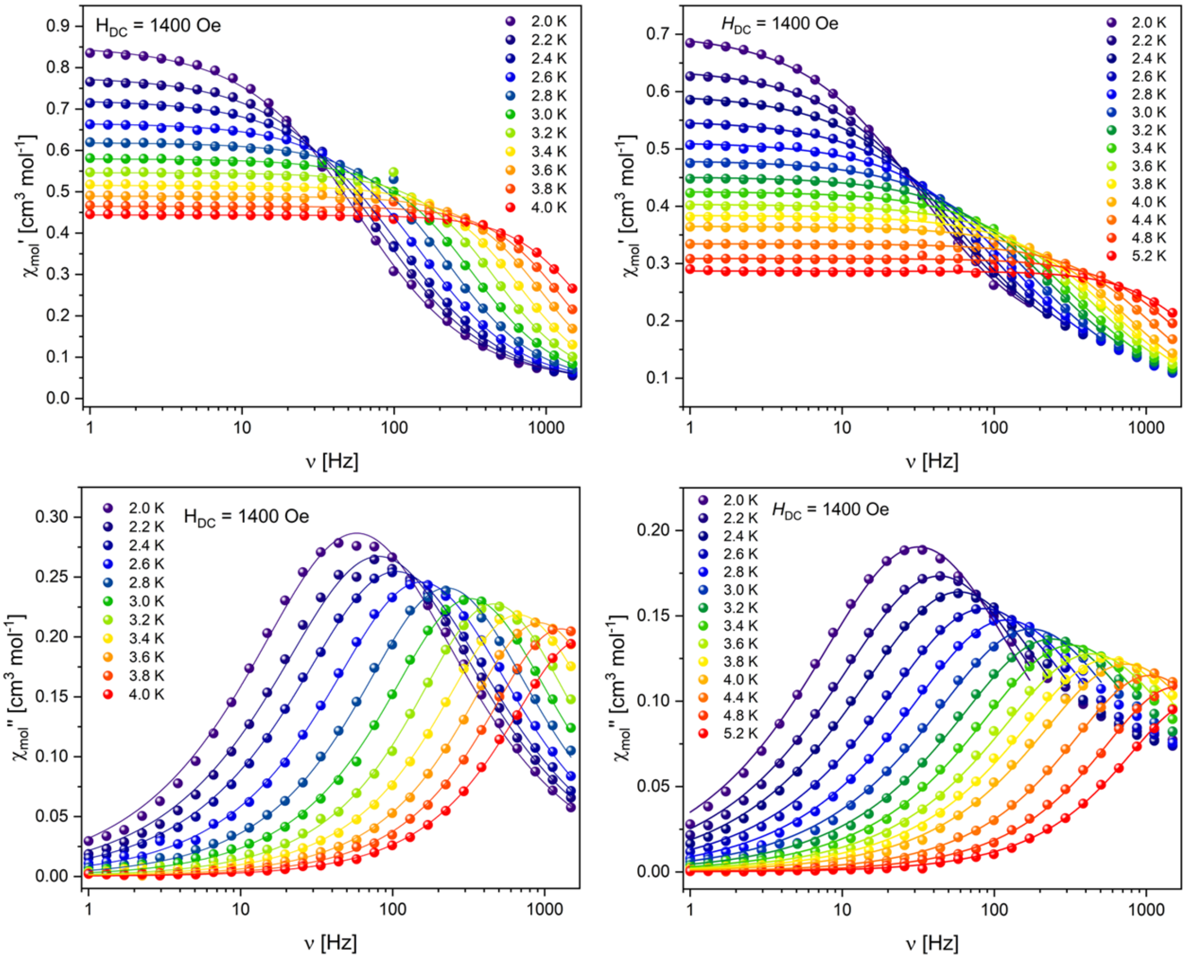

Figure 4.51: Frequency dependency of the in-phase (top) and out-of-phase (bottom) components of the magnetic susceptibility for **3-Yb** (left) and **5-Yb** (right). The solid lines are the best fits to a generalized Debye model.

The AC susceptibility data of **3-Yb** show a single relaxation maximum in the out-of-phase component. It is observable in a temperature range from 2 K to 4 K, shifting from 60 Hz to 1500 Hz in the process. For **5-Yb** a single maximum is also observed, located around 30 Hz at 2 K. The highest observable frequency of 1500 Hz is reached at 4.8 K. Both datasets suggest Raman relaxation at low T, due to a visible change in the intensity of the frequency shift. Comparable to what has been observed in **5-Er**, the AC signal recorded for **5-Yb** is not symmetric, showing unexpectedly high values at frequencies above the maximum. Likely, this is a consequence of a second polymorph, as suggested by the powder X-ray diffraction data (see section 3.3). A second polymorph of **5-Yb** with a different relaxation behaviour, outside of the observable frequency window leads to such behaviour. The Cole-Cole plots give a proper visual representation, showing the symmetric and asymmetric behaviour of **3-Yb** and **5-Yb**, respectively.

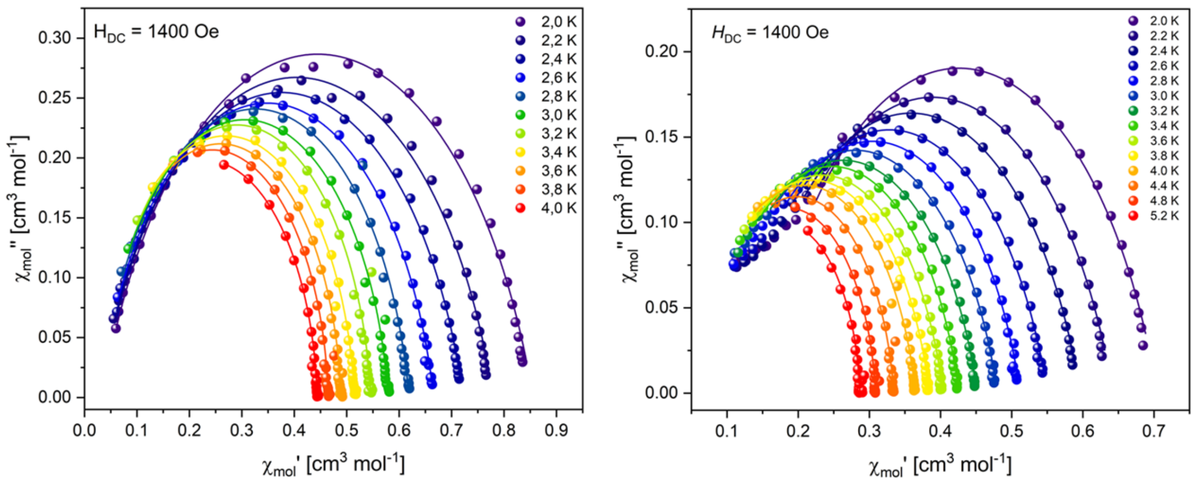

Figure 4.52: Cole-Cole plots for **3-Yb** (left) and **5-Yb** (right). The solid lines are the best fits to a generalized Debye model.

The distribution of active magnetic relaxation mechanisms is characterized by the α parameters obtained from fits to a generalized Debye model. The α values obtained for **3-Yb** are found between 22% at 2 K and 4% at 4 K, signalling pure Orbach-type relaxation at higher T, with other processes, most likely Raman, active at low T. A very comparable distribution is obtained for **5-Yb**, with α parameters ranging from 24% at 2 K to 5% at 5.2 K. The temperature-dependent relaxation times $\tau(T)$ obtained from the Debye fits were fit using equation 2.11, employing Raman- and Orbach-type relaxation mechanisms.

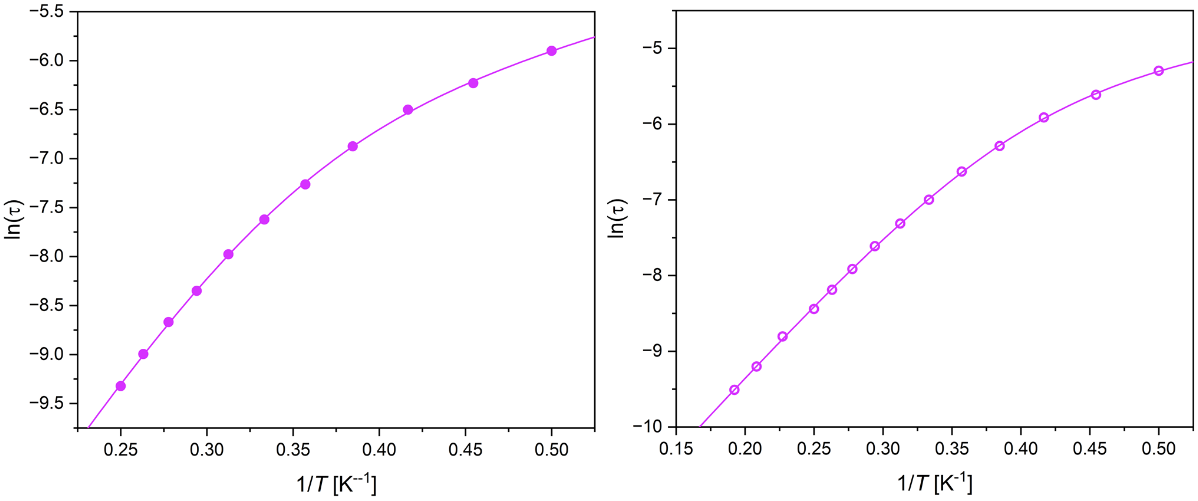

Figure 4.53: Arrhenius plot for **3-Yb** (left) and **5-Yb** (right).

The fitting yielded the relaxation parameters τ_0 = 1.62 x 10^{-7} s, U_{eff} = 26.24 K (18.25 cm^{-1}), C = 55.28 s K^{-n}, and n = 2.68 for **3-Yb** and τ_0 = 1.68 x 10^{-6} s,

U_{eff} = 20.03 K (13.93 cm^{-1}), C = 57.32 s K^{-n}, and n = 1.60 for **5-Yb**, respectively. Both complexes show very comparable relaxation behaviours, which is understandable, as the structural resemblance is very high between **3-Ln** and **5-Ln**. The observed energy barrier is in good agreement, with what is commonly reported for Yb(III) based SMMs, for which relaxation below the energy of the first excited state has been reported.[127] In order to further validate this, CASSCF calculations have been performed, yielding the energetic finestructure of the ground state multiplet.

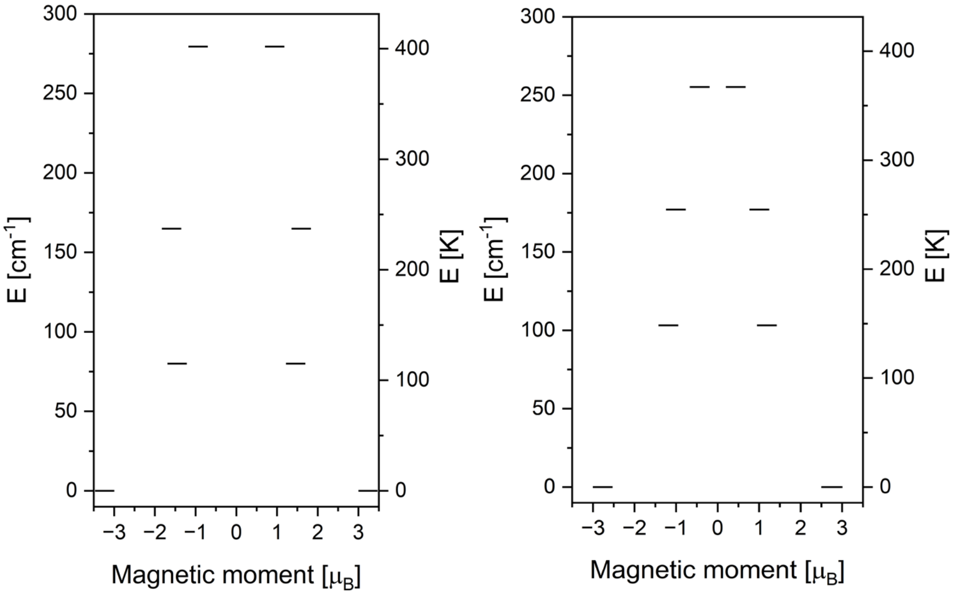

Figure 4.54: *Ab initio* energy diagram for **3-Yb** and **5-Yb**.

The calculated g-tensor of the ground state doublet for **3-Yb** shows strong transverse components with $g_x = 0.62$, $g_y = 0.99$ and $g_z = 6.53$. In comparison a purely axial $m_J = 7/2$ ground state would be characterized by $g_x = g_y = 0$ and $g_z = 8$. The transverse components are even stronger for **5-Yb**, with $g_x = 1.54$, $g_y = 3.16$ and $g_z = 5.23$. Both ground state wavefunctions, therefore, show significant admixing of $m_J = 3/2$, allowing efficient tunnelling within the doublet, which is the reason no slow magnetic relaxation is observed in the absence of an external DC field, that lifts the degeneracy. The energies that are obtained for the first excited KD state, are 115.04 K (80.00 cm^{-1}) and 148.42 K (103.22 cm^{-1}), for **3-Yb** and **5-Yb**, respectively. Both energies are much higher than the observed energy barriers for magnetic relaxation, which is however, in agreement with what has been observed in the literature as well as for the analogues of other lanthanides. Interestingly, the energy separation towards the first excited state is estimated higher for **5-Yb** than for **3-Yb**, while the experimental effective energy barrier is higher for **3-Yb**. This is most likely a result of the stronger transverse components of the g-tensor for **5-Yb** and the admixing of other m_J-states. As the relaxation is not expected to follow a path overcoming the barrier to the first excited state, the stronger transverse components for **5-Yb** allow more efficient under-the-barrier relaxation, which has been observed for Yb(III) before[127] and leads to the lower observed energy barrier.

Similar to Er(III), Yb(III) is supposed to show a single photoluminescent emission band in the IR region.[126,127] The emission is related to the $^2F_{5/2} \rightarrow ^2F_{7/2}$ transition of Yb(III). Photoluminescence spectroscopy measurements were performed on samples of **3-Yb** and **5-Yb** at 3 K, with an excitation wavelength of 369 nm.

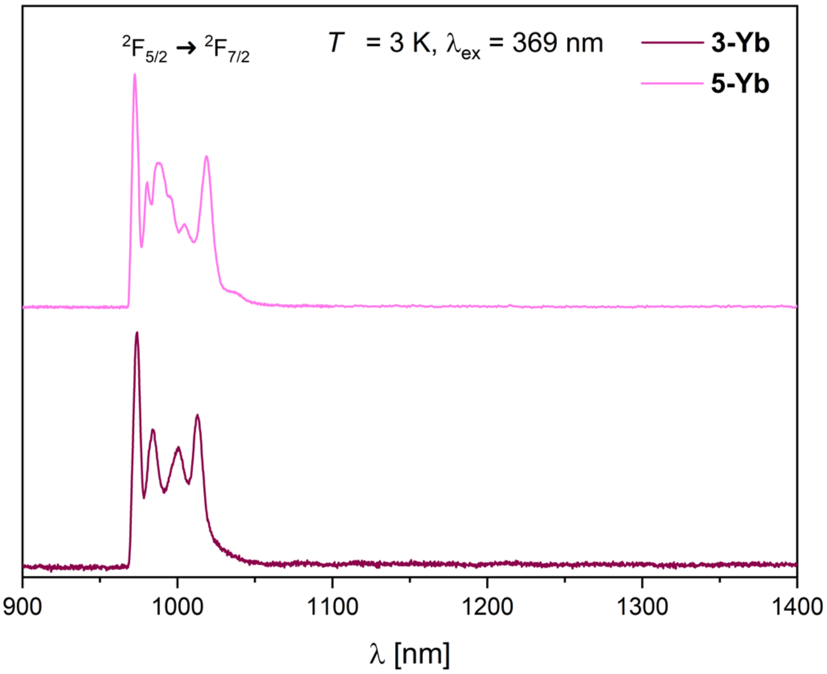

Figure 4.55: Emission spectra recorded at 3 K with λ_{ex} = 369 nm for **3-Yb** and **5-Yb**.

As expected, a single emission band is observed between 960 nm and 1050 nm (figure 4.55), corresponding to $^2F_{5/2} \rightarrow ^2F_{7/2}$. For **3-Yb** the transition is very clearly composed of four distinct lines, while more and less resolved lines are observed for **5-Er**. The shape of the transition can easily be deconvoluted using OriginPro, employing four emission peaks (figure 4.56, left). The first emission peak is found at 973.68 nm, which corresponds to an energy gap between $^2F_{7/2}$ and $^2F_{5/2}$ of 10270.34 cm^{-1}. Choosing the first emission as a relative zero energy line, the peak positions for the following peaks of 983.77 nm, 999.79 nm and 1013.67 nm translate to relative energies of the first, second and third excited Kramers doublet of 105.37 cm^{-1}, 267.96 cm^{-1} and 405.15 cm^{-1}, respectively. As observed previously, the energies obtained from the *ab initio* calculations are 80.00 cm^{-1}, 164.96 cm^{-1} and 279.47 cm^{-1}, significantly lower than the experimental values. As mentioned for the comparison of the calculated energy separation with the effective barrier to magnetic relaxation, proper comparison is not possible, as under-the-barrier relaxation is expected.

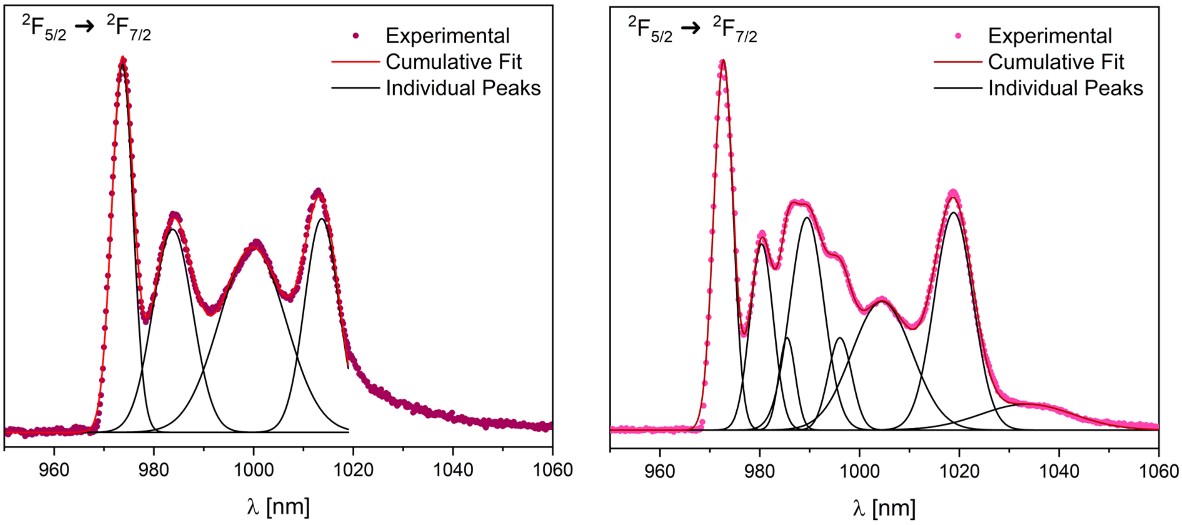

Figure 4.56: Peak deconvolution of the $^2F_{5/2} \rightarrow {}^2F_{7/2}$ transition for **3-Yb** (left) and **5-Yb** (right).

In case of **5-Yb**, eight individual emission lines were necessary to obtain a good fit to the experimental data. The position of the peaks are found at 972.71 nm, 980.37 nm, 985.48 nm, 989.46 nm, 996.07 nm, 1004.49 nm, 1018.85 nm and 1033.55 nm, respectively. As inferred from powder X-ray diffraction, AC susceptibility measurements and the observations for **5-Er**, a second polymorph is expected to be present in the sample of **5-Yb**. The overlap of the two species gives rise to the eight lines. Investigation of the peak shapes, the intensities and the relative spacing between the peaks, allows further interpretation of the emission data. As **5-Yb** is structurally related to **3-Yb**, the emission spectra are expected to show resemblance. The fitted peaks 1, 4, 6 and 7 (from left to right), properly match the relative intensities and the energy spacing observed for **3-Yb**. On top, their intensities are generally higher than those of the other four lines, which is in line with what is expected when **5-Yb** is the dominant species in the sample. Under this assumption the relative energies obtained for **5-Er** are 174.00 cm^{-1}, 325.21 cm^{-1} and 465.52 cm^{-1}, which is in good agreement to the calculated energies of the KDs of 0 cm^{-1}, 103.22 cm^{-1}, 177.12 cm^{-1} and 255.31 cm^{-1}, respectively, assuming underestimation of the calculation. Taking the second emission peak of the deconvolution analysis as the relative zero energy of the four remaining peaks, the KD energies related to a second polymorph are found at 0 cm^{-1}, 52.87 cm^{-1}, 160.75 cm^{-1} and 524.82 cm^{-1}, respectively.

5 Ln(III) complexes as coherent light-matter interfaces

5.1 Sensitized emission of the Eu-analogues

While magnetically mostly uninteresting due to the ground state showing spin-orbit coupled $J = 0$, Eu(III)-based solid-state materials and molecular complexes have been widely employed as emissive materials in optical components.[46,63,128,129] They show intense emission across the visible spectrum with lifetimes that are significantly higher than those observed for other Ln(III) ions. With this in mind, the low temperature photoluminescence properties of polycrystalline samples of **2-Eu** and **4-Eu** have been probed at 3 K using $\lambda_{ex} = 369$ nm.

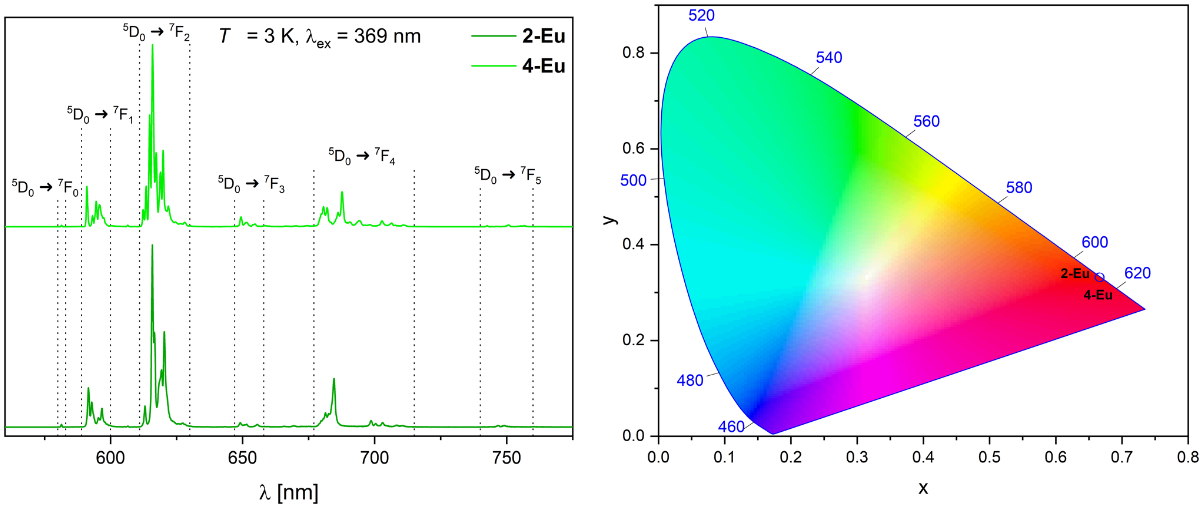

Figure 5.1: Emission spectra recorded at 3 K with $\lambda_{ex} = 369$ nm for **2-Eu** and **4-Eu** (left) and chromaticity diagram (right).

The emission spectrum of each complex reveals six emission bands (figure 5.1, left) that can be assigned to the $^5D_0 \rightarrow {}^7F_J$ transitions, with J = 0, 1, 2, 3, 4 and 5.[63] The experimentally determined branching ratios are 0.20%, 13.28%, 62.49%, 2.25%, 20.41% and 1.37% for the $^5D_0 \rightarrow {}^7F_J$, J = 0, 1, 2, 3, 4 and 5 transitions of **2-Eu**, respectively. In comparison, the branching ratios observed for **4-Eu** are more intense in the deep red emission region of the $^5D_0 \rightarrow {}^7F_3$ and $^5D_0 \rightarrow {}^7F_4$ transitions, while the more orange $^5D_0 \rightarrow {}^7F_1$ and $^5D_0 \rightarrow {}^7F_2$ transitions show slightly lower ratios. The overall observed ratios of **4-Eu** are 0.11%, 11.73%, 61.31%, 3.40%, 22.32% and 1.13% for the $^5D_0 \rightarrow {}^7F_J$, J = 0, 1, 2, 3, 4 and 5 transitions, respectively. The branching ratio describes a more deep red emission for **4-Eu**, however, the resulting chromaticity coordinates are nearly unchanged between **2-Eu** and **4-Eu** (figure 5.1, right). In both recorded spectra the

$^5D_0 \rightarrow {}^7F_0$ transition is observable with low intensities. This is in good agreement with the low symmetry coordination environment observed from single-crystal X-ray diffraction studies (distorted C_{2v} for all polymorphs of **2-Eu** and **4-Eu**), as this transition is generally only observable in C_n, C_{nv} and C_s symmetries.[63] The hypersensitive $^5D_0 \rightarrow {}^7F_2$ electric dipole transition is also a good measure for the symmetry of Eu(III)-complexes. Both transitions $^5D_0 \rightarrow {}^7F_0$ and $^5D_0 \rightarrow {}^7F_2$ show slightly higher relative contributions to the overall emission in **2-Eu** over **4-Eu**, which matches the higher CShM value of 3.520 for **$2_\wedge$-Eu** over 2.802 and 2.532 observed for **$4_\wedge$-Eu** and **$4_\_$-Eu**, respectively. Interestingly, the highest symmetry polymorph is **$2_\_$-Eu** with a CShM value of 1.600, suggesting that **$2_\wedge$-Eu** is more abundant in the sample, matching the powder X-ray diffraction data (see section 3.2). Figure 5.2 shows the position and energy splitting observed for the highest energy $^5D_0 \rightarrow {}^7F_0$ and $^5D_0 \rightarrow {}^7F_1$ transitions.

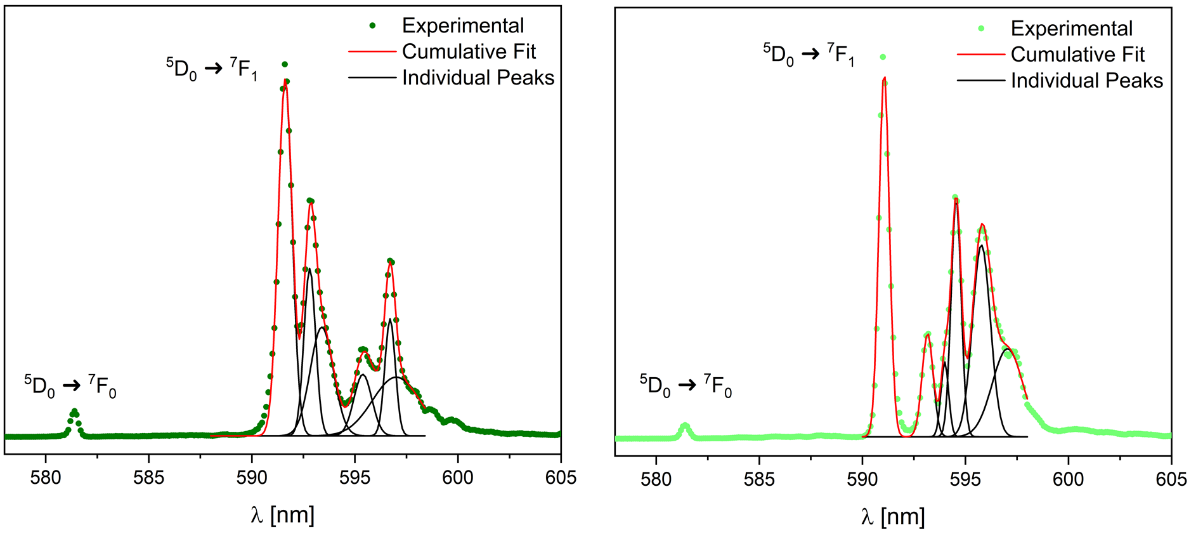

Figure 5.2: Peak position of the $^5D_0 \rightarrow {}^7F_0$ transition and peak deconvolution of the $^5D_0 \rightarrow {}^7F_1$ transition for **2-Eu** (left) and **4-Eu** (right).

The $^5D_0 \rightarrow {}^7F_0$ emission peak is observed around 581 nm for both samples **2-Eu** and **4-Eu** (figure 5.2), corresponding to an energy gap towards the excited $^5D_0$ level of 17212 cm^{-1}. As the energy position of the $^5D_0$ state is mostly determined by spin-orbit coupling and only marginally influenced by the chemical environment of the Eu(III) ion, it is expected that only a single peak is observed despite the presence of two polymorphs, as the resolution of the spectrometer cannot resolve the small energy differences. On the other hand, performing peak deconvolution analysis for the $^5D_0 \rightarrow {}^7F_1$ transition, resulted in good fits employing six individual emission lines. As Eu(III) is a non-Kramers ion, the degeneracy of the $J = 1$ multiplet is lifted, giving three individual lines corresponding to the m_J = -1, 0 and 1 states. Therefore, six observed lines are in good agreement with the presence of the two polymorphs $\mathbf{2}_{\wedge}$**-Eu**/$\mathbf{2}_{\_}$**-Eu** and $\mathbf{4}_{\_}$**-Eu**/$\mathbf{4}_{\_}$**-Eu**. Peak deconvolution analysis was also performed to obtain fits of the $^5D_0 \rightarrow ^7F_2$, $^5D_0 \rightarrow ^7F_3$ and $^5D_0 \rightarrow ^7F_4$ transitions (figure 5.3)

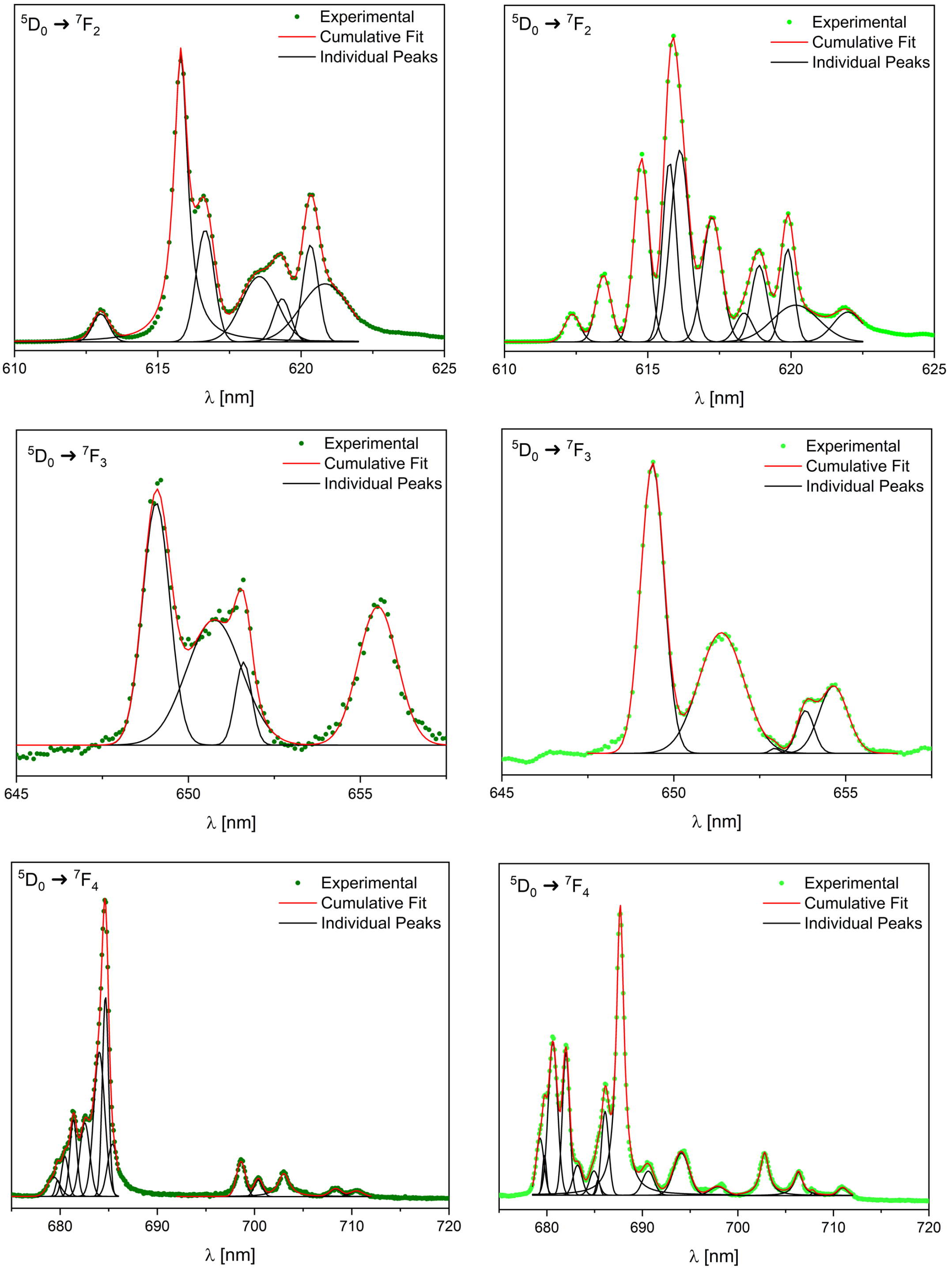

Figure 5.3: Peak deconvolution of the $^5D_0 \rightarrow ^7F_J$, $J = 2, 3, 4$ transitions for **2-Eu** (left) and **4-Eu** (right).

To obtain good fits of the $^5D_0 \rightarrow ^7F_2$ band, seven individual peaks have been employed for **2-Eu** and ten for **4-Eu**, although an additional broad peak was added to account for a high background (figure 5.3, top). Ten lines are the maximum theoretical amount of lines, obtained from two polymorphs with $J = 2$ multiplets being split into five states. The $^5D_0 \rightarrow ^7F_3$ transition was adequately fitted using four and five emission lines for **2-Eu** and **4-Eu**, respectively. The unexpectedly low number of employed peaks is a result of the low intensity of the transition. Finally, the $^5D_0 \rightarrow ^7F_4$ transition has been fitted employing 13 lines for **2-Eu** and 15 lines for **4-Eu**. Considering two molecular configurations and the splitting of the $J = 4$ state, gives a maximum number of observable lines of 18, being in agreement with the experimental results. The peak positions can be translated into the energy of the given transition and using the highest energy line of each multiplet as a reference, the relative energy splitting of the multiplets can be obtained. The results of the peak deconvolution of **2-Eu** and **4-Eu** are gathered in table 5.1.

The excited state lifetimes $T_{1,opt}$ of **2-Eu** and **4-Eu** have been analysed using fluorescence decay measurements at 3 K and $\lambda_{ex} = 369$ nm. Figure 5.4 shows the measured optical decays of **2-Eu** and **4-Eu**. The intensity vs. time plots depicted in figure 5.4 reveal that the decay processes are monoexponential in nature. Performing a single-exponential fit gives the observed lifetimes $T_{1,opt} = 1.425$ ms for **2-Eu** and 1.457 ms for **4-Eu**. The obtained lifetimes are in good agreement to optical lifetimes that are typically observed for Eu(III), usually in the μs to ms region.[46,80,128,130,131]

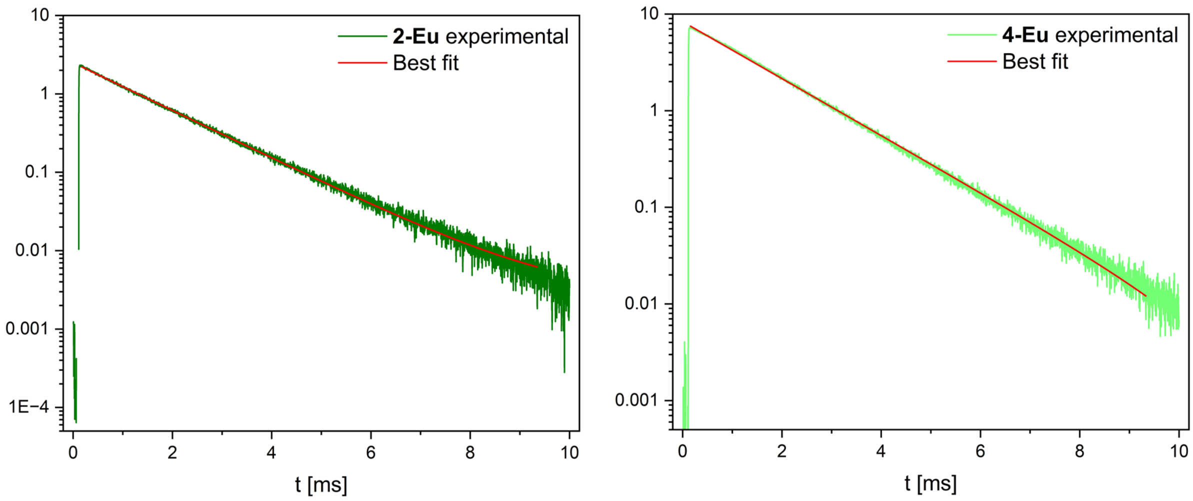

Figure 5.4: Emission decay measurements for **2-Eu** (left) and **4-Eu** (right).

Table 5.1: Experimental peak positions obtained for **2-Eu** and **4-Eu**. The energetically lowest state is given as the absolute value, all other energies as relative values.

peak	**2-Eu**		**4-Eu**	
$^5D_0 \rightarrow ^7F_1$	peak position [nm]	energy [cm^{-1}]	peak position [nm]	energy [cm^{-1}]
1	591.62	16902.83	591.06	16918.87
2	592.81	33.96	593.16	60.16
3	593.39	50.55	594.00	83.74
4	595.38	106.95	594.55	99.35
5	596.70	144.09	595.77	133.99
6	597.00	152.41	597.04	169.58
$^5D_0 \rightarrow ^7F_2$	peak position [nm]	energy [cm^{-1}]	peak position [nm]	energy [cm^{-1}]
1	613.01	16312.93	612.37	16330.125
2	615.80	73.98	613.45	28.89
3	616.65	96.35	614.78	64.18
4	618.54	145.94	615.76	89.94
5	619.34	166.64	616.12	99.56
6	620.33	192.41	617.24	129.06
7	620.84	205.63	618.36	158.32
8			618.89	172.10
9			619.88	198.06
10			621.99	252.68
$^5D_0 \rightarrow ^7F_3$	peak position [nm]	energy [cm^{-1}]	peak position [nm]	energy [cm^{-1}]
1	649.06	15406.79	649.38	15399.31
2	650.75	39.95	651.38	47.37
3	651.60	60.05	652.93	83.75
4	655.51	151.51	653.83	104.76
5			654.64	123.833
$^5D_0 \rightarrow ^7F_4$	peak position [nm]	energy [cm^{-1}]	peak position [nm]	energy [cm^{-1}]
1	679.33	14720.39	679.28	14721.40
2	679.75	20.12	679.75	10.10
3	680.49	25.17	680.63	29.16
4	681.37	44.00	682.00	58.60
5	682.53	69.12	683.21	84.71
6	684.02	101.04	685.36	130.53
7	684.66	114.68	686.10	146.17
8	685.39	130.09	687.68	179.75
9	698.60	406.14	690.61	241.53
10	700.38	442.41	694.08	313.84
11	703.02	496.10	697.89	392.50
12	708.35	603.09	702.80	492.60
13	710.48	645.41	706.34	563.92
14			707.84	593.54
15			710.97	656.11

As discussed in section 2.3, the observed optical lifetimes $T_{1,opt} = \tau_{obs}$ are a result of radiative and non-radiative decay processes. The rate constants for the radiative (k_r) and non-radiative (k_{nr}) decay are described by:[80,130]

$$k_r = \frac{1}{\tau_{rad}} \tag{5.1}$$

$$k_{nr} = \frac{1}{\tau_{obs}} - k_r \tag{5.2}$$

Where the radiative lifetime τ_{rad} can be estimated using the inverse relative intensity of the magnetic dipole $^5\text{D}_0 \rightarrow ^7\text{F}_1$ transition ($\frac{I_{tot}}{I_{MD}}$), the spontaneous emission probability of the $^5\text{D}_0 \rightarrow ^7\text{F}_1$ transition in vacuum ($A_{MD} = 14.65\ \text{s}^{-1}$) and the refractive index (n) of the medium using:[132]

$$\tau_{rad} = \frac{1}{A_{MD} \cdot n^3 \cdot \frac{I_{tot}}{I_{MD}}} \tag{5.3}$$

Assuming $n = 1.5$ for a solid state sample and employing the experimentally determined $\frac{I_{tot}}{I_{MD}}$ and τ_{obs}, equations 5.1, 5.2 and 5.3 yield the parameters $\tau_{rad} = 2.686$ ms, $k_r = 372.3\ \text{s}^{-1}$ and $k_{nr} = 329.5\ \text{s}^{-1}$ for **2-Eu**. For **4-Eu** the obtained parameters are $\tau_{rad} = 2.371$ ms, $k_r = 421.8\ \text{s}^{-1}$ and $k_{nr} = 264.5\ \text{s}^{-1}$. For both compounds **2-Eu** and **4-Eu** the observed rate constants are higher for the radiative over the non-radiative decay. The ratio between the radiative and non-radiative decay is, however, significantly larger for **4-Eu** than for **2-Eu**. This is a result of the methyl-substitution of the ligand in **4-Eu**, moving the closest C-H vibrator to the central Eu(III) ion further away. Although, the introduction of methyl-groups increases the amount of present C-H vibrators, however, the increased distance towards the Eu(III) ion seems to outweigh the effect of having additional C-H vibrations.

Measurements of the quantum yield have been performed, leading to the observation of an overall quantum yield Φ_{tot} of 33 % for **2-Eu** and 38 % for **4-Eu**. The observable quantum yield can be derived as the product of the intrinsic quantum yield of the Eu(III) (Φ_{Eu}) and the sensitization efficiency of the ligand (η_{sens}), while the intrinsic quantum yield is the ratio between τ_{obs} and τ_{rad}:

$$\Phi_{tot} = \Phi_{Eu} \cdot \eta_{sens} \tag{5.4}$$

$$\Phi_{Eu} = \frac{\tau_{obs}}{\tau_{rad}} \tag{5.5}$$

Following equations 5.4 and 5.5, Φ_{Eu} is found at 53 % and 61 % for **2-Eu** and **4-Eu**, respectively. The obtained value of η_{sens} is approximately 62 % for both **2-Eu** and **4-Eu**.

An almost same η_{sens}-value obtained for both complexes is in very good agreement, to the hypothesis of the sensitization and the luminescence properties of the ligand being solely phen-based. The sensitization occurs in both systems following the same mechanism, with near identical parameters (also indicated by the similar excitation wavelengths between all samples **2-Ln** and **4-Ln**), while the Eu(III)-based decay is notably influenced by the (dimethyl-)pyrazole groups. The sensitization efficiency of a system depends on the energy transfer occurring from the ligand onto the central metal ion. An energy gap between 2500 cm^{-1} and 3500 cm^{-1} has been proposed to be optimal for the sensitization of Eu(III).[80] The energy of the europium's $^5D_0$ state has been found at 17212 cm^{-1} for both **2-Eu** and **4-Eu**, *vide supra*, while the ligands triplet state energy was determined by investigation of **2-Gd** and **4-Gd**, giving 19231 cm^{-1} for L_H and 19048 cm^{-1} for L_{Me} (see section 4.1). With that, the energy gap between the triplet state energy and the energy of the excited $^5D_0$ state is determined at 2019 cm^{-1} and 1836 cm^{-1} for **2-Eu** and **4-Eu**, respectively. The energy separation is slightly lower than what has been termed as ideal, justifying the obtained sensitization efficiencies η_{sens} of 62 %. The experimentally determined and derived parameters discussed are gathered in table 5.2.

Table 5.2: Experimentally determined and derived luminescence parameters for **2-Eu** and **4-Eu**.

	2-Eu	**4-Eu**
τ_{obs} [ms]	1.425	1.457
τ_{rad} [ms]	2.686	2.371
k_r [s^{-1}]	372.3	421.8
k_{nr} [s^{-1}]	329.5	264.5
Φ_{tot} [%]	33	38
Φ_{Eu} [%]	53	61
η_{sens} [%]	62	62

5.2 Spectral hole burning studies of the Eu-analogues

Using a dye laser as the excitation source, measurements of the inhomogeneous linewidth and spectral hole burning experiments have been performed on the $^5D_0 \rightarrow ^7F_0$ transitions by Evgenij Vasilenko and Vishnu Unni of Prof. David Hunger's group. The samples were put in a ferrule coupled to optical fibres and cooled down to 4 K. For the polycrystalline sample of **2-Eu** a single excitation line centered at 580.9157 nm has been observed, matching the 581 nm peak observed from the standard PL studies described above. The inhomogeneous linewidth (Γ_{inh}) has been determined at 16.75 GHz for **2-Eu** (figure 5.5).

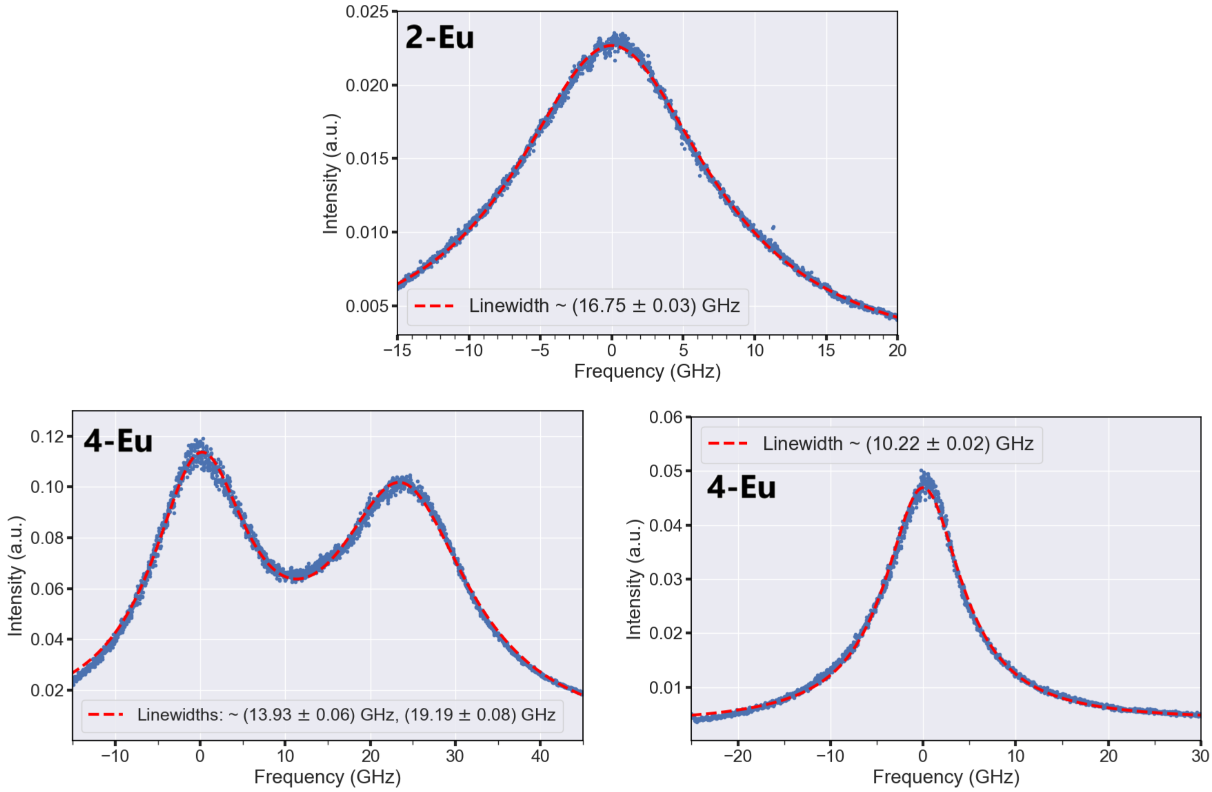

Figure 5.5: Inhomogeneous linewidths measured for **2-Eu** (top) and **4-Eu** (bottom).

For **4-Eu** two sets of excitation peaks have been observed. The first one revealed a double peak structure at 580.7639 nm and 580.7972 nm, while a single line at 580.9376 nm has been observed for the second one. Such multipeak behaviour has been reported for other compounds in the literature, indicating spectroscopically different Eu(III) sites featuring slightly different coordination environments.[80] The determined inhomogeneous linewidths are 19.19 GHz, 13.93 GHz and 10.22 GHz for the double and single peaks, respectively. The two separate inhomogeneously broadened lines observed for **4-Eu** are corresponding to the two polymorphs present in the sample. Interestingly, while two polymorphs for **2-Eu** have been observed crystallographically as well as spectroscopically, in the $^5D_0 \rightarrow ^7F_J$, $J \neq 0$ transitions, no second excitation line is observed for the laser excitation of $^5D_0 \rightarrow ^7F_0$. This could be a result of **2_-Eu** showing a less distorted coordination geometry, *vide supra*, leading to quenching of the $^5D_0 \rightarrow ^7F_0$ line. The widths of the inhomogeneous broadened lines observed are all between 10 GHz and 20 GHz, suggesting high crystallinity of the samples.

Performing SHB studies at every peak position, the observed experimental holewidth Γ_{hole} for **2-Eu** is 3.28 MHz, with **4-Eu** giving $\Gamma_{hole} = 6.69$ MHz, at the single peak (figue 5.6). The double peak position gave broader linewidths of $\Gamma_{hole} = 9.26$ MHz and 14.55 MHz for **4-Eu**. The spectral holes are a result of depopulation of one of the Eu(III)'s nuclear spin state, alongside overpopulation of the others. Following equations 2.13 and 2.14, the measured holewidth gives the homogeneous linewidth $\Gamma_h = 1.64$ MHz for **2-Eu**, $\Gamma_h = 3.35$ MHz for the single peak of **4-Eu** and $\Gamma_h = 4.63$ MHz and 7.28 MHz for the double peak of **4-Eu**. The obtained homogeneous linewidths translate to the optical coherence lifetimes $T_{2,opt} = 194$ ns for **2-Eu**, $T_{2,opt} = 95$ ns for the single peak of **4-Eu** and $T_{2,opt} = 69$ ns and 44 ns for the double peak of **4-Eu**, respectively.

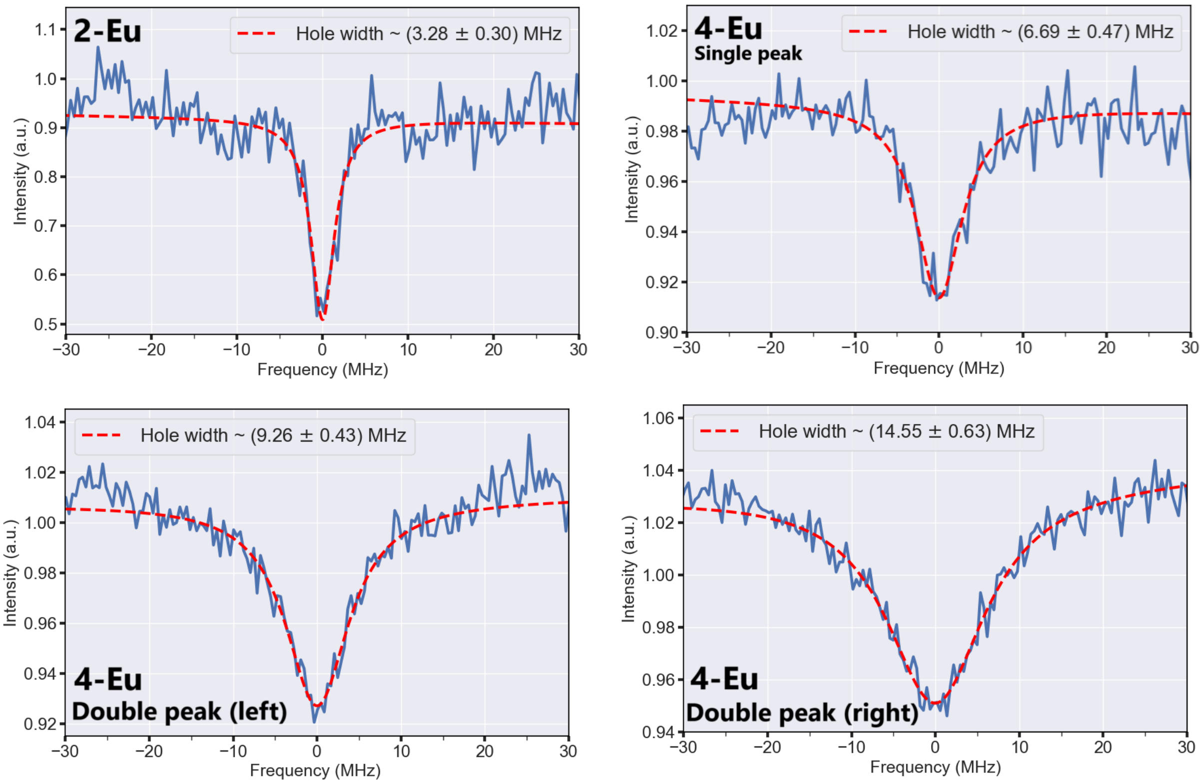

Figure 5.6: Spectral holes observed for **2-Eu** (left) and **4-Eu** (right).

As described earlier, the observed luminescence of **2-Eu** is related to the polymorph **2**$_{\Lambda}$**-Eu**. Based on the structural resemblance, the single peak observed for **4-Eu** is assigned to **4**$_{\Lambda}$**-Eu**, while the double peak correlates to **4**$_{-}$**-Eu**. Interestingly, the observed coherence lifetime of **4-Eu** is lower than the $T_{2,opt}$ observed for **2-Eu**, while $T_{1,opt}$ was almost identical between the two samples, even slightly longer for **4-Eu**. This means that for **4-Eu** the decoherence ($T_{2,d}$) is higher than for **2-Eu**. This is quite interesting, as the increased decoherence has to be related to the methylation of the ligand in **4-Eu**, possibly introduced by ion-ion interactions promoted by the different crystal packing of **4-Eu**.

The observed coherence lifetimes $T_{2,opt}$ for **2-Eu** and **4-Eu** of 194 ns and 95 ns, respectively, compare well with reported $T_{2,opt}$ values for other mononuclear Eu(III) complexes of 370 ns for $[\mathrm{Eu(BA)_4}]^-$ and 114 ns for [Eu(trensal)], obtained from SHB studies[76,80] (see section 2.3). Interestingly, while the observed coherence lifetimes $T_{2,opt}$ of **2-Eu** and **4-Eu** are within the same magnitude of those of $[\mathrm{Eu(BA)_4}]^-$ and [Eu(trensal)], the optical lifetimes $T_{1,opt}$, are significantly longer for **2-Eu** and **4-Eu**. This implies strong dephasing/decoherence is present for both complexes **2-Eu** and **4-Eu**. Nevertheless, the intrinsic homogeneous linewidths are still significantly narrower compared to those of the binuclear complex $[\mathrm{Eu_2(4\text{-}picNO)_6Cl_6}]$ showing 22 MHz, translating to $T_{2,opt} = 14.5$ ns.[65,80] This suggests that **2-Eu** and **4-Eu** could be pursued to establish coherent light-matter interfaces for QIP applications. The existence of two polymorphs is not problematic in this regard, as devices are based on single crystal arrangement. In order to lower the ion-ion interactions doping of Eu(III) complexes into a diamagnetic Y(III) analogue is necessary. As described in section 3.2 and 3.3, the Y(III) complexes are isostructural to the Eu(III) complexes, allowing studies using doped materials. The experimentally determined linewidths and related lifetimes are gathered in table 5.3.

Table 5.3: Experimentally determined optical linewidths for **2-Eu** and **4-Eu**.

	2-Eu	**4-Eu**, single peak	**4-Eu**, double peak	**4-Eu**, double peak
Γ_{inh} [GHz]	16.75	10.22	13.93	19.19
Γ_{hole} [MHz]	3.28	6.69	9.26	14.55
Γ_{h} [MHz]	1.64	3.35	4.63	7.28
$T_{2,opt}$ [ns]	194	95	69	44

5.3 Spectral hole burning studies of the Yb-analogues

As Yb(III) ions have also been proposed to be interesting candidates for QIP applications due to their emission in the near-IR region, the optical characteristics of the Yb(III) samples **3-Yb** and **5-Yb** have been tested by Jannis Hessenauer on the group of Prof. David Hunger, using laser excitation. The absorption scans measured at 4 K are shown in figure 5.7.

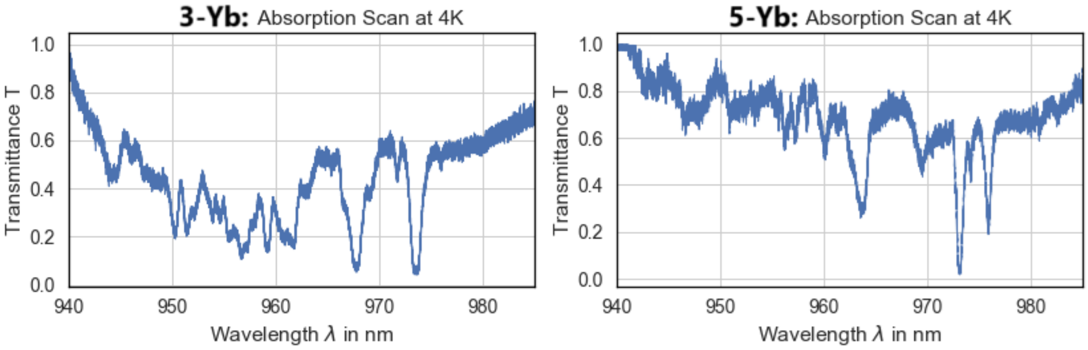

Figure 5.7: Absorption spectra for **3-Yb** (left) and **5-Yb** (right) measured at 4 K using a dye laser as the source of excitation.

At 4 K, only the ground state is expected to show notable population, therefore, three absorption lines would be expected for a single Yb(III) ion, corresponding to the $m_J = \pm 5/2, \pm 3/2$ and $\pm 1/2$ of the excited $^2F_{5/2}$ state. Both recorded spectra show a multitude of absorption lines (figure 5.7), which are related to different environments of the Yb(III) ions. Despite the expected polymorph for **5-Yb** (see sections 3.3 and 4.11), loss of the lattice solvent, could lead to a high number of crystal defects and slightly altered chemical environments. Using laser excitation, the optical lifetimes $T_{1,opt}$ of Yb(III) are accessible. Focusing on the lowest energy absorption peaks around 972 nm for **3-Yb** and 975 nm for **5-Yb**, an exponential emission decay is observed (figure 5.8).

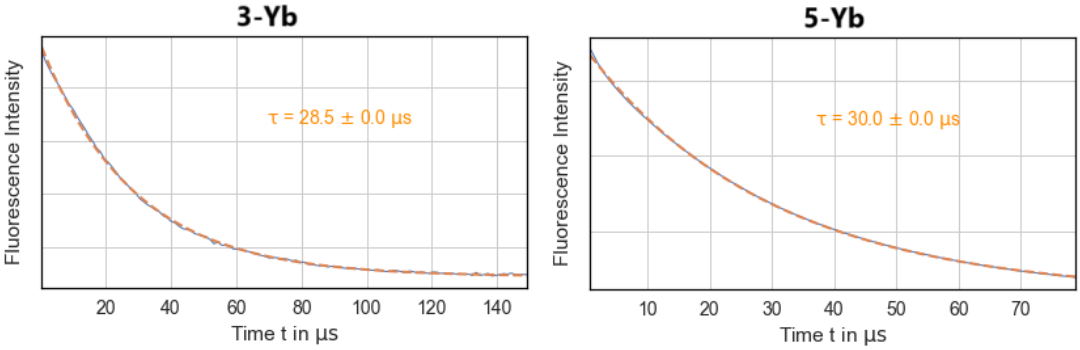

Figure 5.8: Emission decay profiles for **3-Yb** (left) and **5-Yb** (right) measured at 4 K using a dye laser as the source of excitation.

The related optical lifetimes of the $^2F_{5/2}$ state are $T_{1,opt} = 28.5$ μs for **3-Yb** and $T_{1,opt} = 30.0$ μs for **5-Yb**, respectively. Similar to the optical lifetimes obtained for **2-Eu** and **4-Eu**, the two complexes show very comparable lifetimes, with the lifetime of the methyl-substituted L_{Me}-based complex showing a slightly longer $T_{1,opt}$. The observed optical lifetimes are in good agreement with the lifetimes reported for other molecular Yb(III) compounds, typically in the order of tens of μs.[133–136] Longer lifetimes up to milliseconds have been observed for Yb(III)-doped solids.[137]

The inhomogeneous linewidth of **3-Yb** has been analysed, performing Lorentzian fits, as shown in figure 5.9. The different positions of the absorption spectra measured, have given inhomogeneous linewidths of 106 GHz, 366 GHz and 78 GHz at 971.5 nm, 973.3 nm and 975.7 nm, respectively. The observed lines are significantly broader than the lines observed for the Eu(III)-analogues (see section 5.2). The broad inhomogeneous lines are similarly a consequence of low crystallinity, most probably as a result of solvent loss upon drying.

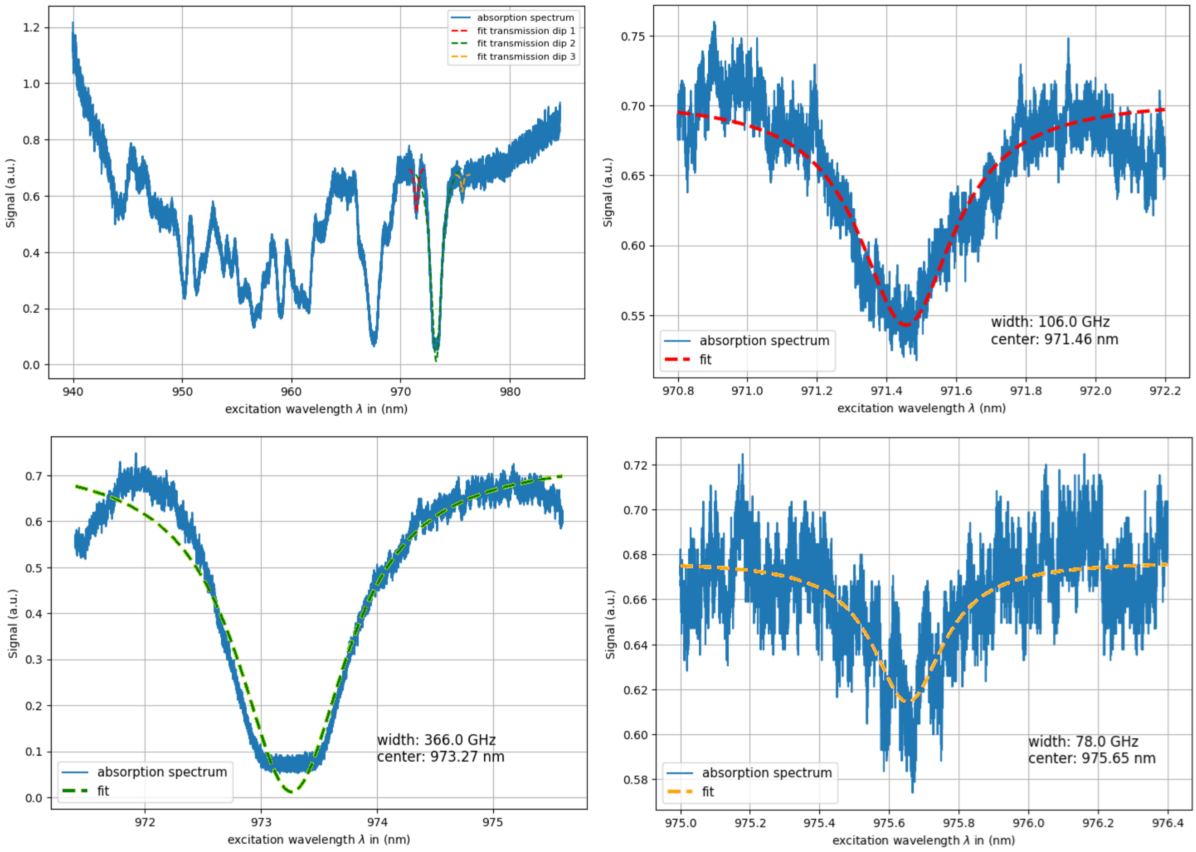

Figure 5.9: Inhomogeneous linewidths measured for **3-Yb**. Top right: Full absorption spectra referencing the single fits top right and bottom.

Spectral hole burning experiments have been performed on **3-Yb** and **5-Yb**, however, no spectral holes could be observed. This is a result of the spin relaxation ($T_{1,spin}$) being fast with respect to the pump rate of the laser excitation. As the transitions between the nuclear spin levels are occurring too fast, a depopulation of a specific energy level is not achieved. It should be noted here, that the samples have been prepared using natural abundant ytterbium, for which 70% of the Yb-isotopes have no nuclear spin. Therefore, the expected intensity of spectral hole would generally be weak. Isotopic enrichment could allow to overcome this problem. Very likely, the absence of any spectral holes for **3-Yb** and **5-Yb** is a consequence of the pure Yb(III) sample, where Yb-Yb interactions are too big, allowing for efficient transitions between the nuclear spin states. While magnetic analysis has shown that dipolar interactions are generally weak for **3-Yb** and **5-Yb**, the nuclear spin states are much more sensitive than those of the electronic spin. In order to observe SHB and narrow lines for **3-Yb** and **5-Yb**, doping of the materials into diamagnetic host materials is essential. As it has been shown in section 3.2 and 3.3, the Lu(III) analogues **3-Lu** and **5-Lu** can function as a well-suited host. It should be noted, that Lu(III) ions possess a nuclear spin $I_{nuc} = 7/2$, which is significantly higher than $I_{nuc} = 1/2$ for Y(III), which is normally used for dilutions studies. However, the Y(III)-analogues crystallize in different molecular structures (see section 3.2 and 3.3). The dilution into a Lu(III) matrix, could achieve the observation of spectral holes and slower dephasing, as the electronic spin $J = 7/2$ of Yb(III) is removed.

6 Concluding Remarks

Employing a pyrazole-substituted 1,10-phenanthroline ligand L_H as well as a dimethylpyrazole-substituted version L_{Me} for the complexation of trivalent rare earth ions resulted in the formation of complexes throughout the full lanthanide series. In total, 41 new complexes have been characterized using single-crystal X-ray diffraction techniques. The complexes have been obtained by slow diffusion of lanthanide nitrates into a solution of the ligand. All complexes share a general motif of a mer-type coordination, where the N_4-arrangement of the ligand occupies one meridian of the Ln(III) ion and three anionic nitrate ligands occupy the other.

For the non-methylated ligand L_H, the bigger Ln(III) ions La, Ce and Pr form eleven coordinate complexes, where the oxygen atom of an additional methanol molecule fills the coordination sphere of the Ln(III) ion. The intermediate lanthanide ions Y(III) and Nd(III) - Tm(III) are obtained as ten coordinate complexes with two different ligand arrangements. In one conformation the pyrazole groups of the ligand rotate in the same direction allowing the Ln(III) ion to enter the N_4-pocket, while the other conformation has the two pyrazole groups rotated in opposite directions, leading to the Ln(III) ion sitting on top of the N_4-arrangement. Analysis of the bond lengths revealed that the first conformation is creating a bigger coordination pocket, beneficial for the larger Ln(III) ions, while the second conformation is better suited for the smaller later lanthanides. Both described polymorphs of the Ln(III) complexes are observed for Eu(III) and Gd(III). The bigger ions Nd(III) and Sm(III) are exclusively forming the first described polymorph and the smaller ions Y(III) and Tb(III) - Tm(III) are exclusively found with the on-top mode of coordination. For the smallest Ln(III) ions Yb(III) and Lu(III), nine coordinate complexes are obtained, due to one of the nitrate ligands coordinating in a monodentate fashion, opposed to the bidentate mode observed for all other nitrate ligands throughout the series. Additionally a single molecule of chloroform is found per complex molecule as a lattice solvent.

The complexes obtained employing the methylated version of the ligand L_{Me} are forming ten coordinate complexes over the full lanthanide series. The complexes of Y(III) and La(III) - Ho(III) crystallized in two polymorphs, similar to what has been observed for the Eu(III) and Gd(III) analogues using L_H. Due to the added steric demand of the methyl-groups, the rotation observed is stronger than what has been observed for the non-methylated equivalents. Therefore, the conformation of the ligand with both dimethylpyrazole-groups rotated in the same direction leads to a pseudo helical arrangement of the complex. The second polymorph reveals a similar on-top type coordination as the non-methylated analogue, although more pronounced. Interestingly, the two polymorphs obtained from L_{Me} show almost identical sizes of the coordination pocket, leading to the observation of both polymorphs throughout the full Ln(III)-series, although X-ray quality single crystals of the pseudo helical configurations of Sm(III) and Tb(III) could not be obtained. The small and heavy ions Er(III) - Lu(III) are forming comparable complexes, but crystallize in a different crystal system with a single chloroform molecule found per complex molecule as lattice solvent. The monodentate coordination of one of the nitrate anions, observed for the Yb(III) and Lu(III) analogues employing L_H, is not observed. Irrespective of the employed ligand and the obtained polymorph, the complexes crystallize as 50:50 racemic mixtures of helical Δ and Λ enantiomers.

Magnetic characterization using SQUID-magnetometry and *ab initio* CASSCF calculations has been performed for the paramagnetic complexes of the series. Field-induced single-molecule magnet behaviour has been observed for all complexes of Kramer ions except Sm(III). Out of all the non-Kramer ion complexes, only the Tb(III) analogues showed an out-of-phase signal of the magnetic susceptibility. Without the application of an external DC field, the slow magnetic relaxation is quenched for all samples, due to efficient quantum tunnelling which is promoted by the low symmetry coordination environment around the Ln(III) ions. The low symmetry is also the reason that no SMM behaviour was observed for most of the non-Kramer ions, as the degeneracy of the ground state is not an intrinsic property of those ions. The high transverse components of the g-tensor, leading to efficient QTM, and the non-degeneracy of the ground states for the non-Kramer ions was confirmed by *ab initio* methods. The observed energy barriers to magnetic relaxation are gathered in table 6.1.

Table 6.1: Determined effective energy barriers in K for the magnetic relaxation of the different Ln(III) complexes. The asterisks indicate non-standard behaviour (see sections 4.2 and 4.6)

Ln(III) ion	U_{eff} of **1-Ln/2-Ln/3-Ln**	U_{eff} of **4-Ln/5-Ln**
Ce	5.12*	37.74
Nd	33.19	38.93
Tb	3.18*	2.69*
Dy	68.71	21.99, 57.14
Er	29.96	18.62
Yb	26.24	20.03

The highest energy barrier has been observed for the Dy(III) analogues, which is common in molecular magnetism. For the Ln(III) ions Tb(III), Dy(III) and Er(III), the determined energy barriers are significantly lower than what has been reported for other complexes of those ions, as specifically designed ligands have lead to very high barriers.[59,138] Interestingly, the barrier observed for the methylated Ce(III) analogue **4-Ce**, is reasonably high compared to barrier reported for other Ce(III)-based SMMs.[92] This observation is in line with the Dy(III) complexes showing a higher U_{eff} than the Er(III) analogues, which can be explained by the electron distribution of the 4f electrons. The higher barrier observed for the Dy(III) analogues suggests that the ligand field exerted by the substituted phen and the nitrate anions can be characterized as more axial type, beneficial for ions with oblate electron density distributions.[56] As Ce(III) shows a strong oblate distribution, the observed energy barrier is reasonably high for a Ce(III)-based SMM. This reasoning doesn't apply to **1-Ce**, due to the added methanol donor, creating a very different environment.

Low temperature photoluminescence measurements have been performed, resulting in the observation of PL emission of the Nd(III), Sm(III), Eu(III), Gd(III), Tb(III), Dy(III), Er(III), Tm(III) and Yb(III) complexes. The emission was observed in the visible and near-IR region at wavelengths characteristic for the given Ln(III) ions. Where possible, peak deconvolution analysis was performed to obtain the peak positions of the emission lines and with that the energies of the related m_J-states of the complexes. The spectroscopically determined energies and the energies obtained from *ab initio* CASSCF calculations and, where possible, the energy barrier to magnetic relaxation have been compared. Overall it is found that the CASSCF calculations are underestimating the energy splitting of the multiplets, especially for the higher excited states. The observed magnetic relaxation barriers have been lower than the energy separations between the ground and the first excited state obtained via PL methods, suggesting under-the-barrier relaxation mechanisms.

For the analogues of Eu(III) and Yb(III), spectral hole burning experiments have been performed. For the Yb(III) complexes, no spectral holes were observed, due to a small $T_{1,spin}$, which is likely promoted by Yb-Yb interaction within the concentrated sample. Optical state lifetimes of 28.5 μs and 30.0 μs have been observed for the Yb(III) samples, being in good agreement with literature reports of Yb(III)-based compounds. The excited state lifetimes of the $^5D_0$ state of Eu(III) have been determined at 1.425 ms and 1.457 ms for the two Eu(III) complexes. Analysis of the optical parameters revealed a weaker non-radiative decay for the Eu(III) complex of the dimethylpyrazole-substituted ligand compared to the complex of the pyrazole-substituted ligand. This suggests, that the increased distance of the nearest C-H vibrator is having a stronger influence on the radiative/ non-radiative decay than the additionally introduced C-H modes. Spectral holes have been observed upon pumping the $^5D_0 \leftarrow {}^7F_0$ transition, showing very narrow optical linewidths. The optical coherence times $T_{2,opt}$ have been determined at 194 ns and

94 ns for **2-Eu** and **4-Eu**, respectively, comparable to those of other Eu(III) complexes in the literature.[80] Despite showing a longer $T_{1,opt}$, the L_{Me}-based Eu(III) complex gives a shorter $T_{2,opt}$. From that it can be deduced that the additional C-H modes increase the observed decoherence and the effect is stronger than the increased distance towards the Eu(III) ion, opposite to the ratio between radiative and non-radiative decay. The narrow observed lines give further evidence that narrow homogeneous lines and with that long coherence lifetimes $T_{2,opt}$ are intrinsically observable for Eu(III) complexes that can show the $^5\mathrm{D}_0 \rightarrow {}^7\mathrm{F}_0$ transition. While the narrow linewidths are an important measure to determine the optical coherence lifetimes, they are also the foundation of QIP schemes. Without the presence of very narrow transitions, the targeted addressing of qubits is impossible. Therefore, the finding of narrow homogeneous lines is a promising feature for the realization of optically addressed qubits. So far narrow optical lines have been observed for Ln(III) ions doped in inorganic host lattices, for example Eu(III):YSO.[139] Recently narrow optical lines have been obtained from Eu(III)-based molecular complexes. A noteworthy difference between the molecular systems and the doped lattices is that narrow linewidths are observed for the molecular complexes even at stoichiometric concentrations. In doped inorganic lattices the concentrations of Eu(III) ions are usually about 0.001%. The high amount of Eu(III) ions and the associated narrow linewidths render the molecular systems as quantum memories for light, as recently demonstrated for a mononuclear Eu(III) complex.[76] Crucially, by tuning the molecular structure, the optical properties, like the homogeneous linewidths, of the molecular complexes can be tuned. Overall, molecules can function as platforms for creating coherent light-matter interfaces, useful for the realization of QIP applications. The obtained narrow Γ_h and $T_{2,opt}$ obtained for two molecular Eu(III) samples in this thesis are a testimony of the above statement.

It might still be a long way to reach a point where fabrication of quantum computers based on lanthanide-based molecular light-matter interfaces is achievable, however, the intrinsic properties of molecular Eu(III) compounds is a promising approach to be pursued. The findings of this thesis are contributing to a general understanding of the narrow optical linewidths observed in molecules, which has so far not been evidenced with enough examples and data. The comparative study between the non-methylated and the methylated versions of the pyrazole-substituted 1,10-phenanthroline helps deepening the understanding of how structural changes influence the magnetic and the optical properties of Ln(III) ions in coordination compounds. On top, the added *ab initio* analysis reveals where the results of the CASSCF procedure compare well with the experiment and where differences are being observed.

7 Experimental details

7.1 Synthesis

Synthesis of 2,9-Bis(pyrazol-1-yl)-1,10-phenanthroline ($\mathbf{L}_H$)

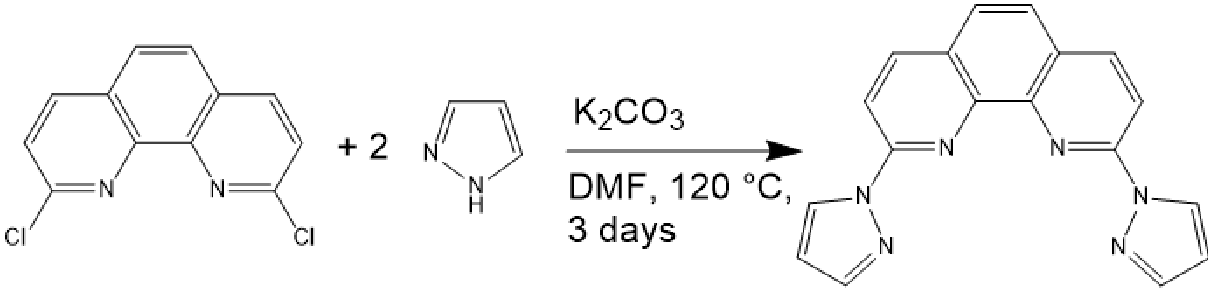

The synthesis is a slightly modified procedure of the one reported by Li *et al.*.[88] In 40 mL of dry DMF were mixed 2.00 g (8.03 mmol, 1 eq.) 2,9-dichloro-1,10-phenanthroline, 1.31 g (19.2 mmol, 2 eq.) 1*H*-pyrazole and 2.65 g (19.2 mmol, 2 eq.) potassium carbonate. The resulting mixture was heated to 120 C for 3 days under Ar atmosphere. The yellowish mixture was allowed to cool to room temperature and poured into 80 mL of cold water. Immediately a white precipitate formed, which was collected by filtration and washed with cold water. Drying yielded 2.057 g (6.59 mmol, 82%) of the pure compound and its purity was confirmed using NMR techniques.

Synthesis of 2,9-Bis(3,5-dimethylpyrazol-1-yl)-1,10-phenanthroline ($\mathbf{L}_{Me}$)

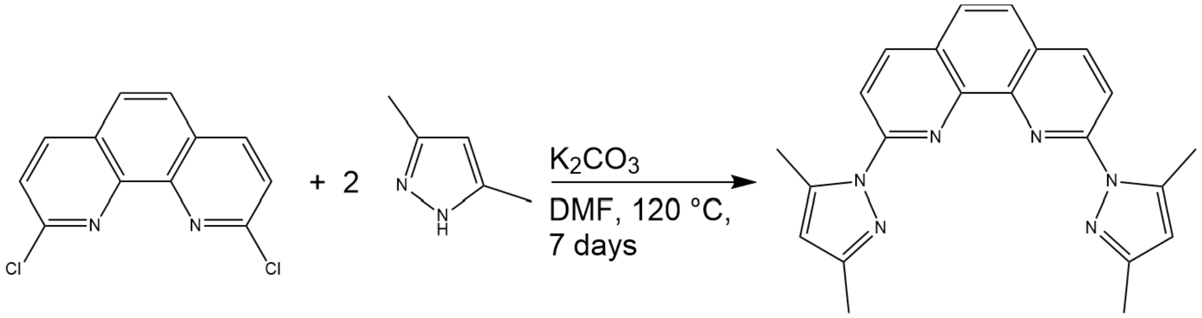

A mixture of 2.00 g (8.03 mmol, 1 eq.) 2,9-dichloro-1,10-phenanthroline, 3.86 g (40.15 mmol, 5 eq.) 3,5-dimethyl-1*H*-pyrazole and 5.55 g (40.15 mmol, 5 eq.) potassium carbonate in

40 mL of dry DMF was prepared. The mixture was heated to 120 C under Ar atmosphere for 7 days. The yellow mixture was allowed to slowly cool to room temperature and poured into 80 mL of cold water. A pale yellow solid formed immediately, which was collected by filtration and washed with cold water. The pure product was obtained by recrystallization from hot acetonitrile yielding 853 mg (2.32 mmol, 29%). ^{1}H-NMR (500 MHz, 300 K, $CDCl_3$): δ [ppm] = 8.33 (d, J = 8.7 Hz, 2H),8.28 (d, J = 8.7 Hz, 2H), 7.78 (s, 2H), 6.09 (s, 2H), 2.98 (s, 6H), 2.36 (s, 6H) (see appendix figure 9.1).

Synthesis of [La$\mathbf{L}_H$(NO_3)$_3$MeOH] (1-La)

In 10 mL MeOH were dissolved 43.3 mg (0.1 mmol, 1 eq.) $La(NO_3)_3 \cdot 6\ H_2O$. Separately 32.0 mg (0.1 mmol, 1 eq.) 2,9-Bis(pyrazol-1-yl)-1,10-phenanthroline ($\mathbf{L}_H$) were dissolved in 20 mL of chloroform. The methanolic solution was carefully layered on top of the chloroformic solution and the mixture was allowed to stand for crystallization at room temperature for several days. After approximately 2 weeks, the product was isolated by decanting off the mother liquor and washing with chloroform and methanol. The product was obtained as 56.9 mg (85 %) of colourless block-shaped crystals.

Synthesis of [La$\mathbf{L}_{Me}$(NO_3)$_3$] (4-La)

In 10 mL MeOH were dissolved 43.3 mg (0.1 mmol, 1 eq.) $La(NO_3)_3 \cdot 6\ H_2O$. Separately 37.0 mg (0.1 mmol, 1 eq.) 2,9-Bis(3,5-dimethylpyrazol-1-yl)-1,10-phenanthroline ($\mathbf{L}_{Me}$) were dissolved in 20 mL of chloroform. The methanolic solution was carefully layered on top of the chloroformic solution and the mixture was allowed to stand for crystallization at room temperature for several days. After approximately 2 weeks, the product was isolated by decanting off the yellowish mother liquor and washing with chloroform and methanol. The product was obtained as 36.3 mg (52%) of colourless needle-shaped crystals.

Synthesis of [Ce$\mathbf{L}_H$(NO_3)$_3$MeOH] (1-Ce)

In 10 mL MeOH were dissolved 43.4 mg (0.1 mmol, 1 eq.) $Ce(NO_3)_3 \cdot 6\ H_2O$. Separately 32.0 mg (0.1 mmol, 1 eq.) 2,9-Bis(pyrazol-1-yl)-1,10-phenanthroline ($\mathbf{L}_H$) were dissolved in 20 mL of chloroform. The methanolic solution was carefully layered on top of the chloroformic solution and the mixture was allowed to stand for crystallization at room temperature for several days. After approximately 2 weeks, the product was isolated by decanting off the mother liquor and washing with chloroform and methanol. The product was obtained as 57.3 mg (85%) of pale yellow plate-shaped crystals.

Synthesis of [CeL$_{Me}$(NO$_3$)$_3$] (4-Ce)

In 10 mL MeOH were dissolved 43.4 mg (0.1 mmol, 1 eq.) $Ce(NO_3)_3 \cdot 6\,H_2O$. Separately 37.0 mg (0.1 mmol, 1 eq.) 2,9-Bis(3,5-dimethylpyrazol-1-yl)-1,10-phenanthroline (**L**$_{Me}$) were dissolved in 20 mL of chloroform. The methanolic solution was carefully layered on top of the chloroformic solution and the mixture was allowed to stand for crystallization at room temperature for several days. After approximately 2 weeks, the product was isolated by decanting off the yellowish mother liquor and washing with chloroform and methanol. The product was obtained as 47.3 mg (68%) of yellow needle-shaped crystals.

Synthesis of [PrL$_H$(NO$_3$)$_3$MeOH] (1-Pr)

In 10 mL MeOH were dissolved 43.5 mg (0.1 mmol, 1 eq.) $Pr(NO_3)_3 \cdot 6\,H_2O$. Separately 32.0 mg (0.1 mmol, 1 eq.) 2,9-Bis(pyrazol-1-yl)-1,10-phenanthroline (**L**$_H$) were dissolved in 20 mL of chloroform. The methanolic solution was carefully layered on top of the chloroformic solution and the mixture was allowed to stand for crystallization at room temperature for several days. After approximately 2 weeks, the product was isolated by decanting off the mother liquor and washing with chloroform and methanol. The product was obtained as 52.0 mg (77 %) of greenish plate-shaped crystals.

Synthesis of [PrL$_{Me}$(NO$_3$)$_3$] (4-Pr)

In 10 mL MeOH were dissolved 43.5 mg (0.1 mmol, 1 eq.) $Pr(NO_3)_3 \cdot 6\,H_2O$. Separately 37.0 mg (0.1 mmol, 1 eq.) 2,9-Bis(3,5-dimethylpyrazol-1-yl)-1,10-phenanthroline (**L**$_{Me}$) were dissolved in 20 mL of chloroform. The methanolic solution was carefully layered on top of the chloroformic solution and the mixture was allowed to stand for crystallization at room temperature for several days. After approximately 2 weeks, the product was isolated by decanting off the yellowish mother liquor and washing with chloroform and methanol. The product was obtained as 47.4 mg (68%) of greenish needle-shaped crystals.

Synthesis of [NdL$_H$(NO$_3$)$_3$](2-Nd)

In 10 mL MeOH were dissolved 43.8 mg (0.1 mmol, 1 eq.) $Nd(NO_3)_3 \cdot 6\ H_2O$. Separately 32.0 mg (0.1 mmol, 1 eq.) 2,9-Bis(pyrazol-1-yl)-1,10-phenanthroline (**L**$_H$) were dissolved in 20 mL of chloroform. The methanolic solution was carefully layered on top of the chloroformic solution and the mixture was allowed to stand for crystallization at room temperature for several days. After approximately 2 weeks, the product was isolated by decanting off the mother liquor and washing with chloroform and methanol. The product was obtained as 50.3 mg (59%) of pinkish block-shaped crystals.

Synthesis of [NdL$_{Me}$(NO$_3$)$_3$] (4-Nd)

In 10 mL MeOH were dissolved 43.8 mg (0.1 mmol, 1 eq.) $Nd(NO_3)_3 \cdot 6\ H_2O$. Separately 37.0 mg (0.1 mmol, 1 eq.) 2,9-Bis(3,5-dimethylpyrazol-1-yl)-1,10-phenanthroline (**L**$_{Me}$) were dissolved in 20 mL of chloroform. The methanolic solution was carefully layered on top of the chloroformic solution and the mixture was allowed to stand for crystallization at room temperature for several days. After approximately 2 weeks, the product was isolated by decanting off the yellowish mother liquor and washing with chloroform and methanol. The product was obtained as 40.5 mg (58%) of pinkish needle-shaped crystals.

Synthesis of [SmL$_H$(NO$_3$)$_3$] (2-Sm)

In 10 mL MeOH were dissolved 44.5 mg (0.1 mmol, 1 eq.) $Sm(NO_3)_3 \cdot 6\ H_2O$. Separately 32.0 mg (0.1 mmol, 1 eq.) 2,9-Bis(pyrazol-1-yl)-1,10-phenanthroline (**L**$_H$) were dissolved in 20 mL of chloroform. The methanolic solution was carefully layered on top of the chloroformic solution and the mixture was allowed to stand for crystallization at room temperature for several days. The first formation crystals could be observed after a few hours already. After approximately 2 weeks, the product was isolated by decanting off the mother liquor and washing with chloroform and methanol. The product was obtained as 52.1 mg (80 %) of colourless block-shaped crystals.

Synthesis of [SmL$_{Me}$(NO$_3$)$_3$] (4-Sm)

In 10 mL MeOH were dissolved 44.5 mg (0.1 mmol, 1 eq.) $Sm(NO_3)_3 \cdot 6\ H_2O$. Separately 37.0 mg (0.1 mmol, 1 eq.) 2,9-Bis(3,5-dimethylpyrazol-1-yl)-1,10-phenanthroline (**L**$_{Me}$)

were dissolved in 20 mL of chloroform. The methanolic solution was carefully layered on top of the chloroformic solution and the mixture was allowed to stand for crystallization at room temperature for several days. After approximately 2 weeks, the product was isolated by decanting off the yellowish mother liquor and washing with chloroform and methanol. The product was obtained as 39.0 mg (55%) of colourless needle-shaped crystals.

Synthesis of [EuL$_H$(NO$_3$)$_3$] (2-Eu)

In 10 mL MeOH were dissolved 44.6 mg (0.1 mmol, 1 eq.) $Eu(NO_3)_3 \cdot 6\ H_2O$. Separately 32.0 mg (0.1 mmol, 1 eq.) 2,9-Bis(pyrazol-1-yl)-1,10-phenanthroline (**L**$_H$) were dissolved in 20 mL of chloroform. The methanolic solution was carefully layered on top of the chloroformic solution and the mixture was allowed to stand for crystallization at room temperature for several days. The first formation crystals could be observed after a few hours already. After approximately 2 weeks, the product was isolated by decanting off the mother liquor and washing with chloroform and methanol. The product was obtained as 53.3 mg (82%) of colourless block-shaped crystals.

Synthesis of [EuL$_{Me}$(NO$_3$)$_3$] (4-Eu)

In 10 mL MeOH were dissolved 44.6 mg (0.1 mmol, 1 eq.) $Eu(NO_3)_3 \cdot 6\ H_2O$. Separately 37.0 mg (0.1 mmol, 1 eq.) 2,9-Bis(3,5-dimethylpyrazol-1-yl)-1,10-phenanthroline (**L**$_{Me}$) were dissolved in 20 mL of chloroform. The methanolic solution was carefully layered on top of the chloroformic solution and the mixture was allowed to stand for crystallization at room temperature for several days. After approximately 2 weeks, the product was isolated by decanting off the yellowish mother liquor and washing with chloroform and methanol. The product was obtained as 33.5 mg (47 %) of colourless needle-shaped crystals.

Synthesis of [GdL$_H$(NO$_3$)$_3$] (2-Gd)

In 10 mL MeOH were dissolved 45.1 mg (0.1 mmol, 1 eq.) $Gd(NO_3)_3 \cdot 6\ H_2O$. Separately 32.0 mg (0.1 mmol, 1 eq.) 2,9-Bis(pyrazol-1-yl)-1,10-phenanthroline (**L**$_H$) were dissolved in 20 mL of chloroform. The methanolic solution was carefully layered on top of the chloroformic solution and the mixture was allowed to stand for crystallization at room temperature for several days. The first formation crystals could be observed after a few hours already. After approximately 2 weeks, the product was isolated by decanting off the mother liquor and washing with chloroform and methanol. The product was obtained as 50.5 mg (77%) of colourless block-shaped crystals.

Synthesis of [GdL$_{Me}$(NO$_3$)$_3$] (4-Gd)

In 10 mL MeOH were dissolved 45.1 mg (0.1 mmol, 1 eq.) Gd(NO$_3$)$_3$· 6 H$_2$O. Separately 37.0 mg (0.1 mmol, 1 eq.) 2,9-Bis(3,5-dimethylpyrazol-1-yl)-1,10-phenanthroline (**L**$_{Me}$) were dissolved in 20 mL of chloroform. The methanolic solution was carefully layered on top of the chloroformic solution and the mixture was allowed to stand for crystallization at room temperature for several days. After approximately 2 weeks, the product was isolated by decanting off the yellowish mother liquor and washing with chloroform and methanol. The product was obtained as 29.7 mg (42%) of colourless needle-shaped crystals.

Synthesis of [TbL$_H$(NO$_3$)$_3$] (2-Tb)

In 10 mL MeOH were dissolved 45.3 mg (0.1 mmol, 1 eq.) Tb(NO$_3$)$_3$· 6 H$_2$O. Separately 32.0 mg (0.1 mmol, 1 eq.) 2,9-Bis(pyrazol-1-yl)-1,10-phenanthroline (**L**$_H$) were dissolved in 20 mL of chloroform. The methanolic solution was carefully layered on top of the chloroformic solution and the mixture was allowed to stand for crystallization at room temperature for several days. The first formation crystals could be observed after a few hours already. After approximately 2 weeks, the product was isolated by decanting off the mother liquor and washing with chloroform and methanol. The product was obtained as 55.9 mg (85%) of colourless block-shaped crystals.

Synthesis of [TbL$_{Me}$(NO$_3$)$_3$] (4-Tb)

In 10 mL MeOH were dissolved 45.3 mg (0.1 mmol, 1 eq.) Tb(NO$_3$)$_3$· 6 H$_2$O. Separately 37.0 mg (0.1 mmol, 1 eq.) 2,9-Bis(3,5-dimethylpyrazol-1-yl)-1,10-phenanthroline (**L**$_{Me}$) were dissolved in 20 mL of chloroform. The methanolic solution was carefully layered on top of the chloroformic solution and the mixture was allowed to stand for crystallization at room temperature for several days. After approximately 2 weeks, the product was isolated by decanting off the yellowish mother liquor and washing with chloroform and methanol. The product was obtained as 50.2 mg (70%) of colourless needle-shaped crystals.

Synthesis of [DyL$_H$(NO$_3$)$_3$] (2-Dy)

In 10 mL MeOH were dissolved 43.9 mg (0.1 mmol, 1 eq.) $Dy(NO_3)_3 \cdot 5\ H_2O$. Separately 32.0 mg (0.1 mmol, 1 eq.) 2,9-Bis(pyrazol-1-yl)-1,10-phenanthroline (**L**$_H$) were dissolved in 20 mL of chloroform. The methanolic solution was carefully layered on top of the chloroformic solution and the mixture was allowed to stand for crystallization at room temperature for several days. The first formation crystals could be observed after a few hours already. After approximately 2 weeks, the product was isolated by decanting off the mother liquor and washing with chloroform and methanol. The product was obtained as 46.9 mg (71%) of colourless block-shaped crystals.

Synthesis of [DyL$_{Me}$(NO$_3$)$_3$] (4-Dy)

In 10 mL MeOH were dissolved 43.9 mg (0.1 mmol, 1 eq.) $Dy(NO_3)_3 \cdot 5\ H_2O$. Separately 37.0 mg (0.1 mmol, 1 eq.) 2,9-Bis(3,5-dimethylpyrazol-1-yl)-1,10-phenanthroline (**L**$_{Me}$) were dissolved in 20 mL of chloroform. The methanolic solution was carefully layered on top of the chloroformic solution and the mixture was allowed to stand for crystallization at room temperature for several days. After approximately 2 weeks, the product was isolated by decanting off the yellowish mother liquor and washing with chloroform and methanol. The product was obtained as 37.1 mg (52%) of colourless needle-shaped crystals.

Synthesis of [HoL$_H$(NO$_3$)$_3$] (2-Ho)

25.4 mg (0.05 mmol, 1 eq.) $Ho_2(CO_3)_3$ were dissolved in approximately 2 mL of concentrated nitric acid. The mixture was diluted with 10 mL of water and Ar was bubbled through, to remove excess HNO_3. The mixture water was evaporated and the pink residue was dissolved in 10 mL of methanol. Separately 32.0 mg (0.1 mmol, 1 eq.) 2,9-Bis(pyrazol-1-yl)-1,10-phenanthroline (**L**$_H$) were dissolved in 20 mL of chloroform. The methanolic solution was carefully layered on top of the chloroformic solution and the mixture was allowed to stand for crystallization at room temperature for several days. The first formation crystals could be observed after a few hours already. After approximately 2 weeks, the product was isolated by decanting off the mother liquor and washing with chloroform and methanol. The product was obtained as 29.7 mg (45%) of pinkish block-shaped crystals.

Synthesis of [HoL$_{Me}$(NO$_3$)$_3$] (4-Ho)

25.4 mg (0.05 mmol, 1 eq.) $Ho_2(CO_3)_3$ were dissolved in approximately 2 mL of concentrated nitric acid. The mixture was diluted with 10 mL of water and Ar was bubbled through, to remove excess HNO_3. The mixture water was evaporated and the pink residue was dissolved in 10 mL of methanol. Separately 37.0 mg (0.1 mmol, 1 eq.) 2,9-Bis(3,5-dimethylpyrazol-1-yl)-1,10-phenanthroline (**L**$_{Me}$) were dissolved in 20 mL of chloroform. The methanolic solution was carefully layered on top of the chloroformic solution and the mixture was allowed to stand for crystallization at room temperature for several days. After approximately 2 weeks, the product was isolated by decanting off the yellowish mother liquor and washing with chloroform and methanol. The product was obtained as 33.1 mg (46%) of pinkish needle-shaped crystals.

Synthesis of [YL$_H$(NO$_3$)$_3$] (2-Y)

In 10 mL MeOH were dissolved 38.3 mg (0.1 mmol, 1 eq.) $Y(NO_3)_3 \cdot$ 6 H_2O. Separately 32.0 mg (0.1 mmol, 1 eq.) 2,9-Bis(pyrazol-1-yl)-1,10-phenanthroline (**L**$_H$) were dissolved in 20 mL of chloroform. The methanolic solution was carefully layered on top of the chloroformic solution and the mixture was allowed to stand for crystallization at room temperature for several days. The first formation crystals could be observed after a few hours already. After approximately 2 weeks, the product was isolated by decanting off the mother liquor and washing with chloroform and methanol. The product was obtained as 44.8 mg (76%) of colourless block-shaped crystals.

Synthesis of [YL$_{Me}$(NO$_3$)$_3$] (4-Y)

In 10 mL MeOH were dissolved 38.3 mg (0.1 mmol, 1 eq.) $Y(NO_3)_3 \cdot$ 6 H_2O. Separately 37.0 mg (0.1 mmol, 1 eq.) 2,9-Bis(3,5-dimethylpyrazol-1-yl)-1,10-phenanthroline (**L**$_{Me}$) were dissolved in 20 mL of chloroform. The methanolic solution was carefully layered on top of the chloroformic solution and the mixture was allowed to stand for crystallization at room temperature for several days. After approximately 2 weeks, the product was isolated by decanting off the yellowish mother liquor and washing with chloroform and methanol. The product was obtained as 30.2 mg (47%) of colourless needle-shaped crystals.

Synthesis of [ErL$_H$(NO$_3$)$_3$] (2-Er)

In 10 mL MeOH were dissolved 46.1 mg (0.1 mmol, 1 eq.) $Er(NO_3)_3 \cdot 6\ H_2O$. Separately 32.0 mg (0.1 mmol, 1 eq.) 2,9-Bis(pyrazol-1-yl)-1,10-phenanthroline (**L**$_H$) were dissolved in 20 mL of chloroform. The methanolic solution was carefully layered on top of the chloroformic solution and the mixture was allowed to stand for crystallization at room temperature for several days. The first formation crystals could be observed after a few hours already. After approximately 2 weeks, the product was isolated by decanting off the mother liquor and washing with chloroform and methanol. The product was obtained as 41.3 mg (62%) of colourless block-shaped crystals.

Synthesis of [ErL$_{Me}$(NO$_3$)$_3$]· CHCl$_3$ (5-Er)

In 10 mL MeOH were dissolved 46.1 mg (0.1 mmol, 1 eq.) $Er(NO_3)_3 \cdot 6\ H_2O$. Separately 37.0 mg (0.1 mmol, 1 eq.) 2,9-Bis(3,5-dimethylpyrazol-1-yl)-1,10-phenanthroline (**L**$_{Me}$) were dissolved in 20 mL of chloroform. The methanolic solution was carefully layered on top of the chloroformic solution and the mixture was allowed to stand for crystallization at room temperature for several days. After approximately 2 weeks, the product was isolated by decanting off the yellowish mother liquor and washing with chloroform and methanol. The product was obtained as 48.0 mg (57%) of pinkish needle-shaped crystals.

Synthesis of [TmL$_H$(NO$_3$)$_3$] (2-Tm)

In 10 mL MeOH were dissolved 44.5 mg (0.1 mmol, 1 eq.) $Tm(NO_3)_3 \cdot 5\ H_2O$. Separately 32.0 mg (0.1 mmol, 1 eq.) 2,9-Bis(pyrazol-1-yl)-1,10-phenanthroline (**L**$_H$) were dissolved in 20 mL of chloroform. The methanolic solution was carefully layered on top of the chloroformic solution and the mixture was allowed to stand for crystallization at room temperature for several days. The first formation crystals could be observed after a few hours already. After approximately 2 weeks, the product was isolated by decanting off the mother liquor and washing with chloroform and methanol. The product was obtained as 51.5 mg (77%) of colourless needle-shaped crystals.

Synthesis of [TmL$_{Me}$(NO$_3$)$_3$]· CHCl$_3$ (5-Tm)

In 10 mL MeOH were dissolved 44.5 mg (0.1 mmol, 1 eq.) Tm(NO$_3$)$_3$· 5 H$_2$O. Separately 37.0 mg (0.1 mmol, 1 eq.) 2,9-Bis(3,5-dimethylpyrazol-1-yl)-1,10-phenanthroline (**L**$_{Me}$) were dissolved in 20 mL of chloroform. The methanolic solution was carefully layered on top of the chloroformic solution and the mixture was allowed to stand for crystallization at room temperature for several days. After approximately 2 weeks, the product was isolated by decanting off the yellowish mother liquor and washing with chloroform and methanol. The product was obtained as 43.5 mg (52%) of colourless needle-shaped crystals.

Synthesis of [YbL$_H$(NO$_3$)$_3$]· CHCl$_3$ (3-Yb)

In 10 mL MeOH were dissolved 46.7 mg (0.1 mmol, 1 eq.) Yb(NO$_3$)$_3$· 6 H$_2$O. Separately 32.0 mg (0.1 mmol, 1 eq.) 2,9-Bis(pyrazol-1-yl)-1,10-phenanthroline (**L**$_H$) were dissolved in 20 mL of chloroform. The methanolic solution was carefully layered on top of the chloroformic solution and the mixture was allowed to stand for crystallization at room temperature for several days. The first formation crystals could be observed after a few hours already. After approximately 2 weeks, the product was isolated by decanting off the mother liquor and washing with chloroform and methanol. The product was obtained as 40.3 mg (51%) of colourless needle-shaped crystals.

Synthesis of [YbL$_{Me}$(NO$_3$)$_3$]· CHCl$_3$ (5-Yb)

In 10 mL MeOH were dissolved 46.7 mg (0.1 mmol, 1 eq.) Yb(NO$_3$)$_3$· 6 H$_2$O. Separately 37.0 mg (0.1 mmol, 1 eq.) 2,9-Bis(3,5-dimethylpyrazol-1-yl)-1,10-phenanthroline (**L**$_{Me}$) were dissolved in 20 mL of chloroform. The methanolic solution was carefully layered on top of the chloroformic solution and the mixture was allowed to stand for crystallization at room temperature for several days. After approximately 2 weeks, the product was isolated by decanting off the yellowish mother liquor and washing with chloroform and methanol. The product was obtained as 32.6 mg (38%) of colourless needle-shaped crystals.

Synthesis of [LuL$_H$(NO$_3$)$_3$]· CHCl$_3$ (3-Lu)

In 10 mL MeOH were dissolved 46.9 mg (0.1 mmol, 1 eq.) Lu(NO$_3$)$_3$· 6 H$_2$O. Separately 32.0 mg (0.1 mmol, 1 eq.) 2,9-Bis(pyrazol-1-yl)-1,10-phenanthroline (**L**$_H$) were dissolved in 20 mL of chloroform. The methanolic solution was carefully layered on top of the chloroformic solution and the mixture was allowed to stand for crystallization at room temperature for several days. The first formation crystals could be observed after a few hours already. After approximately 2 weeks, the product was isolated by decanting off the mother liquor and washing with chloroform and methanol. The product was obtained as 44.7 mg (56%) of colourless needle-shaped crystals.

Synthesis of $[\mathbf{LuL}_{Me}(\mathbf{NO}_3)_3]\cdot \mathbf{CHCl}_3$ (5-Lu)

In 10 mL MeOH were dissolved 46.9 mg (0.1 mmol, 1 eq.) $Lu(NO_3)_3\cdot 6\ H_2O$. Separately 37.0 mg (0.1 mmol, 1 eq.) 2,9-Bis(3,5-dimethylpyrazol-1-yl)-1,10-phenanthroline ($\mathbf{L}_{Me}$) were dissolved in 20 mL of chloroform. The methanolic solution was carefully layered on top of the chloroformic solution and the mixture was allowed to stand for crystallization at room temperature for several days. After approximately 2 weeks, the product was isolated by decanting off the yellowish mother liquor and washing with chloroform and methanol. The product was obtained as 18.5 mg (22%) of colourless needle-shaped crystals.

7.2 X-ray diffraction measurements

Single crystal X-ray diffraction measurements were performed on a “STOE” StadiVari diffractometer equipped with a CCD image plate detector using Mo-K_α radiation. The crystals were mounted in a cold nitrogen stream at 180 K using perfluorinated oil. Data reduction and absorption correction was performed using the CrysAlisPro software. Structure solving by direct methods and refinement against F^2 was performed using the SHELXL package implemented in Olex2. All non hydrogen atoms were refined anisotropically and hydrogen atoms were placed using a riding approach.
Powder diffractograms were recorded on a “STOE” Stadi P diffractometer in a transmission setup using Cu-K_α radiation at room temperature. Simulated powder patterns were obtained based on the single crystal data using Mercury.

7.3 Magnetic measurements

All magnetic measurements were performed on a “Quantum Design” MPMS-XL SQUID magnetometer. The samples were crystalline samples, ground to a powder and mixed with small amounts of eicosane to avoid movement of the sample. The used sampleholders were gelatine capsules, sealed with capton tape and placed in a magnetically clean straw. The static DC magnetic behaviour was recorded upon cooling down the samples from 300 K to 2 K under an applied magnetic field of $H_{DC} = 1000$ Oe (0.1 T). The temperature dependent DC data were corrected for diamagnetic contributions of the sample holder, using reference measurements of empty holders, and for the diamagnetism of the sample itself employing the estimation $\chi_{dia} = \frac{1}{2} M \, 10^{-6} \text{ cm}^3 \text{ mol}^{-1}$, where M is the molar mass of the compound. Dynamic AC susceptibility measurements were performed with an AC amplitude of 3.5 Oe at varying frequencies. The optimal DC fields for each sample were decided based on the field-dependent behaviour at 2 K. The optimal field was taken to be the field at which the AC signal appeared at the lowest frequency. All data analysis was performed in Origin.

7.4 Photoluminescence measurements

Photoluminescence measurements were recorded using a “Horiba” Fluorolog spectrometer with a 920 photomultiplier tube detector for the visible range and a InGaAs detector for the near-IR region. The solid crystalline samples were placed in between two quartz glass plates with a drop of perfluorinated oil and cooled to 3 K under vacuum. Peak deconvolution of the spectra was carried out using the peak deconvolution add-on for OriginPro 2023.

7.5 Spectral hole burning

Determination of the inhomogeneous lines and spectral hole burning measurements were performed on crystalline powder samples of the complexes, that were placed in a ferrule, linked to multimode fibres. The excitation was achieved using a dye laser.

7.6 CASSCF calculations

Ab initio CASSCF calculations were carried out using OpenMolcas. The calculation followed the SEWARD/RASSCF/RASSI/SINGLE-ANISO routine. The input geometries were taken as obtained from single crystal refinement without *ab initio* optimization. The basis sets applied were the relativistic ANO-RCC type sets of the Molcas library. The central lanthanide atom was described using triple zeta with polarization, all non-hydrogen atoms with double zeta with polarization and hydrogens with double zeta without polarization. The size of the active space was chosen to be seven, resembling the 4f orbitals of the lanthanide ion and the amount of active electrons is 1 to 13 according to the elements Ce to Lu. The number of roots taken into the RASSI routine for each Ln is given in table 7.1.

Table 7.1: Number of roots employed in the RASSI step.

Element	N_{e^-}	singlets	doublets	triplets	quadruplets	quintets	sextets	heptets
Ce	1	-	7	-	-	-	-	-
Pr	2	28	-	21	-	-	-	-
Nd	3	-	112	-	35	-	-	-
Sm	5	-	130	-	128	-	21	-
Eu	6	123	-	113	-	140	-	7
Tb	8	123	-	113	-	140	-	7
Dy	9	-	130	-	128	-	21	-
Ho	10	130	-	128	-	35	-	-
Er	11	-	112	-	35	-	-	-
Tm	12	28	-	21	-	-	-	-
Yb	13	-	7	-	-	-	-	-

8 References

[1] A Short History Of ChatGPT: How We Got To Where We Are Today, Bernard Marr, Forbes, https://www.forbes.com/sites/bernardmarr/2023/05/19/a-short-history-of-chatgpt-how-we-got-to-where-we-are-today/, Accessed: 28.08.2023.

[2] ChatGPT sets record for fastest-growing user base - analyst note, Krystal Hu, Reuters, https://www.reuters.com/technology/chatgpt-sets-record-fastest-growing-user-base-analyst-note-2023-02-01/, Accessed: 28.08.2023.

[3] BROOKS, M.: *Quantum Computers: what are they good for?* Nature, 617:S1 – S3, 2023.

[4] LIMA MARQUEZINO; R. PORTUGAL, C. LAVOR F. DE: *A Primer on Quantum Computing.* Springer, Gewerbestrasse 11, 6330 Cham, Switzerland, 1 edition, 2019.

[5] BENIOFF, P.: *The computer as a physical system: A microscopic quantum mechanical hamiltonian model of computers as represented by turing machines.* Journal of Statistical Physics, 22(5):563 – 591, 1980.

[6] Computable and Non-Computable (in Russian), Y. Manin, Sovetskoye Radio, Moscow, 1980.

[7] FEYNMAN, R. P.: *Simulating physics with computers.* International Journal of Theoretical Physics, 21(6):467 – 488, 1982.

[8] DEUTSCH, D.: *Quantum theory, the Church-Turing principle and the universal quantum computer.* Proceedings of the Royal Society of London A: Mathematical, Physical and Engeneering Sciences, 400(1818):97 – 117, 1985.

[9] D. DEUTSCH, R. JOSZA: *Rapid solution of problems by quantum computation.* Proceedings of the Royal Society of London A: Mathematical, Physical and Engeneering Sciences, 439(1907):553 – 558, 1992.

[10] SHOR, P.: *Algorithms for quantum computation: discrete logarithms and factoring.* Proceedings of the 35th Annual Symposium on Foundations of Computer Science, IEEE Computer Society:124 – 134, 1994.

[11] L. M. VANDERSYPEN; M. STEFFEN; G. BREYTA; C. S. YANNONI; M. H. SHERWOOD, I. L. CHUANG: *Experimental realization of Shor's quantum factoring algorithm using nuclear magnetic resonance.* Nature, 414(6866):883, 2001.

[12] Grover, L. K.: *Quantum mechanics helps in searching for a needle in a haystack.* Phys. Rev. Lett., 79:325 – 328, 1997.

[13] IBM skizziert einen Weg zum Quantencomputer, der trotz Fehlern interessante Probleme löst, Christian Speicher, Neue Züricher Zeitung, https://www.nzz.ch/wissenschaft/quantencomputer-ibm-stellt-neuen-osprey-prozessor-vor-ld.1711395, Accessed: 05.09.2023.

[14] F. Arute; K. Arya; R. Babbush; D. Bacon; J. C. Bardin; R. Barends; R. Biswas; S. Boixo; F. G. S. L. Brandao; D. A. Buell; B. Burkett; Y. Chen; Z. Chen; B. Chiaro; R. Collins; W. Courtney; A. Dunsworth; E. Farhi; B. Foxen; A. Fowler; C. Gidney; M. Giustina; R. Graff; K. Guerin; S. Habegger; M. P. Harrigan; M. J. Hartmann; A. Ho; M. Hoffmann; T. Huang; T. S. Humble; S. V. Isakov; E. Jeffrey; Z. Jiang; D. Kafri; K. Kechedzhi; J. Kelly; P. V. Klimov; S. Knysh; A. Korotkov; F. Kostritsa; D. Landhuis; M. Lindmark; E. Lucero; D. Lyakh; S. Mandra; J. R. McClean; M. McEwen; A. Megrant; X. Mi; K. Michielsen; M. Mohseni; J. Mutus; O. Naaman; M. Neeley; C. Neill; M. Y. Niu; E. Ostby; A. Petukhov; J. C. Platt; C. Quintana; E. G. Rieffel; P. Roushan; N. C. Rubin; D. Sank; K. J. Satzinger; V. Smelyanskiy; K. J. Sung; M. D. Trevithick; A. Vainsencher; B. Villalonga; T. White; Z. J. Yao; P. Yeh; A. Zalcman, H. Neven: *Quantum supremacy using a programmable superconducting processor.* Nature, 574:505 – 510, 2019.

[15] V. Bouchiat; D. Vion; P. Joyez; D.Esteve, M. Devoret: *Quantum coherence with a single cooper pair.* Physica Scripta, 1998(T76):165, 1998.

[16] F. Luis; A. Repolles; M. J. Martinez-Perez; D. Aguila; O. Roubeau; D. Zueco; P. J. Alonso; M. Evangelisti; A. Camon; J. Sese; L. A. Barrios, G. Aromi: *Molecular Prototypes for Spin-Based CNOT and SWAP Quantum Gates.* Phys. Rev. Lett., 107:117203, 2011.

[17] Slageren, E. Coronado M. J. Martinez-Perez; S. Cardona-Serra; C. Schlegel; F. Moro; P. J. Alonso; H. Prima-Garcia; J. M. Clemente-Juan; M. Evangelisti; A. Gaita-Arino; J. Jese; J. van: *Gd-Based Single-Ion Magnets with Tuneable Magnetic Anisotropy: Molecular Design of Spin Qubits.* Phys. Rev. Lett., 108:247213, 2012.

[18] H. Mao; R. M. Young; M. D. Krzyaniak, M. R. Wasielewski: *Optical Initialization of Molecular Qubit Spin States using Weak Exchange Coupling to Photogenerated Fullerene Triplet States.* J. Phys. Chem. B, 126:10519 – 10527, 2022.

[19] E. Moreno-Pineda, W. Wernsdorfer: *Measuring molecular magnets for quantum technologies.* Nature Reviews Physics, 3:645 – 659, 2021.

[20] E. Moreno-Pineda; C. Godfrin; F. Balestro; W. Wernsdorfer, M. Ruben: *Molecular spin qudits for quantum algorithms.* Chem. Soc. Rev., 47:501, 2018.

[21] W. Wernsdorfer, M. Ruben: *Synthetic Hilbert Space Engeneering of Molecular Qudits: Isotopologue Chemistry.* Adv. Mater., 31(26):1806687, 2019.

[22] C. Godfrin; A. Ferhat; R. Ballou; S. Klyatskaya; M. Ruben; W. Wernsdorfer, F. Balestro: *Operating Quantum States in Single Magnetic Molecules: Implementation of Grover's Quantum Algorithm.* Phys. Rev. Lett., 119:187702, 2017.

[23] Morello, A.: *Quantum search on a single-atom qudit.* Nature Nanotechnology, 13:9 – 10, 2018.

[24] M. Urdampilleta; S. Klyatskaya; J.-P. Cleuziou; M. Ruben, W. Wernsdorfer: *Supramolecular spin valves.* Nature Materials, 10:502 – 506, 2011.

[25] M. Urdampilleta; S. Klyatskaya; J.-P. Cleuziou; M. Ruben, W. Wernsdorfer: *Magnetic Interaction Between a Radical Spin and a Single-Molecule Magnet in a Molecular Spin-Valve.* ACS Nano, 9:4458 – 4464, 2015.

[26] R. Vincent; S. Klyatskaya; M. Ruben; W. Werndsdorfer, F. Balestro: *Electronic read-out of a single nuclear spin using a molecular spin transistor.* Nature, 488:357 – 360, 2012.

[27] Bettencourt-Dias, A. de: *Lanthanide-based emitting materials in light-emitting diodes.* Dalton Trans., 22:2229 – 2241, 2007.

[28] H. Jin; P. Afiuny; T. McIntyre; Y. Yih, J. W. Sutherland: *Comparative Life Cycle Assesment of NdFeB Magnets: Virgin Production versus Magnet-to-Magnet Recycling.* Procedia CIRP, 48:45 – 50, 2016.

[29] T. Xiaoqiang; L. Lezhong, W. Rui P. long;: *Magnetic properties of SmCo-based permanent magnetic films during 25 to 300 Â°C.* Journal of Rare Earths, 31(10):988 – 991, 2013.

[30] Bettencourt-Dias, A. de: *Modern Applications of Lanthanide Luminescence.* Springer, Gewerbestrasse 11, 6330 Cham, Switzerland, 19 edition, 2023.

[31] S. Thiele; F. Balestro; R. Ballou; S. Klyatskaya; M. Ruben, W. Wernsdorfer: *Electrically driven nuclear spin resonance in single-molecule magnets.* Science, 344:1135 – 1138, 2014.

[32] Haynes, W. M.: *Handbook of Physics and Chemistry.* CRC Press, 6000 Broken Sound Parkway NW, Suite 300, Boca Raton, FL 33487-2742, 95 edition, 2014.

[33] R. Marin; G. Brunet, M. Murugesu: *Shining New Light on Multifunctional Lanthanide Single-Molecule Magnets.* Angew. Chem. Int. Ed., 60:1728 – 1746, 2021.

[34] Uhlig, E.: *Steric and electronic factors influencing the structure of nickel(II) complexes.* Coordination Chemistry Reviews, 10:227 – 264, 1973.

[35] C. Janiak; H.-J. Meyer; D. Gudat, P. Kurz: *Riedel Moderne Anorganische Chemie.* De Gruyter, Berlin, Boston, 5 edition, 2018.

[36] Bünzli, J.-C. G.: *Benefiting from the Unique Properties of Lanthanide Ions.* Acc. Chem. Res., 39:53 – 61, 2006.

[37] Bünzli, J.-C. G.: *Review: Lanthanide coordination chemistry: from old concepts to coordination polymers.* Journal of Coordination Chemistry, 67:3706 – 3733, 2014.

[38] Cotton, S. A.: *Establishing coordination numbers for the lanthanides in simple complexes.* C. R. Chimie, 8:129 – 145, 2005.

[39] P. B. Hitchcock; A. G. Hulkes; M. F. Lappert, Z. Li: *Cerium(III) dialkyl dithiocarbamates from* $[Ce(N(SiMe_3)_2)_3]$ *and tetraalkylthiuram disulfides, and* $[Ce(\kappa^2\text{-}S_2CNEt_2)_4]$ *from the* Ce^{III} *precursor,* Tb^{III} *and* Nd^{III} *analogues.* Dalton Trans., 1:129 – 136, 2004.

[40] K. Dehnicke, A. Greiner: *Unusual Complex Chemistry of Rare-Earth Elements: Large Ionic Radii - Small Coordination Numbers.* Angew. Chem. Int. Ed., 42(12):1340 – 1354, 2003.

[41] L. Münzfeld; C. Schoo; S. Bestgen; E. Moreno-Pineda; R. Köppe; M. Ruben, P. W. Roesky: *Synthesis, structures and magnetic properties of* $[(\eta^9\text{-}C_9H_9)Ln(\eta^8\text{-}C_8H_8)]$ *super sandwich complexes.* Nature Commun., 10:3135, 2019.

[42] M. Xemard; S. Zimmer; M. Cordier; V. Goudy; L. Ricard; C. Clavaguera, G. Nocton: *Lanthanidocenes: Synthesis, Structure, and Bonding of Linear Sandwich Complexes of Lanthanides.* J. Am. Chem. Soc., 140:14433 – 14439, 2018.

[43] W. Yu; F. Schramm; E. Moreno-Pineda; Y. Lan; O. Fuhr; J. Chen; H. Isshiki; W. Wernsdorfer; W. Wulfhekel, M. Ruben: *Single-molecule magnet behavior in 2,2'-bipyrimidine-bridged dilanthanide complexes.* Beilstein J. Nanotechnol., 7:126 – 137, 2016.

[44] H.-H. Zou; L.-B. Sheng; Z.-L. Chen, F.-P. Liang: *Lanthanide nonanuclear clusters with sandglass-like topology and the SMM behavior of dysprosium analogue.* Polyhedron, 88:110 – 115, 2015.

[45] X.-Y.Zheng; X. J. Kong; Z.Zheng; L.-S. Long, L.-S. Zheng: *High-Nuclearity Lanthanide-Containing Clusters as Potential Molecular Magnetic Coolers.* Acc. Chem. Res., 51:517 – 525, 2018.

[46] X.-Y. Li; Y. Jing; J. Zheng; H. Ding; Q. Li; M.-H. Yu, X.-H. Bu: *Two Luminescent High-Nuclearity Lanthanide Clusters Ln_{48} (Ln = Eu and Tb) with a Nanopillar Structure.* Cryst. Growth Des., 20:5294 – 5301, 2020.

[47] D. A. Galico; C. M. S. Calado, M. Murugesu: *Lanthanide molecular cluster-aggregates as the next generation of optical materials.* Chem. Sci., 14:5827, 2023.

[48] Kahn, O.: *Molecular Magnetism.* VCH Publishers, Inc., 220 East 23rd Street, New York N. Y. 10010-4606, 1 edition, 1993.

[49] D. Gatteschi; R. Sessoli, J. Villain: *Molecular Nanomagnets.* Oxford University Press, Great Clarendon Street, Oxford OX2 6DP, 1 edition, 2006.

[50] D. W. Bruce; D. O'Hare, R. T. Walton: *Molecular Materials.* Wiley, Gewerbestrasse 11, 6330 Cham, Switzerland, 1 edition, 2010.

[51] S.-D. Jiang; B.-W. Wang; H.-L. Sun; Z.-M. Wang, S. Gao: *An Organometallic Single-Ion Magnet.* J. Am. Chem. Soc., 133:4730 – 4733, 2011.

[52] R. Sessoli; D. Gatteschi; A. Caneschi, M. A. Novak: *Magnetic bistability in a metal-ion cluster.* Nature, 365:141 – 143, 1993.

[53] R. Sessoli; H.-L. Tsal; A. R. Schake; S. Wang; J. B. Vincent; K. Folting; D. Gatteschi; G. Christou, D. N. Hendrickson: *High-Spin Molecules: $[Mn_{12}O_{12}(O_2CR)_{16}(H_2O)_4]$.* J. Am. Chem. Soc., 115:1804 – 1816, 1993.

[54] A. Zabala-Lekuona; J. M. Seco, E. Colacio: *Single-Molecule Magnets: From Mn12-ac to dysprosium metallocenes, a travel in time.* Coordination Chemistry Reviews, 441:213984, 2021.

[55] N. Ishikawa; M. Sugita; T. Ishikawa; S.-Y. Koshihara, Y. Kaizu: *Lanthanide Double-Decker Compexes Functioning as Magnets at the Single-Molecule Level.* J. Am. Chem. Soc., 125:8694 – 8695, 2003.

[56] J. D. Rinehart, J. R. Long: *Exploiting single-ion anisotropy in the design of f-element single-molecule magnets.* Chem. Sci., 2:2078 – 2085, 2011.

[57] C. A. P. Goodwin; F. Ortu; D. Reta; N. F. Chilton, D. P. Mills: *Molecular magnetic hysteresis at 60 kelvin in dysprosocenium.* Nature, 548:439 – 442, 2017.

[58] F.-S. Guo; B. M. Day; Y.-C. Chen; M.-L. Tong; A. Mansikkamäki, R. A. Layfield: *Molecular hysteresis up to 80 kelvin in a dysprosium metallocene single-molecule magnet.* Science, 362:1400 – 1403, 2018.

[59] C. A. Gould; K. R. McClain; D. Reta; J. G. C. Kragskow; D. A. Marchiori; E. Lachman; E.-S. Choi; J. G. Analytis; R. D. Britt; N. F. Chilton; B. G. Harvey, J. R. Long: *Ultrahard magnetism from mixed-valence dilanthanide complex with metal-metal bonding.* Science, 375:198 – 202, 2022.

[60] Y. Kawamura; Y. Wada; Y. Hasegawa; M. Iwamuro; T. Kitamura, S. Yanagida: *Observation of neodymium electroluminescence.* Applied Physics Letters, 74:3245, 1999.

[61] S. V. Eliseeva, J.-C. G. Bünzli: *Lanthanide luminescence for functional materials and bio-sciences.* Chem. Soc. Rev., 39:189 – 227, 2009.

[62] X. Yi; J. Shang; L. Pan; H. Tan; B. Chen; G. Liu; G. Huang; K. Bernot; O. Guillou, R.-W. Li: *Reversible Luminescence Modulation upon an Electric Field on a Full Solid-State Device Based on Lanthanide Dimers.* ACS Appl. Mater. interfaces, 8:15551 – 15556, 2016.

[63] Binnemans, K.: *Interpretation of europium(III) spectra.* Coordination Chemistry Reviews, 295:1 – 45, 2015.

[64] M. Kou; F. Qin; Y. Wang; X. Zhang; Z. Hu, Z. Zhang: *Insight into the Heavy Atom Effect Induced by Environmental Heavy Atoms for Gadolinium-Labeled Hematoporphyrin Monomethyl Ether.* J. Phys. Chem. B, 127(3):777 – 782, 2023.

[65] S. K. Kuppusamy; D. Serrano; A. M. Nonat; B. Heinrich; L. Karmazin; L. J. Charbonniere; P. Goldner, M. Ruben: *Optical spin-state polarization in a binuclear europium complex towards molecule-based coherent light-spin interfaces.* Nature Communications, 12:2152, 2012.

[66] Lis, S.: *Luminescence spectroscopy of lanthanide(III) ions in solution.* Journal of Alloys and Compounds, 341:45 – 50, 2002.

[67] Dossing, A.: *Luminescence from Lanthanide(3+) Ions in Solution.* Eur. J. Inorg. Chem., 8:1425 – 1434, 2005.

[68] Morais; C. M. S. Calado; I. O. Mazali, F. A. Sigoli A. G. Bispo-Jr; A. J. de: *Lanthanide-doped luminescent perovskites: A review of synthesis, properties, and applications.* Journal of Luminescence, 252:119406, 2022.

[69] J. Zhou; G. Zheng; X. Liu; G. Dong, J. Qiu: *Defect engeneering in lanthanide doped luminescent materials.* Coordination Chemistry Reviews, 448:214178, 2021.

[70] H. Zhang, H. Li: *Efficient visible and near-infrared photoluminescence from lanthanide and bismuth functionalized zeolite L.* J. Mater. Chem., 21:13576, 2011.

[71] Y. Wang; H. Li; L. Gu; Q. Gan; Y. Li, G. Calzaferri: *Thermally stable luminescent lanthanide compexes in zeolite L.* Microporous ans Mesoporous Materials, 121:1 – 6, 2009.

[72] Z. Li; G. Zhu; X. Guo; X. Zhao; Z. Jin, S. Qiu: *Synthesis, StructureAndLuminescent, and Magnetic Properties of Novel Lanthanide Metal-Oragnic Frameworks with Zeolite-like Topology.* Inorg. Chem., 46:5174 – 5178, 2007.

[73] D. Michalik; J. Pilewa; M. Sopicka-Lizer, T. Jüstel: *Cerium doped yttrium aluminium garnet modified by silicon and nitrogen.* Ceramic Materials, 60(4):225 – 228, 2008.

[74] R. Srinivasan; N. R. Yogamalar; J. Elanchezhiyan; R. J. Joseyphus, A. C. Bose: *Structural and optical properties of europium doped yttrium oxide nanoparticles for phosphor applications.* Journal of Alloys and Compounds, 496:472 – 477, 2010.

[75] J. R. Jayaramaiah; B. N. Lakshminarasappa, K. R. Nagabhushana: *Luminescence performance of europium-doped yttrium oxide thin films.* Journal of Luminescence, 157:63 – 68, 2015.

[76] D. Serrano; S. K. Kuppusamy; B. Heinrich; O. Fuhr; D. Hunger; M. Ruben, P. Goldner: *Ultra-narrow optical linewidths in rare-earth molecular crystals.* Nature, 603:241 – 246, 2022.

[77] L. Ungur; B. Szabo; Z. A. ALOthman; A. A. S. Al-Kahtani, L. F. Chibotaru: *Mechanisms of Luminescence in Lanthanide Complexes: A Crucial Role of Metal-Ligand Covalency.* Inorg. Chem., 61:5972 – 5976, 2022.

[78] A. Beeby; B. P. Burton-Pye; S. Faulkner; G. R. Motson; J. C. Jeffery; J. A. McClevery, M. D. Ward: *Synthesis and near-IR luminescence properties of neodymium(III)and ytterbium(III) complexes with poly(pyrazolyl)borate ligands.* Dalton Trans., 1:1923 – 1928, 2002.

[79] R. M. Pettit; F. H. Farshi; S. E. Sullivan; A. V. Osorio, M. K. Singh: *A perspective on the pathway to a scalable quantum internet using rare-earth ions.* arXiv:2304.07272, 2023.

[80] S. K. Kuppusamy; E. Vasilenko; W. Li; J. Hessenauer; C. Ioannou; O. Fuhr; D. Hunger, M. Ruben: *Observation of Narrow Optical Homogeneous Linewidth and Long Nuclear Spin Lifetimes in a Prototypical [Eu(trensal)] complex.* J. Phys. Chem. C, 127(22):10670 – 10679, 2023.

[81] Jensen, F.: *Introduction to Computational Chemistry.* Wiley, The Atrium, Southern Gate, Chichester, West Sussex PO19 8SQ, England, 2 edition, 2007.

[82] Goodwin, C. A. P.: *Blocking like it's hot: a synthetic chemists' path to high-temperature lanthanide single molecule magnets.* Dalton Trans., 49:14320, 2020.

[83] L. Childress, R. Hanson: *Diamond NV centers for quntum computing and quantum networks.* MRS Bulletin, 38(2):134 – 138, 2013.

[84] M. W. Doherty; N. B. Manson; P. Delaney; F. Jelezko; J. Wrachtrup, L. C. L. Hollenberg: *The nitrogen-vacancy colour centre in diamond.* Physics Reports, 528:1 – 45, 2013.

[85] P. Krantz; M. Kjaergaard; F. Yan; T. P. Orlando; S. Gustavsson, W. D. Oliver: *A Quantum Engeneer's Guide to Superconducting Qubits.* Applied Physics Reviews, 6(2):1 – 67, 2019.

[86] Hidary, J. D.: *Quantum Computing: An Applied Approach.* Springer, Gewerbestrasse 11, 6330 Cham, Switzerland, 1 edition, 2019.

[87] C. D. Bruzewicz; J. Chiaverini; R. McConnell, J. M .Sage: *Trapped-Ion Quantum Computing: Progress and Challenges.* Applied Physics Reviews, 6(2):021314, 2019.

[88] G.-L. Li; S.-Q. Wu; L.-F. Zhang; Z. Wang; Z.-W. Ouyang; Z.-H. Ni; S.-Q. Su; Z.-S. Yao; J.-Q. Li, O. Sato: *Field-Induced Slow Magnetic Relaxation in an Octacoordinated Fe(II) Complex with Pseudo-D_{2d} Symmetry: Magnetic, HF-EPR, and Theoretical Investigations.* Inorg. Chem., 56:8018 – 8025, 2017.

[89] N. Armaroli; L. De Cola, V. Balzani: *Absorption and Luminescence Properties of 1,10-Phenantroline, 2,9-Diphenyl-1,10-phenantroline, 2,9-Dianisyl-1,10-phenantroline and their Protonated Forms in Dichloromethane Solution.* J. Chem. Soc. Faraday Trans., 88(4):553 – 556, 1992.

[90] M. Pinsky, D. Avnir: *Continuous Shape Measures: 5. The Classical Polyhedra.* Inorg. Chem., 37:5575 – 5582, 1998.

[91] Shape - Program for the Stereochemical Analysis of Molecular Fragments by Means of Continuous Shape Measures and Associated Tools, Version 2.1, March 2013, M. Llunell, D. Casanova, J. Cirera, P. Alemany, S. Alvarez.

[92] A. Borah, R. Murugavel: *Magnetic relaxation in single-ion magnets formed by less-studied lanthanide ions Ce(III), Nd(III), Gd(III), Ho(III), Tm(II/III) and Yb(III).* Coordination Chemistry Reviews, 453:214288, 2022.

[93] R. J. Holmberg; L. T. A. Ho; L. Ungur; I. Korobkov; L. F. Chibotaru, M. Murugesu: *Observation of unusual slow-relaxation of the magnetisation in a Gd-EDTA chelate.* Dalton Trans., 44:20321, 2015.

[94] A. Vrablova; M. Tomas; L. R. Falvello; L. Dlhan; J. Titis; J. Cernak, R. Boca: *Slow magnetic relaxation in Ni-Ln (Ln = Ce, Gd, Dy) dinuclear complexes.* Dalton Trans., 48:13943, 2019.

[95] T. Yoshida; G. Cosquer; D. C. Izuogu; H. Ohtsu; M. Kawano; Y. Lan; W. Wernsdorfer; H. Nojiri; B. K. Breedlove, M. Yamashita: *Field-Induced Slow Magnetic Relaxation of Gd^{III} Complex with a Pt-Gd Heterometallic Bond.* Chem. Eur. J., 23:4551 – 4556, 2017.

[96] Y.-C. Chen; Y.-Y. Peng; J.-L. Liu, M.-L. Tong: *Field induced slow magnetic relaxation in a mononuclear Gd(III) complex.* Inorg. Chem. Commun., 107:107449, 2019.

[97] Q. Kang; W. Bingwu; W. Zheming; S. Gang, G. Song: *Field-Dependent Magnetic Relaxation and Magnetocaloric Effect in Mononuclear Gd complexes (in Chinese).* Acta Chim. Sin., 71:1022 – 1028, 2013.

[98] S. K. Singh; T. Gupta; L. Ungur, G. Rajamaran: *Magnetic Relaxation in Single-Electron Single-Ion Cerium(III) Magnets: Insights from Ab Initio Calculations.* Chem. Eur. J., 21:13812 – 13819, 2015.

[99] F. A. Mautner; F. Bierbaumer; R. C. Fischer; A. Tubau; S. Speed; E. Ruiz; S. S. Massoud; R. Vicente, S. Gomez-Coca: *Insights into te Spin Dynamics of Mononuclear Cerium(III) Single-Molecule Magnets.* Inorg. Chem., 61:11124 – 11136, 2022.

[100] H. Wada; S. Ooka; T. Yamamura, T. Kajiwara: *Light Lanthanide Complexes with Crown Ether and Its Aza Derivative Which Show Slow Magnetic Relaxation Behaviors.* Inorg. Chem., 56:147 – 155, 2017.

[101] F. A. Mautner; F. Bierbaumer; R. C. Fischer; R. Vicente; A. Tubau; A. Ferran, S. S. Massoud: *Structural Characterization, Magnetic and Luminescent Properties of Praseodymium(III)-4,4,4-Trifluoro-1-(2-Naphthyl)Butane-1,3-Dionato(1-) Complexes.* Crystals, 11:179, 2021.

[102] R. Maouche; S. Belaid; B. Benmerad; S. Bouacida; C. Daiguebonne; Y. Suffren, O. Guillou: *A new praseodymium-based coordination polymers with 1,10-phenantroline and glutarate ligands: Synthesis, crystal structure and luminescent properties.* Journal of Molecular Structure, 1225:129164, 2021.

[103] M. D. Regulacio; M. H. Pablico; J. A. Vasquez; P. N. Myers; S. Gentry; M. Prushan; S.-W. Tam-Chang, S. L. Stoll: *Luminescence of Ln(III) Dithiocarbamate Complexes (Ln = La, Pr, Sm, Eu, Gd, Tb, Dy).* Inorg. Chem., 47(5):1512 – 1523, 2008.

[104] G. Pawlicki, S. Lis: *Luminescence study of Praseodymium complexes with selected phosphonate ligands.* Optical Materials, 33:1544 – 1547, 2011.

[105] F. Pointillart; O. Cador; B. Le Guennic, L. Ouahab: *Uncommon lanthanide ions in purely 4f Single Molecule Magnets.* Coordination Chemistry Reviews, 346:150 – 175, 2017.

[106] A. Beeby; B. P. Burton-Pye; S. Faulkner; G. R. Motson; J. C. Jeffery; J. A. McCleverty, M. D. Ward: *Synthesis and near-IR luminescence properties of neodymium(III) and ytterbium(III) complexes with poly(pyrazolyl)borate ligands.* J. Chem. Soc. Dalton Trans., pages 1923 – 1928, 2002.

[107] O. M. KHREIS; R. J. CURRY; M. SOMERTON, W. P. GILLIN: *Infraredorganic light emitting diodes using neodymium tris-(8-hydroxyquinoline).* J. Appl. Phys., 88:777 – 780, 2000.

[108] S. WANG; J. XU; K.-Y. WANG; S. DANG; S. SONG; D. LIU, C. WANG: *Luminescence of samarium(III) bis-dithiocarbamate frameworks: codoped lanthanide emitters that cover visible and near-infrared domains.* J. Mater. Chem. C, 5:6620, 2017.

[109] M. BEDI; M. PUNIA; N. DUA; P. CHHILLAR; V. B. TAXAK; S. P. KHATKAR, P. B. DOON: *Highly efficient, orange light emanating Sm(III) complexes with furan functionalized ligand for high quality illumination in display devices.* Optical Materials, 132:112765, 2022.

[110] A. CHAUHAN; S. SAINI; R. KUMAR; D. KUMAR, R. LANGYAN: *Luminescence features of mononuclear Sm(III) complexes with heterocyclic ligands.* Optik - International Journal for Light and Electron Optics, 231:166500, 2021.

[111] R. BARHOUMI; A. AMOKRANE; S. KLYATSKAYA; M. BOERO; M. RUBEN, J.-P. BUCHER: *Screening the 4f-electron spin of $TbPc_2$ single-molecule magnets on metal substrates by ligand channeling.* Nanoscale, 11:21167, 2019.

[112] R. PEDERSON; A. L. WYSOCKI; N. MAYHALL, K. PARK: *Multireference Ab Initio Studies of Magnetic Properties of Terbium-Based Single-Molecule Magnets.* J. Phys. Chem. A, 123(32):6996 – 7006, 2019.

[113] L. GU, R. WU: *Origin of the anomalously low Raman exponents in single molecule magnets.* Physical Review B, 103:014401, 2021.

[114] K. LINGANNA; S. JU; C. BASAVAPOORNIMA; V. VENKATRAMU, C. K. JAYASANKAR: *Luminescence and decay characteristics of Tb^{3+}-doped fluorophosphate glasses.* Journal of Asian Ceramic Societies, 6:82 – 87, 2018.

[115] E. HEMMER; V. HUCH; M. ADLUNG; C. WICKLEDER, S. MATHUR: *Homo- and Heterometallic Terbium Alkoxides - Synthesis, Characterization and Conversion to Luminescent Oxide Nanostructures.* Eur. J. inorg. Chem., 13:2148 – 2157, 2011.

[116] H. NAKAI; J. SEO; K. KITAGAWA; T. GOTO; T. MATSUMOTO, S. OGO: *An oxygen-sensitive luminescent Dy(III) complex.* Dalton Trans., 45:9492, 2016.

[117] O. S. BEREZHNYTSKA; I. O. SAVCHENKO; A. E. HORBENKO; O. O. ROHOVTSOV; N. V. RUSAKOVA, O. K. TRUNOVA: *Synthesis, structure of luminescence complexes*

and metalopolymers of Dy(III) and influence of the nature of substitutes on their emission. Journal of Molecular Structure, 1293:136148, 2023.

[118] S.-G. Wu; Z.-Y. Ruan; G.-Z. Huang; J.-Y. Zheng; V. Vieru; G. Taran; J. Wang; Y.-C. Chen; J.-L. Liu; L. T. A. Ho; L. F. Chibotaru; W. Wernsdorfer; X.-M. Chen, M.-L. Tong: *Field-induced oscillation of magnetization blocking barrier in a holmium metallacrown single-molecule magnet.* Chem, 7:982 –992, 2021.

[119] J. D. Hilgar; M. G. Bernbeck; B. S. Flores, J. D. Rinehart: *Metal-ligand pair anisotropy in a series of mononuclear Er-COT complexes.* Chem. Sci., 9:7204, 2018.

[120] J. J. Le Roy; L. Ungur; I. Korobkov; L. F. Chibotaru, M. Murugesu: *Coupling Strategies to Enhance Single-Molecule Magnet Properties of Erbium-Cyclooctatetraenyl Complexes.* J. Am. Chem. Soc., 136:8003 – 8010, 2014.

[121] N. Chanthima, J. Kaewkhao: *Properties of erbium luminescence in barium borophosphate glasses.* Materials Today, 4:6099 – 6104, 2017.

[122] P. Nekvindova; A. Mackova, J. Cajzl: *Erbium Luminescence in Various Photonic Crystalline and Glass Materials - A Review.* 19th International Conference on Transparent Optical Networks (ICTON), 1:1 – 5, 2017.

[123] V. E. Rodionov; M. Y. Rakhilin, A. A. Zolotovskii: *Modelling of Thulium Ion Luminescence in Zinc Sulphide.* Phys. Stat. Sol. B, 173(2):733 – 738, 1992.

[124] S. B. Meshkova; Z. M. Topilova; D. V. Bol'shoi, N. A. Nazarenko: *Luminescence of Trivalent Thulium Ions in Complexes with β-Diketones.* Journal of Applied Spectroscopy, 67(5):893 – 897, 2000.

[125] O. A. Blackburn; M. Tropiano; T. J. Sorensen; J. Thom; A. Beeby; L. M. Bushby; D. Parker; L. S. Natrajan, S. Faulkner: *Luminescence and upconversion from thulium(III) species in solution.* Phys. Chem. Chem. Phys., 14(38):13378 – 13384, 2012.

[126] Y. Sun, J.-L. Zhang Y. Ning; J. Tang; Y.-W. Liu; J. jing;: *Highly luminescent, biocompatible ytterbium(III) complexes as near-infrared fluorophores for living cell imaging.* Chem. Sci., 9:3742, 2018.

[127] F. Guegan; J. Jung; B. Le Guennic; F. Riobe; O. Maury; B. Gillon; J.-F. Jacquot; Y. Guyot; C. Morell, D. Luneau: *Evidencing under-barrier*

phenomena in a Yb(III) SMM: a joint luminescence/neutron diffraction/SQUID study. Inorg. Chem. Front., 6:3152 – 3157, 2019.

[128] M. W. Mara; D. S. Tatum; A.-M. March; G. Doumy; E. G. Moore, K. N. Raymond: *Energy Transfer from Antenna Ligand to Europium(III) Followed Using Ultrafast Optical and X-ray Spectroscopy.* J. Am. Chem. Soc., 141:11071 – 11081, 2019.

[129] J.-S.-Kang; Y.-K. Jeong; Y. S. Shim; S. Rout; K. T. Leung; Y. Sohn, J.-G. Kang: *Structures, and luminescence and magnetic properties of Ln(III) complexes bearing dibenzoylmethane ligand (Ln = Eu and Gd).* Journal of Luminescence, 178:368 – 374, 2016.

[130] S. Miyazaki; K. Goushi; Y. Kitagawa; Y. Hasegawa; C. Adachi; K. Miyata, K. Onda: *highly efficient light harvesting of a Eu(III) complex in a host-guest film by triplet sensitization.* Chem. Sci., 14:6867 – 6875, 2023.

[131] M. Tsurui, Y. Hasegawa Y. kitagawa;: *Bright red emission with high color purity from Eu(III) complexes with π-conjugated polycyclic aromatic ligands and their sensing applications.* RSC Adv., 12:810 – 821, 2022.

[132] M. H. V. Werts; R. T. F. jukes, J. W. Verhoeven: *The emission spectrum and the radiative lifetime of Eu^{3+} in luminescent lanthanide complexes.* Phys. Chem. Chem. Phys., 4:1542 – 1548, 2002.

[133] D. Imbert; M. Cantuel; J.-C. G. Bünzli; G. Bernardinelli, C. Piguet: *Extending Lifetimes of Lanthanide-Based Near-Infrared Emitters (Nd, Yb) in the Millisecond Range through Cr(III) Sensitization in Discrete Bimetallic Edifices.* J. Am. Chem. Soc., 125(51):15698 – 15699, 2003.

[134] R. E. Mor; T. Ohana; A. Borne; Y. Diskin-Posner; M. Asher; O. Yaffe; A. Shanzer, B. Dayan: *Tapered Optical Fibers Coated with Rare-Earth Complexes for Quantum Applications.* ACS Photonics, 9:2676 – 2682, 2022.

[135] X.-S. Ke; B.-Y. Yang; X. Cheng; S. L.-F. Chan, J.-L. Zhang: *Ytterbium(III) Porpholactones: β-Lactonization of Porphyrin Ligands Enhances Sensitization Efficiency of Lanthanide Near-Infrared Luminescence.* Chem. Eur. J., 20:4324 – 4333, 2014.

[136] N. M. Shavaleev; R. Scopelliti; F. Gumy, J.-C. Bünzli: *Surprisingly Bright Near-Ifrared Luminescence and Short Radiative Lifetimes of Ytterbium in Hetero-Binuclear Yb-Na Chelates.* Inorg. Chem., 48:7937 – 7946, 2009.

[137] S. Püschel; S. Kalusniak; C. Kränkel, H. Tanaka: *Temperature-dependent radiative lifetime of Yb:YLF: refined cross sections and potential for laser cooling.* Optics Express, 29:11106 – 11120, 2021.

[138] K. R. Meihaus, J. R. Long: *Magnetic Blocking at 10 K and a Dipolar-Mediated Avalanche in Salts of the Bis(η^8-cyclooctatetraenide) Complex [Er(COT)$_2$]$^-$.* J. Am. Chem. Soc., 135:17952 – 17957, 2013.

[139] M. Zhong; M. P. Hedges; R. L. Ahlefeldt; J. G. Bartholomew; S. E. Beavan; S. M. Wittig; J. J. Longdell, M. J. Sellars: *Optically addressable nuclear spins in a solid with a six-hour coherence time.* Nature, 517:177 – 180, 2015.

9 Appendix

Table 9.1: Crystallographic details for **1-La** and **1-Ce**.

	1-La	**1-Ce**
formula	$La(NO_3)_3(C_{18}N_6H_{12})(CH_3OH)$	$Ce(NO_3)_3(C_{18}N_6H_{12})(CH_3OH)$
formula weight	669.32	670.53
colour	colourless	yellowish
shape	block	plate
crystal dimensions [mm]	0.170 x 0.091 x 0.085	0.194 x 0.177 x 0.019
T [K]	180	180
crystal system	triclinic	triclinic
space group	$P\bar{1}$	$P\bar{1}$
a [Å]	8.7676(4)	9.1606(5)
b [Å]	10.2763(5)	11.3285(6)
c [Å]	13.6794(7)	12.1041(6)
α [°]	98.328(4)	75.800(4)
β [°]	98.634(4)	71.342(4)
γ [°]	96.711(4)	82.471(4)
V [$Å^3$]	1193.51(10)	1151.85(11)
Z	2	2
Z'	1	1
$D_{calc.}$ [g cm^{-3}]	1.862	1.933
μ [mm^{-1}]	1.865	2.054
radiation type	Mo K_α	Mo K_α
wavelength [Å]	0.71073	0.71073
GooF	1.068	1.084
R_{int} [%]	8.91	7.61
wR_2 [%]	10.36	10.76
R_1 [%]	4.16	4.44

Table 9.2: Crystallographic details for **1-Pr**.

	1-Pr
formula	$Pr(NO_3)_3(C_{18}N_6H_{12})(CH_3OH)$
formula weight	671.32
colour	greenish
shape	plate
crystal dimensions [mm]	0.333 x 0.124 x 0.019
T [K]	180
crystal system	triclinic
space group	$P\bar{1}$
a [Å]	9.1399(4)
b [Å]	11.3179(5)
c [Å]	12.0778(6)
α [°]	75.835(4)
β [°]	71.410(4)
γ [°]	82.537(4)
V [$Å^3$]	1146.36(10)
Z	2
Z'	1
$D_{calc.}$ [g cm^{-3}]	1.945
μ [mm^{-1}]	2.203
radiation type	Mo K_α
wavelength [Å]	0.71073
GooF	1.051
R_{int} [%]	7.84
wR_2 [%]	10.96
R_1 [%]	4.27

Table 9.3: Crystallographic details for **2_-Nd** and **2_-Sm**.

	2_-Nd	**2_-Sm**
formula	$Nd(NO_3)_3(C_{18}N_6H_{12})$	$Sm(NO_3)_3(C_{18}N_6H_{12})$
formula weight	642.61	648.72
colour	pinkish	colourless
shape	needle	block
crystal dimensions [mm]	0.240 x 0.040 x 0.030	0.286 x 0.106 x 0.095
T [K]	180	180
crystal system	triclinic	monoclinic
space group	$P\bar{1}$	$P2_1/c$
a [Å]	10.7373(4)	11.1790(2)
b [Å]	11.3278(4)	10.79670(10)
c [Å]	17.9420(6)	18.0733(3)
α [°]	85.794(3)	90
β [°]	85.958(3)	94.3540(10)
γ [°]	87.736(3)	90
V [Å^3]	2169.70(13)	2175.08(6)
Z	4	4
Z'	2	1
$D_{calc.}$ [g cm^{-3}]	1.967	1.981
μ [mm^{-1}]	13.076	2.774
radiation type	Ga K_α	Mo K_α
wavelength [Å]	1.34143	0.71073
GooF	1.106	1.040
R_{int} [%]	38.0	5.00
wR_2 [%]	28.78	7.84
R_1 [%]	7.35	3.12

Table 9.4: Crystallographic details for **2_-Eu** and **2_-Gd**.

	2_-Eu	**2_-Gd**
formula	$Eu(NO_3)_3(C_{18}N_6H_{12})$	$Gd(NO_3)_3(C_{18}N_6H_{12})$
formula weight	650.33	655.62
colour	colourless	colourless
shape	needle	block
crystal dimensions [mm]	0.379 x 0.064 x 0.048	0.160 x 0.140 x 0.078
T [K]	180	180
crystal system	monoclinic	monoclinic
space group	$P2_1/c$	$P2_1/c$
a [Å]	11.1803(2)	11.1722(2)
b [Å]	10.8029(2	10.8000(2)
c [Å]	18.0552(3)	18.0260(3)
α [°]	90	90
β [°]	94.264(2)	94.225(1)
γ [°]	90	90
V [Å^3]	2174.66(7)	2169.10(7)
Z	4	4
Z'	1	1
$D_{calc.}$ [g cm^{-3}]	1.986	2.008
μ [mm^{-1}]	2.958	3.132
radiation type	Mo K_α	Mo K_α
wavelength [Å]	0.71073	0.71073
GooF	1.033	1.091
R_{int} [%]	6.05	7.08
wR_2 [%]	9.23	9.47
R_1 [%]	3.39	3.67

Table 9.5: Crystallographic details for **$2_\wedge$-Eu** and **$2_\wedge$-Gd**.

	$2_\wedge$-Eu	**$2_\wedge$-Gd**
formula	$Eu(NO_3)_3(C_{18}N_6H_{12})$	$Gd(NO_3)_3(C_{18}N_6H_{12})$
formula weight	650.33	655.62
colour	colourless	colourless
shape	block	block
crystal dimensions [mm]	0.211 x 0.124 x 0.056	0.294 x 0.228 x 0.074
T [K]	180	180
crystal system	triclinic	triclinic
space group	$P\bar{1}$	$P\bar{1}$
a [Å]	8.6450(5)	8.6368(5)
b [Å]	9.2078(5)	9.2186(4)
c [Å]	14.1581(8)	14.1407(7
α [°]	78.383(4)	78.338(4
β [°]	79.974(5)	79.922(4)
γ [°]	80.490(4)	80.374(4)
V [Å^3]	1077.12(11)	1075.42(10)
Z	2	2
Z'	1	1
$D_{calc.}$ [g cm^{-3}]	2.005	2.025
μ [mm^{-1}]	2.986	3.158
radiation type	Mo K$_\alpha$	Mo K$_\alpha$
wavelength [Å]	0.71073	0.71073
GooF	1.120	1.086
R_{int} [%]	6.99	7.52
wR_2 [%]	9.73	8.97
R_1 [%]	3.68	3.56

Table 9.6: Crystallographic details for **$\mathbf{2}_{\wedge}$-Tb** and **$\mathbf{2}_{\wedge}$-Dy**.

	$\mathbf{2}_{\wedge}$-Tb	**$\mathbf{2}_{\wedge}$-Dy**
formula	$Tb(NO_3)_3(C_{18}N_6H_{12})$	$Dy(NO_3)_3(C_{18}N_6H_{12})$
formula weight	657.30	660.87
colour	colourless	colourless
shape	block	block
crystal dimensions [mm]	0.249 x 0.108 x 0.077	0.181 x 0.094 x 0.050
T [K]	180	180
crystal system	triclinic	triclinic
space group	$P\bar{1}$	$P\bar{1}$
a [Å]	8.6133(4)	8.6024(6)
b [Å]	9.2356(5)	9.2462(5)
c [Å]	14.1183(6)	14.1380(9)
α [°]	78.283(4)	78.196(5)
β [°]	79.833(4)	79.701(6)
γ [°]	80.175(4)	79.939(5)
V [Å^3]	1071.79(9)	1071.82(12)
Z	2	2
Z'	1	1
$D_{calc.}$ [g cm^{-3}]	2.037	2.048
μ [mm^{-1}]	3.374	3.561
radiation type	Mo K_α	Mo K_α
wavelength [Å]	0.71073	0.71073
GooF	1.120	1.107
R_{int} [%]	8.31	7.11
wR_2 [%]	10.05	14.93
R_1 [%]	3.96	5.38

Table 9.7: Crystallographic details for **$\mathbf{2}_{\wedge}$-Ho** and **$\mathbf{2}_{\wedge}$-Y**.

	$\mathbf{2}_{\wedge}$-Ho	**$\mathbf{2}_{\wedge}$-Y**
formula	$Ho(NO_3)_3(C_{18}N_6H_{12})$	$Y(NO_3)_3(C_{18}N_6H_{12})$
formula weight	663.30	587.28
colour	pinkish	colourless
shape	block	block
crystal dimensions [mm]	0.183 x 0.078 x 0.026	0.180 x 0.050 x 0.030
T [K]	180	180
crystal system	triclinic	triclinic
space group	$P\bar{1}$	$P\bar{1}$
a [Å]	8.5891(5)	8.5916(4)
b [Å]	9.2549(6)	9.2518(5)
c [Å]	14.0807(7)	14.0736(8)
α [°]	78.163(5)	78.174(4)
β [°]	79.720(4)	79.586(4)
γ [°]	80.027(5)	79.929(4)
V [Å^3]	1067.01(11)	1065.80(10)
Z	2	2
Z’	1	1
$D_{calc.}$ [g cm^{-3}]	2.065	1.830
μ [mm^{-1}]	3.783	3.023
radiation type	Mo K_α	Ga K_α
wavelength [Å]	0.71073	1.34143
GooF	1.018	1.087
R_{int} [%]	10.48	1.087
wR_2 [%]	12.24	6.53
R_1 [%]	4.95	2.24

Table 9.8: Crystallographic details for **$2_\wedge$-Er** and **$2_\wedge$-Tm**.

	$2_\wedge$-Er	**$2_\wedge$-Tm**
formula	$Er(NO_3)_3(C_{18}N_6H_{12})$	$Tm(NO_3)_3(C_{18}N_6H_{12})$
formula weight	665.63	667.30
colour	colourless	colourless
shape	block	needle
crystal dimensions [mm]	0.440 x 0.173 x 0.061	0.379 x 0.054 x 0.021
T [K]	180	180
crystal system	triclinic	triclinic
space group	$P\bar{1}$	$P\bar{1}$
a [Å]	8.5812(5)	8.5742(5)
b [Å]	9.2609(4)	9.2729(6)
c [Å]	14.0753(8	14.0458(9
α [°]	78.157(4)	78.076(5)
β [°]	79.571(5)	79.644(5)
γ [°]	79.910(4)	79.883(5)
V [Å^3]	1065.53(10)	1063.66(12)
Z	2	2
Z’	1	1
$D_{calc.}$ [g cm^{-3}]	2.075	2.083
μ [mm^{-1}]	4.014	4.246
radiation type	Mo K_α	Mo K_α
wavelength [Å]	0.71073	0.71073
GooF	1.149	1.065
R_{int} [%]	7.59	11.58
wR_2 [%]	9.82	14.93
R_1 [%]	3.78	5.70

Table 9.9: Crystallographic details for **3-Yb** and **3-Lu**.

	3-Yb	**3-Lu**
formula	$Yb(NO_3)_3(C_{18}N_6H_{12}) \cdot CHCl_3$	$Lu(NO_3)_3(C_{18}N_6H_{12}) \cdot CHCl_3$
formula weight	790.77	792.70
colour	colourless	colourless
shape	needle	needle
crystal dimensions [mm]	0.160 x 0.150 x 0.140	0.257 x 0.079 x 0.039
T [K]	180	180
crystal system	monoclinic	monoclinic
space group	$C2/c$	$C2/c$
a [Å]	27.510(3)	31.7466(10)
b [Å]	12.7874(10	12.8128(2)
c [Å]	15.7335(12)	15.7261(5
α [°]	90	90
β [°]	115.168(6	128.256(5)
γ [°]	90	90
V [Å^3]	5009.4(7)	5025.28(15)
Z	8	8
Z’	1	1
$D_{calc.}$ [g cm^{-3}]	2.097	2.096
μ [mm^{-1}]	4.125	4.321
radiation type	Mo K$_\alpha$	Mo K$_\alpha$
wavelength [Å]	0.71073	0.71073
GooF	0.879	1.043
R_{int} [%]	4.82	7.81
wR_2 [%]	4.43	9.47
R_1 [%]	2.27	3.78

Table 9.10: Crystallographic details for **4_-La** and **4_-Ce**.

	4_-La	**4_-Ce**
formula	$La(NO_3)_3(C_{22}N_6H_{20})$	$Ce(NO_3)_3(C_{22}N_6H_{20})$
formula weight	693.38	694.59
colour	colourless	yellow
shape	needle	needle
crystal dimensions [mm]	0.347 x 0.080 x 0.073	0.488 x 0.062 x 0.059
T [K]	180	180
crystal system	monoclinic	monoclinic
space group	$P2_1/c$	$P2_1/c$
a [Å]	16.0914(11)	16.0829(3)
b [Å]	9.1256(4)	9.1322(1)
c [Å]	19.0568(10)	19.0036(4)
α [°]	90	90
β [°]	113.741(7)	113.732(2)
γ [°]	90	90
V [Å^3]	2561.6(3)	2555.08(9)
Z	4	4
Z’	1	1
$D_{calc.}$ [g cm^{-3}]	1.798	1.806
μ [mm^{-1}]	1.739	1.853
radiation type	Mo K_α	Mo K_α
wavelength [Å]	0.71073	0.71073
GooF	1.058	1.041
R_{int} [%]	12.42	5.60
wR_2 [%]	17.16	7.26
R_1 [%]	7.15	3.03

Table 9.11: Crystallographic details for **4_-Pr** and **4_-Nd**.

	4_-Pr	**4_-Nd**
formula	$Pr(NO_3)_3(C_{22}N_6H_{20})$	$Nd(NO_3)_3(C_{22}N_6H_{20})$
formula weight	695.38	698.71
colour	greenish	colourless
shape	needle	needle
crystal dimensions [mm]	0.366 x 0.123 x 0.100	0.159 x 0.075 x 0.061
T [K]	180	180
crystal system	monoclinic	monoclinic
space group	$P2_1/c$	$P2_1/c$
a [Å]	16.0644(3)	16.0758(4)
b [Å]	9.13000(10)	9.1447(2)
c [Å]	18.9428(3)	18.9290(5)
α [°]	90	90
β [°]	113.728(2)	113.755(3)
γ [°]	90	90
V [Å^3]	2543.44(8)	2546.96(12)
Z	4	4
Z'	1	1
$D_{calc.}$ [g cm^{-3}]	1.816	1.822
μ [mm^{-1}]	1.987	2.110
radiation type	Mo K_α	Mo K_α
wavelength [Å]	0.71073	0.71073
GooF	1.055	1.028
R_{int} [%]	4.66	8.85
wR_2 [%]	7.49	8.26
R_1 [%]	2.99	3.85

Table 9.12: Crystallographic details for **4_-Eu** and **4_-Gd**.

	4_-Eu	**4_-Gd**
formula	$Eu(NO_3)_3(C_{22}N_6H_{20})$	$Gd(NO_3)_3(C_{22}N_6H_{20})$
formula weight	706.44	711.72
colour	colourless	colourless
shape	needle	block
crystal dimensions [mm]	0.368 x 0.061 x 0.047	0.100 x 0.036 x 0.017
T [K]	180	180
crystal system	monoclinic	monoclinic
space group	$P2_1/c$	$P2_1/c$
a [Å]	16.0264(3)	16.0174(7)
b [Å]	9.1482(1)	9.1524(3)
c [Å]	18.7882(3)	18.7586(8)
α [°]	90	90
β [°]	113.719(2)	113.763(5)
γ [°]	90	90
V [Å^3]	2521.91(8)	2516.8(2)
Z	4	4
Z'	1	1
$D_{calc.}$ [g cm^{-3}]	1.861	1.878
μ [mm^{-1}]	2.559	2.707
radiation type	Mo K$_\alpha$	Mo K$_\alpha$
wavelength [Å]	0.71073	0.71073
GooF	1.034	0.989
R_{int} [%]	6.12	16.27
wR_2 [%]	7.93	11.48
R_1 [%]	3.13	5.44

Table 9.13: Crystallographic details for **4_-Dy** and **4_-Ho**.

	4_-Dy	**4_-Ho**
formula	$Dy(NO_3)_3(C_{22}N_6H_{20})$	$Ho(NO_3)_3(C_{22}N_6H_{20})$
formula weight	716.97	719.40
colour	colourless	colourless
shape	needle	needle
crystal dimensions [mm]	0.282 x 0.062 x 0.039	0.303 x 0.062 x 0.047
T [K]	180	180
crystal system	monoclinic	monoclinic
space group	$P2_1/c$	$P2_1/c$
a [Å]	16.0735(4)	15.9752(3)
b [Å]	9.2075(2)	9.1609(1)
c [Å]	18.7592(5)	18.6683(3)
α [°]	90	90
β [°]	113.785(3)	113.721(2)
γ [°]	90	90
V [$Å^3$]	2540.50(12)	2501.24(8)
Z	4	4
Z'	1	1
$D_{calc.}$ [g cm^{-3}]	1.875	1.910
μ [mm^{-1}]	3.013	3.236
radiation type	Mo K_α	Mo K_α
wavelength [Å]	0.71073	0.71073
GooF	1.024	1.056
R_{int} [%]	9.71	7.99
wR_2 [%]	8.87	9.89
R_1 [%]	4.07	3.80

Table 9.14: Crystallographic details for **4_-Y**.

	4_-Y
formula	$Y(NO_3)_3(C_{22}N_6H_{20})$
formula weight	643.38
colour	colourless
shape	needle
crystal dimensions [mm]	0.346 x 0.068 x 0.065
T [K]	180
crystal system	monoclinic
space group	$P2_1/c$
a [Å]	15.9930(4)
b [Å]	9.1657(2)
c [Å]	18.6673(4)
α [°]	90
β [°]	113.709(3)
γ [°]	90
V [Å^3]	2505.43(11)
Z	4
Z'	1
$D_{calc.}$ [g cm^{-3}]	1.706
μ [mm^{-1}]	2.400
radiation type	Mo K$_\alpha$
wavelength [Å]	0.71073
GooF	1.035
R_{int} [%]	8.62
wR_2 [%]	10.16
R_1 [%]	4.26

Table 9.15: Crystallographic details for **$\mathbf{2}_{\wedge}$-La** and **$\mathbf{2}_{\wedge}$-Ce**.

	$\mathbf{4}_{\wedge}$-La	**$\mathbf{4}_{\wedge}$-Ce**
formula	$La(NO_3)_3(C_{22}N_6H_{20})$	$Ce(NO_3)_3(C_{22}N_6H_{20})$
formula weight	693.38	694.59
colour	colourless	yellow
shape	needle	needle
crystal dimensions [mm]	0.316 x 0.098 x 0.089	0.329 x 0.177 x 0.034
T [K]	180	180
crystal system	monoclinic	monoclinic
space group	$P2_1/c$	$P2_1/c$
a [Å]	7.7003(1)	7.70000(10)
b [Å]	19.7053(2)	19.6377(3)
c [Å]	17.2023(2)	17.1912(3)
α [°]	90	90
β [°]	102.452(1)	102.617(2)
γ [°]	90	90
V [$Å^3$]	2548.82(5)	2536.71(7)
Z	4	4
Z’	1	1
$D_{calc.}$ [g cm^{-3}]	1.807	1.819
μ [mm^{-1}]	1.747	1.866
radiation type	Mo K_α	Mo K_α
wavelength [Å]	0.71073	0.71073
GooF	1.090	1.054
R_{int} [%]	7.50	5.78
wR_2 [%]	9.76	8.12
R_1 [%]	3.63	3.13

Table 9.16: Crystallographic details for **$2_\wedge$-Pr** and **$2_\wedge$-Nd**.

	$4_\wedge$-Pr	**$4_\wedge$-Nd**
formula	$Pr(NO_3)_3(C_{22}N_6H_{20})$	$Nd(NO_3)_3(C_{22}N_6H_{20})$
formula weight	695.38	698.71
colour	yellowish	colourless
shape	plate	needle
crystal dimensions [mm]	0.285 x 0.181 x 0.018	0.254 x 0.055 x 0.030
T [K]	180	180
crystal system	monoclinic	monoclinic
space group	$P2_1/c$	$P2_1/c$
a [Å]	7.7015(2)	7.7026(2)
b [Å]	19.5981(4)	19.5530(6)
c [Å]	17.1969(3)	17.1741(5)
α [°]	90	90
β [°]	102.762(2)	102.788(3)
γ [°]	90	90
V [Å^3]	2531.49(10)	2522.41(13)
Z	4	4
Z'	1	1
$D_{calc.}$ [g cm^{-3}]	1.825	1.840
μ [mm^{-1}]	1.996	2.130
radiation type	Mo K$_\alpha$	Mo K$_\alpha$
wavelength [Å]	0.71073	0.71073
GooF	1.040	1.002
R_{int} [%]	8.12	11.13
wR_2 [%]	10.45	10.21
R_1 [%]	3.98	4.52

Table 9.17: Crystallographic details for $\mathbf{2}_{\wedge}$**-Sm** and $\mathbf{2}_{\wedge}$**-Eu**.

	$\mathbf{4}_{\wedge}$**-Sm**	$\mathbf{4}_{\wedge}$**-Eu**
formula	$Sm(NO_3)_3(C_{22}N_6H_{20})$	$Eu(NO_3)_3(C_{22}N_6H_{20})$
formula weight	704.82	706.43
colour	colourless	colourless
shape	needle	needle
crystal dimensions [mm]	0.463 x 0.043 x 0.032	0.290 x 0.071 x 0.008
T [K]	180	180
crystal system	monoclinic	monoclinic
space group	$P2_1/n$	$P2_1/n$
a [Å]	7.68980(10)	7.6902(3)
b [Å]	19.4806(3)	19.4453(10)
c [Å]	17.1463(3	17.1342(5)
α [°]	90	90
β [°]	102.853(2)	102.784(4)
γ [°]	90	90
V [Å^3]	2504.19(7)	2498.70(18)
Z	4	4
Z'	1	1
$D_{calc.}$ [g cm^{-3}]	1.869	1.878
μ [mm^{-1}]	2.417	2.583
radiation type	Mo K_α	Mo K_α
wavelength [Å]	0.71073	0.71073
GooF	1.067	1.034
R_{int} [%]	9.99	16.92
wR_2 [%]	10.40	12.04
R_1 [%]	4.29	6.11

Table 9.18: Crystallographic details for **$2_{\wedge}$-Gd** and **$2_{\wedge}$-Tb**.

	$4_{\wedge}$-Gd	**$4_{\wedge}$-Tb**
formula	$Gd(NO_3)_3(C_{22}N_6H_{20})$	$Tb(NO_3)_3(C_{22}N_6H_{20})$
formula weight	711.72	713.39
colour	colourless	colourless
shape	needle	needle
crystal dimensions [mm]	0.199 x 0.101 x 0.020	0.409 x 0.125 x 0.051
T [K]	180	180
crystal system	monoclinic	monoclinic
space group	$P2_1/n$	$P2_1/n$
a [Å]	7.6891(2)	7.67940(10)
b [Å]	19.4373(5)	19.3950(3)
c [Å]	17.1118(3)	17.0916(2)
α [°]	90	90
β [°]	102.750(2)	102.643(2)
γ [°]	90	90
V [Å^3]	2494.39(10)	2483.93(6)
Z	4	4
Z'	1	1
$D_{calc.}$ [g cm^{-3}]	1.895	1.908
μ [mm^{-1}]	2.732	2.920
radiation type	Mo K_α	Mo K_α
wavelength [Å]	0.71073	0.71073
GooF	1.034	1.063
R_{int} [%]	10.21	5.41
wR_2 [%]	9.78	8.07
R_1 [%]	4.25	3.10

Table 9.19: Crystallographic details for **2**$_{\wedge}$**-Dy** and **2**$_{\wedge}$**-Ho**.

	4$_{\wedge}$**-Dy**	**4**$_{\wedge}$**-Ho**
formula	$Dy(NO_3)_3(C_{22}N_6H_{20})$	$Ho(NO_3)_3(C_{22}N_6H_{20})$
formula weight	716.97	719.40
colour	colourless	pinkish
shape	needle	needle
crystal dimensions [mm]	0.422 x 0.098 x 0.021	0.362 x 0.062 x 0.024
T [K]	180	180
crystal system	monoclinic	monoclinic
space group	$P2_1/n$	$P2_1/n$
a [Å]	7.6785(2)	7.6797(2)
b [Å]	19.3699(4)	19.3563(5)
c [Å]	17.0746(4)	17.0572(4)
α [°]	90	90
β [°]	102.582(2)	102.596(2)
γ [°]	90	90
V [Å^3]	2478.55(10)	2474.54(11)
Z	4	4
Z'	1	1
$D_{calc.}$ [g cm^{-3}]	1.921	1.931
μ [mm^{-1}]	3.088	3.271
radiation type	Mo K_α	Mo K_α
wavelength [Å]	0.71073	0.71073
GooF	1.081	1.034
R_{int} [%]	9.99	9.74
wR_2 [%]	11.67	9.24
R_1 [%]	4.77	4.14

Table 9.20: Crystallographic details for **$\mathbf{4}_{\Lambda}$-Y**.

	$\mathbf{4}_{\Lambda}$-Y
formula	$Y(NO_3)_3(C_{22}N_6H_{20})$
formula weight	643.38
colour	colourless
shape	needle
crystal dimensions [mm]	0.175 x 0.059 x 0.017
T [K]	180
crystal system	monoclinic
space group	$P2_1/n$
a [Å]	7.6712(2)
b [Å]	19.3500(5)
c [Å]	17.0643(4)
α [°]	90
β [°]	102.568(2)
γ [°]	90
V [Å^3]	2472.29(11)
Z	4
Z'	1
$D_{calc.}$ [g cm^{-3}]	1.729
μ [mm^{-1}]	2.432
radiation type	Mo K$_\alpha$
wavelength [Å]	0.71073
GooF	0.987
R_{int} [%]	17.65
wR_2 [%]	15.84
R_1 [%]	6.05

Table 9.21: Crystallographic details for **5-Er** and **5-Tm**.

	5-Er	**5-Tm**
formula	$Er(NO_3)_3(C_{22}N_6H_{20}) \cdot CHCl_3$	$Tm(NO_3)_3(C_{22}N_6H_{20}) \cdot CHCl_3$
formula weight	841.10	842.77
colour	pinkish	colourless
shape	needle	needle
crystal dimensions [mm]	0.179 x 0.087 x 0.024	0.478 x 0.132 x 0.075
T [K]	180	180
crystal system	triclinic	triclinic
space group	$P\bar{1}$	$P\bar{1}$
a [Å]	9.0664(5)	9.0494(4)
b [Å]	12.0587(6)	12.0382(5)
c [Å]	13.7208(8)	13.7144(4)
α [°]	75.550(5)	75.576(3)
β [°]	87.281(4)	87.269(3)
γ [°]	86.483(4)	86.409(3)
V [$Å^3$]	1449.09(14)	1443.30(10)
Z	2	2
Z'	1	1
$D_{calc.}$ [g cm^{-3}]	1.928	1.939
μ [mm^{-1}]	3.241	3.420
radiation type	Mo K_α	Mo K_α
wavelength [Å]	0.71073	0.71073
GooF	1.034	1.094
R_{int} [%]	7.76	6.36
wR_2 [%]	10.47	9.18
R_1 [%]	4.47	3.44

Table 9.22: Crystallographic details for **5-Yb** and **5-Lu**.

	5-Yb	**5-Lu**
formula	$Yb(NO_3)_3(C_{22}N_6H_{20}) \cdot CHCl_3$	$Lu(NO_3)_3(C_{22}N_6H_{20}) \cdot CHCl_3$
formula weight	846.88	848.81
colour	colourless	colourless
shape	needle	needle
crystal dimensions [mm]	0.273 x 0.057 x 0.032	0.265 x 0.044 x 0.010
T [K]	180	180
crystal system	triclinic	triclinic
space group	$P\bar{1}$	$P\bar{1}$
a [Å]	9.0530(5)	9.0497(6)
b [Å]	12.0223(6)	12.0207(10)
c [Å]	13.7124(7)	13.7156(12)
α [°]	75.616(5)	75.572(7)
β [°]	87.287(4)	87.223(6)
γ [°]	86.403(4)	86.362(6)
V [Å^3]	1442.02(13)	1441.2(2)
Z	2	2
Z'	1	1
$D_{calc.}$ [g cm^{-3}]	1.950	1.956
μ [mm^{-1}]	3.589	3.772
radiation type	Mo K_α	Mo K_α
wavelength [Å]	0.71073	0.71073
GooF	0.995	0.981
R_{int} [%]	9.60	6.80
wR_2 [%]	10.23	13.49
R_1 [%]	4.39	6.02

Table 9.23: Continuous Shape measures for **1-Ln**

polyhedron	symmetry	**1-La**	**1-Ce**	**1-Pr**
HP-11	D_{11h}	34.802	33.816	33.932
DPY-11	C_{10v}	22.657	23.609	23.625
EBPY-11	D_{9h}	17.856	16.369	16.440
JCPPR-11	C_{5v}	9.159	7.700	7.638
JCPAPR-11	C_{5v}	**3.774**	**4.283**	**4.274**
JAPPR-11	C_{2v}	10.394	11.919	11.945
JASPC-11	C_s	6.153	6.665	6.568

Table 9.24: Continuous Shape measures for **2_{-}-Ln**

polyhedron	symmetry	**2_{-}-Nd**	**2_{-}-Sm**	**2_{-}-Eu**	**2_{-}-Gd**
DP-10	D_{10h}	35.607	35.607	35.608	35.696
EPY-10	C_{9v}	25.515	25.515	25.472	25.507
OBPY-10	D_{8h}	17.338	17.338	17.181	17.117
PPR-10	D_{5h}	11.240	11.240	11.348	11.417
PAPR-10	D_{5d}	9.892	9.892	10.003	10.001
JBCCU-10	D_{4h}	8.377	8.377	8.434	8.396
JBCSAPR-10	D_{4d}	5.235	5.235	5.103	4.955
JMBIC-10	C_{2v}	6.371	6.371	6.372	6.374
JATDI-10	C_{3v}	18.563	18.563	18.542	18.595
JSPC-10	C_{2v}	3.354	3.354	3.269	3.188
SDD-10	D_2	2.378	2.378	2.488	2.533
TD-10	C_{2v}	**1.548**	**1.548**	**1.600**	**1.639**
HD-10	D_{4h}	5.473	5.473	5.567	5.608

Table 9.25: Continuous Shape measures for **$2_{\wedge}$-Ln**

polyhedron	symmetry	**$2_{\wedge}$-Eu**	**$2_{\wedge}$-Gd**	**$2_{\wedge}$-Tb**	**$2_{\wedge}$-Dy**	**$2_{\wedge}$-Ho**	**$2_{\wedge}$-Y**	**$2_{\wedge}$-Er**	**$2_{\wedge}$-Tm**
DP-10	D_{10h}	35.441	35.526	35.543	35.497	35.579	35.638	35.694	35.562
EPY-10	C_{9v}	24.010	24.004	24.003	24.069	24.006	23.958	23.971	23.983
OBPY-10	D_{8h}	16.094	16.075	16.073	15.949	15.990	16.014	15.903	16.009
PPR-10	D_{5h}	10.637	10.586	10.620	10.709	10.711	10.652	10.725	10.728
PAPR-10	D_{5d}	10.853	10.853	10.857	10.950	10.953	10.883	10.972	10.934
JBCCU-10	D_{4h}	9.477	9.494	9.512	9.556	9.473	9.453	9.488	9.421
JBCSAPR-10	D_{4d}	4.170	4.130	4.112	4.040	3.957	3.962	3.927	3.888
JMBIC-10	C_{2v}	7.462	7.478	7.507	7.564	7.601	7.570	7.651	7.600
JATDI-10	C_{3v}	19.505	19.462	19.410	19.332	19.354	19.397	19.363	19.267
JSPC-10	C_{2v}	**3.520**	**3.453**	**3.429**	**3.384**	**3.284**	**3.286**	**3.261**	**3.247**
SDD-10	D_2	4.808	4.812	4.834	4.891	4.827	4.819	4.849	4.849
TD-10	C_{2v}	3.843	3.839	3.862	3.899	3.861	3.845	3.862	3.879
HD-10	D_{4h}	6.661	6.708	6.714	6.799	6.774	6.764	6.795	6.789

Table 9.26: Continuous Shape measures for **3-Ln**

polyhedron	symmetry	**3-Yb**	**3-Lu**
EP-9	D_{9h}	36.681	36.665
OPY-9	C_{8v}	22.605	22.584
HBPY-9	D_{7h}	18.218	18.269
JTC-9	C_{3v}	14.184	14.127
JCCU-9	C_{4v}	8.963	9.031
CCU-9	C_{4v}	7.499	7.567
JCSAPR-9	C_{4v}	3.381	3.273
CSAPR-9	C_{4v}	2.100	2.008
JTCTPR-9	D_{3h}	3.636	3.530
TCTPR-9	D_{3h}	**1.865**	**1.792**
JTDIC-9	C_{3v}	9.819	9.856
HH-9	C_{2v}	10.498	10.502
MFF-9	C_s	2.520	2.437

Table 9.27: Continuous Shape measures for **4_-Ln**

polyhedron	symmetry	**4_-La**	**4_-Ce**	**4_-Pr**	**4_-Nd**	**4_-Eu**	**4_-Gd**	**4_-Dy**	**4_-Ho**	**4_-Y**
DP-10	D_{10h}	34.969	35.161	35.244	35.353	35.647	35.755	35.965	35.947	35.996
EPY-10	C_{9v}	22.607	22.587	22.614	22.664	22.684	22.735	22.781	22.777	22.818
OBPY-10	D_{8h}	15.681	15.869	15.947	16.096	16.370	16.519	16.654	16.702	16.708
PPR-10	D_{5h}	10.796	10.795	10.823	10.776	10.714	10.660	10.666	10.713	10.658
PAPR-10	D_{5d}	11.759	11.739	11.721	11.687	11.760	11.785	11.839	11.842	11.851
JBCCU-10	D_{4h}	10.913	10.995	11.014	11.011	11.200	11.221	11.427	11.402	11.359
JBCSAPR-10	D_{4d}	5.491	5.492	5.477	5.444	5.489	5.464	5.590	5.532	5.479
JMBIC-10	C_{2v}	7.590	7.565	7.527	7.519	7.540	7.534	7.636	7.584	7.609
JATDI-10	C_{3v}	17.930	17.979	18.063	18.175	18.153	18.183	18.059	18.168	18.117
JSPC-10	C_{2v}	**2.972**	**2.843**	**2.773**	**2.686**	**2.532**	**2.465**	**2.472**	**2.360**	**2.358**
SDD-10	D_2	5.547	5.381	5.300	5.229	5.087	5.053	5.059	4.973	4.994
TD-10	C_{2v}	5.102	4.945	4.847	4.781	4.626	4.593	4.586	4.489	4.516
HD-10	D_{4h}	7.969	7.998	7.995	8.001	8.151	8.161	8.309	8.333	8.309

Table 9.28: Continuous Shape measures for $\mathbf{4}_{\wedge}$**-Ln**

polyhedron	symmetry	$\mathbf{4}_{\wedge}$**-La**	$\mathbf{4}_{\wedge}$**-Ce**	$\mathbf{4}_{\wedge}$**-Pr**	$\mathbf{4}_{\wedge}$**-Nd**	$\mathbf{4}_{\wedge}$**-Sm**	$\mathbf{4}_{\wedge}$**-Eu**
DP-10	D_{10h}	34.961	35.134	35.360	35.365	35.704	35.843
EPY-10	C_{9v}	22.101	22.131	22.224	22.158	22.237	22.344
OBPY-10	D_{8h}	16.564	16.415	16.370	16.312	16.286	16.289
PPR-10	D_{5h}	9.761	9.784	9.770	9.890	9.904	9.949
PAPR-10	D_{5d}	11.935	11.920	11.889	11.912	11.948	11.877
JBCCU-10	D_{4h}	12.343	12.372	12.390	12.438	12.530	12.558
JBCSAPR-10	D_{4d}	6.211	5.991	5.860	5.728	5.443	5.382
JMBIC-10	C_{2v}	8.388	8.372	8.362	8.297	8.269	8.314
JATDI-10	C_{3v}	16.970	17.079	17.114	17.215	17.328	17.389
JSPC-10	C_{2v}	**3.263**	**3.144**	**3.073**	**3.028**	**2.874**	**2.802**
SDD-10	D_2	5.343	5.219	5.136	5.087	4.980	4.916
TD-10	C_{2v}	5.309	5.169	5.074	5.014	4.872	4.784
HD-10	D_{4h}	9.112	9.149	9.153	9.189	9.272	9.285
polyhedron	symmetry	$\mathbf{4}_{\wedge}$**-Gd**	$\mathbf{4}_{\wedge}$**-Tb**	$\mathbf{4}_{\wedge}$**-Dy**	$\mathbf{4}_{\wedge}$**-Ho**	$\mathbf{4}_{\wedge}$**-Y**	
DP-10	D_{10h}	35.840	35.991	35.997	36.036	36.057	
EPY-10	C_{9v}	22.251	22.363	22.300	22.316	22.343	
OBPY-10	D_{8h}	16.218	16.168	16.157	16.176	16.124	
PPR-10	D_{5h}	10.003	10.084	10.127	10.218	10.132	
PAPR-10	D_{5d}	12.047	12.052	12.149	12.248	12.186	
JBCCU-10	D_{4h}	12.728	12.769	12.904	13.064	12.980	
JBCSAPR-10	D_{4d}	5.187	5.089	4.979	4.796	4.831	
JMBIC-10	C_{2v}	8.193	8.198	8.126	8.065	8.117	
JATDI-10	C_{3v}	17.478	17.493	17.582	17.640	17.644	
JSPC-10	C_{2v}	**2.793**	**2.750**	**2.732**	**2.709**	**2.701**	
SDD-10	D_2	4.926	4.900	4.890	4.880	4.856	
TD-10	C_{2v}	4.789	4.758	4.737	4.716	4.696	
HD-10	D_{4h}	9.422	9.443	9.580	9.689	9.600	

Table 9.29: Continuous Shape measures for **5-Ln**

polyhedron	symmetry	**5-Er**	**5-Tm**	**5-Yb**	**5-Lu**
DP-10	D_{10h}	35.938	35.940	35.919	36.162
EPY-10	C_{9v}	23.566	23.569	23.601	23.532
OBPY-10	D_{8h}	16.580	16.544	16.620	16.699
PPR-10	D_{5h}	10.488	10.498	10.494	10.523
PAPR-10	D_{5d}	11.106	11.156	11.165	11.317
JBCCU-10	D_{4h}	11.492	11.558	11.696	11.779
JBCSAPR-10	D_{4d}	5.975	5.940	5.898	5.807
JMBIC-10	C_{2v}	8.006	8.063	8.042	8.048
JATDI-10	C_{3v}	17.788	17.772	17.699	17.717
JSPC-10	C_{2v}	**2.508**	**2.483**	**2.483**	**2.459**
SDD-10	D_2	4.683	4.671	4.694	4.683
TD-10	C_{2v}	4.512	4.491	4.493	4.443
HD-10	D_{4h}	8.226	8.293	8.380	8.455

Table 9.30: Best fit parameters to a generalized Debeye model for **1-Ce**

T [K]	χ_T [cm^3 mol^{-1}]	χ_S [cm^3 mol^{-1}]	τ [s]	α
2.0	1.87190E-01	6.06046E-03	2.00483E-04	1.44546E-01
2.2	1.71277E-01	3.77595E-03	1.66422E-04	1.46249E-01
2.4	1.59510E-01	2.99979E-03	1.42422E-04	1.40944E-01
2.6	1.47665E-01	1.31932E-02	1.34381E-04	9.56811E-02
2.8	1.37682E-01	9.78118E-03	1.07956E-04	1.03414E-01
3.0	1.28656E-01	1.49943E-02	9.65769E-05	7.06055E-02
3.2	1.21137E-01	1.73033E-02	8.42952E-05	5.52330E-02
3.4	1.14737E-01	8.98877E-03	6.53431E-05	7.05378E-02
3.6	1.08782E-01	2.39204E-02	6.75031E-05	1.58527E-02

Table 9.31: Best fit parameters to a generalized Debeye model for **4-Ce**

T [K]	χ_T [cm^3 mol^{-1}]	χ_S [cm^3 mol^{-1}]	τ [s]	α
2.0	2.06096E-01	1.09598E-02	2.12518E-02	3.24837E-01
2.2	1.84110E-01	9.41406E-03	1.60948E-02	3.03254E-01
2.4	1.69252E-01	7.66866E-03	1.29649E-02	2.87308E-01
2.6	1.54812E-01	7.04361E-03	1.02998E-02	2.72818E-01
2.8	1.41731E-01	6.66049E-03	7.84895E-03	2.47159E-01
3.0	1.31812E-01	5.78757E-03	6.32898E-03	2.18798E-01
3.2	1.23616E-01	5.80282E-03	4.75601E-03	2.15257E-01
3.4	1.15280E-01	5.80929E-03	3.72337E-03	1.76834E-01
3.6	1.08810E-01	3.33008E-03	2.71490E-03	1.76508E-01
3.8	1.02428E-01	2.74930E-03	1.98536E-03	1.50250E-01
4.0	9.73275E-02	3.56236E-03	1.48594E-03	1.29537E-01
4.4	8.82261E-02	1.85873E-03	8.50606E-04	1.03209E-01
4.8	8.07256E-02	6.98156E-04	4.78116E-04	8.56065E-02
5.2	7.49760E-02	2.11398E-26	2.93862E-04	5.41120E-02
5.6	6.99806E-02	1.87560E-22	1.79845E-04	2.25769E-02
6.0	6.51386E-02	2.60579E-34	1.18279E-04	9.12362E-03
6.4	6.09979E-02	1.68429E-24	7.89101E-05	1.44311E-03
6.8	5.80341E-02	4.32957E-03	5.72809E-05	3.65776E-03

Table 9.32: Best fit parameters to a generalized Debeye model for **2-Nd**

T [K]	χ_T [cm^3 mol^{-1}]	χ_S [cm^3 mol^{-1}]	τ [s]	α
2.0	3.01042E-01	1.46294E-02	2.68259E-03	1.20482E-01
2.2	2.74571E-01	1.33399E-02	2.06675E-03	1.09583E-01
2.4	2.55987E-01	1.29681E-02	1.66344E-03	1.04646E-01
2.6	2.36822E-01	1.34286E-02	1.25794E-03	8.71033E-02
2.8	2.21011E-01	1.23423E-02	9.48740E-04	8.05123E-02
3.0	2.08277E-01	1.18561E-02	6.92098E-04	6.34951E-02
3.2	1.95062E-01	1.10806E-02	5.02881E-04	5.07414E-02
3.4	1.85058E-01	1.09621E-02	3.63571E-04	4.53035E-02
3.6	1.75660E-01	9.09523E-03	2.65459E-04	4.50214E-02
3.8	1.67447E-01	9.35308E-03	1.90676E-04	3.06806E-02
4.0	1.60041E-01	1.17475E-02	1.41181E-04	1.52664E-02
4.4	1.47004E-01	6.13545E-03	7.30810E-05	2.54712E-02
4.8	1.36054E-01	1.15982E-02	4.14044E-05	1.08853E-02

Table 9.33: Best fit parameters to a generalized Debeye model for **4-Nd**

T [K]	χ_T [cm^3 mol^{-1}]	χ_S [cm^3 mol^{-1}]	τ [s]	α
2.0	2.53299E-01	9.62809E-02	5.07933E-03	1.69090E-01
2.2	2.31409E-01	9.26722E-02	3.70390E-03	1.38438E-01
2.4	2.16084E-01	8.30132E-02	2.48703E-03	1.42287E-01
2.6	2.00177E-01	7.26745E-02	1.46115E-03	1.19954E-01
2.8	1.86620E-01	6.43423E-02	8.28366E-04	1.09659E-01
3.0	1.75859E-01	5.52957E-02	4.34876E-04	1.08567E-01
3.2	1.65371E-01	4.09787E-02	2.14377E-04	1.15965E-01
3.4	1.56636E-01	3.81220E-02	1.14549E-04	1.03601E-01

Table 9.34: Best fit parameters to a generalized Debeye model for **2-Tb**

T [K]	χ_T [cm^3 mol^{-1}]	χ_S [cm^3 mol^{-1}]	τ [s]	α
2.6	3.169797898	1.577409072	0.038949026	0.441029293
2.8	3.008340092	1.620165035	0.03478794	0.427924256
3.0	2.879662691	1.666074056	0.032526216	0.432891
3.2	2.753837944	1.706854009	0.02989297	0.445082998
3.4	2.628790912	1.740164359	0.028256914	0.441016265
3.6	2.528749858	1.748312917	0.028104055	0.453560017

Table 9.35: Best fit parameters to a generalized Debeye model for **4-Tb**

T [K]	χ_T [cm^3 mol^{-1}]	χ_S [cm^3 mol^{-1}]	τ [s]	α
2.0	3.582078872	1.425992612	0.01426608	0.505676982
2.2	3.432032623	1.472406499	0.012860876	0.488511526
2.4	3.312092877	1.497955405	0.011454484	0.488372498
2.6	3.147000465	1.563834975	0.010236638	0.46878753
2.8	3.000376959	1.63168385	0.009796413	0.459692226
3.0	2.864864701	1.689943685	0.009073423	0.459470119
3.2	2.735992071	1.739254584	0.008589243	0.460702692
3.4	2.621044558	1.769398554	0.00836	0.467415767

Table 9.36: Best fit parameters to a generalized Debeye model for **2-Dy**

T [K]	χ_T [cm^3 mol^{-1}]	χ_S [cm^3 mol^{-1}]	τ [s]	α
2.0	0.00446	3.93534E-4	0.00827	0.39539
2.2	0.00409	3.77921E-4	0.00631	0.3934
2.4	0.00379	3.63615E-4	0.00486	0.39121
2.6	0.0035	3.73898E-4	0.00354	0.37198
2.8	0.00326	3.87864E-4	0.00265	0.35227
3.0	0.00304	4.07763E-4	0.00202	0.3295
3.2	0.00285	4.28706E-4	0.00159	0.30625
3.4	0.00269	4.50511E-4	0.00126	0.28028
3.6	0.00254	4.67002E-4	0.00101	0.25556
3.8	0.00241	4.82287E-4	8.24757E-4	0.23019
4.0	0.0023	4.9243E-4	6.74214E-4	0.20573
4.2	0.00219	4.9854E-4	5.55121E-4	0.18326
4.4	0.0021	5.04005E-4	4.60887E-4	0.16211
4.6	0.00202	5.06501E-4	3.85304E-4	0.14395
4.8	0.00194	5.0538E-4	3.19428E-4	0.12662
5.0	0.00187	5.02269E-4	2.67215E-4	0.11235
5.2	0.0018	4.99463E-4	2.24289E-4	0.0985
5.4	0.00174	4.98047E-4	1.89449E-4	0.08609
5.6	0.00169	4.91893E-4	1.5983E-4	0.07691
5.8	0.00163	4.84626E-4	1.35106E-4	0.06816
6.0	0.00158	4.81593E-4	1.14909E-4	0.05994
6.2	0.00154	4.70625E-4	9.72273E-5	0.05601
6.4	0.00149	4.62907E-4	8.28153E-5	0.04895

Table 9.37: Best fit parameters to a generalized Debeye model for the first maximum observed in **4-Dy**

T [K]	χ_T [cm^3 mol^{-1}]	χ_S [cm^3 mol^{-1}]	τ [s]	α
2.0	0.00449	0.00306	0.01671	0.2444
2.2	0.00411	0.00288	0.0148	0.22083
2.4	0.00383	0.00273	0.01294	0.2067
2.6	0.00355	0.00257	0.01073	0.19532
2.8	0.00331	0.00244	0.00872	0.18579
3.0	0.0031	0.00232	0.0071	0.17345
3.2	0.00292	0.00221	0.00552	0.1707
3.4	0.00276	0.00213	0.00464	0.15328
3.6	0.00262	0.00204	0.0038	0.14264
3.8	0.00249	0.00195	0.003	0.14059
4.0	0.00237	0.00188	0.00233	0.12745
4.4	0.00218	0.00174	0.00155	0.11252
4.8	0.00201	0.00162	0.00103	0.10653
5.2	0.00187	0.00151	7.01204E-4	0.08485
5.6	0.00175	0.00142	4.9675E-4	0.07556
6.0	0.00164	0.00134	3.59068E-4	0.06043
6.4	0.00155	0.00127	2.65833E-4	0.04183
6.8	0.00147	0.0012	1.92362E-4	0.04883
7.2	0.00139	0.00116	1.5026E-4	0.03249
7.6	0.00133	0.00111	1.14645E-4	0.01641
8.0	0.00127	0.00105	8.30621E-5	0.01957
8.4	0.00121	0.00102	6.42913E-5	0.01936
8.8	0.00116	9.58257E-4	4.35975E-5	0.03248

Table 9.38: Best fit parameters to a generalized Debeye model for the second maximum observed in **4-Dy**

T [K]	χ_T [cm^3 mol^{-1}]	χ_S [cm^3 mol^{-1}]	τ [s]	α
2.0	0.00375	1.54459E-4	1.28163E-4	0.44234
2.2	0.00345	3.12548E-5	8.96548E-5	0.44405
2.4	0.00323	1.04841E-16	7.04242E-5	0.43423
2.6	0.00297	4.31927E-33	5.38451E-5	0.4095
2.8	0.00276	1.00802E-16	4.14109E-5	0.38162
3.0	0.00259	8.48172E-30	3.11714E-5	0.35742
3.2	0.00243	1.14813E-16	2.24707E-5	0.32285
3.4	0.00229	1.56923E-35	1.5114E-5	0.30255
3.6	0.00218	1E-28	9.17309E-6	0.31132
3.8	0.00208	6.66571E-16	5.18288E-6	0.33903

Table 9.39: Best fit parameters to a generalized Debeye model for **2-Er**

T [K]	χ_T [cm^3 mol^{-1}]	χ_S [cm^3 mol^{-1}]	τ [s]	α
2.0	3.665535539	0.404500783	0.001621167	0.33556683
2.2	3.368267896	0.363800292	0.001313866	0.335453407
2.4	3.148717387	0.342504216	0.001104765	0.329792532
2.6	2.919790511	0.3301371	0.000866009	0.3073389
2.8	2.729829978	0.343554843	0.000691247	0.272163544
3.0	2.564821999	0.349926166	0.000552676	0.242234244
3.2	2.41951577	0.358078632	0.000443287	0.211683008
3.4	2.29195435	0.362434081	0.000355356	0.184725581
3.6	2.177456937	0.372297391	0.000287727	0.155070978
3.8	2.074825679	0.363773221	0.000229846	0.137505496
4.0	1.981020123	0.367975196	0.000186443	0.113755226
4.2	1.898209374	0.369626964	0.00015249	0.093821629
4.4	1.822544826	0.377808037	0.000125845	0.075176119
4.8	1.685681982	0.330305075	8.22037E-05	0.058515511
5.2	1.572577568	0.343071945	5.72963E-05	0.039678719
5.6	1.470876435	0.298729604	3.88516E-05	0.031577588

Table 9.40: Best fit parameters to a generalized Debeye model for **5-Er**

T [K]	χ_T [cm^3 mol^{-1}]	χ_S [cm^3 mol^{-1}]	τ [s]	α
2.0	3.560330382	0.746501092	0.002917717	0.365901103
2.2	3.311787748	0.668918349	0.00232614	0.378470066
2.4	3.119721779	0.61163269	0.001904541	0.385104817
2.6	2.921203064	0.483990434	0.001269327	0.399696393
2.8	2.737575841	0.447159387	0.000896158	0.379201039
3.0	2.579133087	0.37404852	0.000637086	0.367506927
3.2	2.433801373	0.313516667	0.000450971	0.347562946
3.4	2.306242708	0.2684534	0.000331342	0.325837293
3.6	2.193910291	0.21191006	0.000248143	0.310384474
3.8	2.088608134	0.236555532	0.000204765	0.269036743
4.0	1.995572642	0.233062736	0.000166792	0.241243486
4.4	1.838423428	0.233645466	0.000114754	0.18312579
4.8	1.709367135	0.263482068	8.32386E-05	0.129300859

Table 9.41: Best fit parameters to a generalized Debeye model for **3-Yb**

T [K]	χ_T [cm^3 mol^{-1}]	χ_S [cm^3 mol^{-1}]	τ [s]	α
2.0	0.855179373	0.034291387	0.002739422	0.223836744
2.2	0.779269213	0.029832163	0.001968989	0.211171213
2.4	0.722445331	0.029688277	0.001502711	0.19285321
2.6	0.666032961	0.030732236	0.001033524	0.161546252
2.8	0.618832053	0.03283765	0.000700983	0.123913307
3.0	0.579607571	0.031327113	0.000489459	0.105946805
3.2	0.545922473	0.035240317	0.000343402	0.073230832
3.4	0.515178087	0.024010035	0.000236466	0.074345311
3.6	0.489137786	0.029499224	0.00017183	0.051936115
3.8	0.464737315	0.022498592	0.000124072	0.042878895
4.0	0.443721704	0.020532624	8.9462E-05	0.04310845

Table 9.42: Best fit parameters to a generalized Debeye model for **5-Yb**

T [K]	χ_T [cm^3 mol^{-1}]	χ_S [cm^3 mol^{-1}]	τ [s]	α
2.0	0.70442817	0.147698763	0.005012436	0.236351382
2.2	0.642172074	0.135532206	0.003651087	0.236058304
2.4	0.596275811	0.120814899	0.00270629	0.231087683
2.6	0.550343515	0.106097123	0.00185713	0.227194118
2.8	0.512278458	0.096218034	0.001325457	0.214600114
3.0	0.480136996	0.08062712	0.000912994	0.211993155
3.2	0.451705709	0.075103968	0.000666697	0.20184061
3.4	0.425854207	0.069187433	0.000494736	0.184892924
3.6	0.403537852	0.062859044	0.000365325	0.180721136
3.8	0.384189192	0.054818792	0.000277916	0.174011822
4.0	0.364978229	0.051935816	0.000215824	0.158352311
4.4	0.334509284	0.062401264	0.000150166	0.106122816
4.8	0.308781073	0.06371778	0.000100883	0.077981343
5.2	0.286943172	0.069459622	7.4186E-05	0.056074757

Table 9.43: CASSCF calculated Kramers doublet states for **1-Ce**

State	ΔE [cm^{-1}]	ΔE [K]	g$_x$	g$_y$	g$_z$	Wavefunction composition
1	0	0	0.0389	0.3325	3.5631	$\pm 87\% \lvert 5/2\rangle \pm 12\% \lvert 1/2\rangle \pm 1\% \lvert 3/2\rangle$
2	130.87	188.19	0.8404	1.7327	2.6835	$\pm 51\% \lvert 3/2\rangle \mp 45\% \lvert 1/2\rangle \mp 4\% \lvert 5/2\rangle$
3	267.63	384.85	0.2430	0.5333	3.6480	$\mp 48\% \lvert 3/2\rangle \mp 43\% \lvert 1/2\rangle \mp 9\% \lvert 5/2\rangle$

Table 9.44: CASSCF calculated Kramers doublet states for **4$_\wedge$-Ce**

State	ΔE [cm^{-1}]	ΔE [K]	g$_x$	g$_y$	g$_z$	Wavefunction composition
1	0	0	0.9843	1.3667	3.2981	$\pm 87\% \lvert 5/2\rangle \pm 11\% \lvert 3/2\rangle \pm 2\% \lvert 1/2\rangle$
2	245.18	352.57	0.6653	1.3299	2.7873	$\mp 54\% \lvert 3/2\rangle \pm 38\% \lvert 1/2\rangle \pm 8\% \lvert 5/2\rangle$
3	369.45	531.27	0.3311	1.0166	3.1222	$\pm 61\% \lvert 1/2\rangle \mp 35\% \lvert 3/2\rangle \mp 5\% \lvert 5/2\rangle$

Table 9.45: CASSCF calculated Kramers doublet states for **4$_-$-Ce**

State	ΔE [cm^{-1}]	ΔE [K]	g$_x$	g$_y$	g$_z$	Wavefunction composition
1	0	0	0.9156	1.3308	3.3048	$\mp 87\% \lvert 5/2\rangle \pm 9\% \lvert 3/2\rangle \pm 4\% \lvert 1/2\rangle$
2	226.75	326.07	0.4021	0.8266	3.6973	$\mp 68\% \lvert 1/2\rangle \mp 24\% \lvert 3/2\rangle \mp 8\% \lvert 5/2\rangle$
3	322.37	463.57	0.2043	1.0491	3.1386	$\mp 67\% \lvert 3/2\rangle \mp 28\% \lvert 1/2\rangle \mp 5\% \lvert 5/2\rangle$

Table 9.46: CASSCF calculated Kramers doublet states for $\mathbf{2}_{-}$**-Nd**

State	ΔE [cm^{-1}]	ΔE [K]	g$_x$	g$_y$	g$_z$	Wavefunction composition
1	0	0	0.8516	1.2702	4.0241	$\pm 41\%\,\|9/2\rangle \pm 41\%\,\|3/2\rangle \pm 12\%\,\|7/2\rangle \mp 5\%\,\|1/2\rangle \mp 1\%\,\|5/2\rangle$
2	39.91	57.39	0.1537	0.8106	3.4538	$\pm 70\%\,\|5/2\rangle \pm 11\%\,\|9/2\rangle \mp 11\%\,\|1/2\rangle \pm 9\%\,\|7/2\rangle$
3	127.07	182.73	2.5607	2.1046	0.8788	$\pm 44\%\,\|7/2\rangle \pm 43\%\,\|1/2\rangle \pm 13\%\,\|3/2\rangle$
4	371.49	534.20	0.7894	0.9497	3.8140	$\pm 39\%\,\|9/2\rangle \pm 31\%\,\|3/2\rangle \pm 16\%\,\|7/2\rangle \mp 13\%\,\|5/2\rangle$
5	489.57	704.00	3.5961	2.8034	0.6031	$\mp 41\%\,\|1/2\rangle \pm 19\%\,\|7/2\rangle \pm 17\%\,\|5/2\rangle \mp 15\%\,\|3/2\rangle \mp 8\%\,\|9/2\rangle$

Table 9.47: CASSCF calculated Kramers doublet states for $\mathbf{4}_{\wedge}$**-Nd**

State	ΔE [cm^{-1}]	ΔE [K]	g$_x$	g$_y$	g$_z$	Wavefunction composition
1	0	0	0.9364	1.9026	3.9280	$\mp 42\%\,\|9/2\rangle \mp 37\%\,\|5/2\rangle \pm 9\%\,\|3/2\rangle \pm 8\%\,\|1/2\rangle \mp 5\%\,\|7/2\rangle$
2	47.63	68.49	0.8918	1.7398	2.9817	$\pm 43\%\,\|3/2\rangle \pm 17\%\,\|7/2\rangle \mp 15\%\,\|9/2\rangle \pm 14\%\,\|5/2\rangle \mp 11\%\,\|1/2\rangle$
3	140.56	202.13	1.0550	2.1281	4.0018	$\mp 31\%\,\|5/2\rangle \mp 22\%\,\|1/2\rangle \pm 19\%\,\|7/2\rangle \pm 14\%\,\|3/2\rangle \pm 14\%\,\|9/2\rangle$
4	322.88	464.30	3.7238	2.4965	0.1990	$\mp 36\%\,\|7/2\rangle \pm 20\%\,\|3/2\rangle \pm 17\%\,\|1/2\rangle \pm 16\%\,\|9/2\rangle \pm 10\%\,\|5/2\rangle$
5	444.40	639.05	1.1396	1.5415	4.3064	$\mp 42\%\,\|1/2\rangle \mp 23\%\,\|7/2\rangle \mp 15\%\,\|3/2\rangle \mp 14\%\,\|9/2\rangle \mp 7\%\,\|5/2\rangle$

Table 9.48: CASSCF calculated Kramers doublet states for $\mathbf{4}_{-}$**-Nd**

State	ΔE [cm^{-1}]	ΔE [K]	g$_x$	g$_y$	g$_z$	Wavefunction composition
1	0	0	1.1627	1.7130	3.8823	$\mp 43\%\,\|9/2\rangle \mp 27\%\,\|3/2\rangle \mp 15\%\,\|5/2\rangle \pm 11\%\,\|1/2\rangle \mp 5\%\,\|7/2\rangle$
2	50.51	72.63	0.2776	0.4138	3.7508	$\pm 43\%\,\|5/2\rangle \mp 19\%\,\|1/2\rangle \pm 17\%\,\|3/2\rangle \pm 15\%\,\|7/2\rangle \pm 6\%\,\|9/2\rangle$
3	101.28	145.64	0.4262	1.7672	3.2850	$\mp 45\%\,\|7/2\rangle \mp 21\%\,\|1/2\rangle \mp 15\%\,\|3/2\rangle \pm 11\%\,\|5/2\rangle \mp 8\%\,\|9/2\rangle$
4	342.20	492.08	3.0649	2.5625	0.2240	$\mp 25\%\,\|3/2\rangle \mp 23\%\,\|9/2\rangle \mp 20\%\,\|7/2\rangle \pm 18\%\,\|5/2\rangle \mp 14\%\,\|1/2\rangle$
5	455.59	655.14	1.4011	1.6000	4.0089	$\pm 36\%\,\|1/2\rangle \pm 19\%\,\|9/2\rangle \pm 17\%\,\|3/2\rangle \pm 16\%\,\|7/2\rangle \mp 13\%\,\|5/2\rangle$

Table 9.49: CASSCF calculated Kramers doublet states for **$\mathbf{2}_{-}$-Sm**

State	ΔE [cm^{-1}]	ΔE [K]	g$_x$	g$_y$	g$_z$	Wavefunction composition
1	0	0	0.1443	0.3677	0.8194	$\pm65\%\,\vert 5/2\rangle \pm 31\%\,\vert 1/2\rangle \mp 4\%\,\vert 3/2\rangle$
2	43.42	62.44	0.1634	0.5702	1.0500	$\mp56\%\,\vert 3/2\rangle \pm 25\%\,\vert 1/2\rangle \pm 19\%\,\vert 5/2\rangle$
3	102.86	147.91	0.2984	0.4046	1.2205	$\mp44\%\,\vert 1/2\rangle \pm 40\%\,\vert 3/2\rangle \pm 16\%\,\vert 5/2\rangle$

Table 9.50: CASSCF calculated Kramers doublet states for **$\mathbf{4}_{\wedge}$-Sm**

State	ΔE [cm^{-1}]	ΔE [K]	g$_x$	g$_y$	g$_z$	Wavefunction composition
1	0	0	1.0475	0.6268	0.0097	$\mp81\%\,\vert 1/2\rangle \pm 17\%\,\vert 3/2\rangle \pm 2\%\,\vert 5/2\rangle$
2	57.51	82.70	0.2543	0.4093	0.7467	$\mp70\%\,\vert 3/2\rangle \pm 17\%\,\vert 1/2\rangle \pm 13\%\,\vert 5/2\rangle$
3	164.84	237.04	0.0389	0.5104	1.3480	$\pm86\%\,\vert 5/2\rangle \pm 13\%\,\vert 3/2\rangle \pm 2\%\,\vert 1/2\rangle$

Table 9.51: CASSCF calculated Kramers doublet states for **$\mathbf{4}_{-}$-Sm**

State	ΔE [cm^{-1}]	ΔE [K]	g$_x$	g$_y$	g$_z$	Wavefunction composition
1	0	0	1.0293	0.6361	0.0981	$\mp43\%\,\vert 1/2\rangle \mp 41\%\,\vert 3/2\rangle \pm 16\%\,\vert 5/2\rangle$
2	63.91	91.90	0.0142	0.3318	0.8607	$\mp53\%\,\vert 5/2\rangle \pm 40\%\,\vert 3/2\rangle \pm 8\%\,\vert 1/2\rangle$
3	169.40	243.60	0.2259	0.2724	1.3800	$\mp50\%\,\vert 1/2\rangle \mp 31\%\,\vert 5/2\rangle \pm 19\%\,\vert 3/2\rangle$

Table 9.52: CASSCF calculated Kramers doublet states for **$2_\wedge$-Dy**

State	ΔE [cm^{-1}]	ΔE [K]	g_x	g_y	g_z	Wavefunction composition
1	0	0	0.1076	0.2447	17.6824	$\mp 49\% \,\lvert 15/2\rangle \mp 27\% \,\lvert 13/2\rangle \mp 19\% \,\lvert 11/2\rangle \mp 2\% \,\lvert 9/2\rangle \mp 1\% \,\lvert 7/2\rangle$
2	73.92	106.36	0.5441	4.4349	12.3482	$\pm 33\% \,\lvert 5/2\rangle \pm 18\% \,\lvert 3/2\rangle \pm 14\% \,\lvert 9/2\rangle \pm 12\% \,\lvert 7/2\rangle \pm 8\% \,\lvert 13/2\rangle \pm 8\% \,\lvert 11/2\rangle \mp 6\% \,\lvert 1/2\rangle \pm 2\% \,\lvert 15/2\rangle$
3	96.98	139.53	0.5615	3.9907	11.6845	$\pm 32\% \,\lvert 13/2\rangle \pm 23\% \,\lvert 11/2\rangle \mp 21\% \,\lvert 7/2\rangle \mp 9\% \,\lvert 5/2\rangle \pm 5\% \,\lvert 1/2\rangle \mp 5\% \,\lvert 5/2\rangle \mp 4\% \,\lvert 3/2\rangle \pm 1\% \,\lvert 15/2\rangle$
4	127.20	183.01	1.6475	1.6925	11.0635	$\pm 26\% \,\lvert 1/2\rangle \pm 26\% \,\lvert 9/2\rangle \pm 24\% \,\lvert 3/2\rangle \pm 9\% \,\lvert 13/2\rangle \mp 6\% \,\lvert 7/2\rangle \pm 5\% \,\lvert 15/2\rangle \mp 3\% \,\lvert 5/2\rangle \pm 3\% \,\lvert 11/2\rangle$
5	192.06	276.32	0.6192	0.7467	18.6835	$\mp 41\% \,\lvert 15/2\rangle \mp 23\% \,\lvert 11/2\rangle \mp 21\% \,\lvert 13/2\rangle \mp 13\% \,\lvert 9/2\rangle \mp 2\% \,\lvert 7/2\rangle$
6	211.44	304.21	4.7600	6.2307	7.9146	$\mp 29\% \,\lvert 9/2\rangle \pm 20\% \,\lvert 7/2\rangle \mp 20\% \,\lvert 11/2\rangle \mp 19\% \,\lvert 1/2\rangle \mp 5\% \,\lvert 3/2\rangle \pm 4\% \,\lvert 5/2\rangle \mp 2\% \,\lvert 15/2\rangle \mp 2\% \,\lvert 13/2\rangle$
7	278.00	399.98	1.0845	2.6436	10.5132	$\pm 36\% \,\lvert 7/2\rangle \mp 29\% \,\lvert 1/2\rangle \pm 24\% \,\lvert 5/2\rangle \pm 4\% \,\lvert 3/2\rangle \pm 3\% \,\lvert 11/2\rangle \mp 2\% \,\lvert 9/2\rangle \pm 1\% \,\lvert 13/2\rangle$
8	321.09	461.98	0.3546	2.0010	14.7732	$\mp 45\% \,\lvert 3/2\rangle \mp 31\% \,\lvert 5/2\rangle \pm 15\% \,\lvert 1/2\rangle \mp 6\% \,\lvert 9/2\rangle \pm 2\% \,\lvert 7/2\rangle \mp 1\% \,\lvert 13/2\rangle \mp 1\% \,\lvert 15/2\rangle$

Table 9.53: CASSCF calculated Kramers doublet states for $\mathbf{4}_{\Lambda}$**-Dy**

State	ΔE [cm^{-1}]	ΔE [K]	g$_x$	g$_y$	g$_z$	Wavefunction composition
1	0	0	0.4584	1.2248	17.8824	$\mp 81\% \, \vert 15/2\rangle \mp 13\% \, \vert 7/2\rangle \mp 3\% \, \vert 11/2\rangle \mp 1\% \, \vert 9/2\rangle \mp 1\% \, \vert 13/2\rangle \mp 1\% \, \vert 5/2\rangle \mp 1\% \, \vert 3/2\rangle$
2	32.32	46.50	0.1065	0.7873	17.7861	$\mp 32\% \, \vert 9/2\rangle \mp 17\% \, \vert 7/2\rangle \mp 16\% \, \vert 5/2\rangle \mp 15\% \, \vert 11/2\rangle \mp 7\% \, \vert 3/2\rangle \mp 5\% \, \vert 13/2\rangle \mp 4\% \, \vert 15/2\rangle \mp 3\% \, \vert 1/2\rangle$
3	110.49	158.97	2.2813	3.5478	12.0200	$\mp 45\% \, \vert 13/2\rangle \mp 22\% \, \vert 5/2\rangle \mp 18\% \, \vert 7/2\rangle \mp 7\% \, \vert 11/2\rangle \mp 3\% \, \vert 9/2\rangle \mp 2\% \, \vert 3/2\rangle \pm 1\% \, \vert 15/2\rangle \mp 1\% \, \vert 1/2\rangle$
4	147.64	212.42	0.3971	3.5373	12.2716	$\mp 43\% \, \vert 11/2\rangle \mp 27\% \, \vert 9/2\rangle \mp 10\% \, \vert 3/2\rangle \mp 5\% \, \vert 13/2\rangle \pm 5\% \, \vert 7/2\rangle \pm 4\% \, \vert 1/2\rangle \pm 3\% \, \vert 15/2\rangle \mp 3\% \, \vert 5/2\rangle$
5	181.68	261.39	0.8277	2.9986	10.4227	$\pm 27\% \, \vert 9/2\rangle \pm 21\% \, \vert 7/2\rangle \pm 19\% \, \vert 5/2\rangle \pm 11\% \, \vert 11/2\rangle \mp 9\% \, \vert 13/2\rangle \pm 7\% \, \vert 15/2\rangle \mp 3\% \, \vert 1/2\rangle \pm 3\% \, \vert 3/2\rangle$
6	227.43	327.21	2.0118	4.1018	10.0074	$\pm 38\% \, \vert 3/2\rangle \pm 23\% \, \vert 1/2\rangle \pm 17\% \, \vert 7/2\rangle \pm 10\% \, \vert 13/2\rangle \pm 5\% \, \vert 5/2\rangle \mp 3\% \, \vert 9/2\rangle \pm 3\% \, \vert 9/2\rangle \pm 2\% \, \vert 11/2\rangle$
7	279.94	402.77	0.1307	4.3740	10.1902	$\mp 32\% \, \vert 1/2\rangle \pm 25\% \, \vert 5/2\rangle \pm 19\% \, \vert 13/2\rangle \mp 8\% \, \vert 7/2\rangle \pm 6\% \, \vert 3/2\rangle \pm 5\% \, \vert 11/2\rangle \mp 4\% \, \vert 9/2\rangle \pm 1\% \, \vert 15/2\rangle$
8	298.74	429.82	1.4644	4.3275	15.1456	$\mp 34\% \, \vert 1/2\rangle \pm 32\% \, \vert 3/2\rangle \pm 14\% \, \vert 11/2\rangle \pm 9\% \, \vert 5/2\rangle \pm 6\% \, \vert 13/2\rangle \mp 3\% \, \vert 9/2\rangle \pm 1\% \, \vert 7/2\rangle \pm 1\% \, \vert 15/2\rangle$

Table 9.54: CASSCF calculated Kramers doublet states for **4_--Dy**

State	ΔE [cm^{-1}]	ΔE [K]	g$_x$	g$_y$	g$_z$	Wavefunction composition
1	0	0	0.2753	0.4824	17.7344	$\pm 62\%\,\lvert 15/2\rangle \pm 17\%\,\lvert 7/2\rangle \pm 10\%\,\lvert 11/2\rangle \pm 5\%\,\lvert 9/2\rangle \pm 4\%\,\lvert 7/2\rangle \pm 2\%\,\lvert 5/2\rangle$
2	67.56	97.20	1.5085	2.0283	16.5327	$\mp 26\%\,\lvert 5/2\rangle \mp 22\%\,\lvert 3/2\rangle \mp 18\%\,\lvert 9/2\rangle \pm 11\%\,\lvert 1/2\rangle \pm 11\%\,\lvert 7/2\rangle \mp 8\%\,\lvert 11/2\rangle \mp 3\%\,\lvert 13/2\rangle \pm 1\%\,\lvert 15/2\rangle$
3	123.59	177.82	7.1365	4.5378	1.5042	$\mp 35\%\,\lvert 13/2\rangle \pm 18\%\,\lvert 11/2\rangle \mp 15\%\,\lvert 7/2\rangle \pm 15\%\,\lvert 15/2\rangle \mp 5\%\,\lvert 5/2\rangle \mp 5\%\,\lvert 9/2\rangle \mp 4\%\,\lvert 1/2\rangle \mp 3\%\,\lvert 3/2\rangle$
4	132.15	190.14	0.7344	3.4611	8.6322	$\pm 24\%\,\lvert 11/2\rangle \mp 21\%\,\lvert 13/2\rangle \mp 20\%\,\lvert 7/2\rangle \pm 16\%\,\lvert 15/2\rangle \pm 15\%\,\lvert 9/2\rangle \pm 2\%\,\lvert 5/2\rangle \pm 1\%\,\lvert 3/2\rangle \mp 1\%\,\lvert 1/2\rangle$
5	182.70	262.87	0.2439	4.5313	11.7810	$\mp 24\%\,\lvert 9/2\rangle \mp 23\%\,\lvert 3/2\rangle \mp 19\%\,\lvert 1/2\rangle \mp 11\%\,\lvert 5/2\rangle \mp 10\%\,\lvert 7/2\rangle \mp 6\%\,\lvert 11/2\rangle \pm 4\%\,\lvert 13/2\rangle \mp 3\%\,\lvert 15/2\rangle$
6	237.04	341.04	3.1767	4.9014	11.9675	$\mp 31\%\,\lvert 1/2\rangle \mp 16\%\,\lvert 9/2\rangle \mp 15\%\,\lvert 11/2\rangle \mp 14\%\,\lvert 5/2\rangle \mp 13\%\,\lvert 7/2\rangle \mp 8\%\,\lvert 13/2\rangle \mp 3\%\,\lvert 3/2\rangle \mp 1\%\,\lvert 15/2\rangle$
7	296.21	426.17	2.0187	3.4783	11.1244	$\mp 26\%\,\lvert 1/2\rangle \mp 19\%\,\lvert 7/2\rangle \mp 19\%\,\lvert 3/2\rangle \mp 18\%\,\lvert 5/2\rangle \mp 9\%\,\lvert 13/2\rangle \mp 5\%\,\lvert 11/2\rangle \mp 3\%\,\lvert 9/2\rangle \mp 1\%\,\lvert 15/2\rangle$
8	319.70	459.97	1.2735	4.9731	13.1179	$\mp 29\%\,\lvert 3/2\rangle \mp 21\%\,\lvert 5/2\rangle \mp 15\%\,\lvert 9/2\rangle \mp 14\%\,\lvert 11/2\rangle \mp 9\%\,\lvert 7/2\rangle \mp 8\%\,\lvert 1/2\rangle \mp 3\%\,\lvert 13/2\rangle \mp 1\%\,\lvert 15/2\rangle$

Table 9.55: CASSCF calculated Kramers doublet states for $\mathbf{2}_{\wedge}$-**Er**

State	ΔE [cm^{-1}]	ΔE [K]	g_x	g_y	g_z	Wavefunction composition
1	0	0	0.4785	0.7570	14.8531	$\pm71\%\,\lvert 13/2\rangle \pm 13\%\,\lvert 15/2\rangle \pm 8\%\,\lvert 11/2\rangle$ $\pm3\%\,\lvert 5/2\rangle \pm 2\%\,\lvert 7/2\rangle \pm 2\%\,\lvert 9/2\rangle$ $\pm1\%\,\lvert 1/2\rangle \pm 1\%\,\lvert 3/2\rangle$
2	67.93	97.68	1.5199	3.4016	11.3052	$\mp36\%\,\lvert 1/2\rangle \mp 33\%\,\lvert 3/2\rangle \mp 16\%\,\lvert 11/2\rangle$ $\mp10\%\,\lvert 5/2\rangle \pm 2\%\,\lvert 13/2\rangle \pm 1\%\,\lvert 9/2\rangle$ $\pm1\%\,\lvert 7/2\rangle$
3	123.36	177.39	1.6964	4.5707	8.9701	$\pm36\%\,\lvert 1/2\rangle \mp 34\%\,\lvert 11/2\rangle \mp 10\%\,\lvert 9/2\rangle$ $\mp8\%\,\lvert 3/2\rangle \mp 4\%\,\lvert 13/2\rangle \mp 4\%\,\lvert 5/2\rangle$ $\mp3\%\,\lvert 7/2\rangle \mp 1\%\,\lvert 15/2\rangle$
4	201.94	290.39	7.6779	5.1196	0.5437	$\mp22\%\,\lvert 3/2\rangle \mp 19\%\,\lvert 5/2\rangle \mp 19\%\,\lvert 11/2\rangle$ $\mp18\%\,\lvert 1/2\rangle \mp 8\%\,\lvert 13/2\rangle \mp 7\%\,\lvert 9/2\rangle$ $\mp7\%\,\lvert 7/2\rangle \mp 1\%\,\lvert 15/2\rangle$
5	288.50	414.86	2.1998	2.4732	8.6061	$\mp45\%\,\lvert 9/2\rangle \mp 17\%\,\lvert 7/2\rangle \mp 11\%\,\lvert 3/2\rangle$ $\mp7\%\,\lvert 5/2\rangle \pm 7\%\,\lvert 1/2\rangle \mp 7\%\,\lvert 11/2\rangle$ $\mp4\%\,\lvert 13/2\rangle \mp 3\%\,\lvert 15/2\rangle$
6	332.42	478.02	0.7593	3.4723	10.1814	$\mp34\%\,\lvert 5/2\rangle \pm 22\%\,\lvert 15/2\rangle \mp 20\%\,\lvert 3/2\rangle$ $\pm11\%\,\lvert 9/2\rangle \mp 8\%\,\lvert 7/2\rangle \pm 3\%\,\lvert 11/2\rangle$ $\mp2\%\,\lvert 1/2\rangle \mp 1\%\,\lvert 13/2\rangle$
7	344.54	495.45	0.4398	2.9959	10.7954	$\mp41\%\,\lvert 7/2\rangle \mp 23\%\,\lvert 15/2\rangle \mp 13\%\,\lvert 11/2\rangle$ $\mp10\%\,\lvert 9/2\rangle \mp 6\%\,\lvert 13/2\rangle \pm 4\%\,\lvert 5/2\rangle$ $\pm3\%\,\lvert 3/2\rangle$
8	424.15	609.93	0.8352	1.3201	12.7400	$\pm38\%\,\lvert 15/2\rangle \pm 21\%\,\lvert 7/2\rangle \mp 19\%\,\lvert 5/2\rangle$ $\pm14\%\,\lvert 9/2\rangle \mp 5\%\,\lvert 13/2\rangle \pm 3\%\,\lvert 3/2\rangle$ $\pm1\%\,\lvert 11/2\rangle$

Table 9.56: CASSCF calculated Kramers doublet states for **5-Er**

State	ΔE [cm^{-1}]	ΔE [K]	g_x	g_y	g_z	Wavefunction composition
1	0	0	1.5974	1.8593	13.4834	$\pm 44\% \, |15/2\rangle \pm 21\% \, |11/2\rangle \mp 17\% \, |9/2\rangle$ $\mp 13\% \, |7/2\rangle \pm 3\% \, |5/2\rangle \mp 1\% \, |3/2\rangle$ $\pm 1\% \, |1/2\rangle$
2	45.15	64.93	7.1918	5.7546	4.2751	$\mp 32\% \, |7/2\rangle \mp 24\% \, |9/2\rangle \pm 21\% \, |5/2\rangle$ $\mp 7\% \, |3/2\rangle \mp 7\% \, |1/2\rangle \mp 7\% \, |13/2\rangle$ $\mp 2\% \, |15/2\rangle \pm 1\% \, |11/2\rangle$
3	133.93	192.59	0.1809	2.6902	8.2247	$\mp 33\% \, |5/2\rangle \pm 23\% \, |7/2\rangle \pm 16\% \, |3/2\rangle$ $\mp 12\% \, |9/2\rangle \mp 7\% \, |11/2\rangle \mp 5\% \, |1/2\rangle$ $\mp 3\% \, |13/2\rangle \mp 2\% \, |15/2\rangle$
4	181.03	260.32	0.3432	4.1239	9.7859	$\pm 22\% \, |9/2\rangle \pm 20\% \, |7/2\rangle \mp 15\% \, |3/2\rangle$ $\pm 13\% \, |5/2\rangle \pm 13\% \, |15/2\rangle \pm 11\% \, |11/2\rangle$ $\pm 7\% \, |1/2\rangle$
5	255.68	367.67	0.1913	3.0438	8.8552	$\pm 27\% \, |3/2\rangle \pm 18\% \, |1/2\rangle \pm 16\% \, |5/2\rangle$ $\pm 15\% \, |9/2\rangle \pm 12\% \, |11/2\rangle \pm 6\% \, |7/2\rangle$ $\pm 4\% \, |15/2\rangle \pm 3\% \, |13/2\rangle$
6	320.60	461.02	0.5635	3.7153	8.7782	$\pm 24\% \, |13/2\rangle \pm 22\% \, |3/2\rangle \mp 21\% \, |1/2\rangle$ $\mp 13\% \, |15/2\rangle \mp 9\% \, |11/2\rangle \mp 6\% \, |9/2\rangle$ $\mp 6\% \, |5/2\rangle \pm 1\% \, |7/2\rangle$
7	339.57	488.30	1.3346	3.9854	9.5304	$\pm 36\% \, |13/2\rangle \pm 24\% \, |1/2\rangle \pm 16\% \, |11/2\rangle$ $\pm 12\% \, |15/2\rangle \mp 7\% \, |5/2\rangle \pm 3\% \, |3/2\rangle$ $\pm 2\% \, |9/2\rangle \pm 1\% \, |7/2\rangle$
8	408.87	587.96	0.8319	1.5402	13.9956	$\pm 27\% \, |13/2\rangle \pm 25\% \, |11/2\rangle \pm 19\% \, |1/2\rangle$ $\pm 11\% \, |15/2\rangle \pm 9\% \, |3/2\rangle \pm 4\% \, |7/2\rangle$ $\pm 4\% \, |9/2\rangle \pm 2\% \, |5/2\rangle$

Table 9.57: CASSCF calculated Kramers doublet states for **3-Yb**

State	ΔE [cm^{-1}]	ΔE [K]	g$_x$	g$_y$	g$_z$	Wavefunction composition
1	0	0	0.6206	0.9856	6.5331	$\pm 80\% \lvert 7/2\rangle \mp 18\% \lvert 3/2\rangle$ $\mp 2\% \lvert 1/2\rangle \mp 1\% \lvert 5/2\rangle$
2	80.00	115.04	1.6671	2.6872	4.3210	$\mp 46\% \lvert 5/2\rangle \mp 37\% \lvert 1/2\rangle$ $\mp 13\% \lvert 3/2\rangle \pm 4\% \lvert 7/2\rangle$
3	164.96	237.21	0.4501	1.8079	5.1832	$\mp 49\% \lvert 3/2\rangle \pm 32\% \lvert 5/2\rangle$ $\mp 13\% \lvert 7/2\rangle \pm 5\% \lvert 1/2\rangle$
4	279.47	401.88	0.5119	1.6171	6.5441	$\pm 56\% \lvert 1/2\rangle \pm 21\% \lvert 5/2\rangle$ $\pm 21\% \lvert 3/2\rangle \pm 3\% \lvert 7/2\rangle$

Table 9.58: CASSCF calculated Kramers doublet states for **5-Yb**

State	ΔE [cm^{-1}]	ΔE [K]	g$_x$	g$_y$	g$_z$	Wavefunction composition
1	0	0	1.5438	3.1570	5.5275	$\mp 73\% \lvert 7/2\rangle \mp 11\% \lvert 3/2\rangle$ $\pm 10\% \lvert 5/2\rangle \pm 7\% \lvert 1/2\rangle$
2	103.22	148.43	1.5490	2.2270	5.8914	$\pm 53\% \lvert 3/2\rangle \mp 26\% \lvert 1/2\rangle$ $\pm 11\% \lvert 7/2\rangle \mp 11\% \lvert 5/2\rangle$
3	177.12	254.70	2.7745	1.9524	0.8674	$\pm 52\% \lvert 5/2\rangle \mp 22\% \lvert 1/2\rangle$ $\mp 18\% \lvert 3/2\rangle \mp 8\% \lvert 7/2\rangle$
4	255.31	367.14	0.8459	2.0183	5.0007	$\mp 46\% \lvert 1/2\rangle \mp 28\% \lvert 5/2\rangle$ $\pm 18\% \lvert 3/2\rangle \pm 8\% \lvert 7/2\rangle$

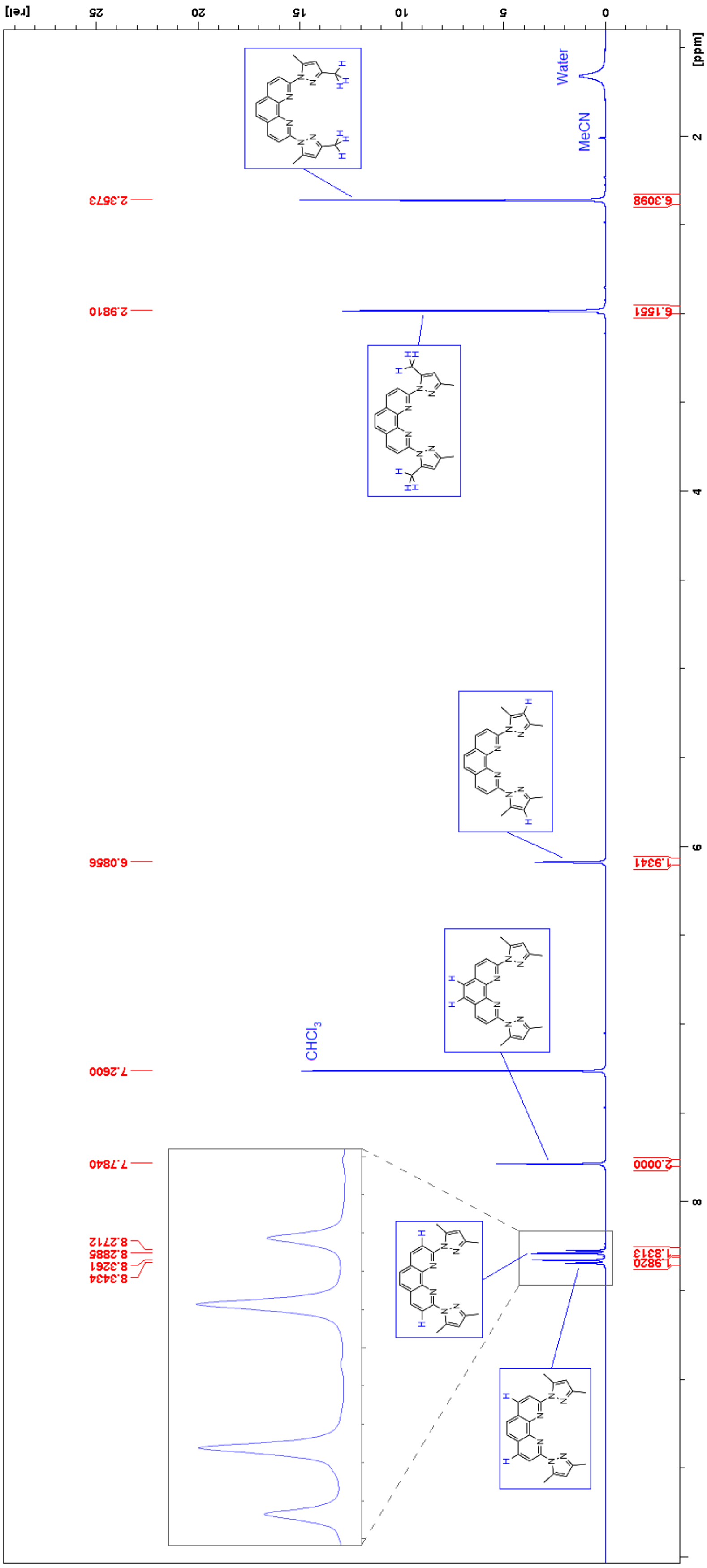

Figure 9.1: NMR spectrum of L$_{Me}$ recorded in CDCl$_3$.

10 List of Publications

1 S. Schlittenhardt, E. Moreno-Pineda, M. Ruben, *Heteroleptic, polynuclear dysprosium(III)-carbamato complexes through in situ carbon dioxide capture*, Dalton Trans., 2021, **50(13)**, 4735 - 4742.

2 R. F. Pfleger, S. Schlittenhardt, M. P. Merkel, M. Ruben, K. Fink, C. E. Anson, J. Bendix, A. K. Powell, *Terminal Ligand and Packing Effect on Slow Relaxation in an Isostructural Set of* $[Dy(H_2dapp)X_2]^+$ *Single Molecule Magnets*, Chemistry - A European Journal, 2021, **27(61)**, 15085 - 15094.

3 L. Münzfeld, X. Sun, S. Schlittenhardt, C. Schoo, A. Hauser, S. Gillhuber, F. Weigend, M. Ruben, P. W. Roesky, *Introduction of plumbole to f-element chemistry*, Chem. Sci., 2022, **13(4)**, 945 - 954.

4 M. Gebrezgiabher, S. Schlittenhardt, C. Rajnak, A. Sergawie, M. Ruben, M. Thomas, R. Boca, *A Tetranuclear Dysprosium Schiff Base Complex Showing Slow Relaxation of Magnetization*, Inorganics, 2022, **10(5)**, 66.

5 Y. Bayeh, N. Suryadevara, S. Schlittenhardt, R. Gyepes, A. Sergawie, P. Hrobarik, W. Linert, M. Ruben, M. Thomas, *Investigations on the Spin States of Two Mononuclear Iron(II) Complexes Based on N-Donor Tridentate Schiff Base Ligands Derived from Pyridine-2,6-Dicarboxaldehyde*, Inorganics, 2022, **10(7)**, 98.

6 M. Gebrezgiabher, S. Schlittenhardt, C. Rajnak, J. Kuchar, A. Sergawie, J. Cernak, M. Ruben, M. Thomas, R. Boca, *Triangulo-*(Er_3^{III}) *complex showing field supported slow magnetic relaxation*, RSC Advances, 2022, **12(33)**, 21674 - 21680.

7 M. Gebrezgiabher, S. Schlittenhardt, C. Rajnak, J. Kuchar, A. Sergawie, J. Cernak, M. Ruben, M. Thomas, R. Boca, *A dinuclear dysprosium Schiff base complex showing slow magnetic relaxation in the absence of an external magnetic field*, New Journal of Chemistry, 2022, **46(35)**, 16702 - 16707.

8 F. Elemo, S. Schlittenhardt, T. Sani, C. Rajnak, W. Linert, R. Boca, M. Thomas, M. Ruben, *Field-Induced Single Molecule Magnetic Behavior of Mononuclear Cobalt(II) Schiff Base Complex Derived from 5-Bromo Vanillin*, Inorganics, 2022, **10(8)**, 105.

9 P. Singh, S. Schlittenhardt, D. Thakre, S. K. Kushvaha, S. Kumar, H. S. Karnamkkott, M. Ruben, M. Ibrahim, A. Banerjee, *Exploration of vanadium(IV)-Based Single-Ion Magnet Properties in Diphosphonate-Supported Mixed-Valent Polyoxovanadates*, Cryst. Growth Des., 2022, **22(9)**, 5666 - 5679.

10 T. Ruppert, S. Schlittenhardt, N. Suryadevara, O. Fuhr, C. A. Anson, M. Ruben, A. K. Powell, *Keeping dysprosium in line: Trinuclear heterometallic* $M_2^{II}Dy^{III}$ *complexes with M = Cd, Co and Cu*, Zeitschrift für Anorganische und Allgemeine Chemie, 2022, **648(17)**, e202200107.

11 A. Reiss, S. Schlittenhardt, M. Ruben, C. Feldmann, *Room-Temperature Oxidation of Thulium-Metal nanoparticles to the Thulium Oxocluster* $[Tm_5O(O^iPr)_{13}]$, Zeitschrift für Anorganische und Allgemeine Chemie, 2022, **648(24)**, e202200299.

12 A. Hauser, L. Münzfeld, S. Schlittenhardt, R. Köppe, C. Uhlmann, U.-C. Rauska, M. Ruben, P. W. Roesky, *Molecular cyclo-*P_3 *complexes of the rare-earth elements via a one-pot reaction and selective reduction*, Chem. Sci., 2023, **14(8)**, 2149 - 2158.

13 J. Jurakova, O. F. Fellner, S. Schlittenhardt, S. Vavreckova, I. Nemec, R. Herchel, E. Cizmar, V. T. Santana, M. Orlita, D. Gentili, G. Ruani, M. Cavallini, P. Neugebauer, M. Ruben, I. Salitros, *Neutral cobalt(II)-bis(benzimidazole)pyridine field-induced single-ion magnets for surface deposition*, Inorg. Chem. Front., 2023, **10**, 5406 - 5419.

14 T. Ruan, E. Moreno-Pineda, M. Schulze, S. Schlittenhardt, T. Brietzke, H.-J. Holdt, S. K. Kuppusamy, W. Wernsdorfer, M. Ruben, *Hilbert Space in Isotopologue Dy(III) SMM Dimers: Dipole Interaction Limit in* $[^{163/164}Dy_2(tmhd)_6(tape)]^0$ *Complexes*, Inorg. Chem., 2023, **62(37)**, 15148 - 15156.